HAL
open science

Role of air-sea-land interactions on the marine boundary layer dynamics in the upwelling region off Central Chile

Orlando Astudillo

To cite this version:

Orlando Astudillo. Role of air-sea-land interactions on the marine boundary layer dynamics in the upwelling region off Central Chile. Ocean, Atmosphere. Université Paul Sabatier - Toulouse III, 2018. English. NNT : 2018TOU30360 . tel-02924557

HAL Id: tel-02924557

https://theses.hal.science/tel-02924557v1

Submitted on 28 Aug 2020

HAL is a multi-disciplinary open access archive for the deposit and dissemination of scientific research documents, whether they are published or not. The documents may come from teaching and research institutions in France or abroad, or from public or private research centers.

L'archive ouverte pluridisciplinaire **HAL**, est destinée au dépôt et à la diffusion de documents scientifiques de niveau recherche, publiés ou non, émanant des établissements d'enseignement et de recherche français ou étrangers, des laboratoires publics ou privés.

THÈSE

En vue de l'obtention du

DOCTORAT DE L'UNIVERSITÉ DE TOULOUSE

Délivré par : *l'Université Toulouse 3 Paul Sabatier (UT3 Paul Sabatier)*

Présentée et soutenue le *31/08/2018* **par :**

Orlando ASTUDILLO

Rôle des interactions océan-atmosphère-continent sur la dynamique de la couche limite marine dans la région d'upwelling du Chili Central

---

JURY

Sylvain COQUILLAT	Professeur	Président du Jury
Boris DEWITTE	Directeur de Recherche	Directeur de thèse
Marc MALLET	Chargé de Recherche	Co-directeur de thèse
Xavier CAPET	Directeur de Recherche	Rapporteur
René GARREAUD	Professeur	Rapporteur
Abderrahim BENTAMY	Chargé de Recherche	Examinateur
Christine PROVOST	Directeur de Recherche	Examinateur
Aurore VOLDOIRE	Chargé de Recherche	Examinateur

École doctorale et spécialité :
SDU2E : Océan, Atmosphère, Climat
Unité de Recherche :
Laboratoire d'Études en Géophysique et Océanographie Spatiales (UMR 5566)
Directeur(s) de Thèse :
Boris DEWITTE et *Marc MALLET*
Rapporteurs :
Xavier CAPET et *René GARREAUD*

I would like to dedicate this thesis to:

Angélica, my dearest wife, who led me through this trip of learnings, efforts and discoveries with all her light of love, hope and support,

My beloved parents, Diogena and Orlando, who always give everything for his sons in countless ways,

My beloved sisters and brothers who encourage and support me always,

My nephews and nieces who always keep in my heart a big portion of tenderness and love.

Acknowledgements

I am very grateful to the many people who have support me along the development of this thesis.

First, I would like to acknowledge my supervisor, Dr. Boris Dewitte, for his help and advice during my period of research. I really appreciate all his contributions of scientific ideas and methods. I would also like to thank my co-supervisors, Dr. Marc Mallet and Dr. José Rutllant, for their valuable guidance during my studies. I am also thankful to my research collaborators Dr. Frédéric Frappart, Dr. Katerina Goubanova, Dr. Luis Bravo, Dr. Serena Illig and Dr. Oscar Pizarro for his constructive comments and advices, which were of great help to improve this research. I am especially grateful to my former advisor Dr Melitta Fiebig and my colleague Dr. Marcel Ramos for introduce me into the numerical modeling of the atmosphere and ocean, encouraging me to pursue a Ph.D.

I would further like to thank to the Directors and Administrative members of the Laboratoire d'Études en Géophysique et Océanographie Spatiales (LEGOS), the Doctoral Department Sciences de l'Univers, de l'Environnement et de l'Espace (SDU2E) and the Université TOULOUSE III Paul Sabatier for allowing me to undertake this work.

Lastly, I would like to gratefully acknowledge the financial support of the Centro de Estudios Avanzados en Zonas Áridas (CEAZA). My thanks are also extended to Dr. Bernardo Broitman, Dr. Carlos Olavarría and Claudio Vazquez, Executive Directors and Corporate Manager of CEAZA, who endorsed my PhD. pursuit.

Résumé

Les systèmes de courant de bords est (EBUS) sont les régions océaniques des latitudes tropicales à moyennes le long des côtes ouest des continents. Ils abritent des écosystèmes marins très productifs en raison de la circulation atmosphérique de surface dirigée vers l'équateur qui font remonter des eaux profondes froides (upwelling) enrichies en éléments nutritifs à l'origine de la vie marine le long de la côte. Si les processus océaniques fondamentaux de l'upwelling côtier sont bien connus (transport et pompage d'Ekman), la modélisation océanique des EBUS reste problématique en raison des difficultés pour prendre en compte de manière réaliste des phénomènes à fine échelle spatiale dans la zone de transition entre le littoral et l'océan du large.

Dans cette thèse, nous nous sommes concentrés sur le système d'upwelling dit de Humboldt (côtes du Pérou et du Chili) et sur l'influence des caractéristiques méso-échelles des vents près de la côte, en particulier la décroissance vers la cotes du vent (appelé "drop-off") qui détermine l'importance relative des processus d'Ekman, et donc, la structure spatiale de la zone d'upwelling. Une approche combinée basée sur l'analyse de données satellitaires et sur la modélisation régionale, océanique et atmosphérique, est utilisée pour étudier la sensibilité de la circulation océanique le long de la côte Chili central aux caractéristiques du drop-off.

Dans un premier temps, la circulation atmosphérique de surface moyenne à saisonnière le long du littoral du Pérou et du Chili est documentée pour la première fois à partir des données altimétriques de quatre missions satellites (ENVISAT, JASON1, JASON2 et SARAL). L'analyse révèle l'existence d'une réduction marquée de la vitesse du vent le long de la côte, bien que le taux de réduction varie en fonction de la latitude. Malgré la répétitivité relativement faible des satellites, nous montrons que les données altimétriques permettent néanmoins d'échantillonner le cycle saisonnier du drop-off. L'estimation de l'upwelling côtier à partir de ces données suggère que le pompage d'Ekman

tend en moyenne à dominer par rapport au transport d'Ekman le long de la côte péruvienne, alors que le long de la côte chilienne, le transport d'Ekman est le processus dominant.

Dans un second temps, un modèle atmosphérique régional (WRF) à différentes résolutions horizontales (36 km, 12 km et 4 km) dans une configuration imbriquée zoomée sur la région centrale du Chili a été développé afin de produire des champs atmosphériques présentant des caractéristiques différentes du drop-off. Les solutions du modèle atmosphérique sont d'abord évaluées par rapport aux observations, indiquant un plus grand réalisme près de la côte que les réanalyses atmosphériques. Le rotationnel du vent cyclonique simulé le long de la côte associé au drop-off présente des échelles transversales comprises entre 8 et 45 km avec une variabilité latitudinale significative, en accord avec les vents altimétriques. Lorsque la résolution du modèle est augmentée, le drop-off est généralement d'autant plus confiné à la côte et le modèle indique une saisonnalité marquée avec un maximum d'intensité au printemps-automne. La contribution relative de la divergence côtière et du pompage d'Ekman présente une modulation latitudinale liée aux détails de l'orographie et de la ligne de côte.

Des expériences avec un modèle océanique régional (ROMS) sont ensuite réalisées pour estimer et comprendre l'influence du drop-off sur la circulation océanique et la dynamique de l'upwelling. Il est montré que la prise en compte d'un drop-off plus réaliste dans le forçage atmosphérique côtier induit à une réduction notoire de l'intensité du jet océanique côtier de surface, un sous-courant plus fort et une dérive d'Ekman cohérente avec les observations disponibles. Les analyses de l'énergie cinétique turbulente et des flux de chaleur turbulent illustrent la réponse non linéaire de la dynamique d'upwelling à la représentation des caractéristiques du vent à méso-échelle. En particulier, alors que la prise en compte du vent dans le forçage atmosphérique du modèle océanique régional conduit à une réduction globale du biais froid côtier observé dans les simulations des modèles océaniques régionaux forcés par les produits atmosphériques couramment utilisés (i.e. Reanalyses globales et vents diffusiometriques), les résultats suggèrent également qu'il influence la dynamique de la couche limite de fond et de surface dans certaines régions et donc la position du front d'upwelling. Nous discutons l'implication de nos résultats pour l'amélioreration des forçages atmosphériques dédiés à la modélisation océanique régionale dans les EBUS.

Abstract

Eastern Boundary Upwelling Systems (EBUS) are the tropical to mid-latitudes oceanic regions along the west coast of the continents. They host very productive marine ecosystems owing to the mean equatorward low-level atmospheric circulation that uplifts cool subsurface nutrient-enriched waters that trigger marine life along the coast. While the fundamental oceanic processes behind such process are well known (i.e. Ekman transport and pumping), the oceanic modeling of the EBUS has remained problematic owing to difficulties in accounting realistically for phenomena at fine spatial scales in the transition zone between the littoral and the off-shore ocean.

In this thesis we have focused on the Peru-Chile Upwelling System (so-called Humboldt system) and on the influence of the cross-shore mesoscale features of the winds near the coast, particularly the shoreward wind drop-off, which determinate the relative importance of the Ekman processes, and thus, the spatial and temporal structure of the upwelling. A combined approach based on satellite data analysis and regional modeling, both oceanic and atmospheric, is used to investigate the sensitivity of the oceanic circulation along the coast of central Chile to the characteristics of the wind drop-off.

As a first step, the mean to seasonal near-shore surface atmospheric circulation along the coast of Peru and Chile is documented for the first time based on the altimeter data from four satellite missions (ENVISAT, JASON1, JASON2 and SARAL). The analysis reveals the existence of a marked shoreward reduction in the wind speed all along the coast, although the reduction rate is latitudinally dependent. Despite the relatively weak repetitivity of the satellites, it is shown that the altimetric data are able to sample the seasonal cycle of the wind drop-off at some locations. The estimate of coastal upwelling from these data suggests that Ekman pumping tends on average to dominate with respect to Ekman transport over the Peruvian coast, whereas over the central-Chilean coast, the Ekman transport is the dominant process.

In a second step, a regional atmospheric model (WRF) at different horizontal resolutions (36km, 12km and 4km) in a nested configuration zoomed over the central-Chile region was developed in order to produce atmospheric fields with different characteristics of the wind-stress curl (drop-off) along the coast. The atmospheric model solutions are first evaluated against the satellite observations, showing a much larger realism than atmospheric Reanalyses near the coast. In particular, the simulated cyclonic wind curl along the coast related to the wind drop-off exhibit length scales between 8 and 45 km with a significant latitudinal variability, which is in agreement with the altimetric winds. The higher model resolution, the more confined to the coast the wind drop-off, with the latter evidencing a marked seasonality with a maximum intensity in spring-fall and minimum in winter. The relative contribution of the coastal divergence and Ekman pumping exhibits a latitudinal modulation linked to details in the orography and coastlines.

Experiments with a regional oceanic model (ROMS) are then carried out to estimate the dynamical impacts of the representation of the drop-off in the atmospheric forcing of the ocean model. It is shown that the consideration of a realistic wind drop-off in the coastal atmospheric forcing induces a notorious reduction in the oceanic coastal jet intensity, a stronger poleward undercurrent and a coherent offshore Ekman drift in agreement with available observations. Additionally, the analyses of the Eddy Kinetic Energy and eddy heat flux in the various sensitivity experiments illustrate the non-linear response of the upwelling dynamics to the representation of the mesoscale wind features. In particular, while the consideration of the wind drop-off in the atmospheric forcing of the regional oceanic model yields an overall reduction of the coastal cold bias found in the regional oceanic model simulations forced by commonly used available atmospheric products, the results also suggest that it can influence the surface and bottom boundary layers in some regions and thus the position of the upwelling front. Implications of our results for the improvement of regional oceanic modeling in EBUS are discussed.

Contents

1 Introduction **1**

1.1 Preamble 1

1.2 The Eastern Boundary Upwelling Systems 2

1.2.1 The Carbon Cycle and Oceanic Carbon Pumps 4

1.2.2 The Role of Upwelling in the Carbon Cycle 6

1.2.3 The Oxygen Minimum Zone 7

1.2.4 Eastern Boundary Upwelling System Dynamics 9

1.3 Scientific Focus, State of the Art, Motivations and Objectives 20

1.3.1 Climate Model Biases in the EBUS, Causes and Impacts 22

1.3.2 Coupled Climate Systems of the Southeast Pacific 24

1.3.3 Atmospheric Circulation, Coastal Wind Variability 26

1.3.4 Response of the PCUS to Coastal Mesoscale Wind Structure 28

1.3.5 Impact of the Wind Stress Forcing on Coastal Circulation 29

1.3.6 The Impact of Mesoscale Wind Patterns on Biological Productivity 32

1.3.7 Mechanism of Air-Sea-Land Interaction 33

1.3.8 PCUS Dynamics Under Climate Change 35

1.3.9 Scientific Objectives and Methodology 37

1.4 Introduction (Français) 39

2 The Mesoscale Atmospheric Circulation Along the Coast of Peru and Chile **41**

2.1 Introduction 41

2.2 Surface Winds Off Peru-Chile: Observing Closer to the Coast From Radar Altimetry: An Observational Study 41

3 Seasonal Dynamics Off the Central Chile Upwelling System **60**

3.1 Introduction 60

3.2 Seasonal Variability of the Ekman Dynamics in the Upwelling System Off Central-Northern Chile (∼30°S): a Modeling Study 61

4 Response of the Central Chile Upwelling System to Coastal Wind Drop-Off 79
4.1 Introduction 79
4.2 Sensitivity of the Near-Shore Oceanic Circulation Off Central Chile to Coastal Wind Profiles Characteristics 79

5 General Conclusions and Future Work 113
5.1 Conclusions et Perspectives (Français) 119

List of Abbreviations 124

Bibliography 127

Chapter 1

Introduction

1.1 Preamble

Eastern Boundary Upwelling Systems (EBUS) are characterized by the phenomenon of rising cold waters under the action of winds parallel to the coast blowing towards the equator. These regions also correspond to the zones of subsidence of dry air masses associated with the descending branches of Hadley-Walker circulation. These atmospheric and oceanographic characteristics of the circulation make it the site of specific air-sea interactions with in particular the formation of a low cloud cover (stratocumulus type) which reflects the solar flux and amplifies the cooling effect of upwelling. Currently the global models are failing to simulate circulation in these regions with the most important warm bias of the tropical belt.

This is particularly the case for the Humboldt Current System (HCS; Peru-Chile coasts), the most productive upwelling region in the world in terms of fisheries. The source of the biases in global models remains poorly known, although it is partly related to the generally too low resolution of these models to realistically simulate the upwelling phenomenon on the one hand and the structure of near-shore winds on the other hand. The latter are in fact characterized by a decrease from the ocean to the coast in a coastal strip of the order of a few dozen kilometers. This phenomenon, called "drop-off" conditions the dynamics of upwelling through the Ekman pumping process. In return, upwelling favors a stable atmospheric boundary layer and therefore low-level winds are decoupled from the winds aloft. This process of interaction between the ocean and the atmosphere on a regional scale is still poorly understood and documented. However, it could be a key element in understanding the dynamics of these regions, which are highly sensitive to changes in global variability.

In order to better understand the dynamics of the Peru-Chile Upwelling System (PCUS), the

study area of this thesis, as well to introduce the mechanisms of air-sea-land interactions in PCUS and its implications on upwelling dynamics, this first chapter will present the main aspects of the EBUS, including the significant role that the coastal upwelling plays in the cycles of carbon and biological productivity. Following, we will describe the main processes that affect the EBUS mean circulation and upwelling variability. Finally, this introductory chapter concludes with the presentation of the scientific focus and motivations of the thesis, along with detailing the objectives and methodological approach.

1.2 The Eastern Boundary Upwelling Systems

Eastern Boundary Upwelling Systems (EBUS) are among the most productive marine ecosystems of the world oceans. While they cover only a tiny fraction of the ocean surface ($\sim$1%), they are responsible for most marine biomass production and account for $\sim$20% of the world's fisheries (Fréon et al., 2009; Narayan et al., 2010). The four main EBUSs, California, Canary/Iberian, Benguela and Humboldt Currents Systems (HCS) are narrow regions of the coastal ocean that extend latitudinally over several thousands of kilometers and longitudinally to beyond the continental shelves whose widths ranging from 10 to 200 km. They are located, on the one hand, in the eastern part of the oceans, and on the other hand, on each side of the Equator from 10-20° in latitude, which are outlined in white in Figure 1.1a. In these regions, intense equatorward, alongshore winds combined with the earth's rotation cause offshore surface Ekman transport, subsurface onshore flow and upwelling of water that is rich in nutrients, low in temperature (sometimes 10°C below the average of normal temperatures at these latitudes), depleted oxigen, and pH. The arrival of nutrients in the surface waters illuminated by the sun (euphotic zone) triggers an exceptionally biological productivity (Carr, 2001; Strub et al., 2013), as illustrated in Figure 1.1b by the high chlorophyll concentrations, a typical proxy for the amount of photosynthetic plankton, or phytoplankton (floating marine plants), present in the ocean. The numerous variety of marine life includes low trophic organisms like bacteria and photosynthetic plants (e.g., sea grasses, seaweeds, and phytoplankton), and larger animals (e.g., zooplankton, crustaceans, fish, birds and mammals), that interact through complex food webs.The dynamics of these interactions are based on the uptake of simple inorganic chemicals and their conversion to more complex organic material by bacteria and phytoplankton, these organisms are known as autotrophs because they produce their own organic matter. Higher on the food web they sustain heterotrophic organisms that require pre-manufactured organic matter (Kämpf and Chapman, 2016).

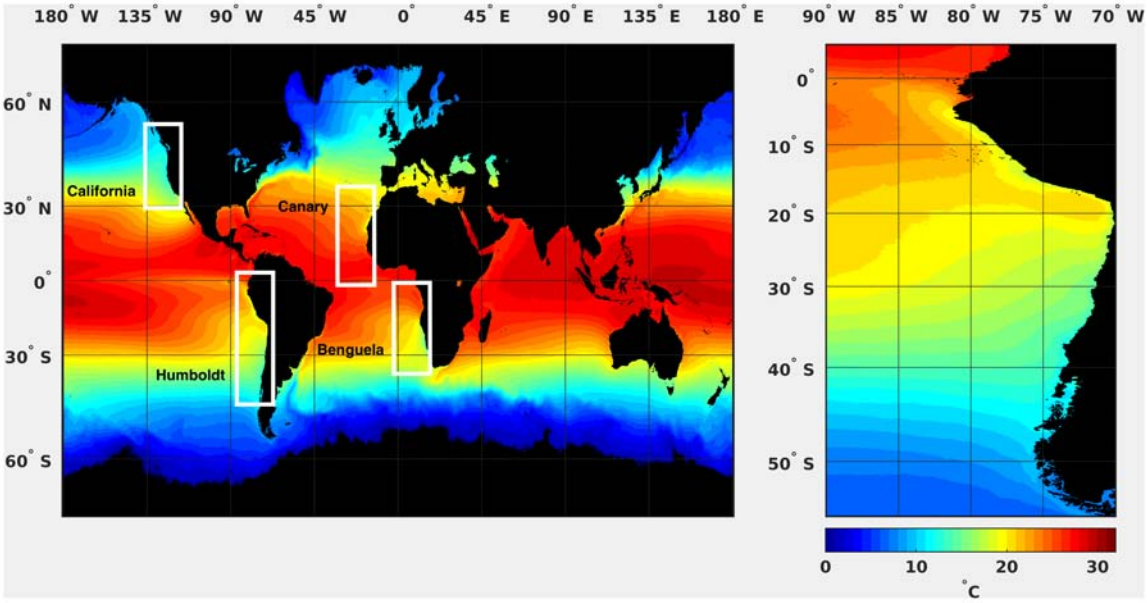

(a) Global mean sea surface temperature (in °C - left panel), with the eastern boundary upwelling systems(EBUS) characterized by cold SST indicated in white boxes, and a zoom over the Humboldt current system (in °C - right panel). From MODIS Aqua (2002-2017).

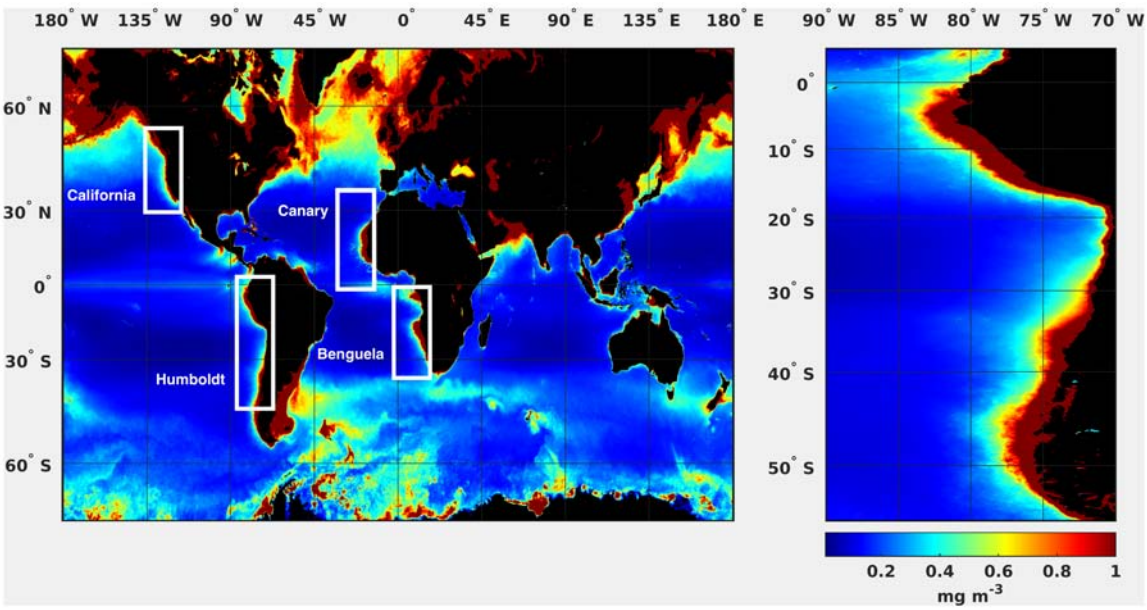

(b) Global mean surface chlorophyll a concentration (in mg m^{-3} - left panel). From MODIS Aqua (2002-2017).

Figure 1.1

1.2.1 The Carbon Cycle and Oceanic Carbon Pumps

The basis for these marine ecosystems is the light-induced photosynthesis carried out by phytoplankton and phototropic bacteria confined to the upper 50 - 100 m of the water column. Through carbon fixation there is conversion of inorganic to organic carbon, which allows marine organisms to grow and reproduce while producing oxygen as a by-product. During photosynthesis, phytoplankton fixes the dissolved inorganic carbon and assimilates nutrients (nitrates, phosphates, silicates, iron, etc.) that are available in the euphotic layer. When the organisms die, part of the organic matter already synthesized is degraded (or remineralized) by bacteria carrying out ammonification then nitrification in the euphotic layer, and the other part is exported to the deep layers where is remineralized or stored in sediments. The rate of carbon fixation is strongly controlled by the availability of nutrients through out dynamical processes. Nutrients are supplied to the euphotic zone via upwelling, vertical mixing, continental runoff of sediment-laden waters via rivers or groundwater seepage, and to some extent by atmospheric dust deposition. Iron is the main limiting nutrient for the upwelling regions of the Humboldt Current (Hutchins et al., 2002); and the California Current (Chase et al., 2007; Hutchins et al., 1998).

The global carbon cycle is the interaction of both biogeochemistry and physics within the ocean; it plays a major role in regulating climate by controlling the amount of the greenhouse gas CO_2 in the atmosphere. From the start of the industrial revolution in the mid-18th century, the atmospheric carbon budget has been substantially disturbed through human activities, such as fossil fuel combustion and cement manufacture, so that the pre-industrial atmospheric CO_2 concentration of about 270 ppm now exceeds 403 ppm and is continuing to increase. Roughly 50 % of the CO_2 produced by human activities is taken up by the ocean, the remainder staying in the atmosphere where it contributes to global warming (Kämpf and Chapman, 2016).

The oceanic carbon cycle can be described by different carbon pumps (See Fig. 1.2), each describing specific mechanisms that transfer carbon dioxide from the upper to the deep ocean or vice versa. These pumps are the *solubility pump* and the *biological pump*. Phytoplankton is the engine of the *biological pump* (responsible for 80 % of total carbon fixation in the ocean) that helps maintain a steep gradient of CO_2 between the atmosphere and deep ocean. The biologic pump comprises

a) the organic carbon pump, associated with primary production in the euphotic zone and remineralization of detritus at depths.

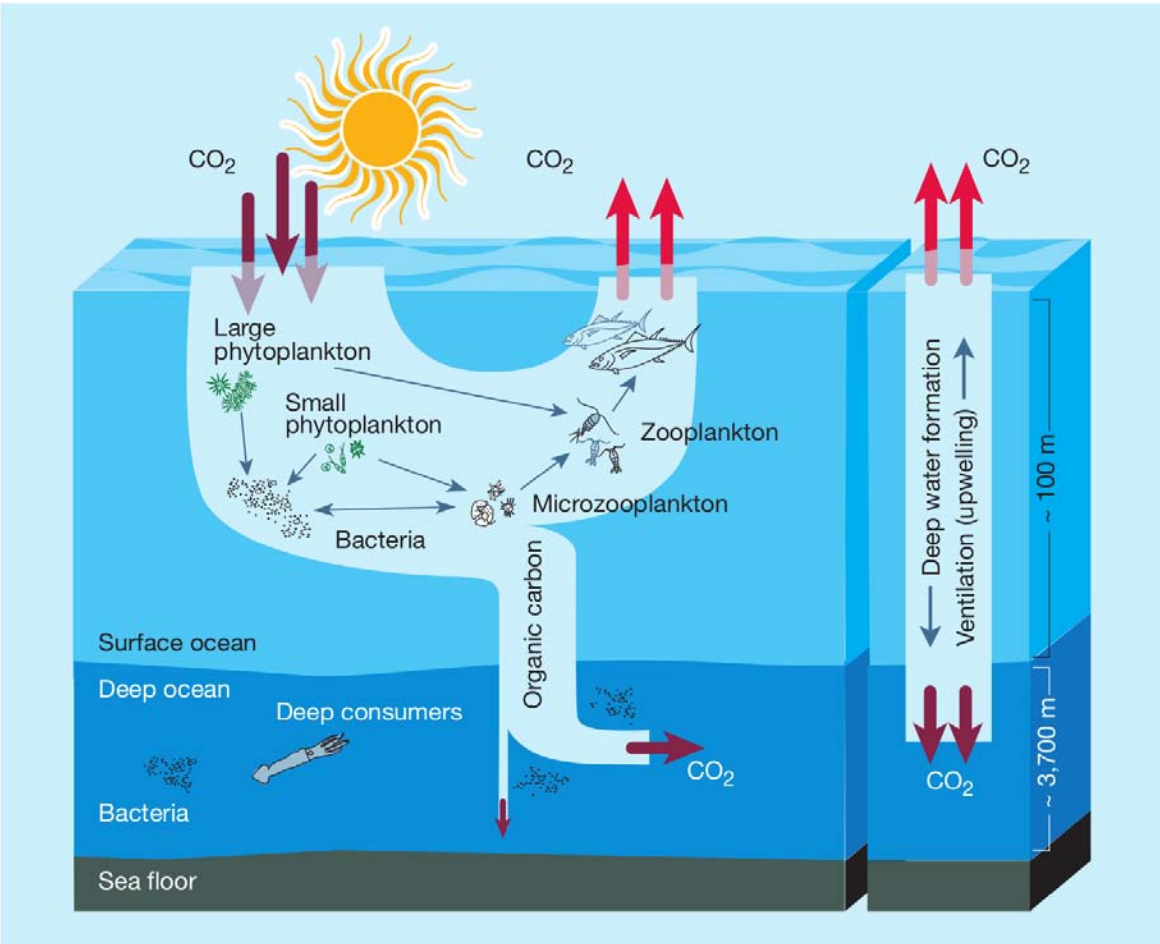

Figure 1.2. Sketch of the basic oceanic carbon cycle: on the left hand side, the *biological pump*, which is a collective property of a complex phytoplankton-based food web; on the right hand side the *solubility pump*, which is driven by chemical and physical processes, both mechanisms transfer carbon dioxide from the upper to the deep ocean or vice versa, maintaining a sharp gradient of CO_2 between the atmosphere and the deep ocean. From Chisholm (2000).

b) the calcium carbonate counter pump, associated with skeleton and shell formation in the surface ocean and the dissolution of calcareous particles at depth.

The *solubility pump* is responsible for about 20 % of the vertical gradient in dissolved inorganic carbon in the ocean. The *solubility pump* is based on:

a) the temperature dependency of the solubility of carbon dioxide in seawater; i.e. under the same atmospheric conditions, cold water can dissolve more CO_2 than warm water before it reaches an equilibrium with the atmosphere.

b) oceanic flows that either export surface water to the ocean interior (called oceanic subduction) or bring deeper cold water back to the sea surface (upwelling).

The deep circulation of the oceans driven by open-ocean convection in sub-polar regions of the North Atlantic Ocean is generally known as one of the branches of the *solubility pump*. The other branch is the reverse process of upwelling in which CO_2 enriched deeper water is returned to the sea surface (Kämpf and Chapman, 2016; Sarmiento et al., 1995).

EBUS have been classified as Large Marine Ecosystems (LMEs) in the first productivity category (>300 g C/m^2/yr), according to their annual Gross Primary Productivity (GPP), that is, the rate of conversion of CO_2 to organic carbon per unit surface area by autotrophic organisms (Sherman and Hempel, 2008), while respiration refers to the energy-yielding oxidation of organic carbon back to carbon dioxide. The basic equation is the same in both cases, although the two mechanisms operate in reverse. The chemical reactions is:

$$Energy + nutrients + 6CO_2 + 6H_2O \leftrightarrow C_6H_{12}O_6 + 6O_2 \tag{1.1}$$

where CO_2 is carbon dioxide, H_2O is the water molecule, energy comes from solar radiation, nutrients are the nutritive salts, $C_6H_{12}O_6$ is a sugar molecule and O_2 is the oxygen molecule. Hence, primary production results in a decrease in carbon dioxide with production of oxygen, while respiration uses up the oxygen to break down organic matter. The process of respiration occurs continuously, while primary production in the surface ocean waters can only take place during daylight (Kämpf and Chapman, 2016).

1.2.2 The Role of Upwelling in the Carbon Cycle

Coastal upwelling regimes associated with eastern boundary currents are the "engine" of GPP and marine productivity in the ocean. Indeed, they play a key role in the microbially mediated cycling of marine nutrients. These systems are characterized by strong natural variations in carbon dioxide concentrations, pH, nutrient levels and sea surface temperatures on both seasonal and interannual timescales (Capone and Hutchins, 2013).

From a biological point of view, EBUS would represent carbon sinks since in the long-term the high CO_2 fixation by phyto-plankton production exceeds plankton community respiration. However, in spite of their high productivity, upwelling systems can facilitate an outgassing of CO_2 into the atmosphere when atmospheric heating reduces the solubility of CO_2 (Paulmier and Ruiz-Pino, 2009). The production of other greenhouse gases, like nitrogen dioxide, methane and other volatile gases, may potentially trigger further acidification of

EBUS (Checkley and Barth, 2009). Certain phytoplankton groups are also known to contribute to increased fluxes of dimethyl-sulphide (Franklin et al., 2009), a trace gas involved in the global biogeochemical cycling of sulphur, which influences climate by inducing aerosol and cloud formation in the atmosphere. On the other hand, the high biological productivity of EBUS generates a significant amount of organic detritus (dead organic matter), this organic matter is degraded in the water column and/or at the sediment by bacterial activity. During the remineralization process, a large amount of O_2 is consumed, thus explaining the reduction of the oxygen concentration below the mixing layer and the formation of Oxygen Minimum Zones (OMZ), see Fig. 1.3.

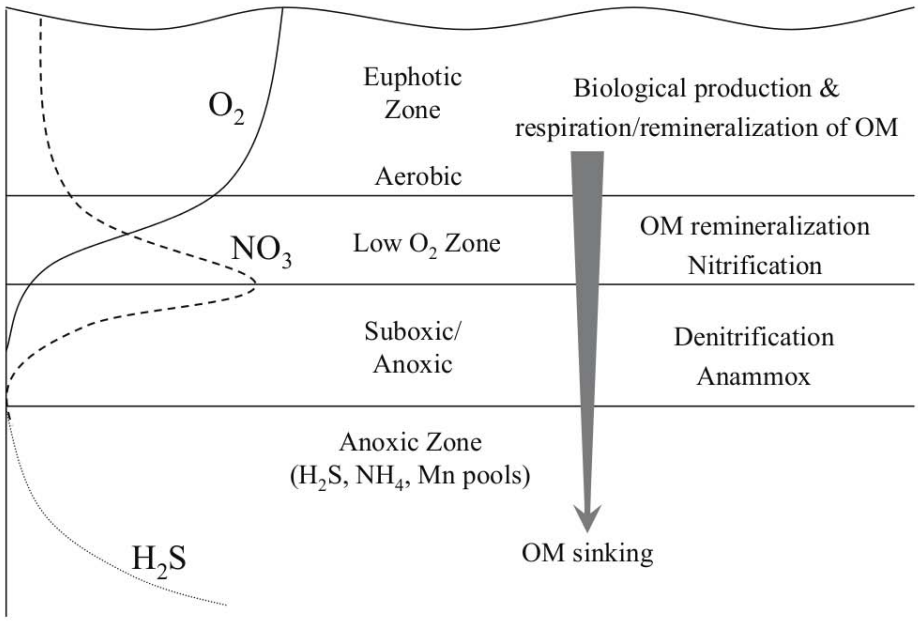

Figure 1.3. Schematic vertical profile of water column processes showing the well oxygenated euphotic zone, oxycline/upper nutricline region, suboxic zone and anoxic layer. OM=organic matter. From Peña et al. (2010).

1.2.3 The Oxygen Minimum Zone

These are regions in the ocean tightly coupled to the EBUS (See Fig. 1.4), they are characterized by extremely low concentrations of Dissolved Oxygen (DO) in the water column (DO < 60 µM), and may frequently reach values of DO lower than 40 µM, in the suboxia range (Naqvi et al., 2010), or even lower levels may also be found in certain areas (Schunck et al., 2013; Ulloa et al., 2012).

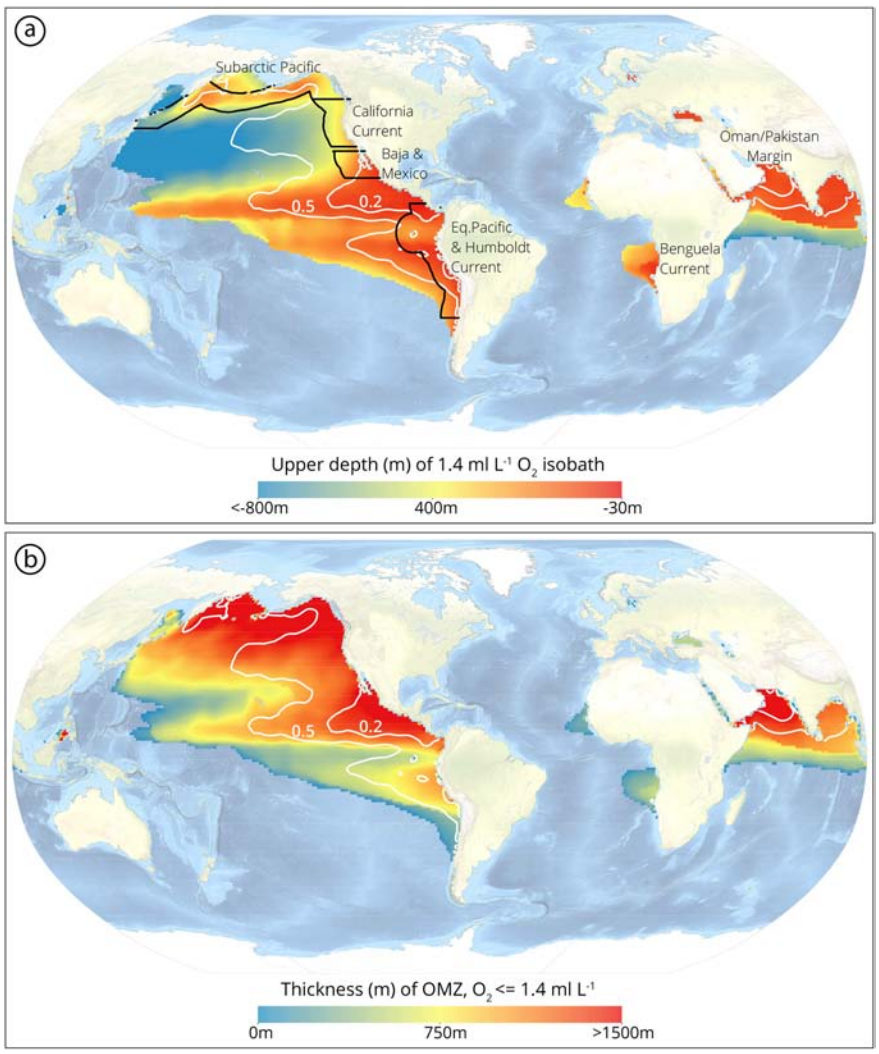

Figure 1.4. Global Oxygen Minimum Zones, including **(a)** Upper depth (in meters) of intermediate water hypoxia ($[O_2]$<1.4 ml L^{-1}) and **(b)** thickness (in meters) of intermediate water hypoxia ($[O_2]$<1.4 ml L^{-1}). The geospatial distributions of severely hypoxic $[O_2]$ minimums (of $[O_2]$ = 0.5 ml L^{-1} and $[O_2]$ = 0.2 ml L^{-1}) are depicted on both panels as white lines. Data from World Ocean Atlas. From Moffitt et al. (2015).

OMZs form at shelf and upper slope depths, and are considered to be unique biological, geochemical and evolutionary environments, analogous to cold seep or deep-sea vent environments (Moffitt et al., 2015). As continental margin ecosystems transition from well oxygenated surface waters to the hypoxic core of the OMZ ($[O_2]$ = 0.5–0.1 ml L^{-1}), faunal diversity, trophic structures and physiological strategies change (Levin et al., 1991). OMZ oxygenation gradients produce successional biological zonation and are fundamental habitat barriers for benthic and pelagic organisms (Moffitt et al., 2015). Additionally, the biogeochemical cycles that take place at extremely low DO concentrations are involved in the local

production of climatically-active gases, such as CO_2 (Paulmier et al., 2006) and N_2O (Kock et al., 2016), which are then outgassed to the atmosphere. In this sense, the OMZ has an impact on both the local ecosystems and on the global climate.

For all these reasons, several international programme such as the Intergovernmental Panel on Climate Change (IPCC), the Integrated Marine Biogeochemistry and Ecosystem Research (IMBeR), the Surface Ocean - Lower Atmosphere Study (SOLAS), the Intergovernmental Oceanographic Commission of UNESCO (IOC-UNESCO) and the United Nations Environment Programme (UNEP) have labeled EBUS a priority study area for the past ten years.

1.2.4 Eastern Boundary Upwelling System Dynamics

Ekman Dynamics

The physical mechanisms that explain the occurrence of coastal upwelling in the EBUS have been known for a long time. Vagn Walfrid Ekman, who studied the ocean response to wind forcing according to the observations of his predecessor the Norwegian scientist and explorer Fridtjof Nansen founded the principles of the upwelling theory in 1905. In the 1890s, Nansen led an expedition across the Arctic ice. His specially designed vessel, the Fram, was allowed to freeze into the ice and drift with it for over a year. During this period, Nansen observed that ice movements in response to wind were not parallel to the wind, but at an angle of 20–40° to the right of it. W. Ekman, a PhD. student in that period, developed his theory of wind-driven currents in order to explain this observation.
First to present the Ekman's solution to wind-driven current we will present the essentials of surface circulation:
Consider quasi-steady, large-scale motions in the atmosphere or the ocean, away from boundaries. For these flows an excellent approximation for the horizontal equilibrium is a balance between the Coriolis force and the pressure gradient:

$$-fv = -\frac{1}{\rho}\frac{\partial p}{\partial x}, \text{ and } fu = -\frac{1}{\rho}\frac{\partial p}{\partial y}. \tag{1.2}$$

Here we have neglected the nonlinear acceleration terms, which are of order U^2/L, in comparison to the Coriolis force $\sim fU$ (U is the horizontal velocity scale, and L is the horizontal length scale). The ratio of the nonlinear term to the Coriolis term is called the

Rossby number:

$$Rossby\ number = \frac{\text{Nonlinear acceleration}}{\text{Coriolis force}} \sim \frac{U^2/L}{fU} = \frac{U}{fL} = Ro. \tag{1.3}$$

For a typical atmospheric value of $U \sim 10\,ms^{-1}$,$f \sim 10^{-4}s^{-1}$ and $L \sim 1000\,km$, the Rossby number turns out to be 0.1. The Rossby number is even smaller for many flows in the ocean ($Ro \sim 10^{-3}$), so that the neglect of nonlinear terms is justified for many flows.
The balance of forces represented by 1.2, in which the horizontal pressure gradients are balanced by Coriolis forces, is called a *geostrophic balance*. In such system the velocity distribution can be determined from a measured distribution of the pressure field. The geostrophic equilibrium breaks down near the equator (within a latitude belt of $\pm 3°$), where f becomes small. It also breaks down if the frictional effects or unsteadiness become important (Cohen et al., 2004).

Ekman Transport

Like the atmosphere, the ocean is a continuous medium and satisfies conservation of mass, momentum and energy. Unlike the atmosphere, the ocean is very nearly incompressible.

$$\frac{\partial u}{\partial x} + \frac{\partial v}{\partial y} + \frac{\partial w}{\partial z} = 0 \text{ continuity equation, incompressible,} \tag{1.4}$$

$$\frac{\mathrm{d}u}{\mathrm{d}t} = -\frac{1}{\rho}\frac{\partial p}{\partial x} + fv + \mathbf{F_x} \approx 0 \text{ u-momentum equation, geostrophic+friction,} \tag{1.5}$$

$$\frac{\mathrm{d}v}{\mathrm{d}t} = -\frac{1}{\rho}\frac{\partial p}{\partial y} - fu + \mathbf{F_y} \approx 0 \text{ v-momentum equation, geostrophic+friction,} \tag{1.6}$$

$$\frac{\mathrm{d}w}{\mathrm{d}t} = -\frac{1}{\rho}\frac{\partial p}{\partial z} - g \approx 0 \text{ z-momentum equation, geostrophic,} \tag{1.7}$$

where $\mathbf{F_x}$ and $\mathbf{F_y}$ stand for the vector components of friction per unit mass in the fluid, z is (close to) zero at the surface and decrease downward. If there are no accelerations (i.e. steady state and zero, or at least negligible advection accelerations), then $\frac{\mathrm{d}u}{\mathrm{d}t} = \frac{\mathrm{d}v}{\mathrm{d}t} = 0$ and we are left with a balance of three forces on unit mass and the **horizontal** equations of motion become:

$$fv + \mathbf{F_x} - \frac{1}{\rho}\frac{\partial p}{\partial x} = 0, \tag{1.8}$$

$$-fu + \mathbf{F_y} - \frac{1}{\rho}\frac{\partial p}{\partial x} = 0, \tag{1.9}$$

i.e. Coriolis + Friction + Pressure = 0
as show schematically in Figure. 1.5.

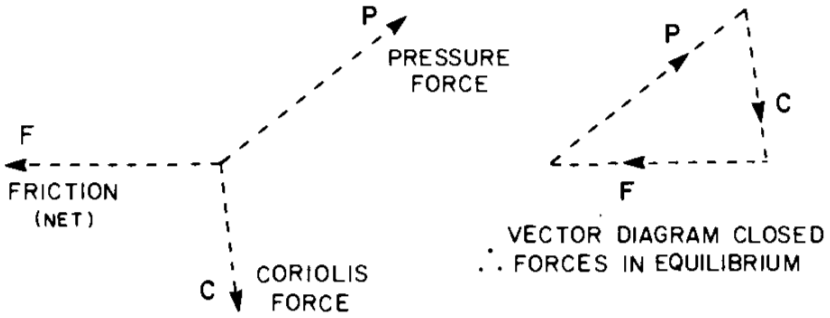

Figure 1.5. Three forces in equilibrium on a water parcel. From Pond and Pickard (1983).

For the frictional forces $\mathbf{F_x}$ and $\mathbf{F_y}$, Newton's Law of Friction states that in a fluid, the friction stress τ, which is the force per unit area on a plane parallel to the flow, is given by

$$\tau = \mu \frac{\partial \mathbf{u}}{\partial z} = \rho \nu \frac{\partial \mathbf{u}}{\partial z}. \tag{1.10}$$

The quantity μ is the coefficient of (molecular) *dynamic* viscosity, while $\nu = \frac{\mu}{\rho}$ is the coefficient of (molecular) *kinematic viscosity*. In the ocean where the motion is generally turbulent, the effective value of kinematic viscosity is the eddy viscosity with values $\mathbf{A}_z$ of up to 10^{-1} $\mathrm{m}^{-2}\mathrm{s}^{-1}$ for vertical shear (e.g. $\frac{\partial \mathbf{u}}{\partial z}$). Then the eddy friction stress $\tau = \rho \mathbf{A}_z \frac{\partial \mathbf{u}}{\partial z}$ express the force of one layer of fluid on an *area* of its neighbour above or below, but for substitution in the equation of motion we need an expression for the force on a *mass* of fluid:

$$\text{the force per unit mass } = \frac{1}{\rho}\frac{\partial \tau}{\partial z} = \frac{1}{\rho}\frac{\partial}{\partial z}\left(\rho \mathbf{A}_z \frac{\partial \mathbf{u}}{\partial z}\right). \tag{1.11}$$

The form of expression 1.11 where A_z is assumed to be constant and consistent with the Boussinesq approximation becomes:

$$\text{friction force per unit mass } = \mathbf{A}_z \frac{\partial^2 \mathbf{u}}{\partial z^2}. \tag{1.12}$$

To simplify the problem, Ekman (1908) assumed the water to be homogeneous and that there was no slope at the surface, so that the pressure terms would be zero. He also assumed an infinite ocean to avoid the complications associated with the lateral friction at the boundaries.

Under these conditions, the horizontal equations of motion reduces to a balance between the Coriolis force and wind friction at the ocean surface (the stress acts along the wind direction):

$$\left.\begin{aligned} \frac{1}{\rho}\frac{\partial p}{\partial x} &= \quad fv + \frac{1}{\rho}\frac{\partial \tau_x}{\partial z} = fv + \mathbf{A}_z\frac{\partial^2 \mathbf{u}}{\partial z^2} = 0 \\ \frac{1}{\rho}\frac{\partial p}{\partial y} &= -fu + \frac{1}{\rho}\frac{\partial \tau_y}{\partial z} = -fu + \mathbf{A}_z\frac{\partial^2 \mathbf{v}}{\partial z^2} = 0 \end{aligned}\right\} \text{the Ekman equations} \tag{1.13}$$

i.e. Coriolis+Friction = 0, as in Figure. 1.6a.
The solution to Ekman's equations are (in the case of a southerly wind):

$$\left.\begin{aligned} u_E &= \pm V_0 \cos\left(\tfrac{\pi}{4} + \tfrac{\pi}{D_E}z\right)\exp\left(\tfrac{\pi}{D_E}z\right), \\ v_E &= \pm V_0 \sin\left(\tfrac{\pi}{4} + \tfrac{\pi}{D_E}z\right)\exp\left(\tfrac{\pi}{D_E}z\right), \end{aligned}\right\} \text{(+(-) for northern(southern) hemisphere)} \tag{1.14}$$

where

$V_0 = \frac{(\sqrt{2}\pi\tau_{y\eta})}{D_E\rho|f|}$ is the total Ekman surface current,

$\tau_{y\eta}$ is the magnitude of the wind stress on the sea surface (approximately proportional to the wind speed squared and acting in the direction of the wind),

$|f|$ is the magnitude of f,

$D_E = \pi\sqrt{\frac{2\mathbf{A}_z}{|f|}}$ is the *Ekman depth* or *depth of frictional influence.*

The surface current is rotated 45° to the right (northern hemisphere) or left (southern hemisphere) of the wind. Further interpretation can be found in Pond and Pickard (1983).
The wind-driven Ekman current has its maximum speed at the surface and the speed decreases with depth. Because the strongest currents are to the right (or left) of the wind direction in the Northern (Southern) Hemispheres, it is easy to appreciate that the net transport will be to the right (or left) of the wind direction (Pond and Pickard, 1983). The basic form of the equations for horizontal motions (equations 1.13) in the absence of any pressure gradient is

$$\rho fv + \frac{\partial \tau_x}{\partial z} = 0 \quad -\rho fu + \frac{\partial \tau_y}{\partial z} = 0 \tag{1.15}$$

which we can write as

$$\rho fvdz = -d\tau_x \quad -\rho fudz = -d\tau_y \tag{1.16}$$

Now $\rho v dz$ is the mass flowing per second in the y-direction through a vertical area of depth dz and width one metre in the x-direction, and $\int_z^0 \rho v dz$ will be the total mass flowing in the y-direction from the level z to the surface for this strip 1 m wide, while $\int_z^0 \rho u dz$ will be the total mass transport per unit width in the x-direction. If we use the symbols M_{yE} and M_{xE} to represent the Ekman mass transport in the y- and x-direction respectively, then

$$\left.\begin{aligned} fM_{yE} &= f\int_{-2D_E}^0 \rho v dz = -\int_{-2D_E}^0 d\tau_x = -\tau_{x\eta} \\ fM_{xE} &= f\int_{-2D_E}^0 \rho u dz = -\int_{-2D_E}^0 d\tau_y = \tau_{y\eta} \end{aligned}\right\} \text{Ekman mass transport} \tag{1.17}$$

Now $(\tau_x)_{-2D_E}$ and $(\tau_y)_{-2D_E}$ will be essentially zero because the velocity below the wind-driven layer is substantially zero and therefore there can be no shear and therefore no friction (Pond and Pickard, 1983).

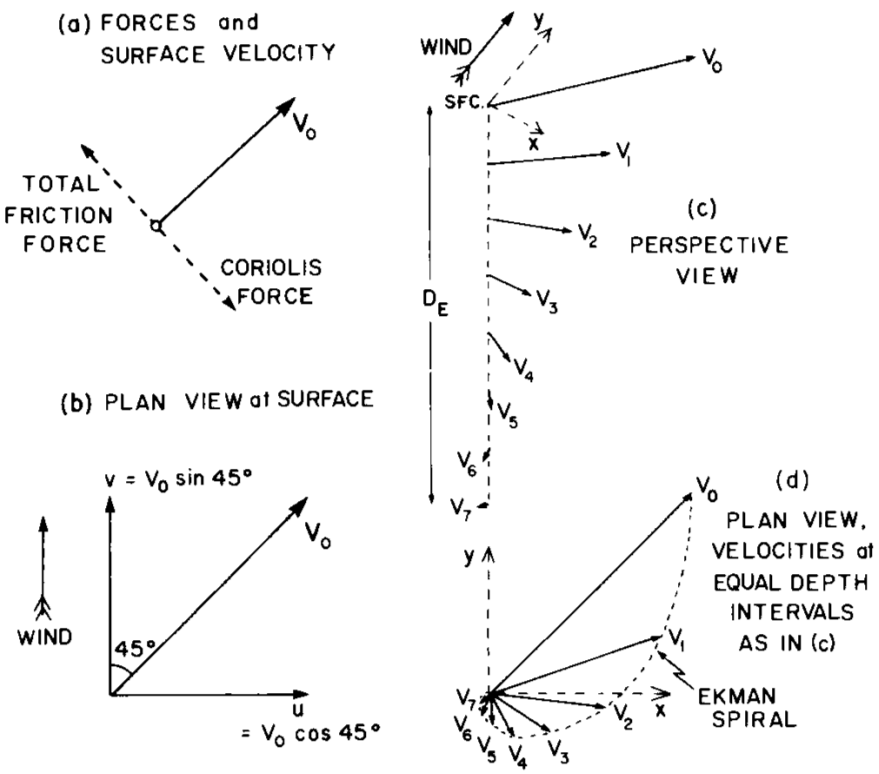

Figure 1.6. Wind-driven currents from Ekman analysis (**a**) net frictional stress balances Coriolis force with surface current $\mathbf{V}_0$ perpendicular to both; (**b**) wind in y-direction, surface velocity $\mathbf{V}_0$ and components; (**c**) perspective view showing velocity decreasing and rotating clockwise with increase in depth; (**d**) plan view of velocities at equal depth intervals, and the "Ekman spiral" (all for northern hemisphere). From Pond and Pickard (1983).

Ekman Pumping

Because of conservation of mass, horizontally divergent surface Ekman transport must be balanced by vertical motion (upwelling or downwelling). From the integral over the Ekman layer of the continuity equation, we have

$$\rho \int_{-D_E}^{0} \left(\frac{\partial u}{\partial x} + \frac{\partial v}{\partial y} + \frac{\partial w}{\partial z} \right) dz \; = \; 0 \tag{1.18}$$

inserting M_{xE} and M_{yE} (i.e. equations 1.17 integrated from bottom of Ekman layer to surface)

$$\frac{\partial}{\partial x} \int_{-D_E}^{0} \rho u dz + \frac{\partial}{\partial y} \int_{-D_E}^{0} \rho v dz \; = \; -\rho (w(0) - w(-D_E)) \tag{1.19}$$

or equivalently

$$\frac{\partial M_{xE}}{\partial x} + \frac{\partial M_{yE}}{\partial y} = \rho \mathbf{w_E} \tag{1.20}$$

equivalent to

$$\nabla_H \cdot \mathbf{M_E} = \rho \mathbf{w_E} \tag{1.21}$$

where $\nabla_H \cdot = [\mathbf{i}(\frac{\partial}{\partial \mathbf{x}}) + \mathbf{j}(\frac{\partial}{\partial \mathbf{y}})]$ is the horizontal divergence operator and $\mathbf{M}$ is the vector mass transport (Pond and Pickard, 1983). Using 1.17, we find that Ekman pumping is proportional to the curl of the wind stress:

$$w_E = \frac{1}{\rho} \widehat{k} \cdot \nabla \times \left(\frac{\overrightarrow{\tau}}{f} \right) \tag{1.22}$$

Sverdrup Balance

The interior flow, i.e. below the Ekman layer, of the (non-equatorial) oceans can be described in terms of its meridional circulation. In the subtropical gyres, the interior flow is toward the equator in both the Northern and Southern Hemispheres. In the subpolar gyres, the interior flow is poleward in both hemispheres. These interior flow directions can be understood through a potential (i.e. relative + planetary) vorticity argument introduced by Sverdrup (1947), so called the Sverdrup ‘balance”. As a reminder, for a frictionless, barotropic fluid (the interior flow), the potential vorticity of a fluid element of depth H is conserved:

$$\left(\frac{\zeta + f}{H} \right) \; = \; constant. \tag{1.23}$$

The fluid element’s absolute vorticity $\zeta + f$ can respond to vertical stretching of the element by increasing ζ (ciclonic(anticiclonic) rotation for the northern(southern) hemisphere) or by migrating poleward (increased f).

Interior ocean is in geostrophic balance, then if we cross-differentiate 1.2 and subtract them, to eliminate the pressure terms, we get:

$$f\left(\frac{\partial u}{x}+\frac{\partial v}{y}\right)+\frac{df}{dy}v \;=\; 0, \tag{1.24}$$

By the continuity equation, and with $\beta = \frac{df}{dy} = \frac{2\Omega\cos\phi}{R}$:

$$\beta v = f\frac{\partial w}{\partial z}. \tag{1.25}$$

This important equation states that water column stretching in the presence of rotation is balanced by a change in latitude (See Fig. 1.7). In 1.25 the vertical velocity w is due to Ekman pumping. Integrating this vertically through the interior ocean and from 1.21 and 1.22:

$$\beta M_y = \int \beta\rho v dz = f\rho \mathbf{w_E} = f\widehat{k}\cdot\nabla\times\left(\frac{\overrightarrow{\tau}}{f}\right) \approx \widehat{k}\cdot\nabla\times\overrightarrow{\tau} \tag{1.26}$$

or

$$M_y = \frac{1}{\beta}\widehat{k}\cdot\nabla\times\overrightarrow{\tau} \tag{1.27}$$

This expression is known as the Sverdrup Balance and it equates the curl of the surface wind stress to the north-south transport over the water column integrated to the depth of no motion.

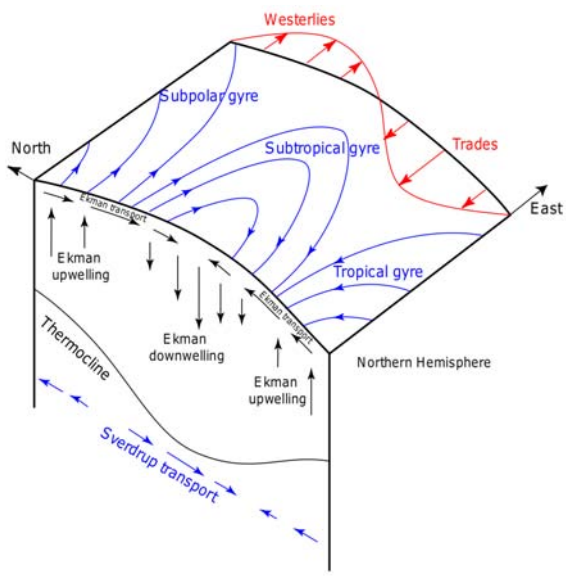

Figure 1.7. Sverdrup balance circulation (Northern Hemisphere). Westerly and trade winds force Ekman transport, creating Ekman pumping and suction and hence Sverdrup transport. From Talley (2011).

Coastal Upwelling

Coastal upwelling owes its existence to the presence of both the coast as an impermeable lateral boundary and the wind blowing at the surface of relatively shallow water on the continental shelf. Under the action of the wind, the atmosphere exerts a tensile force (frictional force) on the ocean surface. The surface water is then drawn in the direction of the wind, but following a deflected trajectory to the right in the northern hemisphere and to the left in the southern hemisphere because of the Coriolis force linked to Earth's rotation. The drift is offshore if the wind blows with the coast on its right (left) in the Southern (Northern) Hemisphere (Cushman-Roisin, 1994). The canonical structure of the oceanic circulation in coastal upwelling situations consists of a coast-parallel geostrophic current, called coastal jet, which is deflected seaward in an Ekman layer near the surface and shoreward in an Ekman layer near the bottom (See Fig. 1.8). The coast-parallel component of the wind stress induces offshore movement in the surface Ekman layer that operates to lower the coastal sea level by about $\sim$5–10 cm until a dynamical equilibrium is reached. This drop in sea level is sufficient to create a shoreward pressure-gradient force driving an inmediate geostrophic upwelling coastal jet of 20–50 cm s^{-1} in speed. In turn, the geostrophic flow becomes subject to frictional effects of the seafloor. This creates a shoreward flow in the bottom Ekman layer, which is about 5–25 m thick. This near-bottom flow is the final agent of the upwelling process as it moves near-bottom water shoreward and, as it hits the coast, upward into the euphotic zone (Kämpf and Chapman, 2016).

Wind Stress Curl Driven Upwelling

In addition to coastal upwelling, there is an additional key physical mechanism known as Ekman pumping. This mechanisms refers to the vertical adjustment of the pycnocline associated with a spatially varying horizontal wind-stress field, known as wind-stress curl (See Fig. 1.9), which induces a divergence of horizontal Ekman transports in addition to boundary effects due to the existence of a coast. While the coastal upwelling process involves a cross-shelf transfer inherent with the dynamics of Ekman layers, Ekman pumping exclusively induces a vertical flow. Previous studies indicate that Ekman pumping contributes significantly (>25 %) to the vertical nutrient flux in major eastern boundary upwelling regions (Messié et al., 2009). A significant difference between the effects of wind stress and wind stress curl is that Ekman pumping caused by the latter takes place considerably farther offshore, often at the shelf edge, and can occur at faster rates in terms of vertical transport than Ekman transport

(Kraus and Businger, 1994). Thus, it is separated from the inshore Ekman transport and can provide a second input of nutrients to the system (Kämpf and Chapman, 2016).

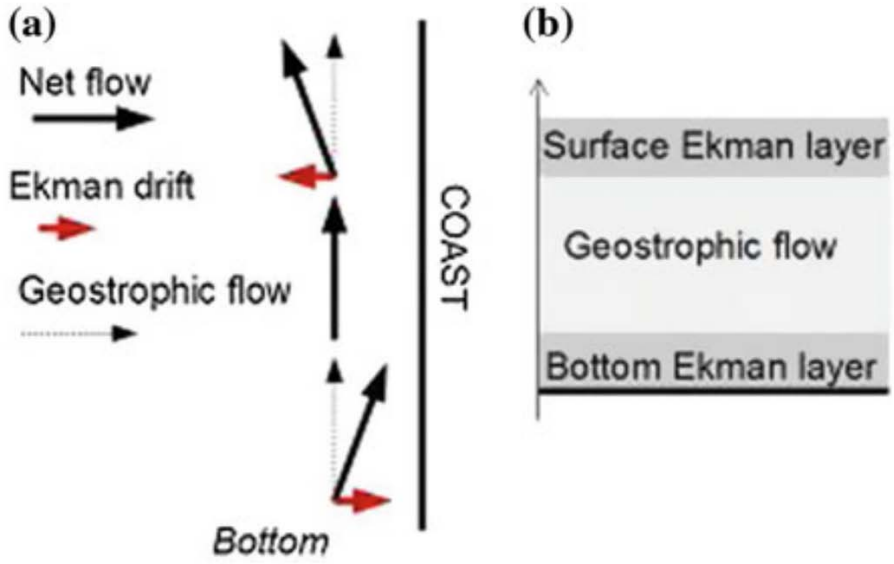

Figure 1.8. The general dynamic structure of coastal upwelling. From Kämpf and Chapman (2016).

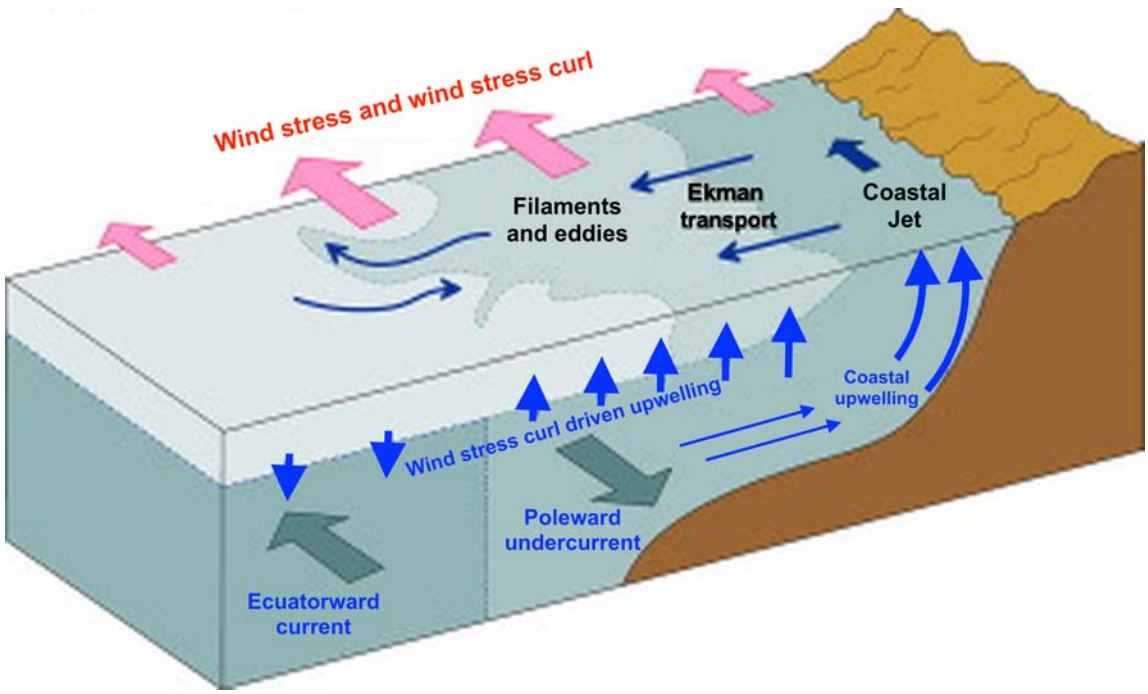

Figure 1.9. The general dynamic structure of the EBUS. Adapted from (Mohrholz et al., 2014).

Cross-Shelf Structure of Coastal Upwelling

As seen in the previous sections, Ekman transport can produce upwelling through flow divergence in the coastal area due to the coastal boundary and in the offshore area due to the wind curl driven vertical flow. The Ekman Coastal Upwelling Index (ECUI) derived by Bakun (1973), provides an estimation of the vertical velocities associated with the former upwelling based on both the Ekman transport and the cross-shore scale of the coastal upwelling cell structure (L_u) as follows:

$$ECUI = \frac{U_{ek}}{L_u} = \frac{\tau_{alongshore}}{\rho f L_u} \tag{1.28}$$

where U_{ek} is the Ekman transport, $\tau_{alongshore}$ is the alongshore wind stress and ρ is the background density of sea water. Usually, for lack of better estimations, L_u is mistakenly taken as the internal Rossby radius $R' = \sqrt{\frac{g'h_0}{f}}$ (with g' the reduced gravity and h_0 the small Ekman upper layer thickness). This scale varies between 5 and 30 km depending on the stratification ratio, and describes the geostrophic adjustment scale of the pycnocline slope and not the cross-shore width of the upwelling cell. Indeed, Estrade et al. (2008) show, using an analytical model, that over shallow depths, coastal upwelling occurs in the frictional inner-shelf, where surface and bottom Ekmal layers overlap. This essential results reveal, on the one hand, how the inner-shelf geometry influences the coastal upwelling scale, and, on the other hand, how the cross-shore wind component drives the near-shore pressure gradient adjustment. The latter leads to an "migration" of the main upwelling cell with a separation from the coast driven by outcropping and homogenization of the water column where the surface and bottom boundary layers are fully merged (inner shelf zone) establishing a "kinematic barrier" to the the Ekman transport divergence, and, coastal incursion driven by a "boundary layers splitting" process caused by shoreward advection of the isopycnal uplift and stratification of the inner shelf. The former mechanism of upwelling separation from the coast could be weakened in case of severe coastal wind drop-off because frictional activity decreases in the near-shore region bringing the kinematic barrier and upwelling closer to the coast.

Overall, the results of Estrade et al. (2008) characterize the geography of the wind-driven upwelling structure. They provide an estimation of vertical velocity which can be used as coastal upwelling indices derived entirely from Ekman's theory. For a local deph h, a constant topographic slope S and Ekman depth D_E (defined in equations 1.14), they show that 90% of the Ekman transport upwells for $\frac{h}{D_E}$ between 1.25 and 0.5 (in the case of an alongshore wind), meaning that $\frac{D_E}{S}$ (the ratio of Ekman depth to topographic slope) is the right scale

to estimate the cross-shore width of an upwelling cell, this result illustrates the frictional nature of coastal upwelling divergence. However, there is a lower limit to the inner-shelf scale when steep slopes are considered as horizontal friction becomes the dominant process in the creation of a frictional boundary layer. In this case, L_u is better scaled by the horizontal Ekman layer width $L_E = \pi\sqrt{\frac{2A_h}{|f|}}$. A_h is the lateral eddy viscosity which is estimated in the range $10 - 100\ m^2s^{-1}$ in coastal upwelling regions (Marchesiello and Estrade, 2010) and depends upon submesoscale activity over the shelf (Capet et al., 2008). Figure 5 summarize the various physical processes at work as a function of depth.

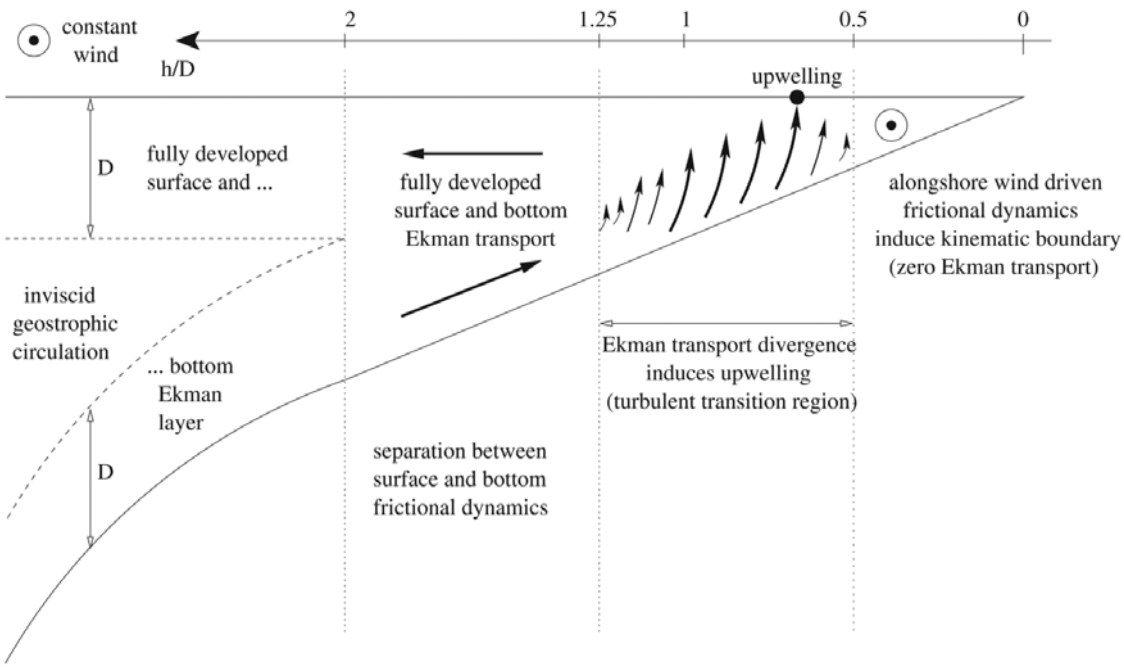

Figure 1.10. Conceptual scheme of the mechanism of upwelling separation from the coast. Adapted from (Estrade et al., 2008).

Poleward Undercurrents and Eddies

An additional dynamical feature of the EBUS is the presence of Poleward UnderCurrent (PUCs) over the shelf and slope, commonly found in midlatitude Eastern Boundary Current (EBC) systems (Fonseca, 1989; Hill et al., 1998; Neshyba et al., 2013). PUC can provide subsurface onshore flow to the upwelling systems where their properties may be significant in determining the biochemical response of the coastal environment to upwelling (phytplankton blooms and subsequent hypoxic decay) (Strub et al., 2013). These subsurface currents generally reach average velocities along the coast of ~ 0.05 m/s to ~ 0.2 m/s, distributed between depths of 150 and 300 m, as reported for the California Undercurrent and the Iberian

Peninsula (0.2 m/s). In the HCS, direct measurements of the PUC have been made off the coast of Peru and Chile. Based on 6 years of data at 30○S, Shaffer et al. (1999) reported an average velocity of 12.8 cm/s at 220 m, with semiannual variation and an intensified poleward flow in spring. The semi-annual variations of the PUC in the HCS are responses to the combination of local wind stress curl and disturbances caused by remote tropical forcing. This flow is also modulated interannually by Rossby waves forced by trapped waves propagating southward along the coast of South America, a physical mechanism that also partly explains the variability in the oxygen minimum zone off Chile (Aguirre et al., 2012; Vergara et al., 2016).

On the other hand, upwelling jets are not smooth (laminar) flows. Like other frontal flows (e.g. western boundary currents) upwelling jets quickly become dynamically unstable on time scales of days to weeks and shed mesoscale eddies. In the four EBUS, these instabilities favor the generation of mesoscale eddies that are mainly formed near the coast and propagate mostly westward toward the interior of subtropical gyres (Chaigneau et al., 2009; Chelton et al., 2011; Morrow and Le Traon, 2012; Pegliasco et al., 2015). These structures are circular flow patterns in which the geostrophic flow surrounds a high-pressure (low-pressure) centre associated with an elevated (depressed) sea level. It is the low-pressure eddies (i.e. cyclones) that largely sustain upwelled water in their centres. Eddies in the coastal ocean can have diameters as small as 10–20 km, in contrast to the more commonly known open-ocean eddies that have diameters of up to 300 km. As a result of eddy shedding, the width of the upwelling zone generally increases along the coast in the direction of the upwelling jet. In addition, upwelling jets often form turbulent wakes in the lee of headlands. Fully developed eddy fields exhibit specific pathways, called filaments, along which upwelled water is advected offshore (See Fig. 1.11b). Filaments, which can be quasi-stationary or transient features, generally operate as an export mechanism of organic matter to the open ocean (Arístegui et al., 1997). Eddies also operate to disperse properties of the upwelling centre (e.g. heat anomalies, organic matter and zooplankton and fish larvae) offshore. These nonlinear mesoscale eddies trap water into their cores and act as transport and mixing mechanism redistributing physical and bio-geochemical properties from the coastal regions to the open ocean (Barton and Arístegui, 2004; Dong et al., 2014; Logerwell and Smith, 2001; Morales et al., 2012; Rubio et al., 2009). Along their paths, they can also modulate the biogeochemistry and ocean productivity (Correa-Ramirez et al., 2007; Gruber et al., 2011; Mahadevan, 2014; Marchesiello and Estrade, 2007; Pegliasco et al., 2015; Stramma et al., 2013) and also impact the overlaying atmosphere interactions affecting heat fluxes at the

sea-air interface, winds, cloud cover and precipitations (Frenger et al., 2013; Mahadevan, 2014; Morrow and Le Traon, 2012; Pegliasco et al., 2015; Villas Bôas et al., 2015).

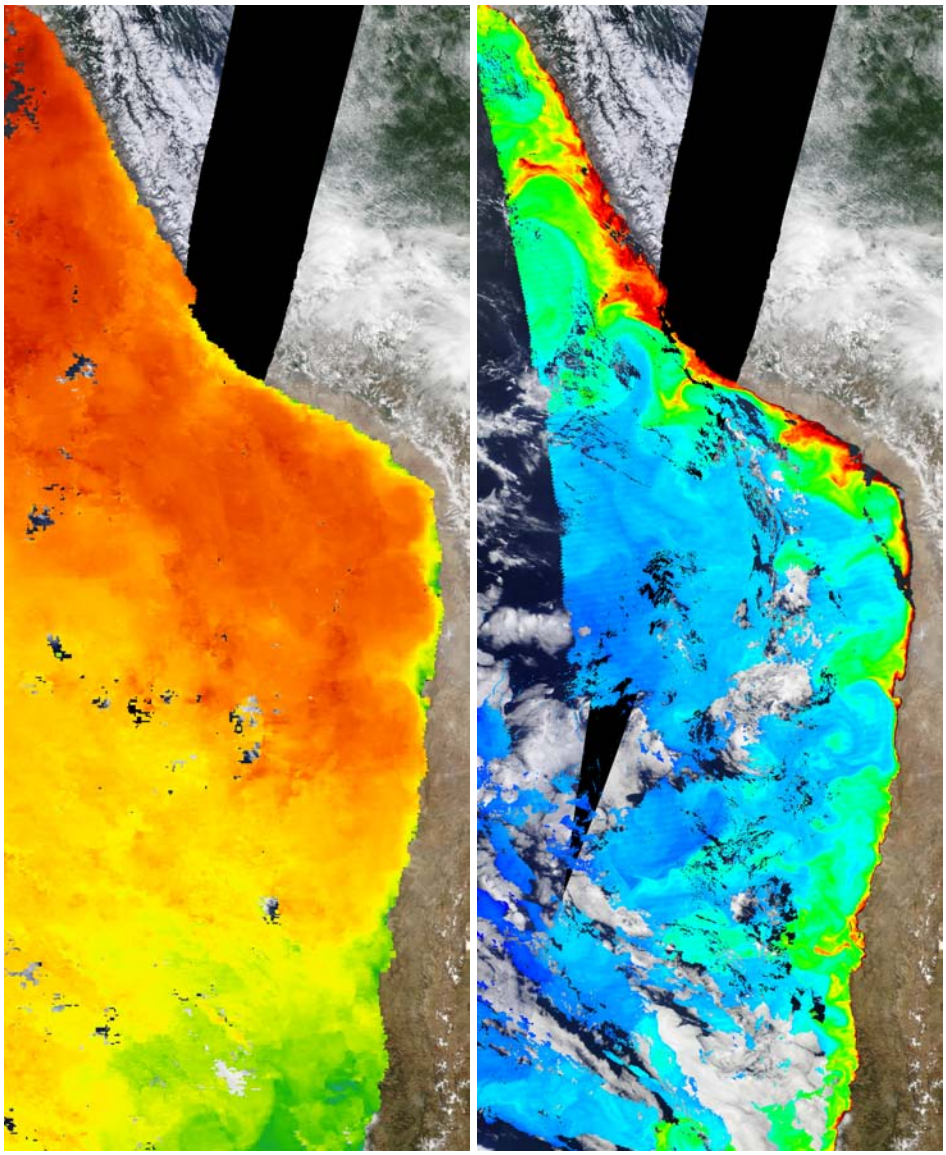

(a) **(b)**

Figure 1.11. Example of mesoscale structures including eddy field and upwelling filaments seen in satellite images, MODIS (Aqua), (**a**) Sea Surface Temperature (L3, Day, 8 Day, Thermal, 4 km) and (**b**) clorophyll-*b* concentrations in the PCUS (28/02/2017). From NASA Worldview https://worldview.earthdata.nasa.gov.

1.3 Scientific Focus, State of the Art, Motivations and Objectives

The oceanic region located along the west coasts of South America (so called Humboldt system) is now recognized as a key region for understanding the evolution of the climate in a warming world. This is primarily due to two main aspects, one related to the biogeochemical environment and the other one to the physical setting. This region is, first, embedded into the most extended and marked Oxygen Minimum Zone (OMZ) of the world (Paulmier and Ruiz-Pino, 2009) that results from the low ventilation of the oceanic circulation and that intervenes in the carbon and nitrogen cycles at global scale (Gruber et al., 2009). The OMZ is also favorable for the development of hypoxic events along the coast that can severely disrupt the rich ecosystem and so the marine resources that are crucial for regional economies.

Second, this region is involved in the climate system through up-scaling effects, the upwelled cold waters feeding back on the marine boundary layer and participating in the maintenance of low-level clouds under the subsidence inversion, the so-called Stratocumulus Cloud Deck (SCD), that influence the earth radiative budget (Bony and Dufresne, 2005). These regions of low-level stratus tend to act as a thermostat for the ocean, blocking solar radiations at the ocean surface and, therefore, contribute significantly to Earth's radiation balance (Mechoso et al., 2014).

1.3.1 Climate Model Biases in the EBUS, Causes and Impacts

Current generation Coupled General Circulation Model (CGCM) have the most severe SST biases in this region (see Fig. 1.12), and may frequently reach in excess of 5° (de Szoeke et al., 2010; Manganello and Huang, 2008; Richter, 2015; Yu and Mechoso, 1999). These warm bias are caused by several factors:

a) The bad representation of the stratocumulus deck, that implies a misrepresentation of the surface shortwave radiation that lead to an overestimation of the solar heat flux.

b) The underestimation of the mesoscale eddy activity that inhibit the offshore transport of cold waters due to the low spatial resolution of these global models.

c) The misrepresentation of the alongshore winds that impact the cooling associated with Ekman dynamics.

d) The normally sharp vertical temperature gradient separating the warm upper ocean layer from the deep ocean is too diffuse in the models

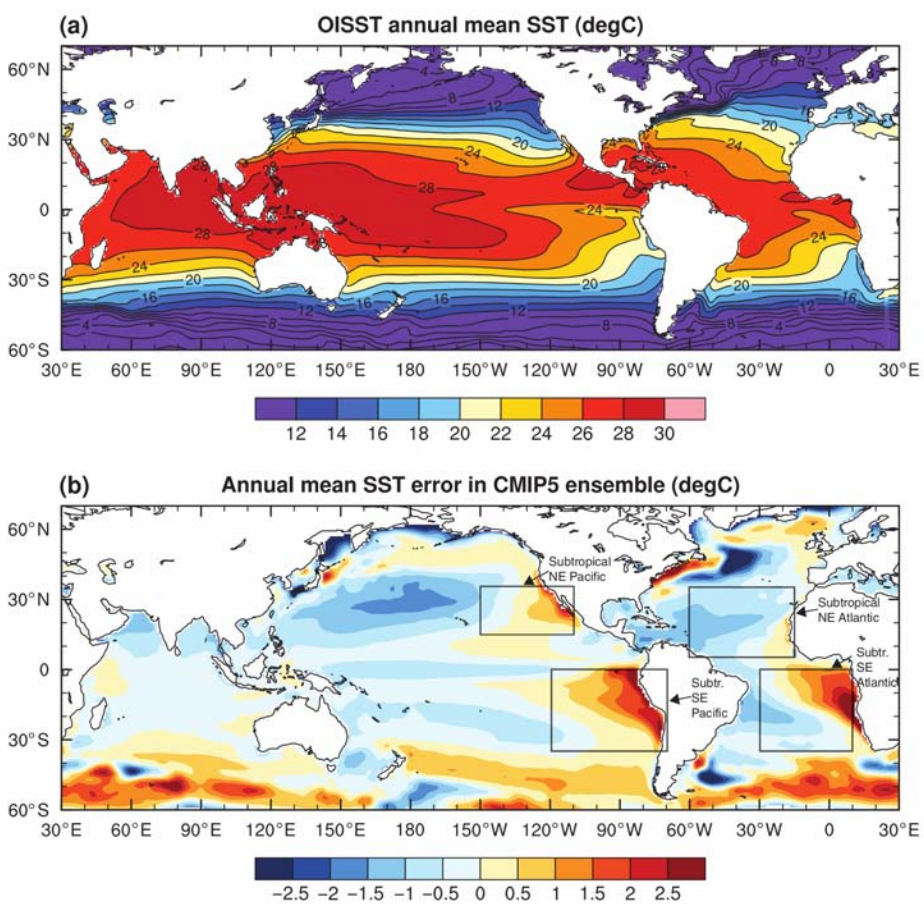

Figure 1.12. (a) Observed annual mean sea-surface temperature (SST) from the optimally interpolated (OI) SST data set. **(b)** Annual mean bias of the CMIP5[2] ensemble relative to OISST. The gray boxes denote the EBUS. From Richter (2015).

Such concern motivated in 2006 a specific international program (VOCALS/VAMOS, http://www.eol.ucar.edu/projects/vocals/) under the auspices of CLIVAR (Climate Variability and Predictability of the ocean-atmosphere system) to address this issue over the offshore South-Eastern Pacific (SEP) sector (Wood et al., 2011). In preparation for VOCALS, a preliminary model assessment (PreVOCA) was conducted for October 2006 by operational forecast, regional, and global models, with a particular focus on the clouds and the Marine Boundary Layer (MBL) in the SEP (Wyant et al., 2010). Results in terms of large-scale dynamics (i.e. observed anticyclonic surface winds) were in agreement with observations but performed poorly on the representation of the stratocumulus with a significant dispersion within the models for the geographic patterns of mean cloud fraction with only a few models agreeing well with MODIS observations. Furthermore, most models also underestimate the MBL depth by several hundred meters (about one-half the observed values) in the eastern part of the study region (See Fig. 1.13). The shallow MBL in the PreVOCA models is usually

accompanied by the lack of clouds in the near-coastal region, but the nearshore surface wind field parallel to the coast is well reproduced in general.

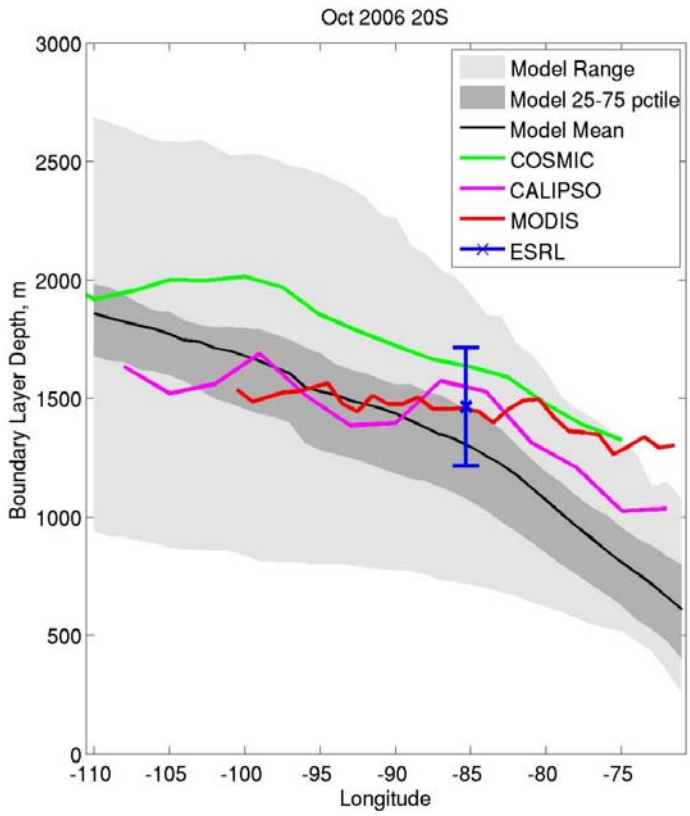

Figure 1.13. Model boundary layer depth (m) compared with observations of boundary layer depth and cloud-top height. From Wyant et al. (2010).

Finally, in addition to the misrepresentation of local processes and/or ocean-atmophere interactions, global connections among regional biases or errors have been found. In fact, Wang et al. (2014) found in 22 climate models, participants in the Coupled Model Intercomparison Project phase 5 (CMIP5), that SST biases are commonly linked with the Atlantic Meridional Overturning Circulation (AMOC), which is characterized by the northward flow in the upper ocean and returning southward flow in the deep ocean. Furthermore, the EBUS seems to be particularly touched by the effect of these remote biasses, this has several outcomes and implications. First, the improvement of regional processes may not suffice for overall better model performance, because remote influences may override them. Second, a better understanding of these global teleconnections is necessary to improve the climate model performance.

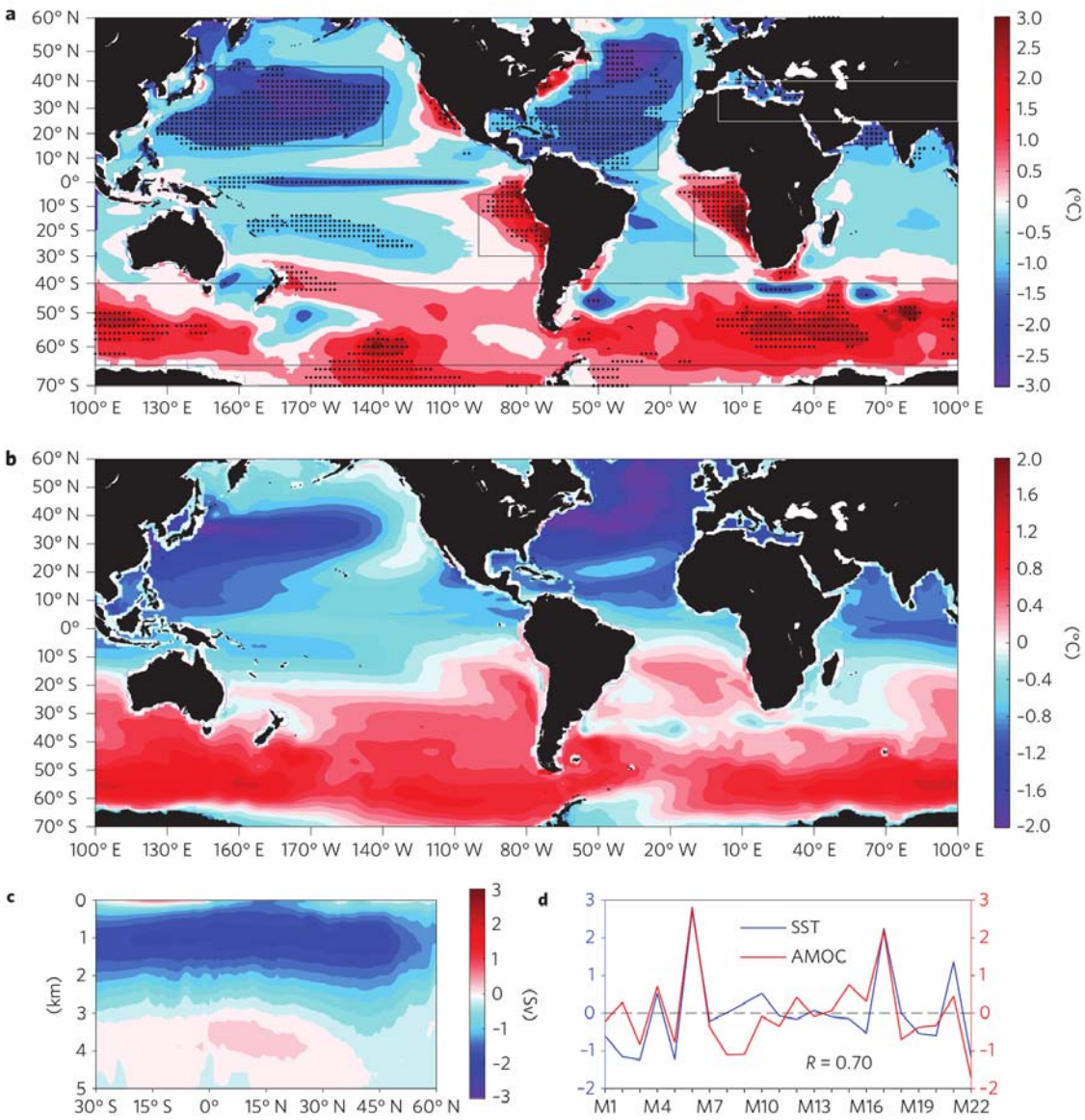

Figure 1.14. Global SST bias and its relationship with the AMOC. (**a**), The annual-mean SST bias averaged in 22 climate models. The SST bias is calculated by the SST difference between the model SST and extended reconstructed SST. The dots denote where at least 18 of 22 models (82%) have the same sign in the SST bias. The rectangles represent the focused regions. (**b**), (**c**) Spatial maps of SST bias and the AMOC for the first inter-model SVD mode (accounting for 45% of total covariance). (**d**), Their corresponding coefficients. The x axis in (**d**) represents different models. From Wang et al. (2014).

1.3.2 Coupled Climate Systems of the Southeast Pacific

The VOCALS program permitted to gather a unique data set and to improve our knowledge of the processes of cloud formation in this region (Mechoso et al., 2014). It also shed light on the importance of mesoscale coastal dynamics in some particular regions along the coast in building up the regional atmospheric circulation. In late spring 2009 the Chilean Upwelling Experiment (CUpEx), a joint program to VOCALS, that took place in the near- shore region of (30°S), focused on the ocean-atmosphere interaction in a major upwelling centre off northern Chile (Garreaud et al., 2011). This experiment provided additional detailed information on coastal processes in a region that experiences the seasonal meridional migration of an atmospheric Low-Level Jet (Garreaud and Muñoz, 2005) having a significant impact on the upwelling seasonal variability (Aguirre et al., 2012; Renault et al., 2009). Overall the results gathered within VOCALS and CUpEx suggest an upscalling effect of the processes at fine scales (the scale of the upwelling cells) upon the regional climate variability, that is, processes of air-sea interactions taking place in a narrow coastal fringe (width of ∼100km) can feedback on the regional climate variability through their impact on the oceanic variability. The central Chile region is in fact located in the southern edge of the SCD of the SEP and the atmospheric Low-Level Jet (see Fig. 1.15) along the Chilean coast is often located at 30°S, particularly in winter and spring (Garreaud and Muñoz, 2005). Consistently, this region is recognized as one of the most active upwelling centres in Chile (Figueroa and Moffat, 2000), presumably in connection with local southerly wind maxima, and as a source of ocean kinetic energy ((see Fig. 1.16**b**)) along the Chilean coast, especially during springtime (Hormazabal, 2004; Rutllant and Montecino, 2002).

1.3.3 Atmospheric Circulation, Coastal Wind Variability

As mentioned above, the Low-Level Jet (LLJ) off central-Chile is a major feature of the atmospheric circulation along the western coast of South-America. It is forced synoptically by the passage of mid latitude migratory anticyclones farther south and results from the equilibrium between the alongshore pressure gradient and the turbulent friction in the MBL (Muñoz and Garreaud, 2005). Recent modelling studies (Rahn et al., 2011; Renault et al., 2012) indicates that the LLJ is associated to finer scale wind jets (∼5km) along the coast, tightly linked to orography (see Fig. 1.15**b**). These mesoscale wind maxima associated are referred as coastal jets (CJs) to differentiate them from the broader, synoptic-scale LLJ. Due to their high variability, they can act as a driver of mixing near the coast eroding the uplifting of the isotherms and thus the upwelling effect at low frequencies. In addition, satellite data reveals areas of minimum low-level cloud frequencies located downstream of those points

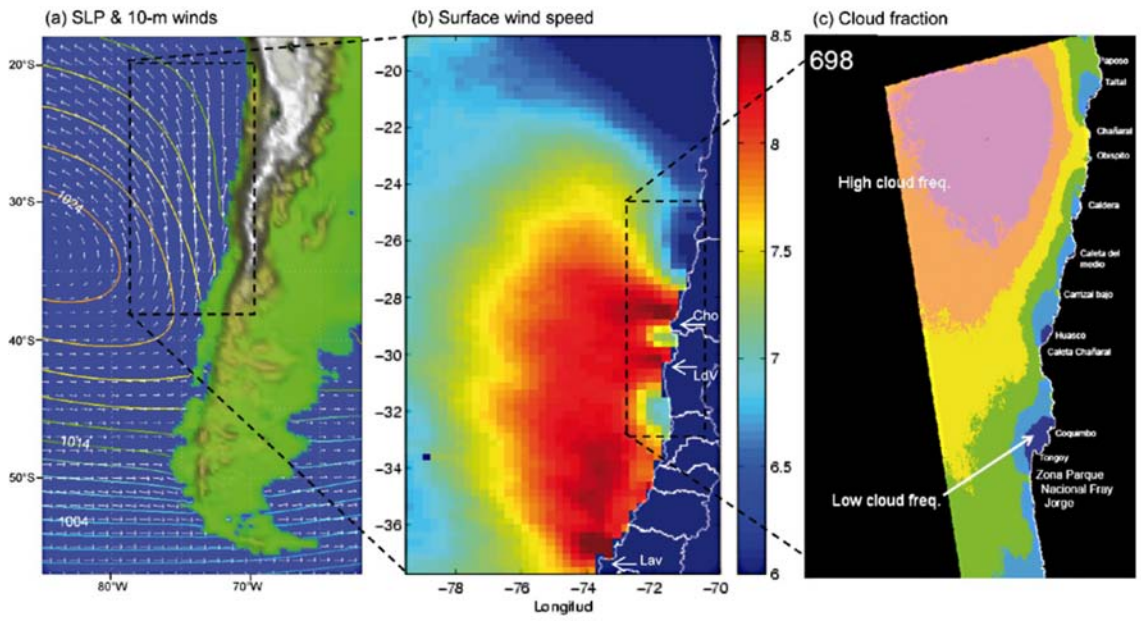

Figure 1.15. (a) Spring-Summer (SONDJF) average of sea level pressure (contoured every 2 hPa) and 10-m wind vectors (arrows) off the Chilean coast. Data source: NCEP-NCAR reanalysis. **(b)** Spring-Summer average of surface wind speed derived from 4 yr of QuikSCAT observations. Color scale at right in m s^{-}1. Note the near coastal jets off points Choros (Cho), Lengua de Vaca (LdV) and Lavapie (Lav). Adapted from Garreaud and Muñoz (2005). **(c)** Spring (SON) climatology of low cloud frequency derived from visible GOES imagery (pink is >80%; blue is less than 30%). From Garreaud et al. (2011).

and capes (Garreaud et al., 2011), indicative of topographically induced alongshore variability in the Atmospheric Boundary Layer (ABL) structure (see Fig. 1.15**c**).

Another feature is an overall wind reduction (not for the CJs) in a narrow coastal fringe of ∼30 km width. The latter is often referred to as the wind drop-off that is thought to be a main feature of the regional atmospheric circulation in upwelling regions (Capet et al., 2004). Several observational and modeling studies have indeed suggested that the mean wind stress in upwelling regions may be systematically reduced (See Fig 1.16**a**) within a narrow coastal strip (of ∼50km), relative to values farther offshore (Bane, 2005; Capet et al., 2004; Perlin et al., 2007; Renault et al., 2012). For instance, Dorman et al. (2006) showed from observations that the summer-mean alongshore wind stress over the shelf off Bodega Bay (California) decreases from 0.14 N m^{-2} at 25 km offshore to 0.04 N m^{-2} at 2 km. During the CupEx experiments, there is also evidence that such cross-shore wind reduction (drop-off) is taking place off Coquimbo (30°S) (Garreaud et al., 2011).

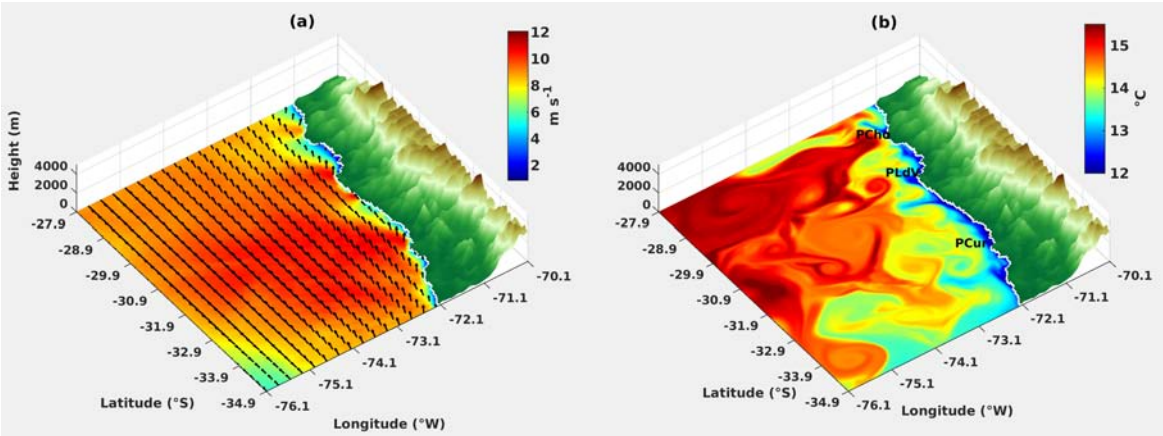

Figure 1.16. Map illustrating the main features of the surface circulation off central Chile (spring 2008), as simulated by the regional atmospheric (WRF) and oceanic (ROMS) models: **(a)** Surface wind magnitude/direction (m s^{-1}) and **(b)** Sea surface temperature (°C). In addition, acronyms indicate upwelling centers(PCho: Punta de Choros, PLdv: Punta Lengua de Vaca and PCur: Punta Curaumilla. From Astudillo et al. (2018), submitted, see Chapter 4.

1.3.4 Response of the PCUS to Coastal Mesoscale Wind Structure

The spatial and temporal structure of the upwelling is mainly driven by the coastal wind variability, in particular, cross-shore variations of the wind have received considerable attention, since the presence of a wind drop-off close to the shore tends to increase (decrease) upwelling through Ekman pumping (transport). Regional oceanic modelling studies show that upwelling response is highly sensitive to such a transition wind shape (Capet et al., 2004; Desbiolles et al., 2014, 2016; Jacox and Edwards, 2012). For instance, in a pionnered modelling study, Capet et al. (2004), carried out twin experiments for the California Current System (CalCS) that differ only in the cross-shore gradient of the nearshore wind, i.e. variable vs uniform drop-off, in a coastal strip 30-km wide. With this differentiated surface forcing, the SST near the coast for the smooth case is 2°C colder than the sharp case (see Fig. 1.17a), for a major upwelling event, revealing that nearshore wind drop-off diminishes upwelling; i.e., the hypothesized compensation between nearshore Ekman transport and upward Ekman pumping does not fully occur. Additionally, they show the preponderant role of the coastal wind profile in determining the mean alongshore current structure (i.e. surface nearshore coastal jet and poleward undercurrent).

However, wind analyses do not represent adequately the mesoscale wind patterns (e.g. COAMPS), and show uncertainties in the crosshore wind profile (see Fig. 1.17b), i.e the drop-off takes place over an increasingly small region as the model resolution increases, overestimating the wind drop-off magnitude which influence the nearshore circulation and

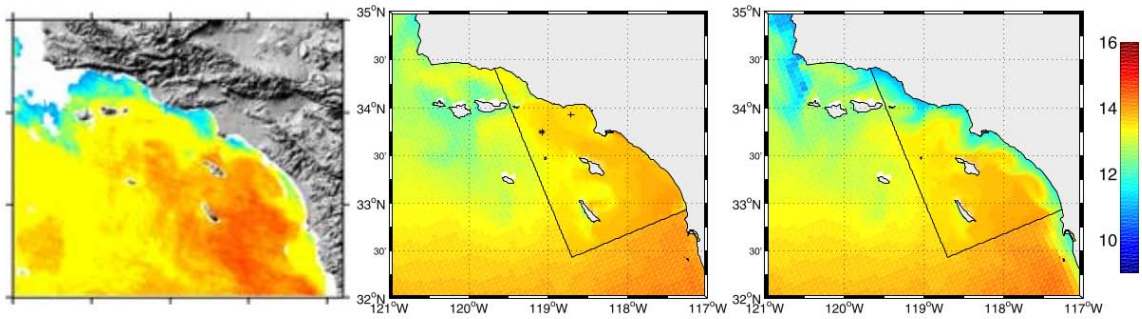

(a) SST in the Southern California Bight for a major upwelling event: observed **(left)** and modeled with a variable-smooth **(middle)** or uniform-sharp **(right)** crosshore gradient. From Capet et al. (2004).

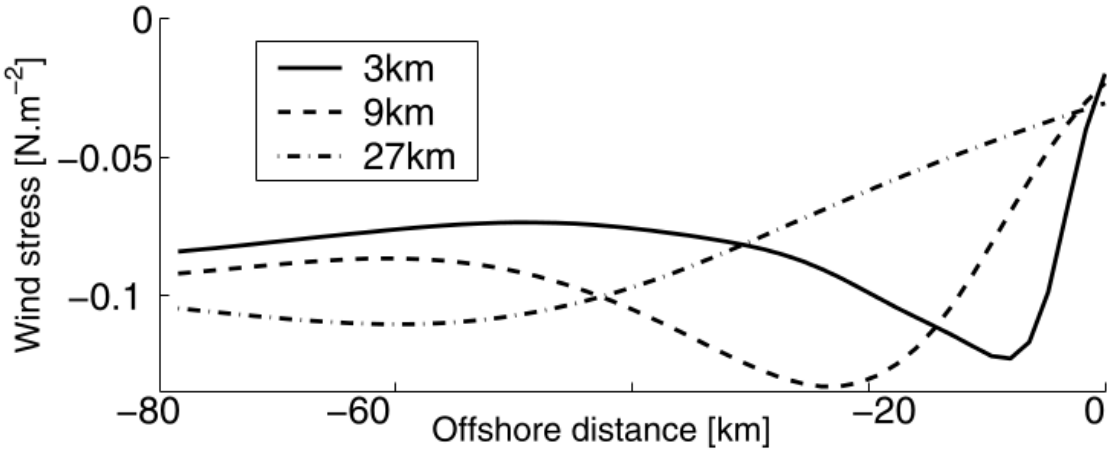

(b) COAMPS alongshore wind stress vs. distance to the coast at 3 different resolutions. The wind is averaged over a 30 km alongshore interval south of Pt. Sur (CalCS) during August 2003. From Capet et al. (2004).

Figure 1.17

the upwelling response. As an illustration of this sensitivity of the SST to the wind drop-off in the PCUS, the Figure 1.18 shows the Ekman advective heat flux for a strong CJ event from 29 to 30 October 2008, based on high resolution oceanic model simulations using contrasted drop-off patterns in surface wind forcing. Both simulations exhibit many mesoscale features related to eddies that induce positive and negative horizontal temperature gradients. The Ekman velocity is directed offshore along the coast and over the open ocean (not shown), which induces negative Ekman flux and SST cooling in the coastal region (50-km). The resulting offshore cooling transport is highly sensitive to the crosshore reduction of the momentum fluxes, and the sensitivity experiments indicate lower mean advective heat flux

magnitude in the 50 km coastal strip (353 vs 169 (w m^2) for the non-drop-off and drop-off cases respectively). This sensitivity is related to the drop-off impact over the offshore and northward surface flows, linked to the Ekman transport and to the geostrophic adjustment to the SST front respectively. This will be detailled in Chapter 4.

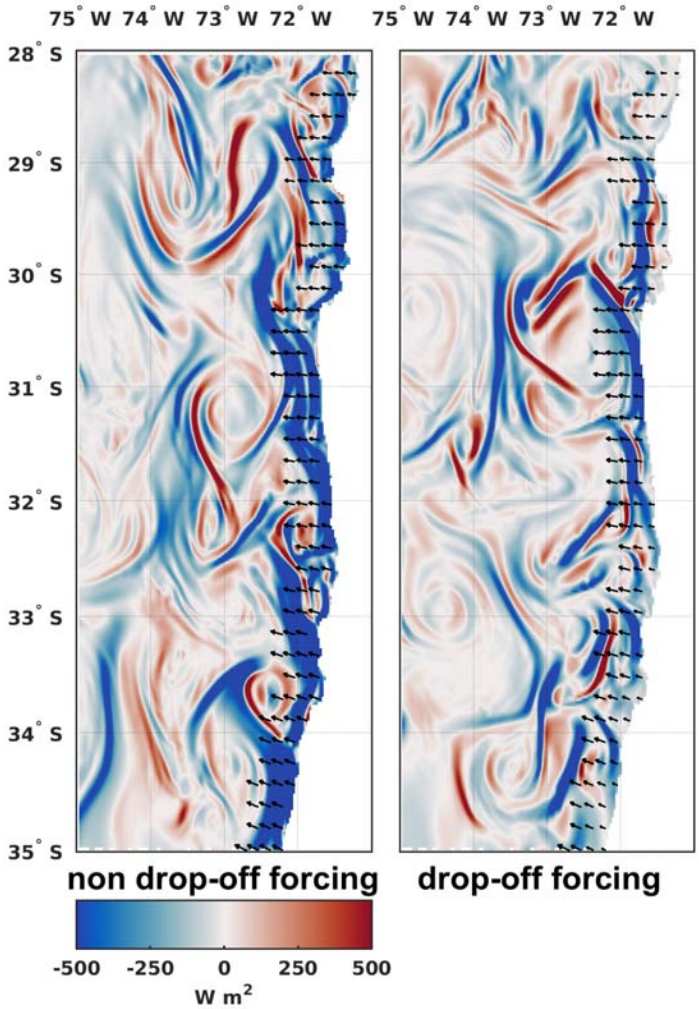

Figure 1.18. Ekman advective heat flux for a CJ event (29 to 30 October, 2008), from high resolution (2.5km grid size) ROMS simulations: **(left)** non drop-off case, **(right)** drop-off case.

1.3.5 Impact of the Wind Stress Forcing on Coastal Circulation

Since the pioneer modeling studies by Marchesiello et al. (2003) and Capet et al. (2004) that showed that a realistic wind drop-off is influential on the undercurrent dynamics and cross-shore eddy fluxes off central California, there has been more concern in the modeling

community on the most appropriate wind forcing for regional EBUS modeling studies. Observational evidence of such drop-off has been elusive due to the sparse data in the coastal fringe, although field experiments do suggest its existence in some regions, in particular off central Chile (Bravo et al., 2016; Garreaud et al., 2011). Close to the shore, the relative contribution of Ekman transport and pumping, has in fact remained ubiquitous due to limitations of the satellite scatterometer measurements (ERS, QuikSCAT and ASCAT) which contain a 25 to 50-km wide blind zone along the coast limiting the description of the mesoscale atmospheric circulation within this narrow coastal fringe. The relatively low spatial resolution of these products has also resulted in uncertainty in the actual magnitude of the wind stress curl near the coast (Croquette et al., 2007) (See Fig. 1.19).

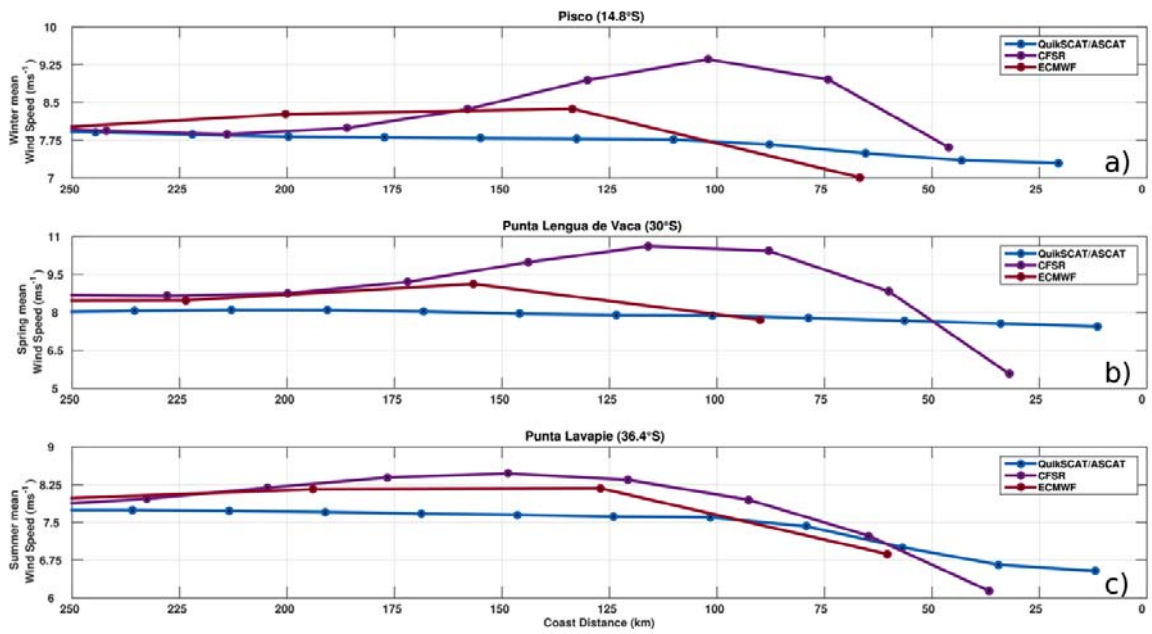

Figure 1.19. Zonal mean cross-shore 10-m wind speed for the upwelling season at **(a)** Pisco (14.8°S), **(b)** Punta lengua de Vaca (30°S) and **(c)** Punta Lavapie (36.4°S) over the period 2000-2010. The blue, purple, and red lines are for QuikSCAT-ASCAT, the CFSR and ECMWF reanalyses respectively.

Despite recent improvements in the spatial resolution of the global atmospheric reanalysis products, the uncertainty in the wind stress curl estimations in the coastal band has persisted due to model biases (Wood et al., 2011) and to the scarcity of in situ observations to constrain atmospheric models through data assimilation. This has resulted in a significant dispersion within the available products of the mean surface winds. To illustrate the latter statement, Figure 1.19 presents the alongshore wind profiles at three major upwelling cells along he coast of Peru and Chile from satellite observations (QuikSCAT, ASCAT), the atmospheric

reanalysis ERA-Interim (Dee et al., 2011) produced by the European Centre for Medium-Range Weather Forecasts (ECMWF) and the Climate Forecast System Reanalysis (CFSR, Saha et al., 2010). First, it is readily apparent that Reanalysis products cannot resolve the coastal zone due to their low resolution; and second, they do not agree in the magnitude and cross-shore variability of the winds in the first 250-km off the coast.

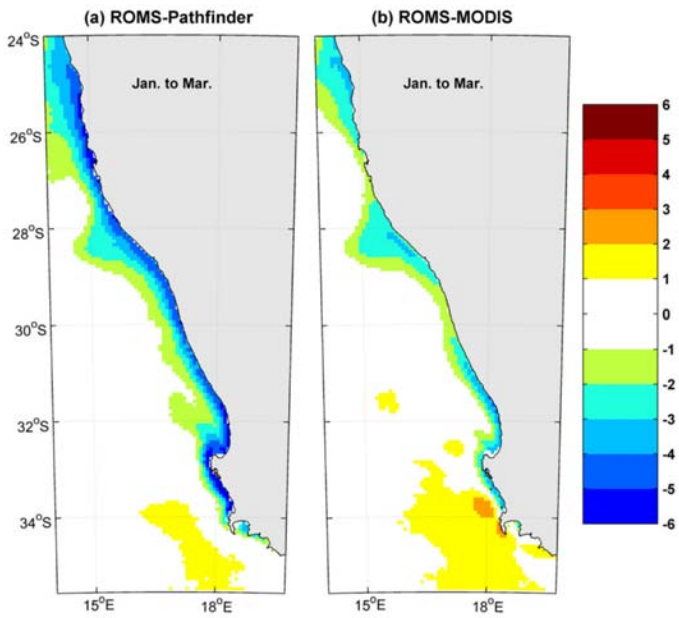

Figure 1.20. (a) Difference between ROMS (Veitch et al., 2010) and Pathfinder v5.0 climatological SST (°C) averaged from January to March. **(b)** Difference between ROMS and MODIS climatological SST (°C) averaged from January to March, in the Benguela system.The cold nearshore bias in this example reaches between 3 and 6 °C everywhere along the coast. From Dufois et al. (2012).

In the meantime, scatterometer winds from QuikSCAT have permitted to produce realistic seasonal oceanic simulations in most EBUS (Aguirre et al., 2012, 2014; Di Lorenzo, 2003; Penven, 2005; Penven et al., 2001), however a surface cold bias near the coast (Fig. 1.20) is usually diagnosed in these simulations (Illig et al., 2014; Penven, 2005; Penven et al., 2001; Veitch et al., 2010; Vergara et al., 2016). Desbiolles et al. (2016) showed that, for the Benguela upwelling system, this cold bias is associated with an overestimated coastal wind that resulted from an earlier release of the gridded QuikSCAT winds at 0.5° resolution. An updated wind product at 0.25° resolution, using a different quality control, has allowed a reduction of the blind zone off the coast to approximately 12.5 km, reducing therefore the mean cold bias. While part of this bias could be also attributed to a correction of the warm bias in the satellite based SST datasets (Dufois et al., 2012), current wind products have in any case inherent limitations for accounting for a realistic wind drop-off (Astudillo et al.,

2017), which has hampered downstreamed applications in particular those directed towards marine resources management.

1.3.6 The Impact of Mesoscale Wind Patterns on Biological Productivity

Naturally, coupled physical-biogeochemical coastal processes show a great sensitivity to near shore wind stress curl in upwelling regions (Albert et al., 2010) and the ecosystem dynamics is also likely critically dependent on the coastal wind pattern through its effects on mesoscale activity. Indeed, eddies and other mesoscale oceanic processes, such as fronts, can enhance biological production in the ocean, according to several open-ocean studies. The effect is thought to be particularly pronounced in low-nutrient environments, where mesoscale processes increase the net upward flux of limiting nutrients. However, eddies have been suggested to damp production in EBUS (see Fig. 1.21).

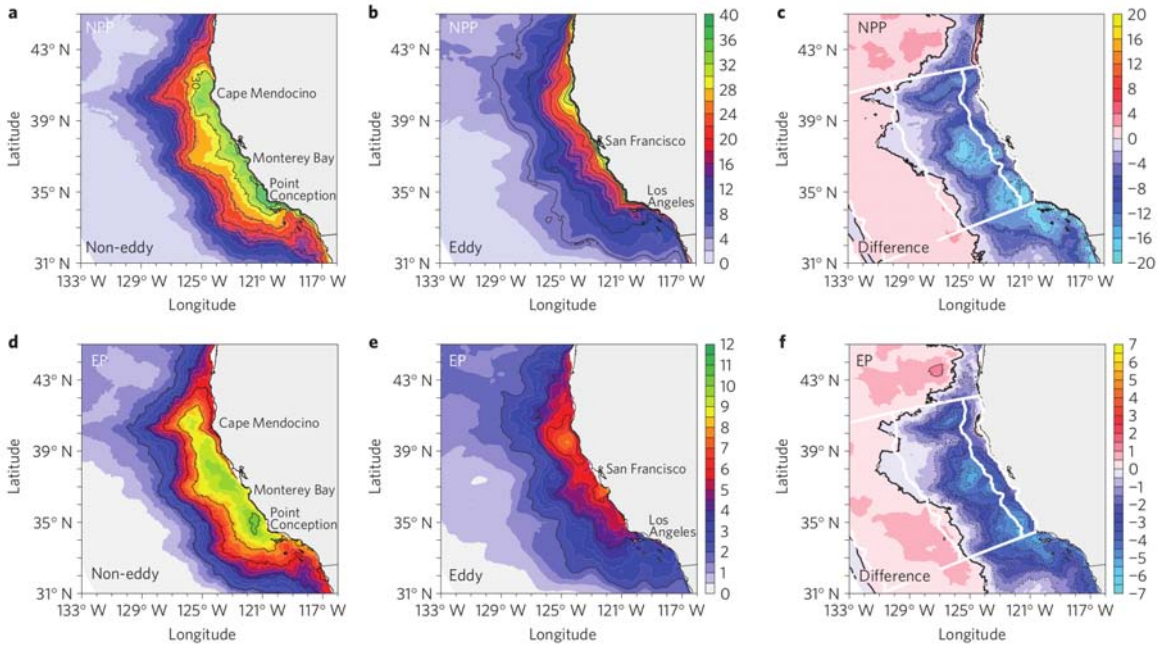

Figure 1.21. Modelled impact of eddies on the distribution of primary and export production in the CalCS. Maps of model-simulated depth integrated primary production (**a** - **c**) and of organic carbon export (across 100 m) (**d** - **f**), in units of mol C m^{-2} yr^{-1} . **a**,**d**, Results from the non-eddy simulation (see text for details) colour scales as for **b** and **e**, respectively. **b**,**e**, results from the eddy simulation. **c**,**f** Difference between the eddy and the non-eddy cases. From Gruber et al. (2011).

Gruber et al. (2011) and Renault et al. (2016a), using eddy-resolving coupled physical-

biogeochemical models of two of these upwelling systems, showed that, eddies suppress production, and that the downward export of organic matter is also reduced. According to these simulations, the reduction in production and export results from an eddy-induced transport of nutrients from the nearshore environment to the open ocean (Gruber et al., 2011), furthermore the net primary productivity is highly dependent on the amplitude of the crosshore wind gradient. In fact, Renault et al. (2016a) shows that a nearshore wind drop-off leads to substantially higher production. This partial decoupling of productivity from upwelling results from the impact of wind patterns on alongshore currents and the eddies they generate. Therefore, eddies might have a similar effect on marine productivity in other EBUS that are characterized by intense eddy activity and mesoscale wind patterns, such as the HCS. The figure 1.21 and 1.22 show, for the CalCS, the suppressing effect of eddies and the impact of the wind drop-off shape on upwelling and NPP.

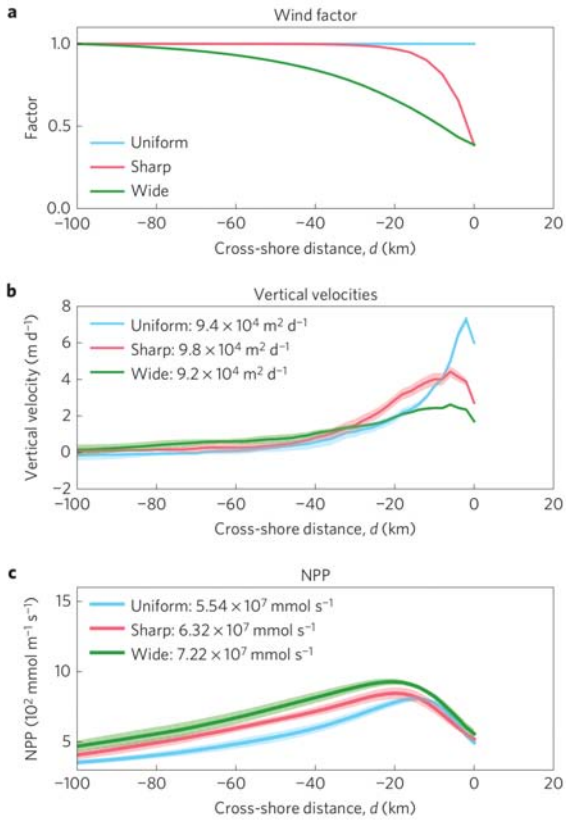

Figure 1.22. Impact of wind drop-off on total upwelling and NPP in the CalCS between 38° N and 43° N during spring (April-June). (**a**), Coastal wind profile factor applied to the wind product. (**b**), Mean vertical velocity at 70 m depth. (**c**), NPP integrated over the photic zone (0–70 m depth). The shaded areas represent the standard deviations. The means and standard deviations are estimated using 8 years of simulations. From Renault et al. (2016a).

1.3.7 Mechanism of Air-Sea-Land Interaction

The role of local air-sea-land interaction in maintaining and modulating the drop-off in upwelling regions is presently unclear. Two main hypotheses have been proposed in the literature to explain the wind drop-off: land-sea change in the surface drag and boundary layer (Capet et al., 2004), and SST-wind coupling (Chelton et al., 2007). The former was recently studied for the coast of California, based on sensitivity experiments with a regional atmospheric model, Renault et al. (2015) showed for instance that coastal orography could produce an enhanced drag coefficient for the low-level circulation that would result in a turbulent momentum flux divergence. This process, combined to orographically-induced vortex stretching, would produce the wind drop-off. The latter is based on the fact that cold

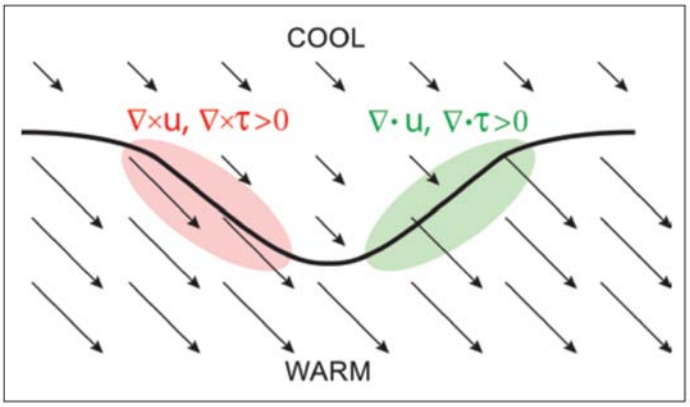

Figure 1.23. Schematic illustration of the divergence and curl of the wind and wind stress fields that result from spatial variations of the SST field. Near a meandering SST front (the heavy black line), surface winds are lower over cool water and higher over warm water, shown qualitatively by the lengths of the vectors. Acceleration where winds blow across the SST front generates divergence (green area). Lateral variations where winds blow parallel to the SST front generate curl (red area). The divergence and curl perturbations are proportional to the downwind and crosswind components of the SST gradient, respectively. From Chelton and Xie (2010).

water from coastal upwelling may modify the nearshore wind stress field in a manner that results in positive wind stress curl due to the stabilization of the atmospheric boundary layer and an associated decrease in the alongshore wind stress toward the coast where the water is the coldest. Jin et al. (2009) show that an empirical coupling which uses the linear relationship between cross-shore SST gradients and wind stress curl (Chelton et al., 2007) leads to substantial changes in wind stress: the stress magnitude decreases dramatically toward the coast, from 0.07 N m^{-2} offshore to about 0.02 N m^{-2}. The reduction in the wind near the coast could also result from the residual effect of the sea breeze and diurnal cycle. On the other hand, the simulation of the drop off is sensitive to various parameters,

including resolution, cloud parametrizations, topography and the characteristics of the Sea Surface Temperature (SST), which limits to a large extent our understanding of its dynamics. The structure and physical forcing of the transition profile is thus an unresolved issue in atmospheric modeling (Jin et al., 2009).

1.3.8 PCUS Dynamics Under Climate Change

The observed trends in upwelling-favorable winds in the last decades, show that alongshore wind in the PCUS are intensifying. For instance, Tokinaga and Xie (2011) using adjusted ship-based measurements from the waves and anemometer-based sea-surface wind (WASWind) show an increase off central Chile (Fig. 1.24), but no trend off Peru. Indirect evidence for this alongshore wind strengthening is also provided by a negative trend in coastal SST, which has been observed off northern Chile since at least 1979 (Falvey and Garreaud, 2009) and off central-southern Peru since mid-twentied century (Gutiérrez et al., 2011). However, it should considered that natural decadal variability could also be an important contributor to the trends (e.g. Vargas et al. (2007)), so the issue of attribution is an open question (Belmadani et al., 2013).

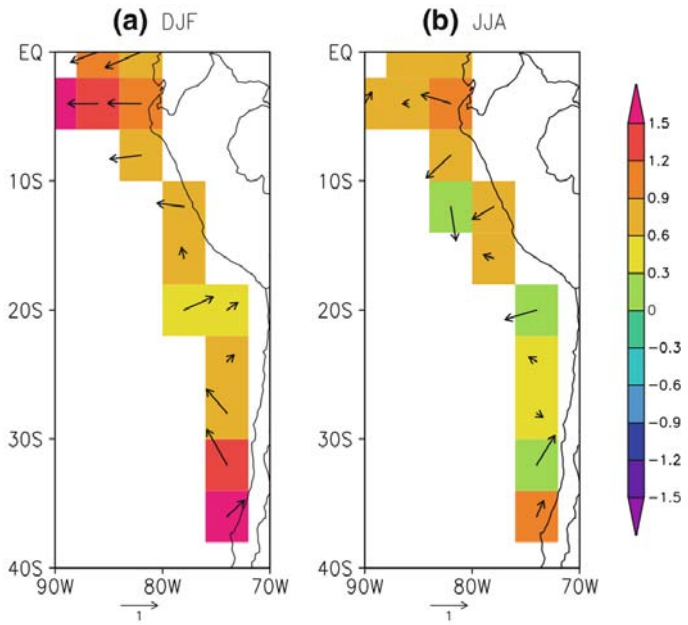

Figure 1.24. 1950–2009 trend in corrected vector and scalar wind (10^{-2} m s^{-1} year^{-1}) from the WASWind product (Tokinaga and Xie, 2011). Only grid cells with data available for 98 % of the time or more are shown. No offshore data is available due to the lack of ship tracks in this region. From Belmadani et al. (2013).

These trends are replicated by CGCM. In fact, early studies have suggested that upwelling

favorable wind would increase under climate change, these future changes in alongshore wind and wind stress curl may be driven by various mechanisms operating on a range of spatial scales (intraseasonal to climatic timescales). Two main hypotheses exist in the climate community to explain the evolution of nearshore equatorward winds (and upwelling) under increasing greenhouse gases conditions. Both hypotheses imply that changes in upwelling-favorable winds are driven by changes in large-scale circulation. As a reminder, the PCUS is immersed in the eastern branch of the SEP, which is also the low level branch of the meridional Hadley circulation between the tropics and the equator. A first hypothesis (Bakun, 1990; Wang et al., 2015) proposes that under anthropogenic forcing, due to increasing ocean-land thermal contrast and associated deepening of the continental thermal low-pressure systems, the cross-shore atmospheric pressure gradient will increase and, by consequence, the alongshore upwelling-favorable winds will intensify. The second hypothesis (Belmadani et al., 2013; Falvey and Garreaud, 2009; Garreaud and Falvey, 2009; Goubanova et al., 2010; Rykaczewski et al., 2015) states that wind and wind stress curl increase off Chile as the result of a strengthening of the large-scale meridional pressure gradient over the subtropical SEP and the decrease off Peru as a consequence of both the slowdown of the Walker circulation and the poleward extension of the Hadley cell.

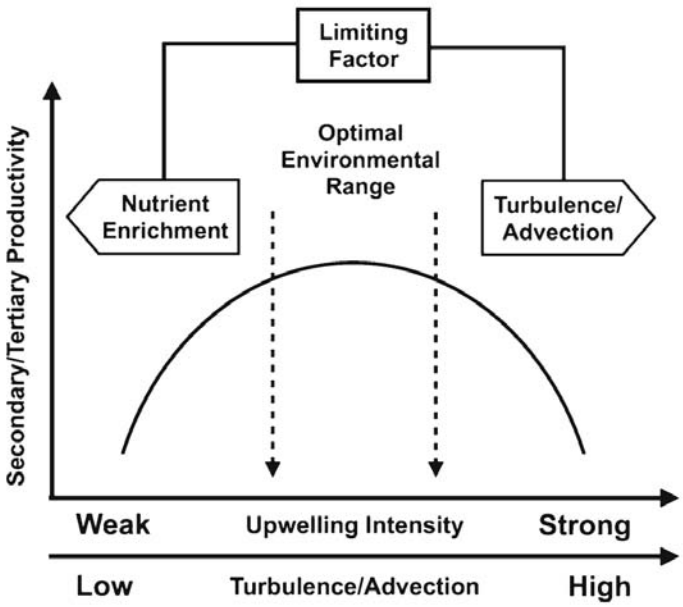

Figure 1.25. The optimal environmental window shows highest levels of productivity at moderate upwelling intensity. When upwelling is strong, biota can be advected offshore, while at low upwelling intensity nutrients in the upper water column can be limiting to productivity. From Bakun (1990) who adapt it from Cury and Roy (1989).

This future scenario with intensified upwelling-favorable winds, at least of central Chile,

would lead to an increased upwelling rate, greater turbulence in the upper ocean, and swifter offshore transport of surface waters. On one hand, mid-amplitude upwelling events and upwelled nutrients would support a robust phytoplankton community (Fig. 1.24), which would in turn sustain flourishing zooplankton and upper trophic level communities. On the other hand, stronger upwelling may lead to enhanced nutrient enrichment, the increased amplitude of alongshore winds could lead to less phytoplankton production within the primary upwelling zone due to deeper wind-driven mixing of the water column and increased light limitation (Bakun et al., 2015).

However, the high intrinsic variability in EBUS suggests that they may be robust and resilient to global warming, discarding over-exploitation or additional major anthropogenic impacts (e.g., pollution). Additionally, the impacts of climate change could be profound and difficult to forecast as they begin to exceed recent millennial ranges of precedent variability (Bakun et al., 2015). Furthermore, given regional peculiarities in both environmental forcings (i.e. wind drop-off), coastline geometry and topography, and the contrasting results of regional oceanic downscaling experiments in different EBUS (Chust et al., 2014; Echevin et al., 2011), further study is required in order to evaluate the sensitivity of the PCUS to climate change.

1.3.9 Scientific Objectives and Methodology

There is therefore a stringent need to better understand the processes of air-sea-land interaction in upwelling region, which is know recognized as a necessary step for improving the realism of the simulations as well as improving our knowledge of the processes of scale interaction in the South Eastern Pacific. We focus within this context on the following specific objectives:

- To document the mesoscale atmospheric circulation along the coast of Peru and Chile from altimetry-derived wind estimates, the focus is on how the observations can account for the spatial variability of the mean wind drop-off near the coast.
- Deployment of the high resolution regional modeling system using the numerical models ROMS and WRF for the atmospheric and oceanic components respectively. This modeling platform will allow simulations with a single domain or several nested domains.
- To evaluate the seasonal variability in Ekman transport, pumping and their relative contribution to the total upwelling along the coast off central-northern Chile, from a high resolution atmospheric (WRF) model.

- To document the fine-scale structures in the wind stress and wind curl in relation to the topographic features along the coast and its impact on the ocean temperature on the basis of the WRF model and high resolution SST satellite data.
- To study the air-sea interactions along the coast of central Chile evaluating the influence of the mesoscale wind patterns on upwelling dynamics and sea surface temperature. We address this issue for the central Chile region based on regional modeling, both oceanic (ROMS) and atmospheric (WRF), high resolution satellite data and in situ observations.
- To assess the mesoscale characteristics of the upwelling dynamics and thermodynamics and how they are linked to the wind drop-off.
- To improve the ability of regional models to reproduce realistically the observed variability near the coast using the modeling platform WRF-ROMS.

1.4 Introduction (Français)

Les systèmes de courant de bord Est sont caractérisés par le phénomène de remontées d'eaux froides sous l'action des vents parallèles à la côte soufflant vers l'équateur (phénoméne appelé en anglais "upwelling"). Ces régions correspondent aussi aux zones de subsidence de masses d'air sec associées aux branches descendantes de la circulation de Hadley-Walker. Ces caractéristiques atmosphériques et océanographiques de la circulation en font le siège d'interactions air- mer spécifiques avec en particulier la formation d'une couverture de nuage bas (de type stratocumulus) qui réfléchit le flux solaire et amplifie l'effet de refroidissement de l'upwelling.

Actuellement les modèles globaux sont défaillants pour simuler la circulation dans ces régions et présentent des biais chauds les plus importants dans la ceinture tropicale. C'est en particulier le cas pour le système de courant de Humboldt (côte Pérou/Chili), la région d'upwelling la plus productive au monde, en termes de ressources halieutiques. La source des biais dans les modèles globaux reste mal connue même si elle est en partie liée à la résolution généralement trop faible de ces modèles pour simuler de manière réaliste le phénomène d'upwelling d'une part et la structure des vents proches de la côte d'autre part. Ces derniers sont en effet caractérisés par une diminution depuis l'océan vers la côte dans une bande côtière de l'ordre de quelques dizaines de kilomètre. Ce phénomène, appelé "drop-off" conditionne la dynamique de l'upwelling par le processus de pompage d'Ekman. En retour, l'upwelling favorise une couche limite atmosphérique stable et donc des vents faibles découplés de la circulation d'altitude. Ce processus d'interaction entre l'océan et l'atmosphère à l'échelle régionale reste encore mal compris et documenté. Il pourrait être pourtant un élément clef pour comprendre la dynamique dans ces régions très sensibles aux changements de la variabilité globale et qui accueillent par ailleurs des écosystèmes très riches. Cette thèse vise à mieux comprendre les interactions océan-atmosphère-continent dans le système d'upwelling du Chili central caractérisé par la présence d'un jet atmosphérique de basse altitude ("Low Level Jet") intense et très variable. Il s'agit en particulier de documenter et de caractériser la diminution des vents moyens à la côte (drop-off). Nous souhaitons ensuite mieux comprendre l'effet de la migration saisonnière du jet côtier atmosphérique sur les processus couplés mis en évidence et la variabilité de l'upwelling. L'approche se base sur l'expérimentation numérique à l'aide des modèles en configuration régionale, océanique et atmosphérique et à haute-résolution et l'analyse de données observées (satellite et données de campagnes). Dans ce contexte, les objectifs et l'approche de ce travail peuvent se résumer comme suit :

- Documenter la circulation atmosphérique à mésoéchelle le long de la côte du Pérou et du Chili à partir d'estimations altimétriques du vent. L'accent est mis sur la variabilité spatiale de la vitesse du vent vers la côte, dans la zone dite de drop-off, motivé par le fait que cette circulation n'est pas observable par les diffusiomètres.

- Développer des configurations du modéle régional atmosphérique WRF et du modéle océanique ROMS afin de mener des expériences de sensibilité au forcage atmosphérique du modele océanique et documenter l'impact du drop-off sur la dynamique de l'upwelling du Chili Central.

- Évaluer la variabilité saisonnière du transport et pompage d'Ekman, et leur contribution relative à l'upwelling côtier du Chili central, à partir des données satellites et du modèle régional atmosphérique WRF.

- Documenter les structures à fines échelles de la tension et rotationnel de vent avec les caractéristiques topographiques le long de la côte du Chili central et son impact sur la température de l'océan sur la base du modèle atmosphérique WRF et les données satellitaires de température à haute résolution.

- Etudier les interactions océan/atmosphàre à mésoéchelle le long de la côte du Chili central. Il s'agit ici d'évaluer la réponse océanique forcée par les variations spatiales de l'intensité des vents sur la dynamique de l'upwelling et la température de surface de la mer.

- Analyser comment les caractéristiques à méso-échelle de l'upwelling du Chili central sont liées à la décroissance vers la côte du vent, afin de mieux comprendre le biais froid côtier observé dans les simulations des modèles océaniques régionaux forcés par les produits atmosphériques couramment utilisés.

Le document présente trois chapitres centraux correspondant a la synthése des résultats sur 1) l'analyse des observations satellites et la caractérisation du drop-off , 2) l'analyse des simulations atmosphériques réalisées avec le modele regionale et la sensibilité de la représentation du drop-off à la résolution horizontale et 3) l'analyse de la sensibilité de la circulation océanique le long de la région centrale du Chili au caractéristique du drop-off. Le dernier chapitre synthétise les résultats et présente des perspectives de ce travail.

Chapter 2

The Mesoscale Atmospheric Circulation Along the Coast of Peru and Chile

2.1 Introduction

This chapter corresponds to the content of the article "Surface winds off Peru-Chile: Observing closer to the coast from radar altimetry" published in the Journal "Remote Sensing of Environment" http://dx.doi.org/10.1016/j.rse.2017.01.010. In this study, we document the near-shore surface atmospheric circulation along the coast of Peru and Chile based on the altimeter data from 4 satellite missions (ENVISAT, Jason-1, Jason-2 and SARAL). The focus is on how the observations can account for the shoreward decrease of wind amplitude, which is influential on the upwelling dynamics and that has been called the “wind drop-off” by modelers. To the authors’ knowledge, our study is the first one that takes advantage of these data to document the surface atmospheric circulation in this coastal region, and we believe it can be valuable for the validation of the regional models of the Eastern boundary current systems.

Remote Sensing of Environment 191 (2017) 179–196

Contents lists available at ScienceDirect

Remote Sensing of Environment

journal homepage: www.elsevier.com/locate/rse

Surface winds off Peru-Chile: Observing closer to the coast from radar altimetry

O. Astudillo [a,b,*], B. Dewitte [a,b,f,g], M. Mallet [c], F. Frappart [b,d], J.A. Rutllant [a,e], M. Ramos [a,f,g,h], L. Bravo [f,g], K. Goubanova [a,f,i], S. Illig [b,j]

[a] Centro de Estudios Avanzados en Zonas Áridas (CEAZA), La Serena, Chile
[b] Laboratoire d'Etudes en Géophysique et Océanographie Spatiale (LEGOS), Toulouse, France
[c] CNRM UMR 3589, Météo-France/CNRS, Toulouse, France
[d] Géosciences Environnement Toulouse (GET), Toulouse, France
[e] Departamento de Geofísica, Facultad de Ciencias Físicas y Matemáticas, Universidad de Chile, Santiago, Chile
[f] Departamento de Biología Marina, Facultad de Ciencias del Mar, Universidad Católica del Norte, Coquimbo, Chile
[g] Millennium Nucleus for Ecology and Sustainable Management of Oceanic Islands (ESMOI), Coquimbo, Chile
[h] Centro de Innovación Acuícola Aquapacifico, Universidad Católica del Norte, Coquimbo, Chile
[i] CECI UMR 5318 - CNRS/CERFACS, Toulouse, France
[j] Departament of Oceanography, MARE Institute, University of Cape Town, South Africa

ARTICLE INFO

Article history:
Received 18 April 2016
Received in revised form 19 December 2016
Accepted 12 January 2017
Available online xxxx

Keywords:
Satellite altimetry
Peru-Chile upwelling system
Coastal surface winds
Wind drop-off

ABSTRACT

The near-shore surface mesoscale atmospheric circulation in the upwelling systems off Peru and Chile is influential on the Sea Surface Temperature through Ekman transport and pumping. There has been a debate whether or not the so-called "wind drop-off", that is a shoreward decrease of the surface wind speed near the coast, can act as an effective forcing of upwelling through Ekman pumping. Although the wind drop-off has been simulated by high-resolution atmospheric models, it has not been well documented due to uncertainties in the scatterometry-derived wind estimates associated with land contamination. Here we use the along-track altimetry-derived surface wind speed data from ENVISAT, Jason-1, Jason-2, and SARAL satellites, to document the spatial variability of the mean wind drop-off near the coast as estimated from the inversion of the radar backscattering coefficient. The data are first calibrated so as to fit with the scatterometer observations of previous and current satellite missions (QuikSCAT, ASCAT). The calibrated data are then analyzed near the coast and a wind drop-off scale is estimated. The results indicate that the wind drop-off takes place all along the coast, though with a significant alongshore variability in its magnitude. Differences between products are shown to be related both to the differences in repeat cycle between the different altimetry missions and to the peculiarities of the coastline shape at the coastal latitudes of the incident tracks. The relative contribution of Ekman pumping and Ekman transport to the total transport is also estimated indicating a comparable contribution off Chile while transport associated to Ekman pumping is on average ~1.4 larger than Ekman transport off Peru. Despite the aliasing effect associated with the weak repetitivity of the satellite orbit and the high frequency variability of the winds in this region, the analysis suggests that the seasonal cycle of the surface winds near the coast could be resolved at least off Peru.

© 2017 Elsevier Inc. All rights reserved.

1. Introduction

Eastern Boundary Current Systems (EBUS) have drawn interest in recent years due to the societal concern on the possible changes that the rich marine ecosystems they host could experience under the influence of anthropogenic climate forcing (Bakun et al., 2015; Wang et al., 2015a). A main driver of the oceanic circulation in these regions is the along-shore momentum flux that promotes upwelling of nutrient-rich waters through Ekman dynamics. While the locally wind-forced processes that generate upwelling are well known and consist in two mechanisms, i.e. Ekman pumping and Ekman transport (Sverdrup et al., 1942) most studies of upwelling systems have focused on the investigation of Ekman transport (i.e., along-shore wind stress) and its relationship to various aspects of the regional oceanic circulation (Sea Surface Temperature (SST), productivity, fisheries) (Carr and Kearns, 2003; Chavez and Messié, 2009; Demarcq, 2009; Wang et al., 2015b; among many others). The relative contribution of both processes has in fact remained ubiquitous due to limitations of the satellite

* Corresponding author at: Centro de Estudios Avanzados en Zonas Áridas (CEAZA), La Serena, Chile.
E-mail address: orlando.astudillo@gmail.com (O. Astudillo).

http://dx.doi.org/10.1016/j.rse.2017.01.010
0034-4257/© 2017 Elsevier Inc. All rights reserved.

scatterometer measurements (ERS, QuikSCAT), which contain a 28 to 50-km wide blind zone along the coast limiting the description of the mesoscale atmospheric circulation within this narrow coastal fringe. The relatively low spatial resolution of these products has also resulted in uncertainty in the actual magnitude of the wind stress curl near the coast (Croquette et al., 2007). Despite recent improvements in the space resolution of the global atmospheric reanalysis products, the uncertainty in the wind stress curl estimations in the coastal band has persisted due to model biases (Wood et al., 2011) and to the scarcity of in situ observations to constrain data assimilation. This has resulted in a significant dispersion within the available products of the mean surface winds. To illustrate the latter statement, Fig. 1 presents the alongshore horizontal wind profiles at three major upwelling cells along the coast of Peru and Chile from satellite observations (QuikSCAT/ASCAT, Jason-1), the atmospheric reanalysis ERA-Interim (Dee et al., 2011) produced by the European Centre for Medium-Range Weather Forecasts (ECMWF) and the National Centers for Environmental Prediction (NCEP) Climate Forecast System Reanalysis (CFSR, Saha et al., 2010). First, it is readily apparent that reanalysis products cannot resolve the coastal zone due to their low resolution; and second, they do not agree in the magnitude and cross-shore variability of the winds in the first 200 km off the coast. In addition, regional modeling studies suggest that the wind stress near the coast in EBUS experiences a shoreward decrease in amplitude, the so-called wind drop-off, that results in a wind stress curl favorable to Ekman pumping (Capet et al., 2004; Renault et al., 2012). Observational evidence of such drop-off has been elusive due to the sparse data in the coastal fringe, although field experiments do suggest its existence in some regions, in particular off central Chile (e.g., Garreaud et al., 2011; Bravo et al., 2015).

The uncertainties resulting from the extrapolation of scatterometer winds in near-coastal regions for forcing high-resolution oceanic models have also been a limitation for gaining confidence in model results (Renault et al., 2012). Indeed, in most EBUS regional modeling studies, gridded QuikSCAT surface wind estimates have been used, implying that wind data have been extrapolated on the ocean model grid from, at best, 28 km offshore to the closest coastal grid point of the ocean model. In the process, there is the possibility that compensating effects exist between the Ekman transport and Ekman pumping on SST (e.g., a weaker (stronger) than observed drop-off would lead to a stronger (weaker) Ekman transport near the coast). Interestingly in regional simulations of upwelling systems, a mean cold bias is usually diagnosed (Penven, 2005; Penven et al., 2001; Veitch et al., 2009; Machu et al., 2009) which could reflect a bias in the balance between Ekman pumping and transport, although such a bias could be also attributed to a warm bias in some satellite based SST datasets (Dufois et al., 2012).

Moreover, coupled physical-biogeochemical coastal processes show a great sensitivity to near shore wind stress curl in upwelling regions (Albert et al., 2010) and the ecosystem dynamics is also likely critically dependent on the coastal wind pattern through its effects on mesoscale activity (Renault et al., 2016).

Therefore, there is a real need to improve our knowledge in the mesoscale atmospheric circulation in coastal regions given the need for a realistic simulation of the oceanic circulation for downstreamed applications (e.g. directed toward resources management). This is particularly true for the Peru-Chile EBUS, known as the Humboldt Current System (HCS), which hosts the most productive marine ecosystem in the world (Chavez et al., 2008). Upwelling off Chile and Peru drive an exceptionally high biological productivity (Carr and Kearns, 2003) due to the persistent equatorward low-level alongshore flow that maintains a coastal band of nutrient-rich cold waters extending from about 40°S to the equator (Hill et al., 1998; Silva et al., 2009). Measurements of surface winds over the HCS are sparse in space and time, lacking systematic,

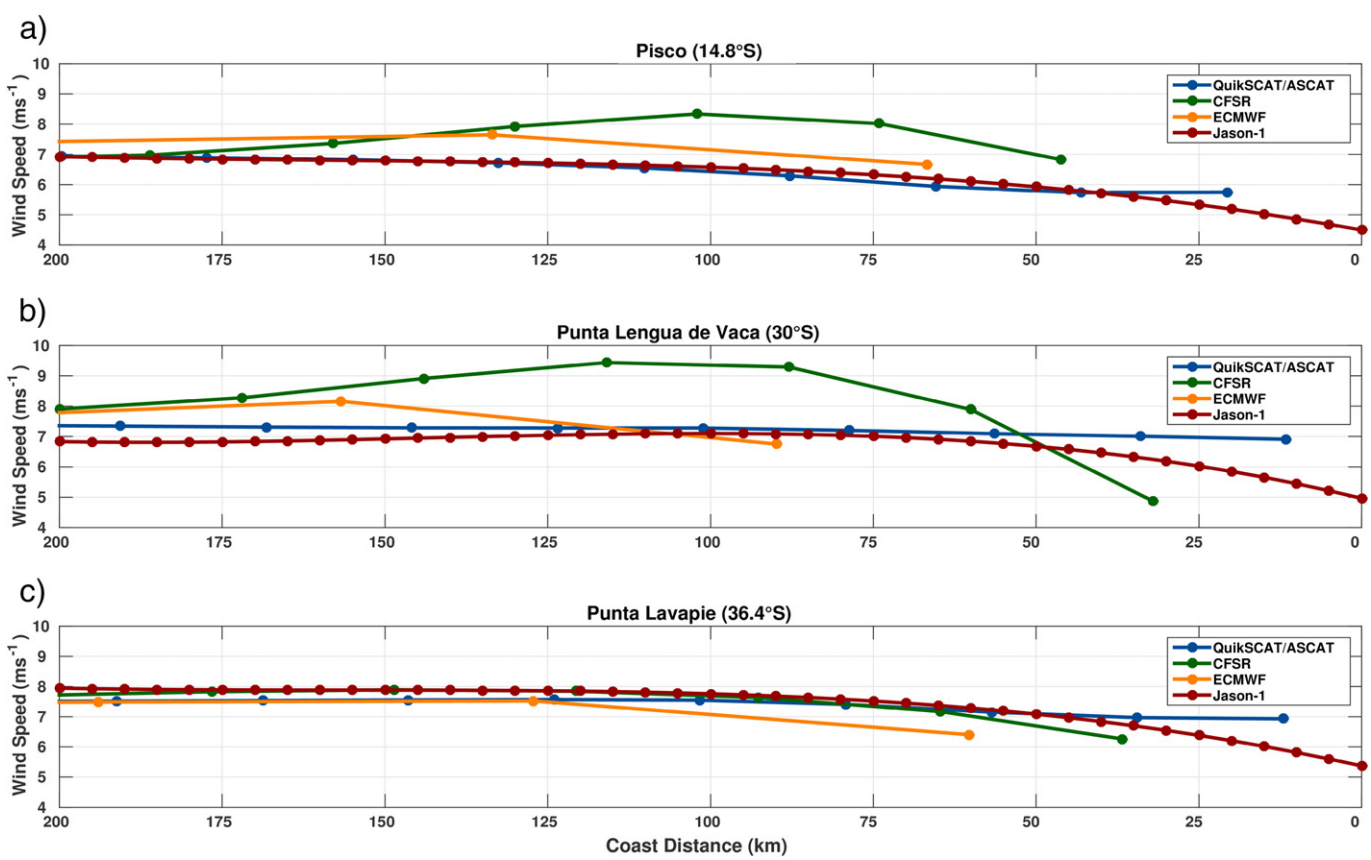

Fig. 1. Zonal mean cross-shore 10-m wind speed at (a) Pisco (14.8°S), (b) Punta Lengua de Vaca (30°S) and (c) Punta Lavapie (36.4°S) over the period 2000–2010. The blue, red, green, and orange lines are for QuikSCAT-ASCAT (0.25° horizontal resolution) scatterometers, Jason-1 (0.045°) altimeter, the CFSR (0.3°) and ERA-Interim (0.75°) reanalyses respectively. (For interpretation of the references to colour in this figure legend, the reader is referred to the web version of this article.)

dense, and long-term monitoring of the near shore area. Most studies analyzing the upwelling favorable winds off Chile and Peru have relied on satellite-borne scatterometer data (Figueroa and Moffat, 2000; Halpern, 2002; Garreaud and Muñoz, 2005; Muñoz, 2008; Renault et al., 2009; Albert et al., 2010; Dewitte et al., 2011; Aguirre et al., 2012) or atmospheric reanalysis and regional models (Renault et al., 2012; Rahn and Garreaud, 2013, Bravo et al., 2015) and have focused on regional features (e.g., large scale coastal jets) rather than on coastal mesoscale circulation.

Here we take advantage of altimeter-derived surface wind speeds from four different altimeter missions (ENVISAT, Jason-1, Jason-2 and SARAL) to assess the near-shore surface atmospheric circulation. The surface wind speeds are retrieved using the backscattering coefficient at Ku-band (Ka-band for SARAL). The focus here is on the mean coastal winds due to inherent limitations of the satellites missions for addressing synoptic-scale variability that is prominent in the region of interest (see Section 2).

The paper is organized as follow: Section 2 provides a detailed description of the satellite sensors and the datasets employed. Section 3 describes the methods used for the altimeter data calibration examining their consistency against winds measured by the scatterometers. In Section 4 mean altimeter-derived coastal winds are analyzed focusing on the intensity and alongshore variability of the wind drop-off, and on estimating the relative contributions of Ekman transport and pumping. Concluding remarks and a discussion are presented in Section 5.

2. Data sources

2.1. Satellite altimetry data

Wind speeds derived from Radar Altimeters (RA) sensors at the Ku-band (13.575 GHz) onboard ENVISAT, Jason-1, Jason-2 and Ka-band (35.75 GHz) onboard SARAL are used in this study. A RA is a nadir-looking active microwave device that measures with high accuracy the time delay, the power and the shape of the reflected radar pulses for determining the satellite height with respect to the earth surface. Radar echo parameters can also be used to derive the significant wave height (*SWH*) and the surface wind speed (U_{10}) (Lefèvre et al., 2006; Queffeulou et al., 1999).

Surface wind speeds are empirically estimated by their effect on the intensity of the return pulse of the radar echo (i.e., backscattering coefficient (σ_0)). With increasing wind speed the sea surface becomes rougher so that the number of specularly reflecting faces decreases and more energy is scattered back in off-nadir directions. This leads to a decrease in the intensity of the mean backscattered power, which can thus be related to the surface wind speed (Ikeda and Dobson, 1995). In order to increase the confidence of the altimeter-derived geophysical parameters, the return pulses are typically averaged over time to provide one data point every second along the satellite ground track. With a satellite ground scanning velocity of 5.8 km^{-1} for Jason-1/Jason-2 and 7.45 km^{-1} for ENVISAT/SARAL each altimeter data value represents an elongated area (footprint) ranging between 1 and 10 km in diameter according to the range, pulse width and SWH (Chelton et al., 1989/2001; Zieger et al., 2009). The small altimeter footprint allows resolving the 50-km fringe along the coast, thus surpassing the scatterometer capabilities subject to retrieval errors onshore due to their large footprint (Yang et al., 2011). On the other hand, unlike scatterometers RA instruments allow deriving only the wind speed because there is no significant dependence of σ_0 on wind direction at small incidence angles.

2.1.1. Jason-1 & 2

These missions were launched on December 7th 2001 and June 20th, 2008. Jason-1 is a cooperative programme between the French Space Agency (Centre National d'Etudes Spatiales, CNES) and the U.S. National Aeronautics and Space Administration (NASA) while Jason-2 is a cooperation among CNES, NASA, the European Meteorological Satellite Organization (EUMETSAT) and the U.S. National Oceanic and Atmospheric Administration (NOAA), respectively. Their main payload is the Poseidon-2(3) radar altimeter from CNES, the Jason/Advanced Microwave Radiometer (JMR/AMR) from JPL/NASA, and a triple system for precise orbit determination: the real-time tracking system DIODE of DORIS instrument from CNES, a GNSS receiver and a Laser Retroflector Array (LRA) from NASA. They orbit at an altitude of 1336 km, with an inclination of 6°, on a 10-day repeat cycle, providing observations of the Earth surface (ocean and land) from 66° South to North, with an equatorial ground-track spacing of about 315 km. Topex/Poseidon formerly used this orbit. Poseidon-2 and Poseidon-3 radar altimeters are dual-frequency solid-state altimeters that measure accurately the distance between the satellite and the surface (range) and provide ionospheric corrections over the ocean. They operate at Ku (13.575 GHz) and C (5.3 GHz) bands. Raw data are processed by SSALTO (Segment Sol multimissions d'ALTimétrie, d'Orbitographie). Jason-1 was decommissioned in July 2013.

2.1.2. ENVISAT (ENVironmental SATellite)

This mission was launched on March 1st 2002 by the European Space Agency (ESA). It carries 10 instruments including the advanced radar altimeter (RA-2). It is based on the heritage of the sensor onboard the European Remote Sensing (ERS-1 and 2) satellites. RA-2 was a nadir-looking pulse-limited radar altimeter operating at Ku- (13.575 GHz), as ERS-1 and 2, and S- (3.2 GHz) bands. Its goal was to collect radar altimetry data over ocean, land and ice caps. ENVISAT orbits at an average altitude of 790 km, with an inclination of 98.54°, on a sun-synchronous orbit with a 35-day repeat cycle. It provided observations of the Earth surface (ocean and land) from 82.4° latitude South to 82.4° latitude North. This orbit was formerly used by ERS-1 and 2 missions, with an equatorial ground-track spacing of about 85 km. ENVISAT remained on its nominal orbit until October 2010 and its mission ended on April 8th 2012.

2.1.3. SARAL (Satellite with Argos and ALtika)

This joint French-Indian mission between the CNES and the Indian Space Research Organization (ISRO) was launched on February 25th 2013. Its payload is composed of the AltiKa radar altimeter, a dual-frequency radiometer and a triple system for precise orbit determination: the real-time tracking system DIODE of DORIS instrument, a Laser Retroflector Array (LRA), and the Advanced Research and Global Observation Satellite (ARGOS-3). Its initial orbital characteristics were the same as for ENVISAT (see above). The first four cycles of SARAL did not follow precisely the ENVISAT orbit. AltiKa radar altimeter is a solid-state monofrequency altimeter that provides accurate range measurements. It is the first and the only altimeter to operate at the Ka-band (35.75 GHz).

Data used in this study are the along-track values of U_{10} made available along with corresponding track and cycle numbers, acquisition time, latitude, longitude and the distance to the coast from the Geophysical Data Records (GDRs) of the different altimetry missions. These data come from GDR T patch 2 for SARAL, GDR v2.1 for ENVISAT, GDR C for Jason-1 and GDR D for Jason-2. They are available at the Centre de Topographie de l'Océan et de l'Hydrosphère (CTOH – http://ctoh.legos.obs-mip.fr/).

The wind speed is estimated through the inversion of a relationship with the Ku-band backscatter coefficient (corrected for atmospheric attenuation) and the significant wave height using a neural network for Jason-1 and Jason-2 (Gourrion et al., 2002). For ENVISAT, the empirical model used to retrieve the wind speed is given by (Abdalla, 2012):

$$U_{10} = U_m + 1.4U_m^{0.096}e^{-0.32U_m^{1.096}} \tag{1}$$

$$\text{With } U_m = \begin{cases} \alpha - \beta\sigma_0^a & \text{if } \sigma_0^a \le \sigma_0^{\lim} \\ \gamma e^{-\delta\sigma_0^a} & \text{if } \sigma_0^a > \sigma_0^{\lim} \end{cases} \tag{2}$$

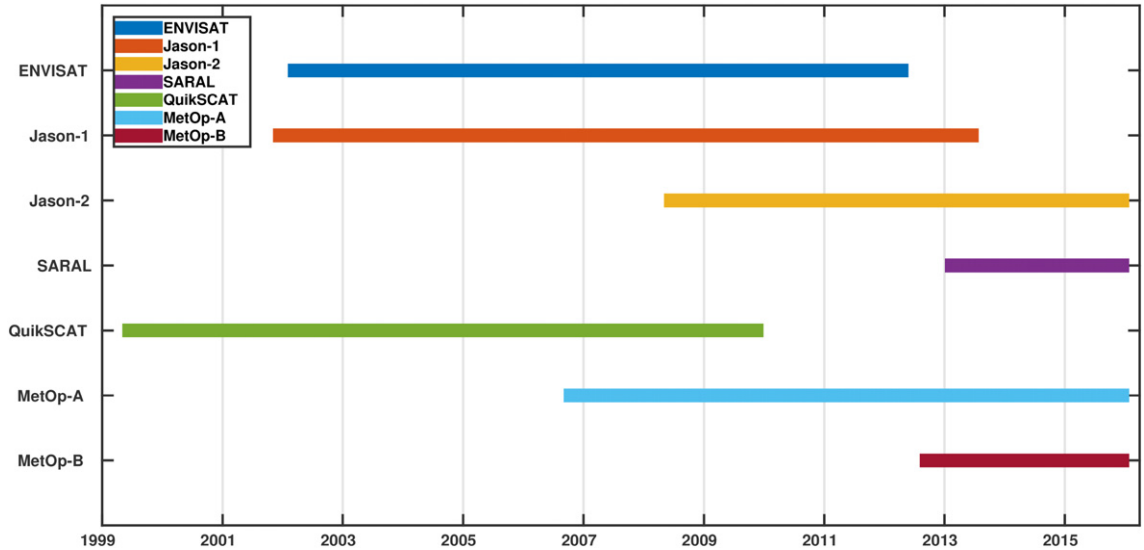

Fig. 2. Temporal coverage of the satellite missions.

where U_m is a first-guess estimation of U_{10} while $\alpha = 46.5$, $\beta = 3.6$, $\gamma = 1690$, $\delta = 0.5$, $\sigma_0^{\mathrm{lim}} = 10.917$ dB are the fitting parameters. For SARAL, the same formulation as for ENVISAT is used with the following fitting parameters values $\alpha = 34.2$, $\beta = 2.48$, $\gamma = 711.6$, $\delta = 0.42$, $\sigma_0^{\mathrm{lim}} = 11.409$ dB (Lillibridge et al., 2014).

Details on the time periods and technical specifications (e.g., repeat cycle, inclination, and footprint) for each satellite mission are provided in Fig. 2 and Table 1.

2.2. Satellite scatterometer data

Wind scatterometry is a widely used technique that measures wind speeds and directions over the ocean surface. The measurement principle differs from the altimeters because it is based on the Bragg resonant scattering mechanism, for which backscatter power is directly proportional to the distribution and density of capillary and short gravity waves on the sea surface (Queffeulou et al., 1999).

This study uses the scatterometer Sea Winds aboard the QuikSCAT satellite and the Advanced SCATterometer (ASCAT) aboard Metop-A and Metop-B satellites. QuikSCAT was a mission that lasted from June 1999 to November 2009; meanwhile the ongoing series of Metop-A and Metop-B satellites were launched on October 2006 and September 2012 respectively. We used two types of scatterometer products:

1. Level-2: The L2-swath products provide wind vector retrievals at 12.5-km sampling resolution on a non-uniform grid within the swath, with 12-hour repeat cycles between the ascending and descending satellite passes, enabling their utilization for the altimeter validation and calibration. Here we used the new reprocessed datasets (QuikSCAT, ASCAT) optimized for coastal ocean (Fore et al., 2014; KNMI, 2010, 2013; SeaPAC, 2013).
2. Level-3: The L3-gridded products contain wind vector fields corresponding to the daily average of both L2-swath passes interpolated onto a regular grid of 0.25° in longitude and latitude using objective method. We used the new daily-averaged gridded wind fields (QuikSCAT, ASCAT) to validate the calibrated altimeters winds (Bentamy and Fillon, 2012).

The accuracy of scatterometer products was determined in several studies using moored buoys, in which the RMS differences did not exceed 2 ms^{-1} and 20° for wind speed and direction, respectively at global scale (Bentamy et al., 2008; Vogelzang et al., 2011; Verhoef and Stoffelen, 2013).

3. Methods

3.1. Calibration of the altimeter data

3.1.1. Quality control

A three-pass quality-control process was applied to the data. Firstly, we have rejected from the analysis all quality-flagged data and all measurements identified as over land. Secondly, if $U_{10} < 1\ \mathrm{ms}^{-1}$, then the data point was flagged as erroneous due to the significant biases related to damping of Bragg waves at very low wind speeds (Yang et al., 2011). Finally, if $U_{10} > 20\ \mathrm{ms}^{-1}$, then the data point was discarded because the

Table 1
Summary of the main technical characteristics by satellite mission. The effective footprint size for the altimeters is related to SWH = 5 m (Chelton et al., 1989, 2001; Zieger et al., 2009; Callahan and Lungu, 2006; Verhoef and Stoffelen, 2013; Verron et al., 2015; http://www.aviso.altimetry.fr/missions).

Satellite	Operation period	Repetitivity	Inclination	Altitude	Instrument	Frequency	Footprint	Format	Agency
ENVISAT	March 2002–April 2012	35 days (cycle)	98.54°	790 km	Radar Altimeter-2	Ku band (13.575 GHz)	~5.6 × 15 km	Alongtrack	ESA
Jason-1	December 2001–June 2013	10 days (cycle)	66.04°	1336 km	POSEIDON-2	Ku band (13.575 GHz)	~6.9 × 20 km	Alongtrack	NASA,CNES
Jason-2	June 2008–present	10 days (cycle)	66.04°	1336 km	POSEIDON-3	Ku band (13.575 GHz)	~6.9 × 20 km	Alongtrack	NASA, CNES, NOAA, EUMESAT
SARAL	February 2013–present	35 days (cycle)	98.55°	790 km	AltiKa	Ka band (35.75 GHz)	~5.6 × 8 km	Alongtrack	ISRO,CNES
QuikSCAT	June 1999–November 2009	12 h (pass)	98.61°	802.4 km	SeaWinds	Ku band (13.4 GHz)	~25 × 37 km	Swath Gridded	NASA
Metop-A Metop-B	October 2006–present September 2012–present	12 hour (pass)	98.7°	817 km	ASCAT-A ASCAT-B	C band (5.255 GHz)	~10 × 20 km	Swath Gridded	ESA, EUMETSAT

wind vector algorithms for QuikSCAT are developed for the wind speeds less than this limit (Quilfen et al., 2007).

3.1.2. Validation

The wind speeds derived from the altimeters were matched against the L2-swath (12.5-km) and L3-gridded (28-km) scatterometer products considered here as the "reference" source data. The comparison between the altimeter and scatterometer data was carried out over a domain that excludes the 50-km width coastal band and extends offshore for 250 km. The outliers that had a wind speed difference between paired altimeter and scatterometer greater than three standard deviations were excluded from the analysis. The sequential procedure was performed in three steps:

1. We matched all the valid altimeter values by mission with the L2-swath scatterometer data. A collocation criteria was chosen in order to get statistically significant number of comparison from both ascending/descending scatterometer passes in the minimum space/time limits, i.e. 12.5 km in space and 60 min for Jason-1/Jason-2 and 120–240 min for ENVISAT/SARAL. The temporal relaxation for ENVISAT/SARAL is necessary given the limited time span of their overpass over the study region.
2. The daily averages (reference time 12:00) from the L3-gridded data were interpolated to the altimeter tracks locations using a natural neighbor interpolation scheme (Shanas et al., 2014) producing a daily temporal match-up.
3. Statistics describing the comparisons were conducted characterizing the differences between the altimeters and both scatterometer products including conventional, linear moments and the regression parameters.

Table 2 summarizes the statistics of the validation of the altimeter data against the reference products over the selected time periods (i.e., ENVISAT: Jan. 2003–Dec. 2009; SARAL: Mar. 2013–Apr. 2014; Jason-1: Jan. 2002–Dec. 2008; Jason-2: Jan. 2009–Dec. 2013). Additionally we provide the statistics classified into three categories of low (<4 ms^{-1}), medium (4–10 ms^{-1}) and high (>10 ms^{-1}) wind speeds.

The first collocated datasets (i.e., altimeter versus L2-swath) were limited in number (62,110/30,375 hits of the total available for ENVISAT/SARAL and 19,748/13,262 for Jason-1/Jason-2, respectively) due to the stringent time/space collocation criteria and to the reduced time periods of the morning (descending passes) and the evening (ascending passes) orbit segments from the L2-swath scatterometer. The frequency distribution of the altimeter/scatterometer by wind speed category corresponds on average to ~20%, ~72% and ~8% for low, medium and high winds respectively. The outliers account for ~5% of the paired values for ENVISAT/SARAL and ~8% for Jason-1/Jason-2. The overall Pearson's correlation coefficients (ρ) are high for all satellites (above 0.95) and the wind speed differences are characterized by a rather small mean bias of ~−0.5 ms^{-1}, Root-Mean-Square Error (RMSE) of ~0.9 ms^{-1} and Mean Absolute Error (MAE) of ~0.8 ms^{-1}. The highest discrepancies were found for low winds in ENVISAT and Jason-1 (see Table 2).

The second collocated dataset (i.e., altimeter versus L3-gridded) amounts to ~95% of the valid altimeter values. The frequency distribution presents similar percentages for wind categories as for the L2-swath data. The agreement in statistics between altimeter and scatterometer decreases unsurprisingly as a function of the temporal gridding of the reference products (i.e. daily averages in L3-gridded versus instantaneous values for L2-swath) consistent with Monaldo (1988). The mean correlation coefficients, bias, RMSE and MAE are ~0.9, ~−0.4 ms^{-1}, ~1.2 ms^{-1} and ~1 ms^{-1}, respectively.

Table 2
Summary of the statistics by altimeter mission using swath and gridded scatterometer as ground-truth reference. Mean bias, RMSE, MAE, Pearson's correlation coefficient (ρ) and standard deviation along with the number of collocated data points and outliers are provided. The wind speed is classified as: low (<4 ms^{-1}), medium (4–10 ms^{-1}) and high (>10 ms^{-1}). Statistics are obtained outside the coastal area (50–300 km offshore).

Validation	Dates	Range	Length		Outliers	ρ	Bias	RMSE	MAE	STD		Mean	
			ALT	SCA						ALT	SCA	ALT	SCA
Altimeter ENVISAT vs. scatterometer (swath)	2003-01-01–2009-12-31	**All**	**62,110 (22.6%)**		**3532**	**5.4%**	**0.96**	**−0.40**	**0.89**	**0.74**	**2.64**	**2.80**	**6.08**	**6.48**
		<4	13,491 (21.7%)	11,959 (19.3%)	851	24.1%	0.69	−0.35	0.91	0.74	0.88	0.87	2.68	2.69
		4–10	43,460 (70.0%)	42,964 (69.2%)	2465	69.8%	0.91	−0.42	0.87	0.72	1.53	1.60	6.50	6.70
		≥ 10	5159 (8.3%)	7187 (11.6%)	216	6.1%	0.75	−0.35	1.04	0.83	1.23	1.31	11.46	11.50
Altimeter ENVISAT vs. scatterometer (gridded)		**All**	**260,704 (94.7%)**		**14,711**	**5.3%**	**0.90**	**−0.29**	**1.22**	**0.96**	**2.66**	**2.47**	**6.11**	**6.40**
		<4	54,695 (21.0%)	41,957 (16.1%)	2881	19.6%	0.54	−0.95	1.51	1.20	0.91	0.85	2.65	2.85
		4–10	183,658 (70.4%)	196,922 (75.5%)	10,520	71.5%	0.79	−0.21	1.08	0.87	1.51	1.51	6.48	6.60
		≥ 10	22,351 (8.6%)	21,825 (8.4%)	1310	8.9%	0.57	0.65	1.54	1.20	1.30	1.14	11.58	11.40
Altimeter SARAL vs. scatterometer (swath)	2013-03-14–2016-01-16	**All**	**30,375 (24.8%)**		**1702**	**5.3%**	**0.94**	**−0.20**	**0.98**	**0.79**	**2.52**	**2.82**	**6.33**	**6.52**
		<4	5238 (17.2%)	5513 (18.1%)	283	16.6%	0.52	0.01	1.10	0.90	0.79	0.89	2.98	2.67
		4–10	22,395 (73.7%)	21,364 (70.3%)	1336	78.5%	0.87	−0.20	0.93	0.75	1.58	1.56	6.49	6.66
		≥ 10	2742 (9.0%)	3498 (11.5%)	83	4.9%	0.81	−0.59	1.10	0.88	1.15	1.46	11.44	11.78
Altimeter SARAL vs. scatterometer (gridded)		**All**	**115,754 (94.6%)**		**6579**	**5.4%**	**0.91**	**−0.12**	**1.07**	**0.86**	**2.57**	**2.56**	**6.17**	**6.29**
		<4	22,092 (19.1%)	21,303 (18.4%)	1423	21.6%	0.57	−0.42	1.18	0.96	0.89	0.93	2.76	2.74
		4–10	83,844 (72.4%)	84,749 (73.2%)	4684	71.2%	0.82	−0.09	1.02	0.82	1.56	1.50	6.45	6.58
		≥ 10	9818 (8.5%)	9702 (8.4%)	472	7.2%	0.67	0.32	1.27	1.00	1.10	1.18	11.39	11.50
Altimeter Jason-1 vs. scatterometer (swath)	2002-01-01–2008-12-31	**All**	**19,748 (5.4%)**		**1564**	**7.3%**	**0.97**	**−0.85**	**1.09**	**0.94**	**2.48**	**2.71**	**5.87**	**6.72**
		<4	3938 (19.9%)	2900 (14.7%)	208	13.3%	0.81	−0.50	0.76	0.63	0.85	0.74	2.92	2.97
		4–10	14,323 (72.5%)	14,373 (72.8%)	1267	81.0%	0.93	−0.93	1.15	1.01	1.54	1.58	6.10	6.61
		≥ 10	1487 (7.5%)	2475 (12.5%)	89	5.7%	0.87	−0.92	1.20	1.05	1.36	1.48	11.47	11.70
Altimeter Jason-1 vs. scatterometer (gridded)		**All**	**345,836 (94.3%)**		**20,910**	**5.7%**	**0.89**	**−0.75**	**1.37**	**1.13**	**2.42**	**2.43**	**5.89**	**6.64**
		<4	67,995 (19.7%)	44,495 (12.9%)	4357	20.8%	0.43	−1.08	1.59	1.31	0.82	0.70	2.93	3.08
		4–10	253,124 (73.2%)	267,308 (77.3%)	15,323	73.3%	0.79	−0.73	1.32	1.10	1.50	1.54	6.15	6.62
		≥ 10	24,717 (7.1%)	34,033 (9.8%)	1230	5.9%	0.64	0.01	1.25	0.98	1.26	1.23	11.44	11.41
Altimeter Jason-2 vs. scatterometer (swath)	2009-01-01–2015-12-31	**All**	**13,262 (4.1%)**		**1110**	**7.7%**	**0.98**	**−0.50**	**0.75**	**0.64**	**2.47**	**2.67**	**6.01**	**6.51**
		<4	2627 (19.8%)	2298 (17.3%)	144	13.0%	0.84	−0.19	0.58	0.47	0.85	0.84	2.85	2.78
		4–10	9733 (73.4%)	9455 (71.3%)	872	78.6%	0.96	−0.57	0.78	0.67	1.63	1.58	6.38	6.64
		≥ 10	902 (6.8%)	1509 (11.4%)	94	8.5%	0.91	−0.70	0.84	0.76	1.00	1.11	11.24	11.36
Altimeter Jason-2 vs. scatterometer (gridded)		**All**	**307,583 (94.3%)**		**18,686**	**5.7%**	**0.91**	**−0.38**	**1.12**	**0.91**	**2.46**	**2.43**	**5.98**	**6.36**
		<4	60,826 (19.8%)	48,495 (15.8%)	3769	20.2%	0.47	−0.70	1.32	1.08	0.83	0.81	2.89	2.93
		4–10	224,123 (72.9%)	232,904 (75.7%)	13,736	73.5%	0.82	−0.35	1.06	0.86	1.53	1.50	6.27	6.51
		≥ 10	22,634 (7.4%)	26,184 (8.5%)	1181	6.3%	0.60	0.20	1.20	0.95	1.15	1.07	11.38	11.35

3.1.3. Calibration

This stage consists in a linear regression analysis to derive the correction coefficients for the altimeter estimates of the wind speed, in order to increase the agreement between scatterometer and altimeter. Similar procedures were applied for various regions in the past using buoys as the ground-truth reference (Desai and Vincent, 2003; Ray and Beckley, 2003; Queffeulou, 2003; Abdalla, 2006; Zieger et al., 2009). In our region of interest, we do not have access to any buoy data and available airport meteorological data are too far inland, so that our reference data were provided by the scatterometers. The slope and offset of the best linear fit between the scatterometer (L2-swath) data and the altimeter data in the off shore region (i.e. excluding the 50-km width coastal band) provides the calibration parameters by mission. The altimeter U_{10} data are taken as the independent variable. Then the calibrated wind speed (U^c_{10}) can be written as follows:

$$U^c_{10} = U_{10} \times slope + offset \tag{3}$$

The suitability of the calibration coefficients was evaluated matching the calibrated altimeter winds against both scatterometer products, repeating the same statistical analysis performed in the previous validation phase. The calibration procedure was successful in removing the negative bias, reducing the errors and increasing the match between the Probability Distribution Functions (PDF) of the scatterometer and the altimeter data (not shown). However there are slightly increased densities of medium wind conditions for the altimeter data in comparison with the scatterometer data. Such values are mostly present in ENVISAT and Jason-1 wind estimates. Table 3 provides the calibration results by satellite mission and Fig. 3 illustrates a typical calibration result for the Jason-2 altimeter data.

3.1.4. Time window differences

To quantify the impact of the relaxed temporal proximity between altimeter-scatterometer (L2-swath) for the ENVISAT/SARAL missions we apply the same temporal window (120–240 min) to the Jason-1/Jason-2 winds. The statistics for the validation experiments exhibit lower correlation coefficients (0.94 vs. 0.97/0.96 vs. 0.98) and higher bias (-0.87 ms^{-1} vs. -0.85 ms^{-1}/-0.54 ms^{-1} vs. -0.50 ms^{-1}) and RMS (1.26 ms^{-1} vs. 1.09 ms^{-1}/0.95 ms^{-1} vs. 0.75 ms^{-1}) values with regard to the former time criteria (60 min), for Jason-1/Jason-2 respectively. For the calibration the results were: correlation coefficients (0.94 vs. 0.97/0.96 vs. 0.98), bias (-0.12 ms^{-1} vs. -0.09 ms^{-1}/-0.09 ms^{-1} vs. -0.07 ms^{-1}) and RMS (0.90 ms^{-1} vs. 0.67 ms^{-1}/0.76 ms^{-1} vs. 0.53 ms^{-1}).

Finally, in order to gain confidence in the calibration within the blind zone, we have paired the L2-swath scatterometer data with the altimeter data for the nearest points from the coast (0–50 km). Our analysis indicates that statistics are comparable, although with slightly reduced scores relative to those performed offshore. The statistics are listed in Table 4.

3.1.5. Gridding, averaging and track selection

The calibrated wind speeds U^c_{10} were converted to neutral wind stress (τ) using the bulk formula:

$$\tau = \rho_a \times C_d \times \left(U^c_{10}\right)^2 \tag{4}$$

with ρ_a the constant air density (1.22 kg×m^{-3}) and C_d the neutral drag coefficient varying with U^c_{10} as in Large and Pond (1981) and Gill (1982).

For each altimetry mission, data were first stacked into along-track cells of 7 km of length during the complete observation period considered in this study, similarly to what was done by Blarel et al. (2015) and Frappart et al. (2016). Altimetry data location in longitude and

Table 3
Calibration functions and statistics: The superscript "c" denotes the calibrated wind speed (U^c_{10}). Mean bias, RMSE, MAE, Pearson's correlation coefficient (ρ) and standard deviation along with the number of collocated concurrent data points and outliers are provided. Statistics are obtained outside the coastal area (50–300 km offshore).

Calibration	Calibration function/dates	Range	Length		Outliers		ρ	Bias	RMSE	MAE	STD		Mean	
			ALT	SCA							ALT	SCA	ALT	SCA
Altimeter ENVISAT vs. scatterometer (swath)	$U^c_{10} = 1.0162*U_{10}+0.3031$/[2003-01-01, 2009-12-31]	**All**	**62,370 (23%)**		**3272**	**5.0%**	**0.96**	**−0.06**	**0.79**	**0.63**	**2.68**	**2.80**	**6.49**	**6.55**
		<4	11,163 (17.9%)	11,511 (18.5%)	705	21.5%	0.64	−0.08	0.84	0.68	0.78	0.88	2.76	2.70
		4–10	44,666 (71.6%)	43,392 (69.6%)	2271	69.4%	0.91	−0.08	0.75	0.61	1.54	1.61	6.67	6.72
		≥ 10	6541 (10.5%)	7467 (12.0%)	296	9.0%	0.79	0.04	0.91	0.71	1.29	1.31	11.56	11.49
Altimeter ENVISAT vs. scatterometer (gridded)		**All**	**260,606 (95%)**		**14,809**	**5.4%**	**0.90**	**0.07**	**1.21**	**0.93**	**2.71**	**2.48**	**6.50**	**6.43**
		<4	45,325 (17.4%)	41,099 (15.8%)	2326	15.7%	0.49	−0.69	1.38	1.07	0.81	0.85	2.73	2.85
		4–10	187,328 (71.9%)	197,263 (75.7%)	10,861	73.3%	0.79	0.10	1.05	0.83	1.51	1.52	6.64	6.62
		≥ 10	27,953 (10.7%)	22,244 (8.5%)	1622	11.0%	0.60	1.04	1.74	1.36	1.39	1.14	11.69	11.41
Altimeter SARAL vs. scatterometer (swath)	$U^c_{10} = 1.0546*U_{10}-0.1438$/[2013-03-14, 2016-01-16]	**All**	**30,426 (25%)**		**1651**	**5.1%**	**0.94**	**−0.03**	**0.95**	**0.76**	**2.67**	**2.84**	**6.54**	**6.57**
		<4	4936 (16.2%)	5430 (17.8%)	259	15.7%	0.51	0.02	1.10	0.90	0.82	0.89	2.93	2.67
		4–10	22,142 (72.8%)	21,377 (70.3%)	1309	79.3%	0.87	−0.02	0.91	0.73	1.60	1.56	6.57	6.67
		≥ 10	3348 (11.0%)	3619 (11.9%)	83	5.0%	0.82	−0.13	0.95	0.73	1.29	1.46	11.61	11.79
Altimeter SARAL vs. scatterometer (gridded)		**All**	**115,711 (95%)**		**6622**	**5.4%**	**0.91**	**0.04**	**1.10**	**0.88**	**2.71**	**2.57**	**6.35**	**6.31**
		<4	21,007 (18.2%)	21,143 (18.3%)	1367	20.6%	0.56	−0.43	1.19	0.97	0.91	0.93	2.70	2.74
		4–10	82,638 (71.4%)	84,717 (73.2%)	4678	70.6%	0.81	0.06	1.02	0.82	1.58	1.50	6.52	6.59
		≥ 10	12,066 (10.4%)	9851 (8.5%)	577	8.7%	0.70	0.76	1.44	1.11	1.24	1.20	11.54	11.51
Altimeter Jason-1 vs. scatterometer (swath)	$U^c_{10} = 1.0631*U_{10}+0.4770$/[2002-01-01, 2008-12-31]	**All**	**20,363 (6%)**		**949**	**4.5%**	**0.97**	**−0.09**	**0.67**	**0.54**	**2.62**	**2.73**	**6.75**	**6.84**
		<4	2293 (11.3%)	2801 (13.8%)	108	11.4%	0.72	0.06	0.60	0.48	0.73	0.73	2.97	2.98
		4–10	15,573 (76.5%)	14,886 (73.1%)	759	80.0%	0.93	−0.14	0.67	0.54	1.49	1.60	6.49	6.69
		≥ 10	2497 (12.3%)	2676 (13.1%)	82	8.6%	0.90	0.07	0.72	0.57	1.54	1.55	11.81	11.72
Altimeter Jason-1 vs. scatterometer (gridded)		**All**	**347,690 (95%)**		**19,055**	**5.2%**	**0.89**	**−0.01**	**1.18**	**0.93**	**2.56**	**2.44**	**6.72**	**6.73**
		<4	40,673 (11.7%)	41,831 (12.0%)	2401	12.6%	0.31	−0.70	1.40	1.12	0.70	0.69	3.01	3.10
		4–10	266,002 (76.5%)	269,825 (77.6%)	14,444	75.8%	0.79	−0.04	1.07	0.86	1.46	1.55	6.51	6.67
		≥ 10	41,015 (11.8%)	36,034 (10.4%)	2210	11.6%	0.69	0.88	1.52	1.21	1.46	1.24	11.76	11.42
Altimeter Jason-2 vs. scatterometer (swath)	$U^c_{10} = 1.0621*U_{10}+0.1304$/[2009-01-01, 2015-12-31]	**All**	**13,566 (4%)**		**806**	**5.6%**	**0.98**	**−0.07**	**0.53**	**0.43**	**2.63**	**2.70**	**6.56**	**6.64**
		<4	2048 (15.1%)	2207 (16.3%)	118	14.6%	0.81	0.07	0.55	0.45	0.81	0.83	2.85	2.79
		4–10	9959 (73.4%)	9686 (71.4%)	618	76.7%	0.95	−0.11	0.53	0.43	1.60	1.59	6.57	6.69
		≥ 10	1559 (11.5%)	1673 (12.3%)	70	8.7%	0.92	−0.02	0.47	0.38	1.18	1.12	11.40	11.38
Altimeter Jason-2 vs. scatterometer (gridded)		**All**	**307,991 (94%)**		**18,278**	**5.6%**	**0.91**	**0.04**	**1.09**	**0.87**	**2.60**	**2.44**	**6.46**	**6.42**
		<4	47,612 (15.5%)	46,612 (15.1%)	2806	15.4%	0.40	−0.50	1.25	1.02	0.79	0.81	2.90	2.95
		4–10	227,131 (73.7%)	234,111 (76.0%)	13,545	74.1%	0.81	0.04	0.99	0.79	1.51	1.51	6.46	6.54
		≥ 10	33,248 (10.8%)	27,268 (8.9%)	1927	10.5%	0.65	0.84	1.46	1.17	1.31	1.08	11.58	11.36

latitude of each cell was obtained as the mean the whole data during the whole study period. Monthly averages, mean seasonal cycles and total means of U_{10}^{c} and τ were subsequently computed by cell. Because the distance from the shore to the nearest cell varies between 3 and 10 km depending on the track/mission, we decided to interpolate the data to a common 5-km grid. The interpolated value at a query point is based on linear interpolation of the values at neighboring grid points. The points outside the domain were extrapolated using the same method. The resulting datasets provide information with enough resolution for documenting the surface atmospheric circulation in the coastal areas, which is addressed in the followings sections.

Considering the primary focus of the present work, i.e., the cross-shore wind reduction near the coastal zone, we have selected a subset of altimeter tracks searching the best approximations to orthogonal transects across the coastline (Wang et al., 2011; Pickett and Paduan, 2003). Table 5 provides the detail of the selected 200-km track segments (see right hand panels in Fig. 6a and b), including the coastal incident latitude, coastline direction angle (θ), track direction angle and orthogonal angular difference (ε) depicted in Fig. 5a. The coastline direction was calculated for each track using the tangent at the shoreline points within ~0.5° width segments around the incident latitude, as in Dewitte et al. (2011) or Pickett and Paduan (2003), based on the high-resolution (200-meter) shoreline database: Global Self-consistent, Hierarchical, High-resolution Geography Database (GSHHS). Although these formulations present a low difference in angle with respect to real orthogonal transects, they offer the possibility to compare objectively the shoreward wind drop-off at different latitudes.

Fig. 4a presents the mean state of the wind speed with superimposed arrows showing the mean wind speed and direction as derived from the QuikSCAT–ASCAT satellite data calculated over 2000–2014. Note that the mean wind direction is nearly parallel to the coastline. The variance for daily intraseasonal anomalies of the wind speed is displayed in Fig. 4b. Intraseasonal anomalies are calculated following Lin et al. (2000). It consists in first calculating the monthly means of the daily time series and then interpolating them back to a daily temporal grid using spline functions. The result is then retrieved from the original time series to derive daily intraseasonal anomalies.

Noteworthy, the region of interest experiences a large variability in the alongshore winds at intraseasonal timescales as illustrated in Fig. 4b, resulting in the intensification of surface winds at time periods near 10–25 days and 35–60 days (Rutllant et al., 2004; Renault et al., 2009; Dewitte et al., 2011). This variability corresponding to periods shorter than twice the repeat cycle of the satellite (35 days and 10 days for ENVISAT/SARAL and Jason-1/Jason-2, respectively) will alias into the altimeter wind speed (Tierney et al., 2000), leading to uncertainty in the estimate of the low frequency variability, including the seasonal cycle. This issue will be addressed in Section 5.

3.2. Estimate of the wind drop-off scale

In order to characterize the shoreward decrease in wind speed, we define a wind drop-off scale (L_d) following Renault et al. (2015). This scale is obtained along the satellite track by estimating the cross-shore rate of change of the wind speed from a certain coastal distance L_d. The drop-off index DO_G is thus estimated as:

$$DO_G(lat) = 100 * \left[\frac{U_{10}^{c}(L_d, lat) - U_{10}^{c}(0, lat)}{U_{10}^{c}(L_d, lat)}\right] \quad (5)$$

where lat is the incident latitude of the track at the coast, $U_{10}^{c}(L_d, lat)$ and $U_{10}^{c}(0, lat)$ are the wind speed estimates from the altimeter at the given distance L_d and at the grid point nearest to the coast respectively. The coastal wind speed $U_{10}^{c}(0, lat)$ is estimated as the average of the wind between 10 km offshore and the coast. The distance L_d, is estimated by defining a threshold value for the mean wind curl beyond which we are no longer within the drop-off zone. This value (negative in the Southern Hemisphere) is chosen at $-1.8 \times 10^{-5}\ s^{-1}$ which leads to L_d ranging from 10 to 150 km. Note that although such threshold is rather arbitrary, it corresponds to the distance from the coast beyond which the wind curl show very small offshore variability. Note also that Renault et al. (2015) use a larger value ($3 \times 10^{-5}\ s^{-1}$, positive in Northern Hemisphere) for the threshold of mean wind curl to derive L_d along the US west coast, since they address the seasonal variability of the wind drop-off along the coast with model data instead of observations.

The estimation of the alongshore wind stress curl from the altimeter data requires assuming some mean wind direction considering that the altimeter only provides the wind amplitude. Since along the Chile/Peru coast the winds are predominantly oriented alongshore from about 40°S to the equator (Hill et al., 1998; Aguirre et al., 2012; Rahn, 2012), as illustrated in Fig. 4a, we derive a mean angle for the wind direction that is based on the already described coastline direction angle θ. In

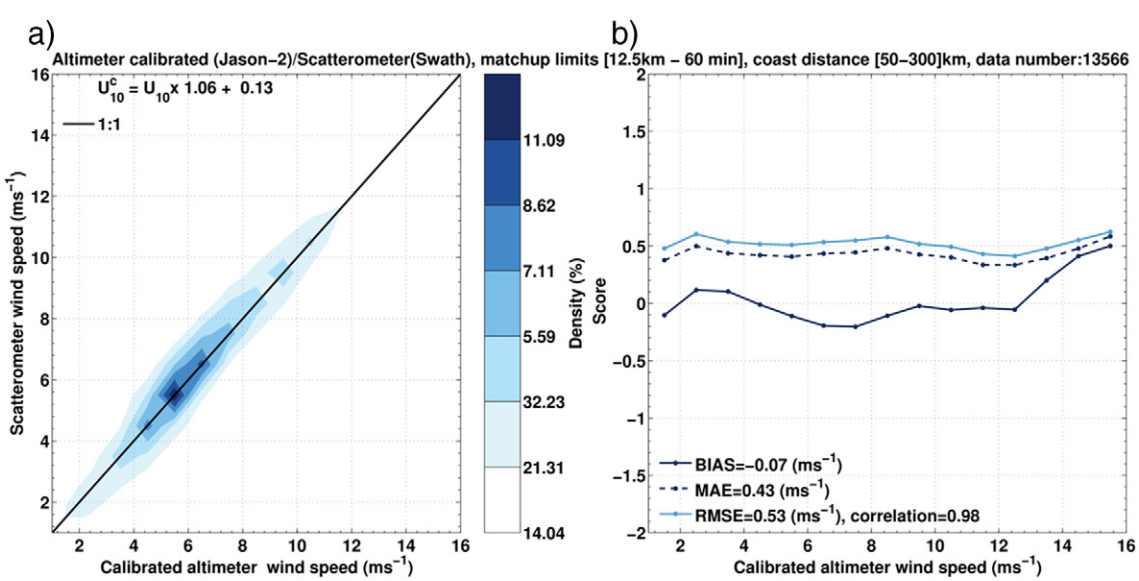

Fig. 3. Calibration result for Jason-2: (a) scatter density plot (shading), (b) mean bias, MAE, RMSE as function of the magnitude of the wind speed (divided in 16 bins). The correlation between the calibrated winds derived from Jason-2 and the swath scatterometer data is provided in panel (b). Statistics are obtained outside the coastal area (50–300 km offshore).

Table 4
Summary of the statistics by altimeter mission using swath scatterometer as ground-truth reference within the first 50 km off the coast. The statistics for the calibrated winds consider the calibration functions given in Table 3.

Validation/calibration 0–50 km off the coast	Dates	Range	Length		Outliers		ρ	Bias	RMSE	MAE	STD		Mean	
			ALT	SCA							ALT	SCA	ALT	SCA
Altimeter ENVISAT vs. scatterometer (swath)	2003-01-01–2009-12-31	**All**	**10,513 (94.4%)**		**621**	**5.6%**	**0.92**	**−0.55**	**1.16**	**0.94**	**2.55**	**2.65**	**4.75**	**5.30**
		<4	4603 (43.8%)	3739 (35.6%)	282	45.4%	0.59	−0.68	1.21	0.97	0.88	0.84	2.52	2.71
		4–10	5533 (52.6%)	6135 (58.4%)	319	51.4%	0.85	−0.47	1.11	0.91	1.52	1.58	6.14	6.24
		≥ 10	377 (3.6%)	639 (6.1%)	20	3.2%	0.66	−0.26	1.40	1.12	1.51	1.40	11.59	11.45
Calibrated altimeter ENVISAT vs. scatterometer (swath)		**All**	**10,499 (94.3%)**		**635**	**5.7%**	**0.93**	**−0.23**	**1.03**	**0.83**	**2.59**	**2.66**	**5.12**	**5.34**
		<4	4031 (38.4%)	3671 (35.0%)	238	37.5%	0.54	−0.41	1.07	0.85	0.78	0.84	2.66	2.72
		4–10	5976 (56.9%)	6172 (58.8%)	370	58.3%	0.86	−0.12	0.98	0.79	1.55	1.58	6.24	6.25
		≥ 10	492 (4.7%)	656 (6.2%)	27	4.3%	0.69	0.02	1.31	1.05	1.54	1.43	11.62	11.48
Altimeter SARAL vs. scatterometer (swath)	2013-03-14–2016-01-16	**All**	**3041 (93.5%)**		**212**	**6.5%**	**0.92**	**−0.21**	**1.11**	**0.91**	**2.48**	**2.74**	**5.54**	**5.75**
		<4	882 (29.0%)	870 (28.6%)	53	25.0%	0.52	−0.18	1.09	0.89	0.81	0.87	2.88	2.68
		4–10	2000 (65.8%)	1915 (63.0%)	145	68.4%	0.84	−0.22	1.13	0.94	1.65	1.61	6.25	6.40
		≥ 10	159 (5.2%)	256 (8.4%)	14	6.6%	0.84	−0.28	0.78	0.64	1.01	1.06	11.31	11.31
Calibrated altimeter SARAL vs. scatterometer (swath)		**All**	**3044 (93.6%)**		**209**	**6.4%**	**0.92**	**−0.08**	**1.09**	**0.90**	**2.62**	**2.76**	**5.70**	**5.78**
		<4	836 (27.5%)	864 (28.4%)	50	23.9%	0.50	−0.16	1.10	0.90	0.83	0.86	2.83	2.67
		4–10	1991 (65.4%)	1916 (62.9%)	144	68.9%	0.83	−0.08	1.11	0.92	1.67	1.61	6.28	6.42
		≥ 10	217 (7.1%)	264 (8.7%)	15	7.2%	0.82	0.17	0.83	0.64	1.15	1.08	11.37	11.32
Altimeter Jason-1 vs. scatterometer (swath)	2002-01-01–2008-12-31	**All**	**3343 (92.5%)**		**209**	**5.9%**	**0.96**	**−0.86**	**1.19**	**1.01**	**2.66**	**2.81**	**5.15**	**6.01**
		<4	1185 (35.4%)	864 (25.8%)	50	23.9%	0.70	−0.72	1.03	0.85	0.85	0.71	2.76	2.99
		4–10	1972 (59.0%)	2169 (64.9%)	144	68.9%	0.90	−0.96	1.24	1.08	1.53	1.57	5.93	6.36
		≥ 10	186 (5.6%)	310 (9.3%)	15	7.2%	0.81	−0.62	1.55	1.27	2.23	2.04	12.18	12.02
Calibrated altimeter Jason-1 vs. scatterometer (swath)		**All**	**3395 (93.9%)**		**220**	**6.1%**	**0.96**	**−0.15**	**0.82**	**0.65**	**2.80**	**2.84**	**5.97**	**6.11**
		<4	802 (23.6%)	840 (24.7%)	57	25.9%	0.60	−0.21	0.77	0.61	0.70	0.71	2.91	2.99
		4–10	2268 (66.8%)	2212 (65.2%)	147	66.8%	0.91	−0.17	0.78	0.64	1.47	1.59	6.17	6.39
		≥ 10	325 (9.6%)	343 (10.1%)	16	7.3%	0.86	0.17	1.16	0.85	2.18	2.00	12.08	11.95
Altimeter Jason-2 vs. scatterometer (swath)	2009-01-01–2015-12-31	**All**	**1498 (93.3%)**		**107**	**6.7%**	**0.97**	**−0.52**	**0.84**	**0.69**	**2.47**	**2.76**	**5.22**	**5.74**
		<4	492 (32.8%)	430 (28.7%)	25	23.4%	0.81	−0.25	0.63	0.51	0.87	0.81	2.88	2.88
		4–10	924 (61.7%)	933 (62.3%)	69	64.5%	0.94	−0.63	0.92	0.78	1.51	1.58	5.91	6.20
		≥ 10	82 (5.5%)	135 (9.0%)	13	12.1%	0.97	−0.87	0.95	0.87	1.58	1.51	11.58	11.68
Calibrated altimeter Jason-2 vs. scatterometer (swath)		**All**	**1525 (95.%)**		**80**	**5.0%**	**0.98**	**−0.11**	**0.63**	**0.51**	**2.66**	**2.82**	**5.74**	**5.86**
		<4	380 (24.9%)	420 (27.5%)	17	21.3%	0.76	0.04	0.61	0.48	0.84	0.81	2.89	2.87
		4–10	1017 (66.7%)	950 (62.3%)	58	72.5%	0.94	−0.17	0.65	0.53	1.52	1.59	6.05	6.23
		≥ 10	128 (8.4%)	155 (10.2%)	5	6.3%	0.94	−0.13	0.59	0.47	1.65	1.46	11.78	11.69

the following we will use a rotated coordinate system where x is perpendicular to the coast and y is along the coast, with positive y equatorward, as in Fig. 5a. Wind speed and wind stress vector components can therefore be written as:

$$U_x = \cos(\theta - \phi) * U_{10}^c;\ U_y = \sin(\theta - \phi) * U_{10}^c \tag{6}$$

$$\tau x = \cos(\theta - \phi) * \tau;\ \tau y = \sin(\theta - \phi) * \tau \tag{7}$$

where U_{10}^c is the wind speed, τ the wind stress, θ the coastal orientation angle, and ϕ the track angle. With the assumptions that mean winds are predominantly alongshore, the along-track wind stress curl is the x derivative of the wind stress (e.g. Figueroa and Moffat, 2000). This hypothesis was tested from the mean ERA-Interim and CFSR winds, which shows that the error in the estimation of the wind curl near the coast is <10% on average between 5°S and 40°S (not shown).

Another assumption consists in neglecting the angle between the track of the satellite and the x-direction, which is acceptable considering that we are focusing on a relatively short distance from the coast.

While DO_G provides a mean rate of alongshore wind change near the coast, it does not provide information on the shape of the along-shore wind variations as a function of the distance from the coast and on how the drop-off shape deviates from the linear fit of the horizontal wind profile. We thus define an index DO_I that characterizes the wind drop-off shape. It writes as follows:

$$DO_I(lat) = 100 * \left[\frac{\left(\int_{L_d}^{0} U_{10}^c(x, lat)dx - \int_{L_d}^{0} y(x)dx \right)}{\int_{L_d}^{0} y(x)dx} \right] \tag{8}$$

where lat is the incident latitude of the track at the coast, $y(x)$ is the straight line from $(L_d, U_{10}^c(L_d, lat))$ to the nearest point to the coast $(0, U_{10}^c(0, lat))$. Both integrals are calculated along the track using the trapezoidal method with dx equals to 5 km.

A negative/positive DO_I indicates a convex/concave horizontal wind profile. A concave horizontal profile would tend to locate the peak Ekman pumping close to the coast, which has implication in terms of the efficiency of the Ekman pumping in generating upwelling (Capet et al., 2004).

4. Results

4.1. Wind drop-off characterization

As a first step, we present Fig. 6a and b that display the mean wind speed for the altimeter and the scatterometer along the selected tracks for Jason-1/Jason-2 and SARAL/ENVISAT respectively. The data are shown for a 200-km coastal strip interpolated at a 5-km resolution. There is an overall good agreement between the altimeter and the scatterometer (i.e. RMS = 0.33, 0.28, 0.51 and 0.55 ms^{-1} for Jason-1/Jason-2 and ENVISAT/SARAL respectively) although discrepancies arise locally due in part to differences in repeat cycle, spatial resolution, and technology of the onboard instruments (see Table 1). Despite differences between products, the details of the circulation near the coast (i.e. between the coast and 50-km offshore) can be inferred from the altimeter data.

The most noticeable feature is the marked shoreward reduction in wind speed. This wind drop-off takes place at all latitudes independently of the offshore wind speed, although the reduction rate is latitudinally dependent. Observed wind speed differences between 100 km offshore and the coast are ubiquitous ranging between [1–2.5] ms^{-1} for Jason-1/Jason-2 and [0–4] ms^{-1} for ENVISAT/SARAL.

The coastal wind speed $U_{10}^c(0, lat)$ is illustrated for all the missions with long enough time periods (i.e. ENVISAT, Jason-1 and Jason-2) in

Table 5
Details of the selected tracks by mission including, number id, incident latitude at coast, track angle, coastline orientation angle and orthogonal difference (see Figs. 5 and 6a, b for illustration).

ENVISAT-SARAL																														
Track number	1	2	3	4	5	6	7	8	9	10	11	12	13	14	15	16	17	18	19	20	21	22	23	24	25	26	27	28	29	30	31
Latitude at coast (°S)	–	–	–	–	–	–	–	–	–	–	–	–	–	–	–	−17°	−17°	−18°	−18°	−19°	−24°	−26°	−28°	−29°	−30°	−33°	−34°	−35°	−36°	−37°	−40°
	6.2°	6.6°	7.1°	8.1°	8.9°	10.0°	11.0°	11.9°	12.7°	14.1°	15.0°	15.5°	15.8°	16.3°	16.4°																
Track angle	257°	257°	257°	257°	257°	257°	257°	257°	257°	257°	257°	257°	257°	257°	257°	256°	256°	256°	256°	256°	104°	104°	104°	104°	105°	105°	105°	106°	106°	106°	107°
Coastline angle	149°	147°	123°	133°	110°	113°	102°	109°	119°	121°	141°	148°	150°	153°	157°	151°	148°	141°	139°	102°	86°	84°	68°	67°	84°	66°	85°	49°	70°	47°	72°
Orthogonal difference	18°	21°	45°	34°	57°	54°	65°	58°	48°	46°	26°	18°	17°	13°	10°	15°	18°	26°	27°	64°	72°	70°	54°	53°	70°	50°	70°	33°	54°	31°	55°
Jason-1-Jason-2																															
Track number			1			2		3		4		5		6		7		8		9		10		11		12					
Latitude at coast(°S)			−6.2°			−8.5°		−11.7°		−14.9°		−16.4°		−17.9°		−23.4°		−24.5°		−28.7°		−33.4°		−36.2°		−39.7°					
Track angle			250°			249°		249°		248°		247°		247°		244°		113°		115°		118°		120°		122°					
Coastline angle			144°			117°		123°		135°		155°		140°		94°		87°		69°		78°		69°		58°					
Orthogonal difference			16°			42°		35°		23°		2°		17°		61°		64°		44°		51°		39°		26°					

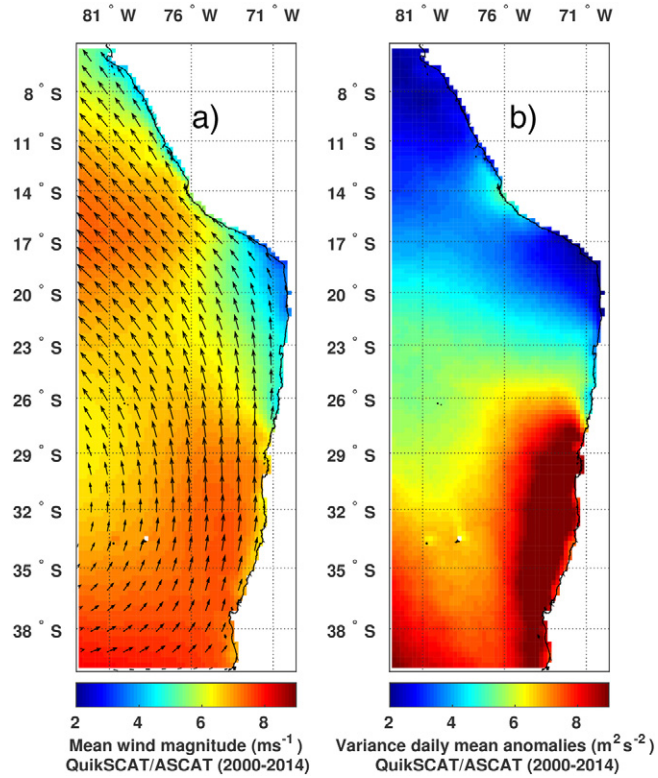

Fig. 4. (a) Mean surface wind speed and wind vectors. (b) Variance of daily intraseasonal anomalies. Intraseasonal anomalies are defined as departures from the monthly means (Lin et al., 2000). Data are from the gridded daily averages QuikSCAT-ASCAT (2000–2014).

Fig. 7a. There is an overall good agreement between the three altimeters although ENVISAT exhibits a larger alongshore variability, with in particular larger (weaker) coastal wind at 28°S (12°S), the region of the maximum (minimum) wind, with respect to Jason-1 and Jason-2.

In order to characterize the wind drop-off, the coastward decaying rate of along-shore wind is estimated (see Section 3.2 and Eq. (5) for DO_G definition). The DO_G index shows a significant latitudinal variability (Fig. 7b), out of phase with the coastal wind speeds $U^c_{10}(0,lat)$ (Fig. 7a). In particular, regions where the coastal jet is strong ($U^c_{10}(0,lat) > \sim 4\ \mathrm{m \cdot s^{-1}}$), between 34°S and 29°S off Chile and between 17°S and 13°S off Peru, correspond to low value of DO_G. Conversely, in regions of relatively weak coastal winds, DO_G is larger, reaching almost 80% off Callao at 12°S.

While DO_G is a linear estimate of the rate of cross-shore wind reduction, DO_I (Fig. 7c) provides a measure of the shape of this wind speed reduction from the offshore horizontal wind profile (see Section 3.2 and Eq. (8) for DO_I definition). In particular, it indicates where the steepest offshore wind decrease is located along the track. For instance, a large positive DO_I value (i.e. concave horizontal wind profile) indicates a position of the maximum wind stress close to the coast. While DO_I is highly correlated to DO_G (R = 0.89), it is negatively correlated to the outer offshore wind speeds (R = −0.70), indicating that when the wind is strong, the horizontal wind profile is more concave and the maximum wind curl moves closer to the coast. The apparent differences in variability of DO_G and DO_I between ENVISAT and Jason-1/Jason-2 can be explained in terms of the influence of coastline meandering on the wind drop-off. Since there are slight differences in the latitudes of the tracks between ENVISAT and Jason-1/Jason-2, winds can experience the effect of bays, promontories and small islands depending on the satellite and the incident latitude at the coast.

The wind drop-off has been also shown to be sensitive to the orography, which is prominent over the west coast of South America due to

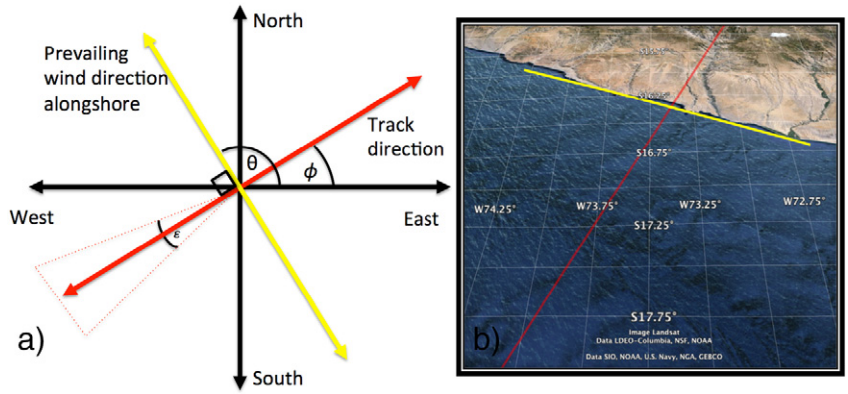

Fig. 5. (a) Coordinate systems used for the calculation: The x-axis (red) is in the cross-shore direction and the y-axis (yellow) is parallel to the shore direction, θ: the coastline angle, ϕ: the rotation angle and ε: the angular difference between the rotated x-axis and the ground track. (b) Map of the coast of Peru with the Jason-1/Jason-2 ground track (red line) that intersects the coast at 16.4°S. The yellow line is the tangent to the coastline. Note that the angular difference (ε) between the track of the satellite and the x-direction is neglected. (For interpretation of the references to colour in this figure legend, the reader is referred to the web version of this article.)

the presence of coastal mountain ranges. For the coast of California, based on sensitivity experiments with a regional atmospheric model, Renault et al. (2015) showed for instance that land shape could produce an enhanced drag coefficient for the low-level circulation that would result in a turbulent momentum flux divergence. The latter, combined to orographically-induced vortex stretching, would produce the wind drop-off. They defined an along-shore orography index (Hindex) as the mean orographic height over the strip of land within 100 km of the coast and show that is significantly correlated with the wind drop-off spatial length L_d. Here, while we also observe an overall agreement between meridional changes in DO_G and the coastal orographic height (i.e. the larger the Hindex, the weaker the wind at the coast, not shown), we did not evidence a significant linear relationship between Hindex and L_d, most likely due to the coarse meridional resolution of the altimetric wind data. On the other hand, the relationship between the coastline geometry, estimated from the GSHHS shoreline, and DO_G can be appreciated from a meandering index (Mindex). It consists of searching the local maxima and minima in the coastline longitude and imposing an amplitude threshold of 23 km for promontories and 4 km for bays. Fig. 7d shows the main filtered peaks along the coast as red circles for the main promontories and black circles for the main bays. It indicates that when there is a significant difference between ENVISAT and Jason-1/Jason-2 in DO_G (or coastal wind), it can be explained to some extent by the effect of a bay or a promontory. For instance, the Gulf of Arauco at 37.23°S (ENVISAT track N°30) experiences a notorious wind reduction and a high drop-off index explained by the abrupt change of the coastline orientation from N-S to E-W and favored by the presence of Santa María Island (73.52°W 37.03°S). Note that the ENVISAT track impinges inside the bay, which may explain the larger drop-off there. ENVISAT tracks at Punta Lengua de Vaca (30°S) and Punta Choros (29°S), on the other hand, indicate a large coastal wind and a weak wind drop-off compared to Jason-1/Jason-2, which might results from the alternation of promontories and bays. The difference in the repeat cycles and wind speed algorithms between ENVISAT and Jason-1/Jason-2 may also produce a residual effect on the mean at some locations. Due to the complexity of small scales processes (see Renault et al., 2015) in the near-coastal regions, the explanation of the differences between altimeter missions remains here qualitative and would require further studies using regional atmospheric modeling.

4.2. Transport and upwelling

The altimeter data offers the opportunity to estimate Ekman pumping and Ekman transport and compare their relative contributions to the vertical velocities and transports near the coast. The Ekman pumping vertical velocity, $\boldsymbol{W}$, and the Ekman transport, $\boldsymbol{M}$, were estimated following Pickett and Paduan (2003) who based it on Smith (1968) and Bakun (1973) as:

$$\boldsymbol{W} = \frac{1}{\rho_w f} \nabla \times \tau \tag{9}$$

$$\boldsymbol{M} = \frac{1}{\rho_w f} \tau \times \boldsymbol{\kappa} \tag{10}$$

where $\nabla \times \tau$ is the along-track curl of the derived mean wind stress (obtained in Section 3.2) calculated as the along-track gradient of the alongshore wind. For Ekman transport (10) τ is the mean wind stress vector nearest to the coast, ρ_w is the density of seawater (assumed constant at 1024 kg m^{-3}), f is the Coriolis parameter; and $\boldsymbol{\kappa}$ is the unit vertical vector. The offshore component of the Ekman transport was calculated from the dot product of the above transport vector with a unitary vector orthogonal to the coastline (Pickett and Paduan, 2003).

In order to compare both upwelling processes, we had to convert Ekman pumping into vertical transport by integrating the vertical velocities over some offshore distance from the coast. Following former studies (Pickett and Paduan, 2003; Aguirre et al., 2012), we use a distance of 150 km from the coast, which corresponds to the maximum value of L_d estimated along the coast. The resulting vertical transports, for the different altimetry missions, are displayed in Fig. 8. It first shows an overall good agreement between the different satellite products for both Ekman transport (Fig. 8a) and pumping (Fig. 8b). The most prominent differences are observed around 12°S, 30°S and 37°S, with ENVISAT transport estimations differing from both Jason-1 and Jason-2. As mentioned earlier, they can be attributed both to the differences in repeat cycle and to the local presence of bays or promontories depending on the satellite incident latitude at the coast. Second, Fig. 8 indicates that the magnitudes of Ekman transport and pumping are comparable although there can be large differences locally at some latitudes sampled by ENVISAT (e.g. at ~29°S). The agreement is on average larger off Chile than off Peru where the transport associated with Ekman pumping is larger than Ekman transport (between 20°S and 7°S) by an average factor of ~1.4. Noteworthy, in a former study for the coast of California from regional atmospheric model outputs, Pickett and Paduan (2003) found comparable magnitudes and relative contributions of Ekman transport versus Ekman pumping, which is in agreement with our estimate. On the other hand, Aguirre et al. (2012) using QuikSCAT data found a much larger contribution of Ekman transport versus Ekman pumping for the central Chile region compared to our estimate. As mentioned

by these authors, the scatterometer data lead to an underestimation on the contribution of Ekman pumping.

Messié et al. (2009) have already mentioned that the caveats associated with the calculation of upwelling from the QuikSCAT data result from resolution and lack of nearshore pixels. However although the relative proportion of Ekman transport and pumping may be biased, the total transport should not change (Pickett and Paduan, 2003). This is what we observed here since the differences between satellite products are reduced when summing up the contributions of Ekman transport and pumping. The latitudinally-averaged standard deviation between products reduces to 0.09 for the total transport compared to 0.12 and 0.13 for Ekman transport and pumping respectively (units = $m^3\ s^{-1}$ per meter of coast). In order to highlight the latitudinal variability between Ekman transport and pumping, Fig. 8d presents the results in the form of a histogram for Jason-2. Clearly, the Ekman pumping tends on average to dominate with respect to Ekman transport over the Peruvian coast north of 15°S, whereas over the central Chilean coast (33°S–27°S), Ekman transport is the dominant process. Fig. 8d also illustrates the large alongshore variability resulting from the intricate coastline (see Fig. 7d).

Similar comparison is done for the vertical velocity estimates associated with both Ekman pumping and transport. The vertical velocities resulting from Ekman transport are estimated using an upwelling scale (L_{cu}) of the order of ~10 to 5 km (from 5°S to 40°S), calculated

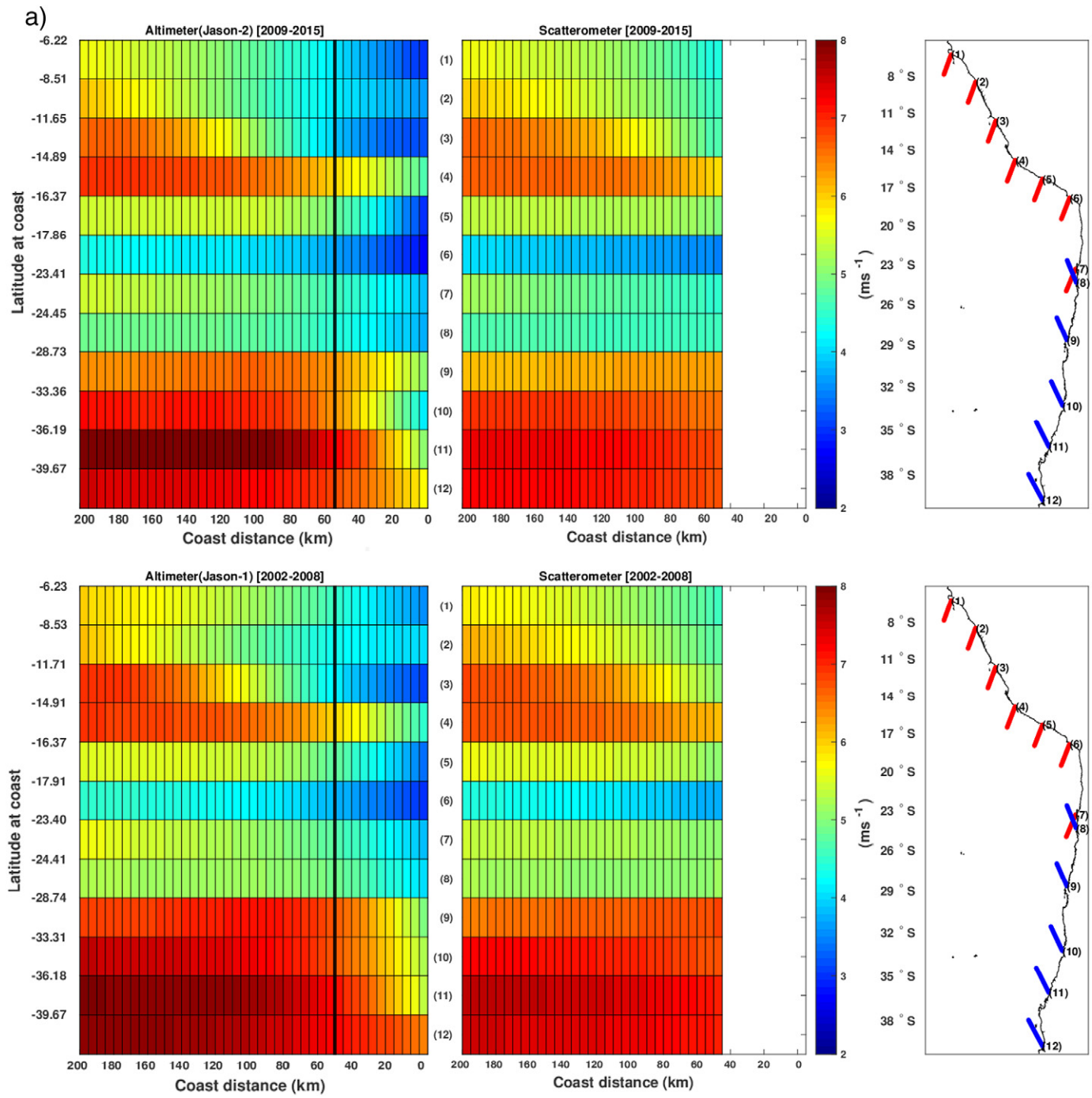

Fig. 6. a: Mean wind speed for Jason-1 and Jason-2 (left column) and scatterometer (middle column) calculated over the same periods. The vertical black lines on the left hand side panels indicate the offshore distance (50 km) defined as the limit for the scatterometer confidence. Reference maps (right hand panels) show the altimeter tracks positions by mission. b: Mean wind speed for ENVISAT and SARAL (left column) and scatterometer (middle column) calculated over the same periods.

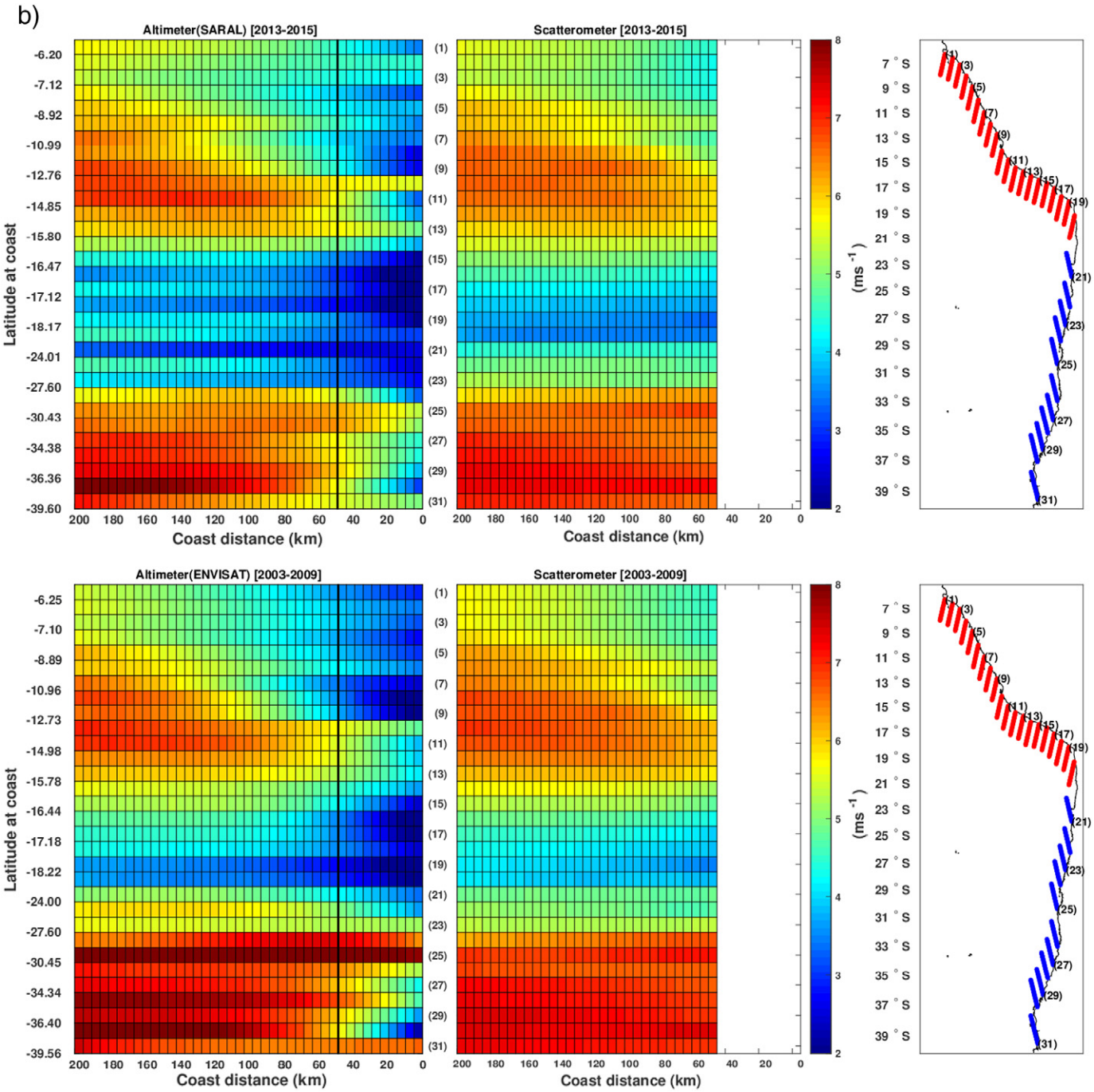

Fig. 6 (*continued*).

following Marchesiello and Estrade (2010) and Renault et al. (2012). The Ekman pumping vertical velocities are averaged within a 10-km width coastal band (10 km corresponding to the location where the maximum in Ekman Pumping is detected). The results of the comparison are presented in Fig. 9.

Differences between products are larger than those found for the estimates of transport due, on the one hand, to the larger sensitivity of the estimated velocity to the upwelling scale and to the assumed location of maximum upwelling, on the other hand. Here we consider, that the upwelling is confined to the frictional inner shelf zone where surface and Ekman bottom layers overlap, which implies that upwelling (i.e., where vertical velocities are maximum) is confined within 5 to 10 km from the coast (Marchesiello and Estrade, 2010). This results in a different balance between both processes, with vertical velocities associated with Ekman transport having much larger amplitude than vertical velocities associated with Ekman pumping (Fig. 9a, b). However, this is not observed in the areas with a strong wind drop-off, which leads to a larger contribution of Ekman pumping velocity over Ekman transport vertical velocity (e.g. near 12°S). Fig. 9d illustrates the large alongshore variability of the relative contribution of vertical velocities induced by Ekman transport and pumping from the Jason-2 data.

5. Discussion and conclusions

In this study, we have documented the mesoscale atmospheric circulation along the coast of Peru and Chile from wind speed

altimeter data, motivated by the consideration that this circulation is not observable by the scatterometers (i.e. blind zone for the instrument) despite its potentially strong impact on the coastal oceanic circulation (Capet et al., 2004; Renault et al., 2012, 2016). We first presented the calibration method of the altimeter data, which is based on the comparison between the scatterometer and altimeter datasets outside the coastal area (50–300 km offshore). Statistically, the ocean surface winds from both instruments agree very well, with high correlation coefficients and low bias and RMSE differences. The missions Jason-1 and Jason-2 exhibit higher scores with respect to scatterometer than the ENVISAT and SARAL missions. The calibration coefficients are inferred from the slope and offset of the regression between both altimeter and scatterometer data, with values consistent with those from former studies (Queffeulou, 2003; Zieger et al., 2009) (i.e. slopes near 1.00, small offsets and RMS errors less than 0.7 ms^{-1}).

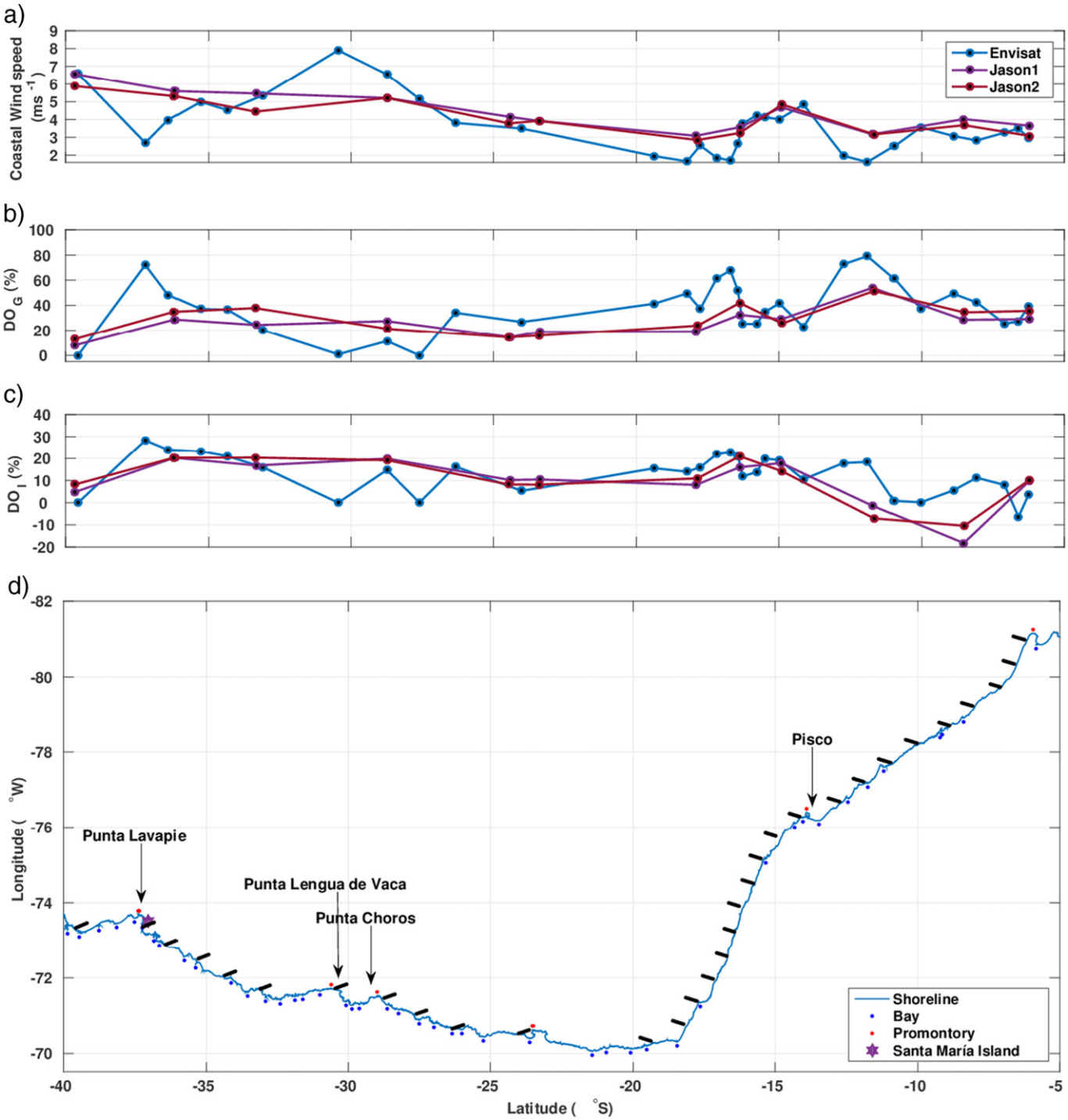

Fig. 7. (a) Coastal wind estimated as the average of the wind speed within the first 10 km off the coast. (b) Wind drop-off index (DO_G). (c) Drop-off shape index (DO_I). (d) Meandering index estimated performing a peak analysis to the coastal longitude. Red circles correspond to the main promontories whereas blue circles indicate the main bays. The black segments correspond to the ENVISAT tracks. Black arrows indicate the location of the main promontories at Punta Lavapie, Punta Lengua de Vaca, Punta Choros and Pisco. (For interpretation of the references to colour in this figure legend, the reader is referred to the web version of this article.)

Calibrated and gridded measurements were then used to characterize the mean state of the dominant alongshore flow and assess the along-track wind drop-off and its likely influence on coastal upwelling through Ekman pumping/transport. We find that the altimeter winds have the appropriate resolution for documenting the characteristics of the mean near-shore winds, highlighting in particular a significant alongshore variability of the wind drop-off. The latter tends to be larger at latitudes where the coastal winds are weak, which implies a dominant contribution of Ekman pumping with respect to Ekman transport there.

Differences between products (Jason-1/Jason-2 versus ENVISAT/SARAL) can be understood in terms of (i) the location where the satellite track impinges at the coast, revealing the influence of details in the coastline (bays and promontories), (ii) the differences in time sampling between the different missions (both the observation period and the sampling frequency), and (iii) the differences caused by the characteristics of the sensors, the frequency used and the algorithms used for processing the data.

While we have documented here the mean coastal circulation, we may wonder to which extend the altimeter data could help addressing the temporal variability in the wind drop-off, considering the significant intraseasonal wind variability in the region of interest (e.g. Renault et al., 2009; Dewitte et al., 2011; see also Fig. 4b). Here it is only expected at best to be able to resolve the seasonal cycle. To evaluate this, the scatterometer and the calibrated altimeter data are compared in terms of the annual harmonics over the domain consisting in the fringe of 50 km from the coast and extending up to 100 km offshore. Results (Fig. 10) suggest that altimeter data near the coast could be used to document the seasonal cycle of the wind drop-off, although large differences between products can be observed locally, in particular off central Chile where the coastal jet experiences a significant intraseasonal variability (Renault et al., 2009) associated to its seasonal meridional migration (Garreaud and Muñoz, 2005), which is likely to result in more pronounced aliasing effect than off Peru. To reduce the uncertainties associated with these differences, these results would need to be combined with those from a regional modeling study to gain confidence in the satellite data products and provide a more quantitative physical explanation. This is planned for future work.

At this stage, we can note that the altimeter data are highly valuable for the regional modeling community interested in EBUS since they offer a benchmark dataset to validate regional atmospheric models in near coastal areas and investigate to which extent they can simulate the wind drop-off and its alongshore variability. These results can also help in assessing the optimal resolution of regional atmospheric models (convergence issues) and thus open the possibility to investigate

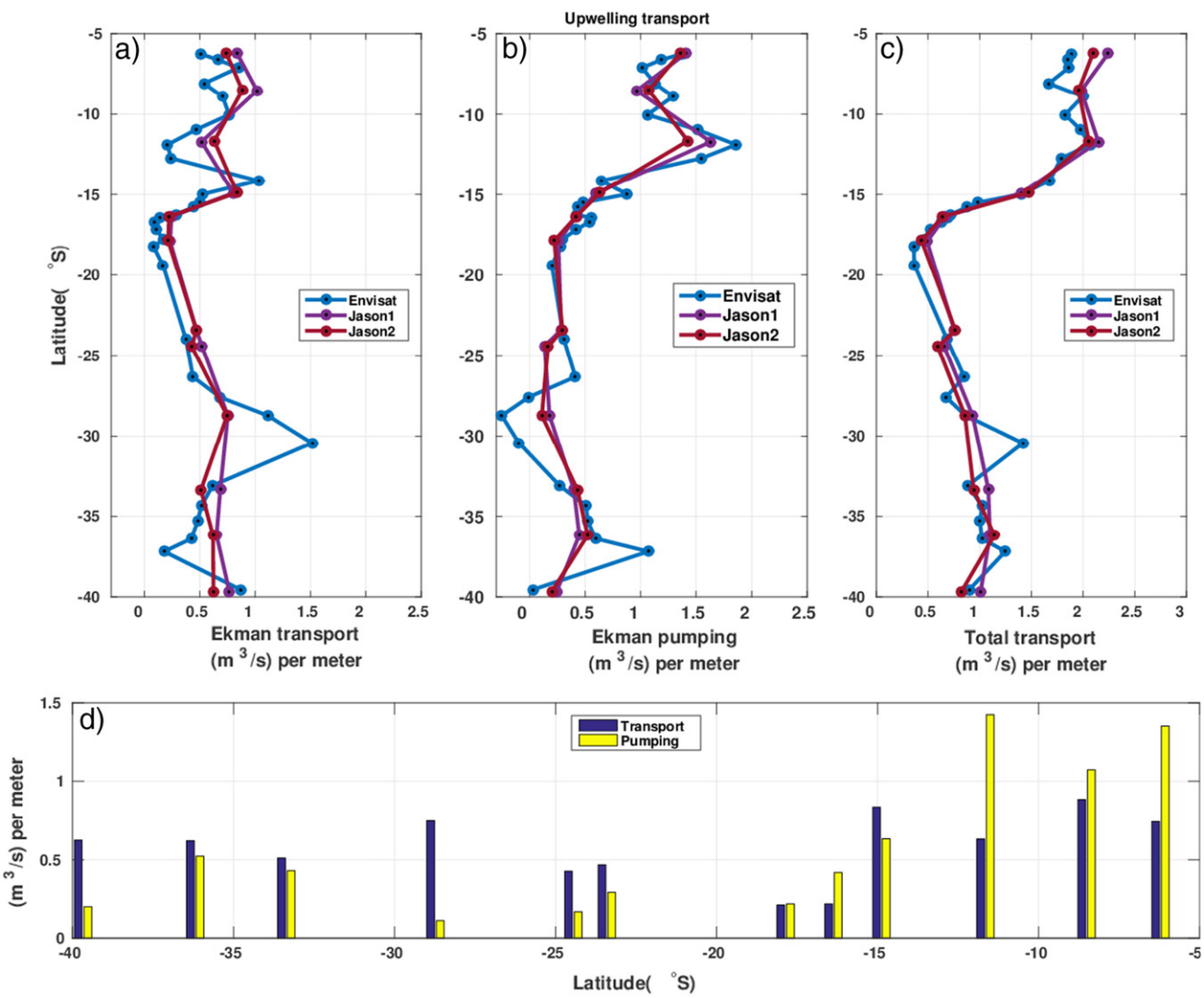

Fig. 8. Contribution of the Ekman transport (a) and Ekman pumping (b) to the mean vertical transport near the coast (within 150 km offshore). (c) Total transport (Ekman transport + Ekman pumping). (d) Comparative detail with the Jason-2 vertical transport associated with Ekman transport and Ekman pumping.

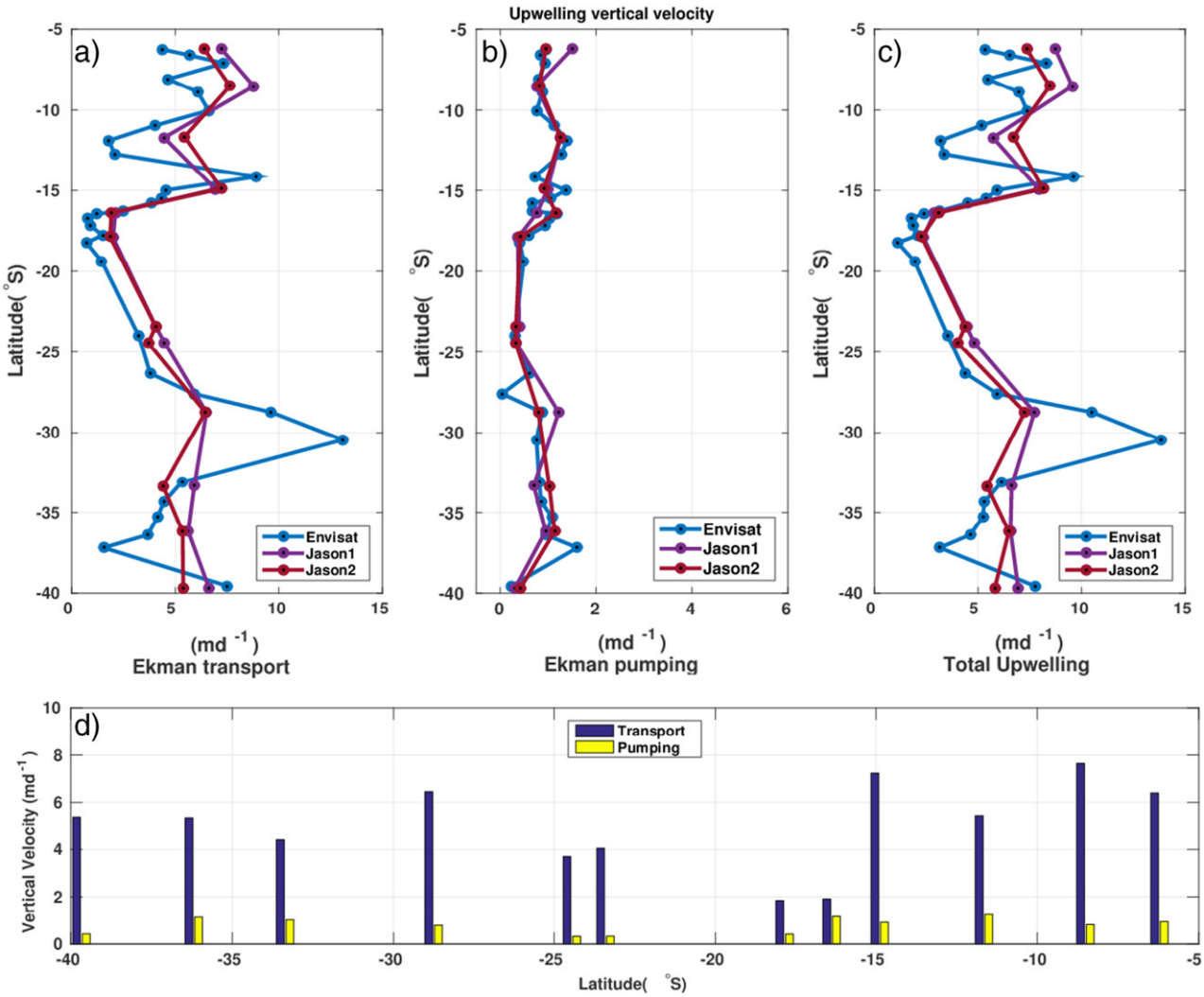

Fig. 9. Mean vertical velocities in the nearshore upwelling zone from (a) Ekman transport, (b) Ekman Pumping and (c) total upwelling (Ekman transport + Ekman pumping). (d) Comparative detail with the Jason-2 vertical velocities contributions induced by Ekman transport and Ekman pumping.

quantitatively to which extent the wind drop-off is influential on the regional oceanic circulation and biogeochemistry.

Finally, it is worth mentioning the limitations associated with the blind zone in scatterometer coverage for modeling wind-stress forcing over the inner shelf since regional ocean models are now run at high resolution spatial. Therefore special attention must be paid on how the scatterometer gridded data are extrapolated on the model grid near the coast in the region where the scatterometer data are not available. The interpolation method may indeed produce unrealistic wind stress patterns within the coastal fringe. For instance, Desbiolles et al. (2016) investigate the sensitivity of the oceanic response to the method for filling the blind zone in QuikSCAT coverage near the coast in the Benguela upwelling system using two approaches. In the first one, the estimates of surface wind stress components are extrapolated toward the coast to fill the wind data gaps in this zone, and then interpolated to the model grid. The second one completes the coastal gaps with zonal gradients derived from ECMWF reanalysis (ERA-Interim) data. The local and daily zonal gradient in the ERA-Interim meridional stress component is applied from the first missing grid cell toward the coast. They conclude that upwelling dynamics adjust quickly to a local change of the momentum fluxes, and that the upwelling circulation (i.e. surface flows and poleward undercurrent) is highly sensitive to the alteration of the alongshore wind stress components. They show also that a wind reduction in the coastal band often reduces the SST cooling, but the two mechanisms, Ekman transport and Ekman pumping, compensate each other when the characteristic length scales of the coastal upwelling and the orography-induced wind drop-off are similar.

Altimeter data could thus provide a benchmark for evaluating the extrapolation procedure and adjust it, if necessary. Note that, at this stage, it seems difficult to go further and propose to “nudge” altimeter and scatterometer data in order to include a near-shore drop off in the scatterometer products, due to the relatively large gaps between tracks in the meridional direction.

Acknowledgements

O. Astudillo and J. Rutllant wish to thank the Center for Advanced Studies in Arid Zones (CEAZA), La Serena, Chile for financial support. CNES is also acknowledged for financial support through the TOSCA project EBUS-South. M. Ramos, B. Dewitte and L. Bravo acknowledge support from FONDECYT (projects 1140845 and 1151185) and the Chilean Millenium Initiative (NC 120030). L. Bravo acknowledges Postdoctoral FONDECYT 586 (project 3130671). This work was supported by the CNES OSTST grant "Surface Winds At Near Shore - SWANS".

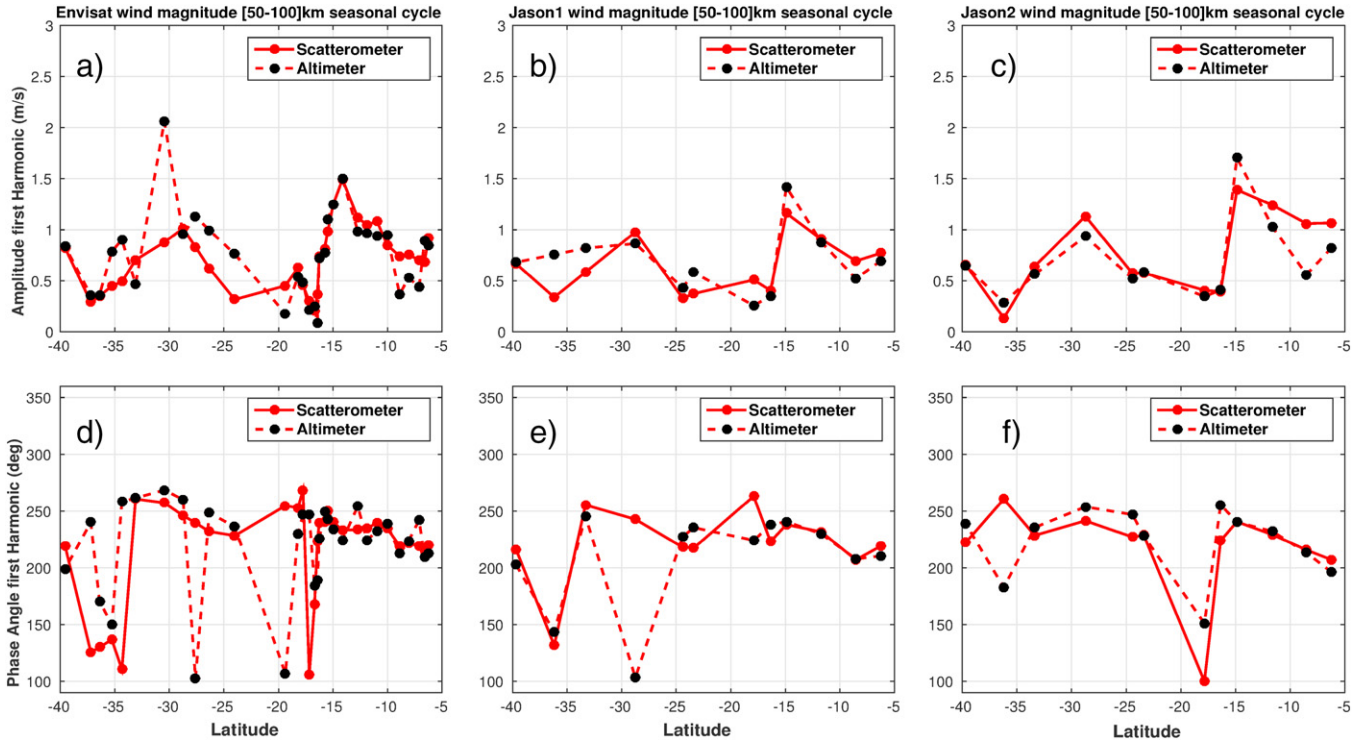

Fig. 10. Amplitude (top panels) and phase (bottom panels) of the annual harmonics of the mean wind speed near the coast (average between 50 and 100 km offshore) for the altimeter (black dots, dashed red line) and the scatterometers (red dots, plain red line). (a, d) ENVISAT, (b, e) Jason-1 and (c, f) Jason-2. (For interpretation of the references to colour in this figure legend, the reader is referred to the web version of this article.)

References

Abdalla, S., 2006. Global Validation of ENVISAT Wind, Wave and Water Vapour Products From RA-2, MWR, ASAR and MERIS, ECMWF, ESA Contract Report 17585 (81 pp).

Abdalla, S., 2012. Ku-band radar altimeter surface wind speed algorithm. Mar. Geod. 35 (Suppl. 1):276–298. http://dx.doi.org/10.1080/01490419.2012.718676 (Informa UK Limited, online).

Aguirre, C., Pizarro, Ó, Strub, P.T., Garreaud, R., Barth, J.A., 2012. Seasonal dynamics of the near-surface alongshore flow off central Chile. J. Geophys. Res. 117, C01006. http://dx.doi.org/10.1029/2011JC007379.

Albert, A., Echevin, V., Lévy, M., Aumont, O., 2010. Impact of nearshore wind stress curl on coastal circulation and primary productivity in the Peru upwelling system. J. Geophys. Res. 115 (C12). http://dx.doi.org/10.1029/2010jc006569 (Wiley-Blackwell, online).

Bakun, A., 1973. Coastal upwelling indices, west coast of North America, 1946–71. U.S. Dept. of Commerce, NOAA Tech. Rep., NMFS SSRF-671 (103p).

Bakun, A., Black, B.A., Bograd, S.J., García-Reyes, M., Miller, A.J., Rykaczewski, R.R., Sydeman, W.J., 2015. Anticipated effects of climate change on coastal upwelling ecosystems. Current Climate Change Reports 1 (2):85–93. http://dx.doi.org/10.1007/s40641-015-0008-4 (Springer Science + Business Media, online).

Bentamy, A., Fillon, D.C., 2012. Gridded surface wind fields from Metop/ASCAT measurements. Int. J. Remote Sens. 33 (6):1729–1754. http://dx.doi.org/10.1080/01431161.2011.600348 (Informa UK Limited, online).

Bentamy, A., Croize-Fillon, D., Perigaud, C., 2008. Characterization of ASCAT measurements based on buoy and QuikSCAT wind vector observations. Ocean Sci. 4 (4): 265–274. http://dx.doi.org/10.5194/os-4-265-2008 (Copernicus GmbH, online).

Blarel, F., Frappart, F., Legrésy, B., Blumstein, D., Rémy, F., Fatras, C., Mougin, E., Papa, F., Prigent, C., Niño, F., Borderies, P., Biancamaria, S., Calmant, S., 2015. Altimetry backscattering signatures at Ku and S bands over land and ice sheets. In: Neale, C.M.U., Maltese, A. (Eds.), Remote Sensing for Agriculture, Ecosystems, and Hydrology XVII, SPIE-Intl Soc Optical Eng http://dx.doi.org/10.1117/12.2194498 (online).

Bravo, L., Ramos, M., Astudillo, O., Dewitte, B., Goubanova, K., 2015. Seasonal variability of the Ekman transport and pumping in the upwelling system off central-northern Chile (~ 30° S) based on a high-resolution atmospheric regional model (WRF). Ocean Sci. Discuss. 12 (6):3003–3041. http://dx.doi.org/10.5194/osd-12-3003-2015 (Copernicus GmbH, online).

Callahan, P.S., Lungu, T. (Eds.), 2006. QuikSCAT Science Data Product User's Manual, Version 3.0. D-18053 - Rev A, JPL/NASA (85 pp).

Capet, X.J., Marchesiello, P., McWilliams, J.C., 2004. Upwelling response to coastal wind profiles. Geophys. Res. Lett. 31 (13). http://dx.doi.org/10.1029/2004gl020123 (Wiley-Blackwell, online).

Carr, M., Kearns, E.J., 2003. Production regimes in four Eastern Boundary Current systems. Deep-Sea Res. II Top. Stud. Oceanogr. 50 (22–26):3199–3221. http://dx.doi.org/10.1016/j.dsr2.2003.07.015 (Elsevier BV, online).

Chavez, F.P., Messié, M., 2009. A comparison of Eastern Boundary Upwelling Ecosystems. Prog. Oceanogr. 83 (1–4):80–96. http://dx.doi.org/10.1016/j.pocean.2009.07.032 (Elsevier BV, online).

Chavez, F.P., Bertrand, A., Guevara-Carrasco, R., Soler, P., Csirke, J., 2008, October. The northern Humboldt Current System: brief history, present status and a view towards the future. Prog. Oceanogr. http://dx.doi.org/10.1016/j.pocean.2008.10.012 (Elsevier BV).

Chelton, D.B., Walsh, E.J., MacArthur, J.L., 1989. Pulse compression and sea level tracking in satellite altimetry. J. Atmos. Ocean. Technol. 6:407–438. http://dx.doi.org/10.1175/1520-0426(1989)006,0407:PCASLT.2.0.CO;2.

Chelton, D.B., Ries, J.C., Haines, B.J., Fu, L.-L., Callahan, P.S., 2001. Chapter 1 satellite altimetry. International Geophysics. Elsevier BV http://dx.doi.org/10.1016/s0074-6142(01)80146-7 (p. 1–ii., online).

Croquette, M., Eldin, G., Grados, C., Tamayo, M., 2007. On differences in satellite wind products and their effects in estimating coastal upwelling processes in the southeast Pacific. Geophys. Res. Lett. 34 (11). http://dx.doi.org/10.1029/2006gl027538 (Wiley-Blackwell, online).

Dee, D.P., Uppala, S.M., Simmons, A.J., Berrisford, P., Poli, P., Kobayashi, S., Andrae, U., Balmaseda, M.A., Balsamo, G., Bauer, P., Bechtold, P., Beljaars, A.C.M., van de Berg, L., Bidlot, J., Bormann, N., Delsol, C., Dragani, R., Fuentes, M., Geer, A.J., Haimberger, L., Healy, S.B., Hersbach, H., Hólm, E.V., Isaksen, L., Kållberg, P., Köhler, M., Matricardi, M., McNally, A.P., Monge-Sanz, B.M., Morcrette, J.-J., Park, B.-K., Peubey, C., de Rosnay, P., Tavolato, C., Thépaut, J.-N., Vitart, F., 2011. The ERA-Interim reanalysis: configuration and performance of the data assimilation system. Q. J. R. Meteorol. Soc. 137 (656):553–597. http://dx.doi.org/10.1002/qj.828 (Wiley-Blackwell, online).

Demarcq, H., 2009. Trends in primary production, sea surface temperature and wind in upwelling systems (1998–2007). Prog. Oceanogr. 83 (1–4):376–385. http://dx.doi.org/10.1016/j.pocean.2009.07.022 (Elsevier BV, online).

Desai, S., Vincent, P., 2003, July 1. Statistical Evaluation of the Jason-1 Operational Sensor Data Record Special Issue: Jason-1 Calibration/Validation. UMGD. Informa UK Limited http://dx.doi.org/10.1080/714044518.

Desbiolles, F., Blanke, B., Bentamy, A., Roy, C., 2016. Response of the Southern Benguela upwelling system to fine-scale modifications of the coastal wind. J. Mar. Syst. 156: 46–55. http://dx.doi.org/10.1016/j.jmarsys.2015.12.002 (Elsevier BV, online).

Dewitte, B., Illig, S., Renault, L., Goubanova, K., Takahashi, K., Gushchina, D., Mosquera, K., Purca, S., 2011. Modes of covariability between sea surface temperature and wind stress intraseasonal anomalies along the coast of Peru from satellite observations (2000–2008). J. Geophys. Res. 116 (C4). http://dx.doi.org/10.1029/2010jc006495 (Wiley-Blackwell, online).

Dufois, F., Penven, P., Peter Whittle, C., Veitch, J., 2012. On the warm nearshore bias in Pathfinder monthly SST products over Eastern Boundary Upwelling Systems. Ocean Model. 47:113–118. http://dx.doi.org/10.1016/j.ocemod.2012.01.007 (Elsevier BV, online).

Figueroa, D., Moffat, C., 2000. On the influence of topography in the induction of coastal upwelling along the Chilean Coast. Geophys. Res. Lett. 27 (23):3905–3908. http://dx.doi.org/10.1029/1999gl011302 (Wiley-Blackwell, online).

Fore, A.G., Stiles, B.W., Chau, A.H., Williams, B.A., Dunbar, R.S., Rodriguez, E., 2014. Point-wise wind retrieval and ambiguity removal improvements for the QuikSCAT climatological data set. IEEE Trans. Geosci. Remote Sensing 52 (1):51–59. http://dx.doi.org/10.1109/tgrs.2012.2235843 (Institute of Electrical and Electronics Engineers (IEEE), online).

Frappart, F., Legrésy, B., Niño, F., Blarel, F., Fuller, N., Fleury, S., Birol, F., Calmant, S., 2016. An ERS-2 altimetry reprocessing compatible with ENVISAT for long-term land and ice sheets studies. Remote Sens. Environ. 184:558–581. http://dx.doi.org/10.1016/j.rse.2016.07.037 (Elsevier BV, online).

Garreaud, R., Muñoz, R.C., 2005. The low-level jet off the west coast of subtropical South America: structure and variability. Mon. Weather Rev. 133 (8):2246–2261. http://dx.doi.org/10.1175/mwr2972.1 (American Meteorological Society, online).

Garreaud, R.D., Rutllant, J.A., Muñoz, R.C., Rahn, D.A., Ramos, M., Figueroa, D., 2011. VOCALS-CUpEx: the Chilean Upwelling Experiment. Atmos. Chem. Phys. 11 (5):2015–2029. http://dx.doi.org/10.5194/acp-11-2015-2011 (Copernicus GmbH, online).

Gill, A., 1982. Atmosphere-Ocean Dynamics. Academic Press, New York.

Gourrion, J., Vandemark, D., Bailey, S., Chapron, B., Gommenginger, G.P., Challenor, P.G., Srokosz, M.A., 2002. A two-parameter wind speed algorithm for Ku-band altimeters. J. Atmos. Ocean. Technol. 19 (12):2030–2048. http://dx.doi.org/10.1175/1520-0426(2002)019<2030:atpwsa>2.0.co;2 (American Meteorological Society, online).

Halpern, D., 2002. Offshore Ekman transport and Ekman pumping off Peru during the 1997–1998 El Niño. Geophys. Res. Lett. 29 (5):19-1–19-4. http://dx.doi.org/10.1029/2001gl014097 (Wiley-Blackwell, online).

Hill, A.E., Hickey, B., Shillington, F., Strub, P.T., Brink, K.H., Barton, E., Thomas, A., 1998. Eastern boundary currents: a pan-regional review. In: Robinson, A.R., Brink, K.H. (Eds.), The SeaThe Global Coastal Ocean: Regional Studies and Syntheses vol. 11. John Wiley, Hoboken, N. J, pp. 29–68.

Ikeda, M., Dobson, F., 1995. Oceanographic Applications of Remote Sensing. CRC Press, Boca Raton.

KNMI, 2010. Metop-A ASCAT Level 2 Ocean Surface Wind Vectors Optimized for Coastal Ocean. Ver. Operational/Near-real-time. PO.DAAC, CA, USA (Dataset accessed [2014-06-01]).

KNMI, 2013. Metop-B ASCAT Level 2 Ocean Surface Wind Vectors Optimized for Coastal Ocean. Ver. Operational/Near-Real-Time. PO.DAAC, CA, USA (Dataset accessed [2014-06-01]).

Large, W., Pond, S., 1981. Open ocean momentum flux mea- surements in moderate to strong winds. J. Phys. Oceanogr. 11, 324–336.

Lefèvre, J.M., Aouf, L., Skandrani, S., Queffeulou, P., 2006. Contribution of satellite altimetry to wave analysis and forescasting. 15 Years of Progress in Radar Altimetry Symposium, Venice, Italy.

Lillibridge, J., Scharroo, R., Abdalla, S., Vandemark, D., 2014. One- and two-dimensional wind speed models for Ka-band altimetry. J. Atmos. Ocean. Technol. 31 (3):630–638. http://dx.doi.org/10.1175/jtech-d-13-00167.1 (American Meteorological Society, online).

Lin, J.W.-B., Neelin, J.D., Zeng, N., 2000. Maintenance of tropical intraseasonal variability: impact of evaporation–wind feedback and midlatitude storms. J. Atmos. Sci. American Meteorological Society http://dx.doi.org/10.1175/1520-0469(2000)057<2793:motivi>2.0.co;2.

Machu, E., Ettahiri, O., Kifani, S., Benazzouz, A., Makaoui, A., Demarcq, H., 2009. Environmental control of the recruitment of sardines (*Sardina pilchardus*) over the western Saharan shelf between 1995 and 2002: a coupled physical/biogeochemical modelling experiment. Fish. Oceanogr. 18 (5):287–300. http://dx.doi.org/10.1111/j.1365-2419.2009.00511.x (Wiley-Blackwell, online).

Marchesiello, P., Estrade, P., 2010, January 1. Upwelling limitation by onshore geostrophic flow. J. Mar. Res. http://dx.doi.org/10.1357/002224010793079004.

Messié, M., Ledesma, J., Kolber, D.D., Michisaki, R.P., Foley, D.G., Chavez, F.P., 2009. Potential new production estimates in four eastern boundary upwelling ecosystems. Prog. Oceanogr. 83 (1–4):151–158. http://dx.doi.org/10.1016/j.pocean.2009.07.018 (Elsevier BV, online).

Monaldo, F., 1988. Expected differences between buoy and radar altimeter estimates of wind speed and significant wave height and their implications on buoy-altimeter comparisons. J. Geophys. Res. http://dx.doi.org/10.1029/jc093ic03p02285 (Wiley-Blackwell).

Muñoz, R.C., 2008. Diurnal cycle of surface winds over the subtropical southeast Pacific. J. Geophys. Res. 113 (D13). http://dx.doi.org/10.1029/2008jd009957 (Wiley-Blackwell, online).

Penven, P., 2005. Average circulation, seasonal cycle, and mesoscale dynamics of the Peru Current System: a modeling approach. J. Geophys. Res. http://dx.doi.org/10.1029/2005jc002945 (Wiley-Blackwell).

Penven, P., Roy, C., Brundrit, G., Colin de Verdière, A., Fréon, P., Johnson, A., Lutjeharms, J., Shillington, F., 2001. A regional hydrodynamic model of upwelling in the Southern Benguela. S. Afr. J. Sci. 97 (11–12), 472–475.

Pickett, M.H., Paduan, J.D., 2003. Ekman transport and pumping in the California Current based on the U.S. Navy's high-resolution atmospheric model (COAMPS). J. Geophys. Res. 108 (C10):3327. http://dx.doi.org/10.1029/2003JC001902 (Wiley-Blackwell).

Queffeulou, P., 2003. Validation of ENVISAT RA-2 and JASON-1 altimeter wind and wave measurements. IGARSS 2003. 2003 IEEE International Geoscience and Remote Sensing Symposium. Proceedings (IEEE Cat. No. 03CH37477). Institute of Electrical & Electronics Engineers (IEEE) http://dx.doi.org/10.1109/igarss.2003.1294656 (online).

Queffeulou, P., Chapron, B., Bentamy, A., 1999. Comparing Ku-band NSCAT scatterometer and ERS-2 altimeter winds. IEEE Trans. Geosci. Remote Sensing 37 (3):1662–1670. http://dx.doi.org/10.1109/36.763285 (Institute of Electrical & Electronics Engineers (IEEE), online).

Quilfen, Y., Prigent, C., Chapron, B., Mouche, A.A., Houti, N., 2007, September 27. The potential of QuikSCAT and WindSat observations for the estimation of sea surface wind vector under severe weather conditions. J. Geophys. Res. http://dx.doi.org/10.1029/2007jc004163 (Wiley-Blackwell).

Rahn, D.A., 2012. Influence of large scale oscillations on upwelling-favorable coastal wind off central Chile. J. Geophys. Res. Atmos. http://dx.doi.org/10.1029/2012jd018016 (Wiley-Blackwell).

Rahn, D.A., Garreaud, R.D., 2013. A synoptic climatology of the near-surface wind along the west coast of South America. Int. J. Climatol. 34 (3):780–792. http://dx.doi.org/10.1002/joc.3724 (Wiley-Blackwell, online).

Ray, R.D., Beckley, B.D., 2003. Simultaneous Ocean Wave Measurements by the Jason and Topex Satellites, with Buoy and Model Comparisons Special Issue: Jason-1 Calibration/Validation. UMGD. Informa UK Limited http://dx.doi.org/10.1080/714044527.

Renault, L., Dewitte, B., Falvey, M., Garreaud, R., Echevin, V., Bonjean, F., 2009. Impact of atmospheric coastal jet off central Chile on sea surface temperature from satellite observations (2000–2007). J. Geophys. Res. 114 (C8). http://dx.doi.org/10.1029/2008jc005083 (Wiley-Blackwell, online).

Renault, L., Dewitte, B., Marchesiello, P., Illig, S., Echevin, V., Cambon, G., Ramos, M., Astudillo, O., Minnis, P., Ayers, J.K., 2012. Upwelling response to atmospheric coastal jets off central Chile: a modeling study of the October 2000 event. J. Geophys. Res. 117 (C2). http://dx.doi.org/10.1029/2011jc007446 (Wiley-Blackwell, online).

Renault, L., Deutsch, C., McWilliams, J.C., Frenzel, H., Liang, J.H., Colas, F., 2016. Partial decoupling of primary productivity from upwelling in the California Current system. Nat. Geosci. 9 (7):505–508. http://dx.doi.org/10.1038/ngeo2722 (Springer Nature).

Renault, L., Hall, A., McWilliams, J.C., 2015. Orographic shaping of US West Coast wind profiles during the upwelling season. Clim. Dyn. http://dx.doi.org/10.1007/s00382-015-2583-4 (Springer Science + Business Media).

Rutllant, J.A., Rosenbluth, B., Hormazabal, S., 2004, May. Intraseasonal variability of wind-forced coastal upwelling off central Chile (30°S). Cont. Shelf Res. http://dx.doi.org/10.1016/j.csr.2004.02.004 (Elsevier BV).

Saha, S., Moorthi, S., Pan, H.-L., Wu, X., Wang, J., Nadiga, S., Tripp, P., Kistler, R., Woollen, J., Behringer, D., Liu, H., Stokes, D., Grumbine, R., Gayno, G., Wang, J., Hou, Y.-T., Chuang, H.-Y., Juang, H.-M.H., Sela, J., Iredell, M., Treadon, R., Kleist, D., Van Delst, P., Keyser, D., Derber, J., Ek, M., Meng, J., Wei, H., Yang, R., Lord, S., Van Den Dool, H., Kumar, A., Wang, W., Long, C., Chelliah, M., Xue, Y., Huang, B., Schemm, J.-K., Ebisuzaki, W., Lin, R., Xie, P., Chen, M., Zhou, S., Higgins, W., Zou, C.-Z., Liu, Q., Chen, Y., Han, Y., Cucurull, L., Reynolds, R.W., Rutledge, G., Goldberg, M., 2010. The NCEP climate forecast system reanalysis. Bull. Am. Meteorol. Soc. 91 (8):1015–1057. http://dx.doi.org/10.1175/2010bams3001.1 (American Meteorological Society, online).

SeaPAC, 2013. QuikSCAT Level 2B Ocean Wind Vectors in 12.5km Slice Composites Version 3. Ver. 3. PO.DAAC, CA, USA http://dx.doi.org/10.5067/QSX12-L2B01 (Dataset accessed [2014-06-01]).

Shanas, P.R., Sanil Kumar, V., Hithin, N.K., 2014, June. Comparison of gridded multi-mission and along-track mono-mission satellite altimetry wave heights with in situ near-shore buoy data. Ocean Eng. http://dx.doi.org/10.1016/j.oceaneng.2014.03.014 (Elsevier BV).

Silva, A., Palma, S., Oliveira, P.B., Moita, M.T., 2009. Composition and interannual variability of phytoplankton in a coastal upwelling region (Lisbon Bay, Portugal). J. Sea Res. 62 (4):238–249. http://dx.doi.org/10.1016/j.seares.2009.05.001 (Elsevier BV, online).

Smith, R.L., 1968. Upwelling. Oceanogr. Mar. Biol. Annu. Rev. 6, 11–46.

Sverdrup, H.U., Johnson, M.W., Fleming, R.H., 1942. The Oceans, Their Physics, Chemistry, and General Biology. Prentice-Hall Inc.

Tierney, C., Wahr, J., Bryan, F., Zlotnicki, V., 2000. Short-period oceanic circulation: Implications for satellite altimetry. Geophys. Res. Lett. 27 (9):1255–1258. http://dx.doi.org/10.1029/1999gl010507 (Wiley-Blackwell, online).

Veitch, J., Penven, P., Shillington, F., 2009. The Benguela: a laboratory for comparative modeling studies. Prog. Oceanogr. 83 (1–4):296–302. http://dx.doi.org/10.1016/j.pocean.2009.07.008 (Elsevier BV, online).

Verhoef, A., Stoffelen, A., 2013. Validation of ASCAT Coastal Winds, Version 1.5 Document External Project: 2013, SAF/OSI/CDOP/KNMI/TEC/RP/176, EUMETSAT.

Verron, J., Sengenes, P., Lambin, J., Noubel, J., Steunou, N., Guillot, A., Picot, N., Coutin-Faye, S., Sharma, R., Gairola, R.M., Murthy, D.V.A.R., Richman, J.G., Griffin, D., Pascual, A., Rémy, F., Gupta, P.K., 2015. The SARAL/AltiKa altimetry satellite mission. Mar. Geod. 38 (Suppl. 1):2–21. http://dx.doi.org/10.1080/01490419.2014.1000471 (Informa UK Limited, online).

Vogelzang, J., Stoffelen, A., Verhoef, A., Figa-Saldaña, J., 2011, October 28. On the quality of high-resolution scatterometer winds. J. Geophys. Res. http://dx.doi.org/10.1029/2010jc006640 (Wiley-Blackwell).

Wang, Q., Kalogiros, J., Ramp, S., Paduan, J., Buzorius, G., Jonsson, H., 2011. Wind stress curl and coastal upwelling in the area of Monterey Bay observed during AOSN-II. J. Phys. Oceanogr. 41 (5), 857–877.

Wang, Y., Castelao, R.M., Yuan, Y., 2015a. Seasonal variability of alongshore winds and sea surface temperature fronts in Eastern Boundary Current Systems. J. Geophys. Res. Oceans 120 (3):2385–2400. http://dx.doi.org/10.1002/2014jc010379 (Wiley-Blackwell, online).

Wang, D., Gouhier, T.C., Menge, B.A., Ganguly, A.R., 2015b. Intensification and spatial homogenization of coastal upwelling under climate change. Nature 518 (7539):390–394. http://dx.doi.org/10.1038/nature14235 (Nature Publishing Group, online).

Wood, R., Mechoso, C.R., Bretherton, C.S., Weller, R.A., Huebert, B., Straneo, F., Albrecht, B.A., Coe, H., Allen, G., Vaughan, G., Daum, P., Fairall, C., Chand, D., Gallardo Klenner, L., Garreaud, R., Grados, C., Covert, D.S., Bates, T.S., Krejci, R., Russell, L.M., de Szoeke, S., Brewer, A., Yuter, S.E., Springston, S.R., Chaigneau, A., Toniazzo, T., Minnis, P.,

Palikonda, R., Abel, S.J., Brown, W.O.J., Williams, S., Fochesatto, J., Brioude, J., Bower, K.N., 2011. The VAMOS Ocean-Cloud-Atmosphere-Land Study Regional Experiment (VOCALS-REx): goals, platforms, and field operations. Atmos. Chem. Phys. 11 (2): 627–654. http://dx.doi.org/10.5194/acp-11-627-2011 (Copernicus GmbH, online).

Yang, X., Li, X., Pichel, W.G., Li, Z., 2011. Comparison of ocean surface winds from ENVISAT ASAR, Metop ASCAT scatterometer, buoy measurements, and NOGAPS model. IEEE Trans. Geosci. Remote Sensing 49 (12):4743–4750. http://dx.doi.org/10.1109/tgrs.2011.2159802 (Institute of Electrical & Electronics Engineers (IEEE), online).

Zieger, S., Vinoth, J., Young, I.R., 2009. Joint calibration of multiplatform altimeter measurements of wind speed and wave height over the past 20 years. J. Atmos. Ocean. Technol. 26 (12):2549–2564. http://dx.doi.org/10.1175/2009jtecha1303.1 (American Meteorological Society, online).

Chapter 3

Seasonal Dynamics Off the Central Chile Upwelling System

3.1 Introduction

This chapter corresponds to the content of the article "Seasonal variability of the Ekman transport and pumping in the upwelling system off central-northern Chile (∼30°S) based on a high-resolution atmospheric regional model (WRF)" published in the Journal "Ocean Science" https://doi.org/10.5194/os-12-1049-2016. This study is based on the analysis of the atmospherics simulations performed in the framework of this thesis. Here, we evaluated the seasonal variability in Ekman transport, pumping and their relative contribution to total upwelling along the central-northern Chile region (∼30°S) from a high-resolution WRF model simulation. As a first step, the simulation is validated from satellite observations and in-situ automatic weather stations, which indicates a realistic representation of the spatial and temporal variability of the wind along the coast.

The simulation exhibits a cyclonic wind curl (negative) on a coastal-band all along the coast and inside the bays. This negative wind curl is mainly due to the onshore decay of the wind (wind drop-off), which presented length scales (L_d) between 8 and 45 km with a significant latitudinal variability, in agreement with the altimetry-derived wind speed data. When the resolution of the model is increased, the wind drop-off takes place closer to the coast and exhibits a larger meridional/latitudinal variability, consistent with previous studies . Both, wind stress and wind curl had a clear seasonal variability with annual and semiannual components. Alongshore wind stress maximum peak occurred in spring, with a secondary peak in fall and minimum in winter.

The relative contribution of the coastal divergence and Ekman pumping to the vertical transport along the coast, considering the estimated wind drop-off length, indicated meridional alternation between both mechanisms, modulated by orography and the intricate coastline. Prevalence of positive Ekman pumping is associated with large L_d values, observed in regions with high orography and the presence of embayments along the coast, as the Coquimbo bay system. On the other hand, there is a prevalence of coastal divergence with smaller values of L_d and more intense winds near the coast in sectors characterized by a low topography and the presence of headlands as Punta Lengua de Vaca and Punta Choros. There is also a combination of both mechanisms in which neither divergence nor coastal Ekman pumping dominated over the other. In terms of total upwelling rates, the vertical transport induced by coastal divergence and Ekman pumping represented 60 and 40 % of the total upwelling transport, respectively.

Concluding, the model allowed for an estimate of the nearshore (coastal fringe of ∼50km) low-level circulation and evidences fine-scale structure of the wind stress curl that cannot be estimated from satellite observations. Considering the overall realism of the model simulation, this study could be used to guide field experiments and gather in situ measurements in order to gain further knowledge in the processes that constrain such features.

Ocean Sci., 12, 1049–1065, 2016
www.ocean-sci.net/12/1049/2016/
doi:10.5194/os-12-1049-2016
© Author(s) 2016. CC Attribution 3.0 License.

Ocean Science
Open Access

Seasonal variability of the Ekman transport and pumping in the upwelling system off central-northern Chile (∼ 30° S) based on a high-resolution atmospheric regional model (WRF)

Luis Bravo[1,2,3], **Marcel Ramos**[2,3,1,6], **Orlando Astudillo**[1,4], **Boris Dewitte**[4,3], **and Katerina Goubanova**[5]

[1]Centro de Estudios Avanzados en Zonas Áridas (CEAZA), Coquimbo, Chile
[2]Departamento de Biología, Facultad de Ciencias del Mar, Universidad Católica del Norte, Coquimbo, Chile
[3]Millennium Nucleus for Ecology and Sustainable Management of Oceanic Islands (ESMOI), Coquimbo, Chile
[4]Laboratoire d'Etudes en Géophysique et Océanographie Spatiales (LEGOS), Toulouse, France
[5]Centre Européen de Recherche et de Formation Avancée en Calcul Scientifique (CERFACS), Toulouse, France
[6]Centro de Innovación Acuícola Aquapacífico, Coquimbo, Chile

Correspondence to: Luis Bravo (luis.bravo@ceaza.cl) and Marcel Ramos (marcel.ramos@ucn.cl)

Received: 1 October 2015 – Published in Ocean Sci. Discuss.: 8 December 2015
Revised: 8 August 2016 – Accepted: 16 August 2016 – Published: 8 September 2016

Abstract. Two physical mechanisms can contribute to coastal upwelling in eastern boundary current systems: offshore Ekman transport due to the predominant alongshore wind stress and Ekman pumping due to the cyclonic wind stress curl, mainly caused by the abrupt decrease in wind stress (drop-off) in a cross-shore band of 100 km. This wind drop-off is thought to be an ubiquitous feature in coastal upwelling systems and to regulate the relative contribution of both mechanisms. It has been poorly studied along the central-northern Chile region because of the lack in wind measurements along the shoreline and of the relatively low resolution of the available atmospheric reanalysis. Here, the seasonal variability in Ekman transport, Ekman pumping and their relative contribution to total upwelling along the central-northern Chile region (∼ 30° S) is evaluated from a high-resolution atmospheric model simulation. As a first step, the simulation is validated from satellite observations, which indicates a realistic representation of the spatial and temporal variability of the wind along the coast by the model. The model outputs are then used to document the fine-scale structures in the wind stress and wind curl in relation to the topographic features along the coast (headlands and embayments). Both wind stress and wind curl had a clear seasonal variability with annual and semiannual components. Alongshore wind stress maximum peak occurred in spring, second increase was in fall and minimum in winter. When a threshold of $-3 \times 10^{-5}\,\mathrm{s}^{-1}$ for the across-shore gradient of alongshore wind was considered to define the region from which the winds decrease toward the coast, the wind drop-off length scale varied between 8 and 45 km. The relative contribution of the coastal divergence and Ekman pumping to the vertical transport along the coast, considering the estimated wind drop-off length, indicated meridional alternation between both mechanisms, modulated by orography and the intricate coastline. Roughly, coastal divergence predominated in areas with low orography and headlands. Ekman pumping was higher in regions with high orography and the presence of embayments along the coast. In the study region, the vertical transport induced by coastal divergence and Ekman pumping represented 60 and 40 % of the total upwelling transport, respectively. The potential role of Ekman pumping on the spatial structure of sea surface temperature is also discussed.

1 Introduction

In the eastern boundary current systems wind-induced upwelling has mainly been described using two primary mechanisms (Sverdrup et al., 1942; Gill 1982; Pickett and Paduan, 2003; Capet et al., 2004; Jacox and Edwards, 2012). The first one is coastal divergence, which is the result of

offshore Ekman transport due to alongshore winds (with an equatorward component) and earth's rotation and the presence of the coast (i.e., coastal upwelling). The second one is Ekman pumping, which is the result of a cyclonic wind stress curl caused mainly by the wind drop-off that extends only tens of kilometers in width along the coast and is a typical feature of the eastern boundary current systems (Bakun and Nelson, 1991; Pickett and Paduan, 2003; Capet et al., 2004; Jacox and Edwards, 2012). Starting in the mid-1970s, a series of studies began assessing the contribution of Ekman pumping on coastal upwelling for the California Current system (Halpern, 1976; Nelson, 1977), which later expanded to the other four upwelling systems (Bakun and Nelson, 1991). In one of these four regions, the coast of north and central Chile, this mechanism has been poorly evaluated, primarily due to the scarcity of in situ data, limitations in diffusiometer winds that have a "blind zone" near the coast and the relatively low spatial resolution of the atmospheric reanalysis. This has caused a limited progresses in the understanding of the upwelling dynamics and the coastal circulation of the region, among other factors.

Coastal upwelling has been widely studied in several regions of the world, in particular along the eastern boundary upwelling systems (EBUSs). Currently, there is no generalized conceptual model for the upwelling structure that considers the region near the coast, the coastal boundary and the open ocean (Mellor, 1986; Marchesiello and Estrade, 2010). Traditionally a simple relationship based on wind stress along the coast has been used as an index of the coastal upwelling intensity (Bakun, 1973); this approximation does not consider other more complex physical processes, such as the wind curl (Pickett and Paduan, 2003; Capet et al., 2004; Jacox and Edwards, 2012) and the geostrophic flow toward the coast, which is in balance with the alongshore pressure gradient and could potentially limit upwelling (Marchesiello et al., 2010; Marchesiello and Estrade, 2010). In the case of the wind curl, several modeling studies from different upwelling systems suggest that wind stress decreases within a narrow coastal band of 10–80 km called wind "drop-off" (Capet et al., 2004; Bane et al., 2005; Perlin et al., 2007; Renault et al., 2012, 2015) that is highly sensitive to the resolution of the model. Thus, regional ocean modeling studies show that the upwelling response is sensitive to the transition in the structure of the wind near the coast (Capet et al., 2004; Jacox and Edwards, 2012), where the structure and physical forcing of the transitional coastal wind profile is not well understood (Jin et al., 2009). In the literature at least three main hypotheses have been proposed to explain the weakening of the wind close to the coast (drop-off) that generates the wind stress curl within the coastal band. The first is related to the change of surface and boundary layer friction in the land–sea interface (Capet et al., 2004). The second is related to the ocean–atmosphere coupling between the sea surface temperature (SST) and the wind (Chelton et al., 2007); particularly cold water upwelling tends to stabilize the atmospheric boundary layer, decoupling the high atmospheric circulation from the surface circulation. The last one is related to coastal orography (Edwards et al., 2001), coastline shape (Perlin et al., 2011), and the combination of both (Renault el at., 2015) constraining the vorticity budget of the low-level atmospheric circulation. Other possible mechanisms that could potentially contribute to wind drop-off near the coast are the effects of sea breeze and pressure gradients (across or along the coast) at sea level.

The central-northern Chile region is characterized by nutrient-rich cold surface waters, attributed to the surface circulation of the Humboldt system and mainly coastal upwelling driven by alongshore winds that are associated with the southeast Pacific anticyclone (Shaffer et al., 1999; Halpern, 2002). A strong seasonal variability of the southeast Pacific anticyclone produces favorable upwelling winds to peak during spring and summer and decrease during winter (Strub et al., 1998). Within central-northern Chile the area around 30° S is characterized by the most intense upwelling favorable winds (Shaffer et al., 1999; Rutllant and Montecino, 2002). Additionally, local high-frequency forcing in the region is associated with atmospheric coastal jets with periods less than 25 days, which are related to synoptic dynamics of the mid-latitude pressure perturbations, in this case high pressures that migrate toward the east (Muñoz and Garreaud, 2005; Rahn and Garreaud, 2013) and play a major role in coastal upwelling (Renault et al., 2009, 2012; Aguirre et al., 2012). All these features make the region a natural laboratory to explore the forcing mechanisms and describe the physical processes that modulate coastal upwelling.

In a recent modeling study Renault et al. (2012) analyzed the main physical processes that explain changes in sea surface temperature in an upwelling event during the occurrence of an atmospheric coastal jet along the central-northern Chile region. The results showed a clear drop-off of the coastal wind that was not observed in the QuikSCAT data due to the "blind zone" in the satellite measurements ($\sim$ 25 km offshore). The oceanic response to the atmospheric coastal jet produced significant cooling of the sea surface that significantly contributed to ocean vertical mixing equivalent to the magnitude of the vertical advection near the coast. Their sensitivity analyses showed that the response of the coastal ocean highly depends on the representation of the wind drop-off. This is because the total upwelling (i.e., the sum of coastal upwelling and Ekman pumping) depends on the scale of the wind drop-off. The authors suggest that there is a negative effect on coastal upwelling, due to a reduced Ekman transport near the coast that is not balanced by Ekman pumping. In addition, the drop-off has a strong effect on vertical mixing and consequently the cooling of the coastal ocean. In a previous modeling study, Capet et al. (2004) suggested that a poor representation of the wind drop-off off the coast of California could underestimate Ekman pumping and overestimate coastal upwelling (and vice versa), with consequences for the coastal circulation processes. Meanwhile,

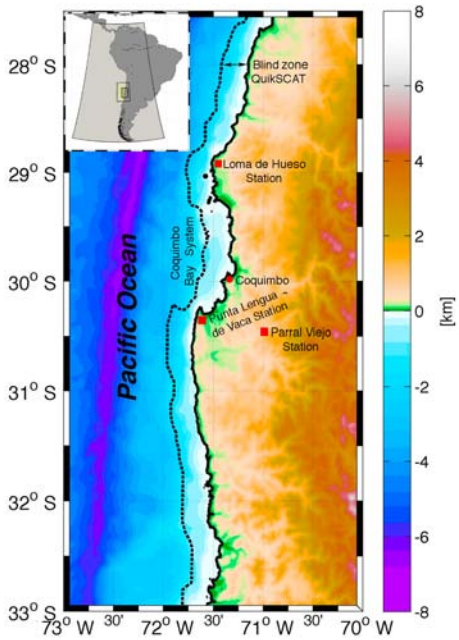

Figure 1. Study area showing bathymetry and topography of the coastal terrain. The dotted thick line indicates the western boundary of the coastal band where satellite information (∼ 25 km offshore) is absent. Red squares indicate the location of the three weather stations at Loma de Hueso, Punta Lengua de Vaca and Parral Viejo. The inset plot shows the three model domains used in the WRF simulations (36, 12 and 4 km).

Garreaud et al. (2011), using observations, found a local atmospheric coastal jet just north of one of the most prominent geographic points of the region: Punta Lengua de Vaca (see Fig. 1). This coastal jet shows a distinct daily cycle as a result of the strong baroclinicity due to heating differential in the region. In a later study Aguirre et al. (2012), using climatological QuikSCAT winds to force a regional ocean model, found the importance of the wind stress curl over the regional circulation exerting control over the seasonal cycle of an equatorward coastal jet. This study also evaluated the contribution of Ekman pumping to the total upwelling, which was not well resolved due to a poor resolution of the satellite winds within the first 30 km near the coast. In particular, due to the narrow continental shelf off central-northern Chile, the cells of upwelling due to coastal divergence are trapped near the coast (Estrade et al., 2008); consequently, the use of QuikSCAT winds could be overestimating the effect of upwelling driven by coastal divergence and Ekman pumping.

Although previous studies have documented the importance of the wind stress curl near the coast of central Chile (Renault et al., 2012; Aguirre et al., 2012), the impact of the abrupt transition of the wind near the coast (i.e., drop-off) and its seasonal variability on upwelling are still poorly understood. Here, prior to addressing this issue from an oceanic perspective, our objective is to document the wind stress curl (drop-off) and its seasonal variability off central-northern Chile (∼ 30° S) using a high-resolution (∼ 4 km) atmospheric model. Our focus in on the Ekman pumping and its contribution to the total upwelling, and the factors that could contribute to its meridional variability (i.e., topography, coastline and air–sea interactions).

The paper is organized as follows: a description of the atmospheric simulations and the methods used to estimate different upwelling terms are described in Sect. 2. Section 3 presents results and discussions and was subdivided into four subsections. The first one describes wind stress curl pattern and the spatial scale of the wind drop-off. The second and third present an analysis of the annual variability in Ekman pumping and coastal divergence, and their relationship with coastal topography and their contribution to upwelling transport. The fourth presents a study of the relationship between Ekman pumping and surface temperature near the coast. Finally, Sect. 4 presents a summary.

2 Methods and model configuration

2.1 Model output

The Weather Research and Forecasting (WRF) model version 3.3.1 (Skamarock and Klemp, 2008) was configured with three nested domains (Fig. 1) with increasing horizontal grid spacing over the region of interest by a factor of 3 from one domain to the next. The largest synoptic domain covers most of South America and the eastern Pacific in a Mercator projection with a horizontal resolution of 36 km. The northerly extension of the parent domain extends to 10° N because beyond the focus of the present study we are also interested (future work) in assessing the impact of the downscaled winds from the coarse domain over a regional ocean model of the Humboldt system, whose domain extends from 5° N to 40° S following the approach of Cambon et al. (2013). The second domain covers the coast of central-northern Chile (25–35° S) with a horizontal resolution of 12 km. The innermost domain is centered over the Coquimbo Bay system with a horizontal grid spacing of 4 km (Fig. 1). The use of such near-kilometer resolution improves the representation of complex terrain and is necessary for dynamical downscaling of near-surface wind speed climate over complex terrain (Horvath, 2012). WRF employs a terrain-following hydrostatic-pressure coordinate in the vertical, defined as eta (η) levels. Here a total of 42 η levels were used in the vertical with increasing resolution toward the surface, 20 of them in the lowest 1.5 km with ∼ 30 m in the vertical for the surface level. Such telescopic resolution is a common choice in precedent studies to properly simulate the marine boundary layer depth over the ocean (Muñoz and Garreaud, 2005; Rahn and Garreaud 2013; Toniazzo et al., 2013; Renault et al., 2012; Rutllant et al., 2013).

Given the complex interactions between alongshore winds, topography, cloudiness, land heating and coastal upwelling in the study region (Rahn and Garreaud, 2013; Wood et al., 2011; Toniazzo et al., 2013), we have tested the WRF model in different combinations of parameterizations (cumulus – planetary boundary layer – soil model), surface data (SST forcing, topography and land surface) and nesting technique. A set of eight sensitivity simulations (for more details see response to referee 1, http://www.ocean-sci-discuss.net/os-2015-94/#discussion) was carried out for the control period, i.e., from 1 October to 31 December 2007, corresponding to the upwelling season in central-northern Chile. The results were evaluated against surface observations from meteorological automatic stations and scatterometers (QuikSCAT, ASCAT). Particular attention was paid to the shoreward decrease and temporal variability of the surface wind speed near the coast. The configuration with the best estimates of observed surface variability and mean state was then used for the long simulation 2007–2012 (Table 1).

The initial and lateral boundary and conditions (LBCs) were derived from the National Centers for Environmental Prediction (NCEP) Final Analysis Data (FNL) (Kalnay et al., 1996; available online at http://dss.ucar.edu/datasets/ds083.2/) at $1° \times 1°$ global grid resolution every 6 h. The boundary conditions are prescribed over the coarser domain with the depth of five grid cells where simulated variables are relaxed towards the FNL solution. The SST forcing data are based on the daily Operational Sea Surface Temperature and Sea Ice Analysis (OSTIA) at $0.05° \times 0.05°$ global grid resolution (Stark et al., 2007). To include the diurnal cycle we have calculated the 6 h anomalies with respect to the daily mean from the 6 h FNL SST and then added to the daily OSTIA SST. In this way we generate the 6 h lower boundary updates with the same update rate used for the LBCs as Renault et al. (2015).

For each year the model was re-initialized with the FNL reanalysis every 3 months leaving 6 overlap days as a spin-up, the outputs during this period were excluded from the analysis. This scheme was suggested by Lo et al. (2008) in order to mitigate the problems of systematic error growth in long integrations and inconsistences between the flow developing and the lateral boundary conditions. The instantaneous model diagnoses were stored at hourly intervals, and the time steps were set to 108, 36 and 12 s for the domains of 36, 12 and 4 km resolution respectively.

The simulated winds were validated using QuikSCAT and observations from two weather stations near the coast in Loma de Hueso (LDH) and Punta Lengua de Vaca (PLV) and a third station farther inland named Parral Viejo (Figs. 1 and 2). A spatial comparison for 2007–2009 was done between satellite and WRF using the coarse-resolution grid (36 km). The comparison showed a good agreement between observations and modeling results with a similar spatial structure and magnitudes of the same order, especially within the study region (27–33° S). The root mean square of the difference for observations and model results was less than $1\,\mathrm{m\,s^{-1}}$ (Fig. 2c). The high-resolution model outputs (4 km) were also compared with available observations. Initially, for each of the weather stations daily wind cycles were compared with simulations (not shown). The results indicate a better fit in diurnal variability when the model is forced with SST (OSTIA), which was finally chosen for the simulations performed in this study. The best fit between observations and model outputs was found when the wind intensifies during the afternoon between 17 and 19 h. A good model representation of the afternoon winds is key for a proper representation of coastal upwelling in the region. Finally, for each weather station, linear regressions and dispersion plots were done between the meridional component of simulated (4 km) and observed winds (Fig. 2d–f). A good agreement was observed for all the cases.

2.2 Upwelling estimates

The relative importance of coastal upwelling due to coastal divergence (Smith, 1968) was estimated using wind stress obtained by the WRF model:

$$\mathrm{Et} = \frac{1}{\rho_\mathrm{w} f}\tau \times \hat{k}, \tag{1}$$

where Et is Ekman transport ($\mathrm{m^2\,s^{-1}}$), τ is the wind stress at the land–sea margin (~ 4 km from the coast), ρ_w is water density, f is the Coriolis parameter and k is a unit vertical vector. The vertical velocity from Ekman pumping (EP) was estimated using a definition given by Halpern (2002) and Renault et al. (2012).

$$w_\mathrm{EP} = \frac{\mathrm{Curl}(\tau)}{\rho_\mathrm{w} f} + \frac{\beta \tau_x}{\rho_\mathrm{w} f^2}, \tag{2}$$

where $\tau(x, y)$ is wind stress, β is the Coriolis parameter gradient and τ_x is the cross-shore wind stress. Latitude variations were not significant; therefore, the last term in Eq. (2) was neglected. In order to compare the two upwelling processes, Ekman pumping was converted into transport by integrating the vertical velocity within a certain distance from the coast, which in our case was the length scale of the wind drop-off (L_d) obtained from a reference value (defined by Renault et al., 2015) where cross-shore wind curl was $< -3 \times 10^{-5}\,\mathrm{s^{-1}}$. The wind drop-off spatial length (L_d) varies meridionally (Fig. 3b–c).

Note that if we assume that the wind is parallel to the coast and that the wind curl is dominated by its cross-shore gradient component (and this gradient is nearly constant in the drop-off zone), then the total upwelling transport is simply $\tau/(\rho f)$ or expressed as vertical velocity is $W = \tau/(\rho f L_\mathrm{d})$, where τ is the wind stress at L_d. Consequently it is apportioned to Ekman transport and pumping according to the amount of drop-off (for more details see Renault et al., 2012). On the other hand, in our study region there is a marked decline toward the coast of the meridional wind component;

Table 1. Information of the physics options and main features used in the simulations.

Parameterization	References
Microphysics: WRF Single-Moment six-class scheme. A scheme with ice, snow and graupel processes suitable for high-resolution simulations.	Hong et al. (2006)
Longwave/shortwave radiation: Rapid Radiative Transfer Model (RRTMG). An accurate scheme using look-up tables for efficiency, accounts for multiple bands, trace gases, and microphysics species. It includes the Monte Carlo independent column approximation (MCICA) method of random cloud overlap.	Iacono et al. (2008).
Boundary layer: University of Washington turbulent kinetic energy (TKE) boundary layer scheme. This scheme is TKE based, and it is characterized by the use of moist-conserved variables, an explicit entrainment closure, downgradient diffusion of momentum, and conserved scalars within turbulent layers.	Bretherton and Park (2009)
Surface layer: Based on Monin–Obukhov with Carlson–Boland viscous sub-layer and standard similarity functions from look-up tables.	Paulson (1970) Dyer et al. (1970) Webb (1970) Beljaars (1994) Zhang and Anthes (1982)
Land surface model: The NOAH Land Surface Model. For land surface processes including vegetation, soil, snowpack and land–atmosphere energy, momentum and moisture exchange.	Tewari et al. (2004)
Cumulus: Betts–Miller–Janjic scheme. Operational eta scheme. Column moist adjustment scheme relaxing towards a well-mixed profile.	Janjic (2000)

therefore, the wind drop-off has an impact on the total upwelling velocity. Thus a proper assessment of scales involved in both mechanisms is crucial to the upwelling problem.

3 Results and discussion

3.1 Mean wind stress curl and the wind drop-off spatial scale

From the wind stress simulations (model wind outputs) we obtained the mean of the wind stress curl in the three model domains with spatial resolutions of 36, 12 and 4 km (Fig. 3a–c). The mean wind stress curl patterns show clear differences when resolution is increased. In the simulations of higher resolution, small-scale or finer-scale structures are well defined, especially close to the coast, which are not present in the simulation of coarse resolution and have not been resolved or studied in previous studies (Aguirre et al., 2012; Renault el al., 2012). The simulations with higher resolution (12 and 4 km) show a cyclonic wind stress curl (negative) within the coastal band and within the Coquimbo Bay system that is associated with a positive Ekman pumping (producing upwelling), while in the oceanic sector a less intense anticyclone wind curl predominates. The negative curl within the coastal band is the result of an onshore decay in wind intensity (drop-off) that is characteristic of EBUSs (Capet et al., 2004; Renault et al., 2012).

In the central-northern Chile region the drop-off length scale (L_d) is between 8 and 45 km (Fig. 3b–c, segmented yellow line). When the resolution of the model is increased, the wind drop-off takes place closer to the coast and exhibits a larger meridional/latitudinal variability, with in particular a larger drop-off scale in the central region of the domain than in the region south of 30.25° S. The meridional differences of L_d could be associated with coastal orography and the shape of the coastline; this will be discussed later in Sect. 3.3. The finer structures in the wind stress curl close to shore and cannot be determined with confidence from observations of the scatterometers of previous and current satellite missions, such as QuikSCAT and/or other satellite, because of the blind zone in measurements within the first 25 km from the shore. Note that the blind zone increases to 50 km when wind stress curl is estimated, as a result of the estimate of the spatial derivative.

Renault et al. (2012), based on atmospheric simulations (obtained with WRF), determined that the extent of the wind drop-off was ~ 70 km. This length was different from the one obtained in this study (which varied between 8 and 45 km), possibly because of the lower resolution used in their study. To further explain the zonal wind structure and drop-off, Fig. 3d shows zonal profiles of the meridional wind of the more exposed region. The results indicate a clear decay of the wind along the coast in the three simulations (36, 12 and 4 km) that is not observed in the satellite data from QuikSCAT. It should be noted that there is the small differ-

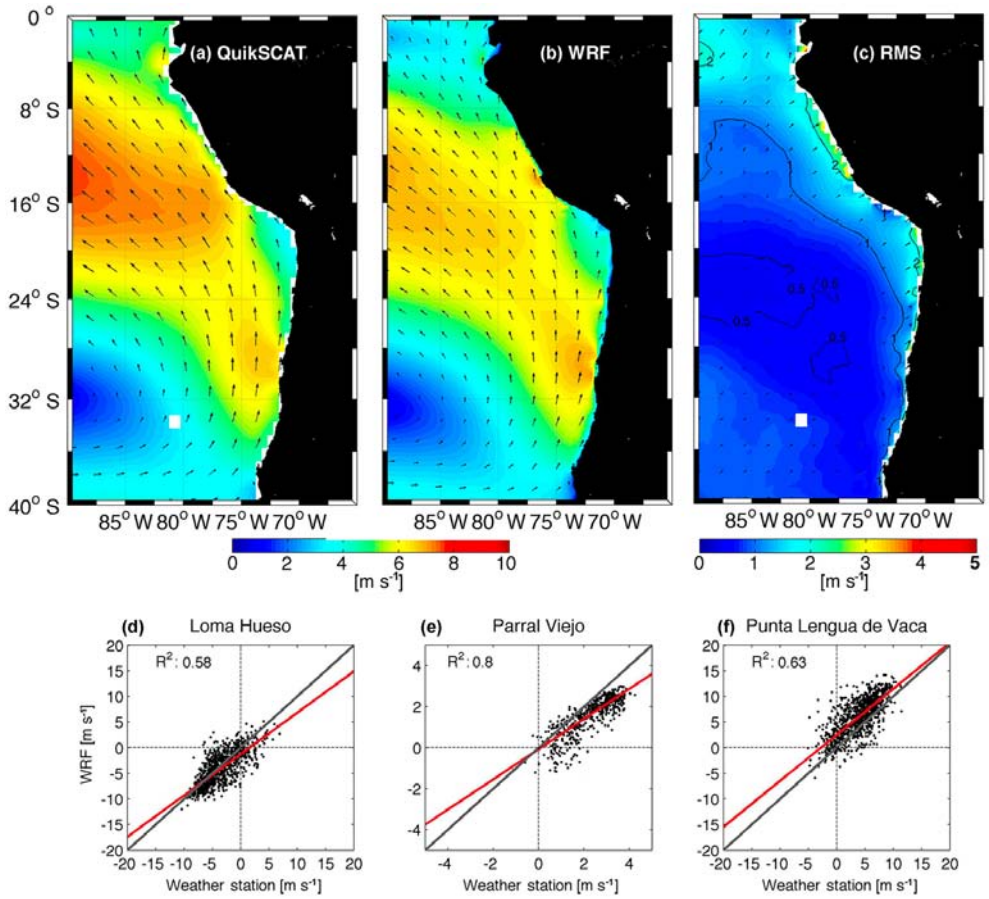

Figure 2. Comparisons of the spatial patterns of the mean velocity fields of winds obtained (common period 2007–2009) from **(a)** QuikSCAT, **(b)** WRF simulation for the 36 km grid configuration and **(c)** root mean square differences between observations and model results. The lower panels show dispersion plots between the observed and modeled N–S winds at **(d)** Loma de Hueso, **(e)** Parral Viejo and **(f)** Punta Lengua de Vaca (Fig. 1). Red line represent to linear regress and black line is 1 : 1 relation.

ence with the satellite product. As mentioned above, in the study region there is a lack of wind information within the coastal band that covers the blind zone of the satellites and that can be used for validation purpose. One of the first in situ measurements in the region was done during the field campaign CupEX (Garreaud et al., 2011). During this experiment a zonal profile of wind was measured using airborne meteorological techniques. These observations allowed detection of an atmospheric coastal jet with a marked daily cycle that extended north of Punta Lengua de Vaca towards the Coquimbo Bay system.

Such a coastal jet is present in our simulations that produce a wind curl in the bay system, which affects the circulation and coastal upwelling in the region. Other recent wind observations were collected under the scope of this study (FONDECYT postdoctoral project 3130671), which are presented in Fig. 3e. These wind observations were made with a marine weather station (AirMar) installed on a fishing boat. Measurements were made for 22 April, 18 May, 15 September and 28 October 2014. Although these measurements do not cover the period of the simulations, they are presented here to illustrate observed features of the zonal wind profiles in the southern region. Despite the large spatial and temporal variability of the observations, they suggest a tendency towards a reduction of the alongshore winds toward the coast comparable to what is simulated by the model (Fig. 3d).

Focusing now on the model results, in our study region the atmospheric coastal jet extends from the coast for several tens of kilometers to the west, showing some nearshore maximums, like in Punta Lengua de Vaca (Garreaud and Muñoz, 2005; Muñoz and Garreaud, 2005, among others). In addition, near Punta Lengua de Vaca the atmospheric local and baroclinic jet (local origin), with a marked diurnal cycle, has a maximum around 18:00 LT (local time) (Garraeud et al., 2011; Rahn et al., 2011). We compared the differences between using of WRF wind averaged only during afternoon hours and wind averaged daily during the spring months (not shown). The simulation showed an intensification of the wind in the afternoon, emphasizing the coastal jet at Punta Lengua de Vaca (∼ 30.5° S, south of Tongoy Bay). Strong

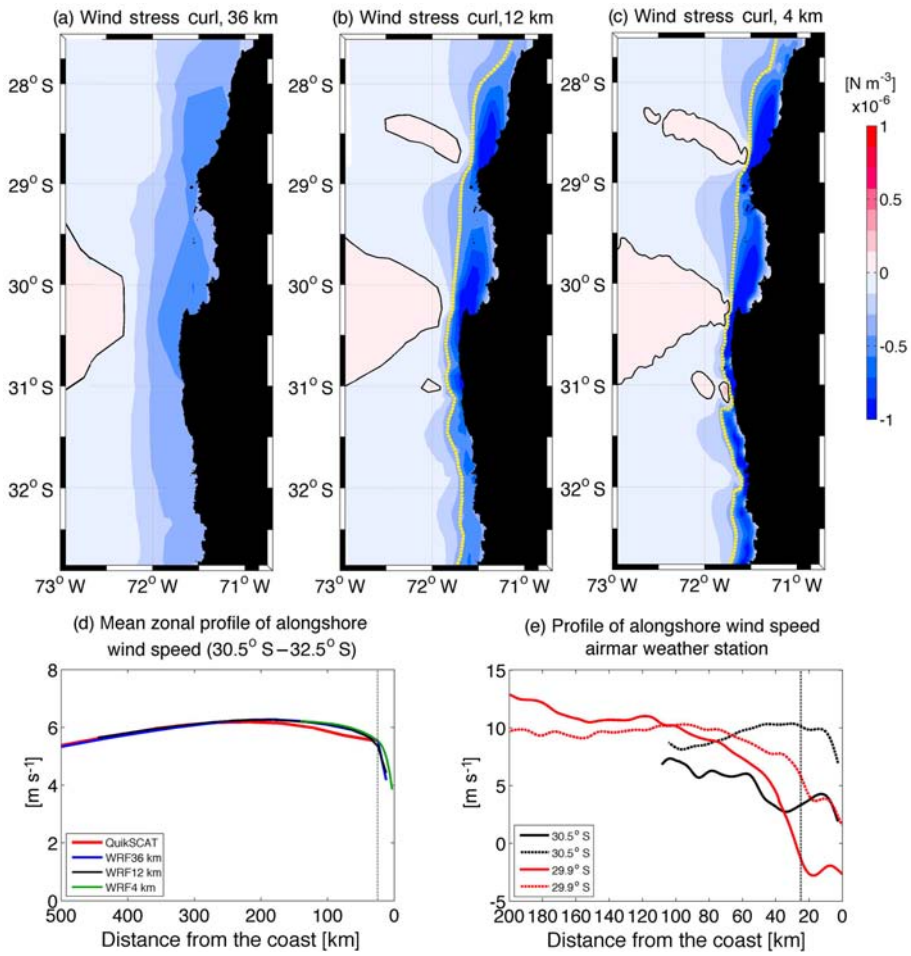

Figure 3. Mean wind stress curl obtained by the model (for 2007–2012) using three model domains: **(a)** 36, **(b)** 12 and **(c)** 4 km. The yellow dotted line represents the length scale of the wind drop-off determined from a threshold value of $-0.3 \times 10^{-4}\,\mathrm{s}^{-1}$ (Renault et al., 2015). **(d)** Mean zonal profiles of alongshore wind speed obtained from the three model configurations (36, 12 and 4 km) and QuikSCAT observations are shown. **(e)** Zonal profiles of alongshore wind speed from a weather station obtained onboard of a fishing boat during 22 April (black line), 18 May (black dashed line), 15 September (red line) and 28 October (red dashed line) of 2014 are also shown. The segmented line in **(d)** and **(e)** indicates the location of the satellite blind spot.

winds were also observed north of Punta Choros (29° S) and south of 31° S. However, when we used the daily averages, we can distinguish the coastal jet and high winds in Punta de Choros and south of 31° S, but with smaller magnitudes than in the afternoon. This is due to the smoothing produced by the averaging to daily mean data. On the other hand, if we look at the structure of Ekman pumping for the two cases, all showed a similar pattern near the coast, with a positive values (favorable to upwelling), but differed in their magnitude, which was greater in the afternoon. Therefore, we believe that for the purposes of this article, using daily averages of wind from the WRF simulation time was valid.

3.2 Annual variability of the wind stress and Ekman pumping

The seasonal analysis of the wind stress and the Ekman pumping is based on the simulation having the highest resolution (4 km), considering the daily average from instantaneous wind values with an hourly sampling over the period between 1 January 2007 and 31 December 2012. Figure 4 presents the mean seasonal cycle of the wind stress for the study area in the coastal fringe extending 150 km from the coast. The wind stress presents a seasonal and spatial variability, with predominance of upwelling favorable winds (with equatorwards component) during all year-round, with maximum values ($\sim 0.15\,\mathrm{N\,m^{-2}}$) between September and November, which is characteristic of the central-northern region of Chile (Shaffer et al., 1999; Rutllant and Montecino, 2002; Ranh and Garreaud, 2013). The seasonal variability

of the wind stress determines the behavior of the coastal upwelling and primary productivity in the region. This is through two main mechanisms – the coastal divergence and the Ekman pumping – which will be evaluated in the following section. The wind also induces vertical mixing and surface cooling. This cooling effect can be even comparable to the one by vertical advection (Renault et al., 2012). In general, these mechanisms may covary in time, responding to the seasonal cycle of the wind stress; hence in a grouped statistical analysis (like SVD) it is difficult to isolate the spatio-temporal combined variability of two mechanisms without rejecting the effect of the third. On the other hand, the model simulates well the coastal atmospheric jet observed in the zone of Punta Lengua de Vaca ($\sim 30°$ S), in particular the maximum intensity during spring (Rahn and Garreaud, 2011, 2013).

Close to the coast, where the satellite data have no coverage or the estimate in wind stress is uncertain (Fig. 1), a wind decay towards the coast (drop-off) is observed during practically all the calendar months of the year, with still a more pronounced tendency in the period between September and December. The horizontal gradient of the wind stress that is most intense close to the coast produces a wind curl with a clockwise rotation direction (cyclonic for the SH) generating a positive Ekman pumping favorable to the upwelling.

In addition to a non-uniform spatial distribution, the drop-off length (L_d) in the area of interest also exhibits a marked seasonal variability. Based on an atmospheric simulation in the west coast of USA, Renault et al. (2015) also suggested that the drop-off presents seasonal and spatial variability, but with an extension ranging from 10 to 80 km. These authors propose that the drop-off dynamics of the wind is due mainly to orographic effects and the shape of the coastline, reaching a maximal reduction of the wind ($\sim 80\,\%$) when these are combined. According to these authors, the drop-off length scale of the wind in front of Chile should be approximately 30 km, less than the scale off the west coast of USA. This would result from the different shape of the Chilean coastline characterized by a straighter coastline and the reduced numbers of capes compared to the US west coast. In addition the Andes would induce a sharper onshore decline of the wind (drop-off) than the mountains of the west coast of the USA (Renault et al., 2015). In the Sect. 3.3 the length scale of the drop-off along the central-northern coast of Chile will be analyzed in relation to the coastal orography and the shape of the coastline.

Despite that the length scale of the wind drop-off in front of central-northern Chile (~ 45 km) is on average less than that estimated in the California Current system (Enriquez and Friehe, 1996; Renault et al., 2015), the wind-stress curl from this zonal gradient of the wind generates an Ekman pumping with a marked seasonality (Fig. 5) and positive vertical velocities (upward) that reach $4\,\mathrm{m\,d^{-1}}$, similar values to that obtained by Pickett and Paduan (2003) in front of the region of the California Current system.

The simulation (4 km) has allowed the depiction and documentation of the mesoscale atmospheric circulation in the first 50 km from the coast (Fig. 3), where the spatial patterns of the Ekman pumping are much more marked, especially at latitudes where there are sharp topographic changes in the coastline (Fig. 5). Thus, structures of Ekman pumping are highlighted to the north of the main headlands of the region (Punta Lengua de Vaca and Punta Choros) and experience a seasonal cycle. In addition, the Ekman pumping presents negative values (downwelling) off-shore associated with an anti-cyclonic wind curl around 28.5° S and between 30 and 31° S that reaches the greatest extent during August, while decreasing considerably in the summer months and beginning of fall (Fig. 5). Mean Ekman pumping in spring is much larger than in the other seasons (i.e., summer, fall and winter), indicating that the spring positive pumping dominates the other, especially north of 29° S, in the interior of the Coquimbo Bay system and south of 31.5° S (not shown).

With the objective of analyzing in more details the seasonal and spatial variability of the wind stress and its zonal gradient, three specific sectors of the study area were selected (28.5, 30.5 and 32.5° S), which are outside the Coquimbo Bay system (Fig. 6). As was mentioned before, the region is characterized by a marked wind stress seasonality more pronounced to the south of the study area (Fig. 6c). In general, the wind component along the coast shows a predominance of southerly winds favorable to the upwelling during all year-round, emphasizing a decrease in the wind stress towards the coast for the spring and summer months at 32.5° S, and in summer at 28.5 and 30.5° S. When estimating the zonal gradient of the wind stress taking as a reference the wind at the coast, the most intense positive gradients (due to the wind drop-off towards the coast) are obtained in a coastal band with a width smaller than 50 km, indicating that the Ekman pumping is the most effective inside the coastal band, as is evidenced in Figs. 4 and 5. On the other hand, the negative zonal gradient extent (Ekman pumping and downwelling) is greater in the sections located farther north, at 28.5 and 30.5° S, than in the section located at 32.5° S (Fig. 6d, e and f), indicating that in the southern part of the study region, the positive Ekman pumping region extends farther than in the zones where the wind stress is more intense seasonally close to the coast (Fig. 4).

3.3 Contributions of Ekman transport and Ekman pumping to the upwelling rate

The central-northern Chile continental shelf is very narrow and very steep so the scale of coastal divergence is < 10 km (considering the theoretical framework of Estrade et al., 2008), while the length scale L_d of Ekman pumping (previously defined, based on Renault et al., 2015) is ~ 45 km. To compare the seasonal contribution of coastal divergence and Ekman pumping to the total transport of coastal upwelling in the study region, the annual cycle of coastal divergence

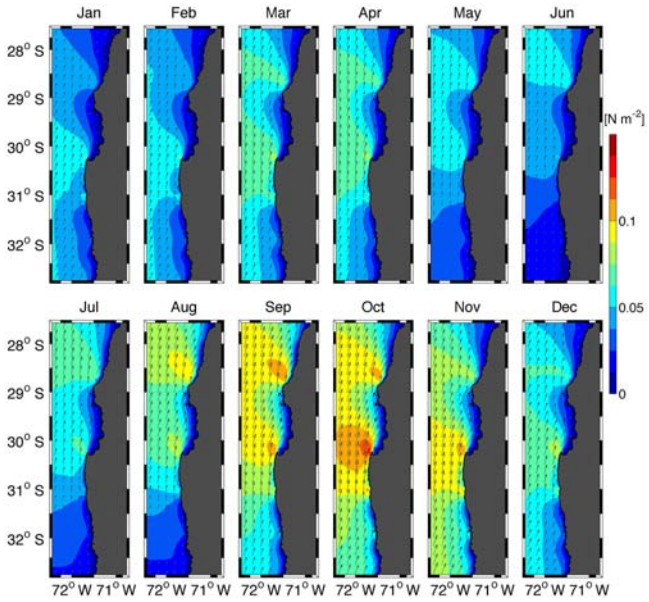

Figure 4. Wind stress annual cycle obtained from the simulation at 4 km resolution (for 2007–2012). Color represents the magnitude of wind stress (in $\mathrm{N\,m^{-2}}$) and the arrows indicate the wind stress direction.

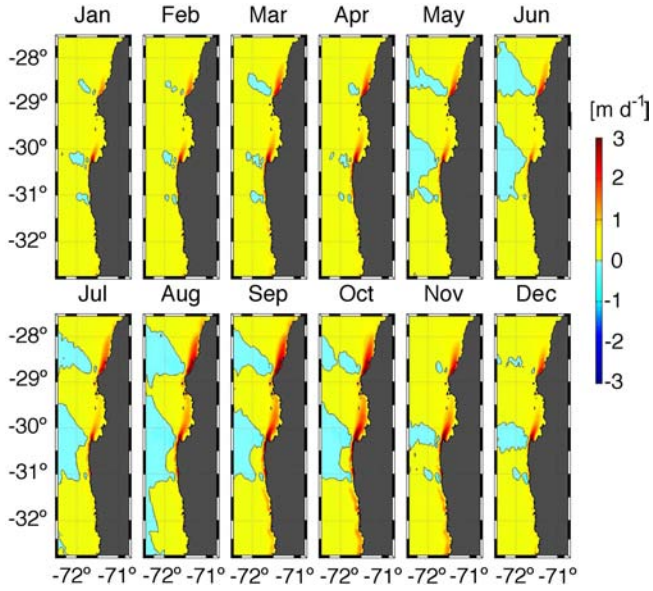

Figure 5. Annual cycle of Ekman pumping (vertical velocity in $\mathrm{m\,d^{-1}}$) obtained from the simulation at 4 km resolution (for 2007–2012).

was obtained first by taking the wind of WRF closest to the coast (< 8 km) and meridionally integrated every 0.25° (Fig. 7e), while the annual cycle of Ekman pumping transport (from wind of WRF) was obtained by integrating the vertical velocity from the shoreline to the distance corresponding to the drop-off (L_d) value, also within 0.25° latitude bands (Fig. 7f).

The results indicate a marked annual cycle with maximum vertical transport in the spring, both induced by coastal divergence and Ekman pumping, with secondary maximum in some areas during fall accounting for a weaker semiannual component. As expected, there is a large temporal coherency along the coast between both processes (the meridional average correlation between Ekman pumping and coastal divergence reaches 0.8), except locally at some latitudes (e.g., at 31.25° S) where there is a weak seasonal cycle in Ekman pumping (Fig. 7f) due to either a weak drop-off or a compensation effect by the zonal wind stress component. The high correlations indicate a seasonal consistency between both mechanisms, which has been previously reported in other upwelling systems (e.g., Pickett and Paduan, 2003; Renault et al., 2015). Although both mechanisms are highly correlated at seasonal timescales, they exhibit significant differences in relative magnitude as a function of latitude; that is, when one is intense the other is weak. For instance, coastal divergence strongly dominates over Ekman pumping between 30.25 and 31.25° S (Fig. 7d), which is the most recognized upwelling center in the region (located south of PLV), as well as in the region between 28.5 and 29.25° S (north of Punta Choros). In those regions Ekman pumping tends to be weaker, whereas it is predominant for the area between 29.25 and 30.25° S, inside the Coquimbo Bay system and the area between 28.0 and 28.75° S, north of LDH. South of 31.25° S, both mechanisms vary meridionally more uniformly. The estimate of the meridional correlation between both mechanisms as a function of calendar month indicates that they are better related in spring and summer (~ -0.72) than in winter (~ 0.45). Possible processes that could explain the inverse (negative) spatial relationship between the two mechanisms and its seasonal modulation are discussed below. Before continuing, we should mention that processes such as upwelling shadow can be important in the Coquimbo Bay system and would affect the temperature distribution inside the bay, especially in the southern part of the bay close to the coast, where higher temperatures are observed (and higher thermal front) compared to the lower temperature area that extends north from Punta Lengua de Vaca (Fig. 10). In fact a study in the southern part of the Coquimbo Bay system (Moraga-Opazo et al., 2011) shows cyclonic circulation when there are upwelling favorable winds, and the circulation is attributed to the separation of oceanic flow in Punta Lengua de Vaca, which is in agreement with the process of upwelling shadow and mainly affects the area indicated above. However, we think that this is not inconsistent with the effect of the wind curl in the area, which would favor upwelling north of Punta Lengua de Vaca. The oceanic response in the area clearly needs more attention and research in future.

Considering the influence of topography and the geometry of the coastline to describe the spatial variability of the wind stress (e.g., Winant et al., 1988; Burk and Thompson, 1996;

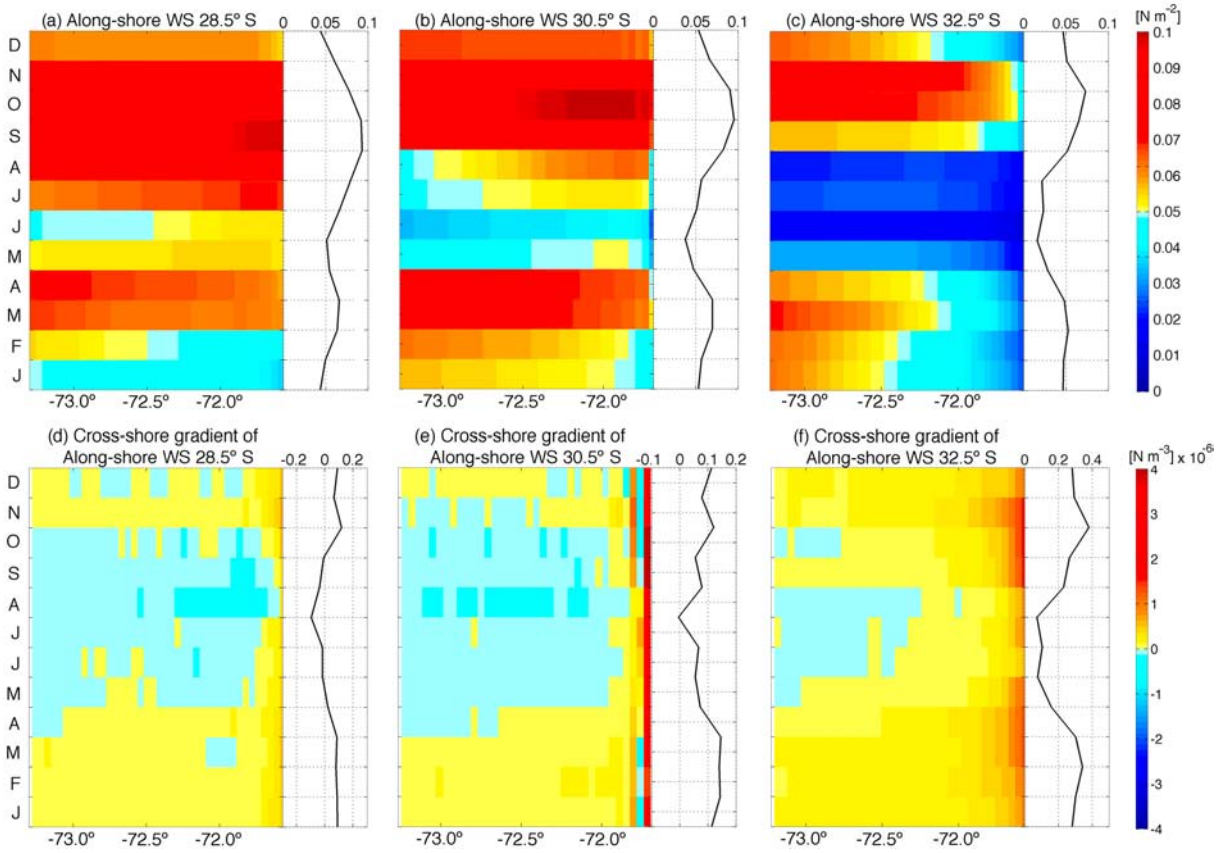

Figure 6. Hovmöller diagrams of alongshore wind stress seasonal cycle (top panels) and the zonal gradient of alongshore wind (lower panels) for the regions at 28.5 **(a, d)**, 30.5 **(b, e)** and 32.5° S **(c, f)**. The monthly mean zonal wind stress and mean zonal gradient are also shown (side black line).

Haack, et al., 2001; Koračin et al., 2004; Renault et al., 2015, among others), we now document the relationship between the relative importance of Ekman transport and pumping, and the coastal topography and shape of the coastline in the region. An along-coast orography index (H_{index}) is estimated from the average of the orographic height between the coastline and 100 km inland (as in Renault et al., 2015). In addition, the coastline meandering index (M_{index}) is estimated by converting the position of the coastline into distances; afterwards using a high-variability pass filter (with 10 km half-width) the small fluctuations in the index are smoothed. Consequently, the index only considers the abrupt change in coastline configuration at relatively large scale (Renault et al., 2015). Figure 7a shows the H_{index} (black line) and M_{index} (red line). In the latter index negative values are associated with headlands, while positive values are associated with bays. The drop-off scale and alongshore wind at the coast and at L_{d} are also included (Fig. 7b–c). Note that L_{d} is inversely proportional to coastal wind (R^2 of ~ 0.81), while the wind evaluated at L_{d} is spatially more homogenous. This differs from the results obtained by Renault et al. (2015) along the western coast of USA. From the inspection of H_{index}, M_{index} and L_{d} three scenarios are defined that could explain the observed upwelling pattern (Fig. 7d–f):

1. There is a prevalence of positive Ekman pumping: in sectors such as the Coquimbo Bay system and the region north of 28.5° S (LDH), where the wind curl intensifies due to the sharp decline of onshore wind, with a large drop-off scale (L_{d}). In addition, the combination of a high orography (large H_{index}) and the presence of bays favors a decrease in the meridional onshore wind.

2. There is a prevalence of coastal divergence: in sectors characterized by a low topography (small H_{index}) and a negative M_{index} due to the presence of headlands such as Punta Lengua de Vaca and Punta Choros, with a smaller drop-off scale (L_{d}) and stronger winds alongshore (Fig. 7b–c).

3. South of 31.25° S the pattern is more complex than previous scenarios. Both mechanisms are present but with a slight dominance of coastal divergence compared with Ekman pumping. South of this latitude, L_{d} increases, coastal wind decreases and wind curl increases (Fig. 7b–c). M_{index} shows the presence of small inlets

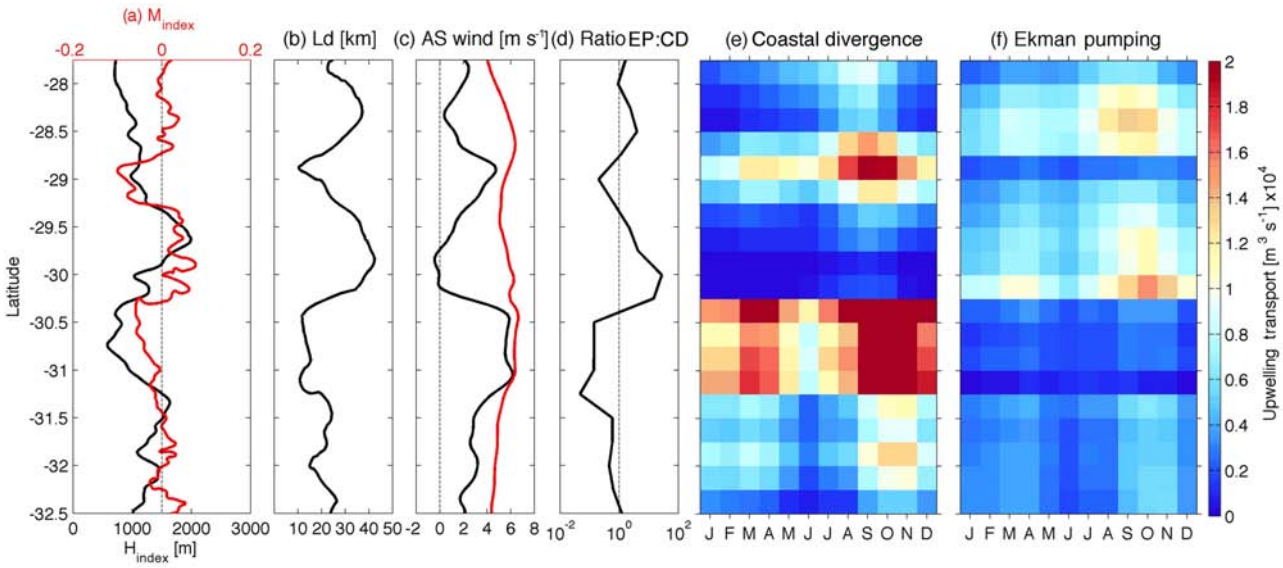

Figure 7. Contributions of the coastal divergence (CD) and Ekman pumping (EP) to the vertical transport near the coast. **(a)** Integrated orography index (H_{index}, black line) and coastline meander index (M_{index}, red line, see text). **(b)** Drop-off spatial length. **(c)** Alongshore wind at L_{d} (red line) and coastal (black line). **(d)** Ratio between Ekman pumping and coastal divergence. **(e)** Seasonal vertical transport associated with coastal divergence and **(f)** seasonal vertical transport associated with Ekman pumping. To estimate the coastal divergence the wind stress closest to the coast was used, while Ekman pumping was integrated from the coast to the longitude corresponding to a distance from the coast equal to the length of the drop-off (see text).

and headlands, and the orography index is moderately high without largest changes as in the northern coastal region.

Renault et al. (2015) proposed that the coastal topography induces a decrease in the intensity of the wind towards the coast through the vortex stretching term. Similarly, Archer and Jacobson (2005) from atmospheric numerical simulations showed that the topography in the Santa Cruz, California, region, is required for the formation of turbulence and vorticity. On the other hand, the shape of the coastline with capes and headlands increases the orographic effect through the vortex stretching term, tilting–twisting and turbulent flux divergence (Archer and Jacobson, 2005; Renault et al., 2015). The sea–land drag coefficient difference mainly acts as a barrier that turns the wind alongshore.

Another minor factor is the sharp coastal sea surface temperature front associated with upwelling. Renault et al. (2015) show that in their sensitivity experiment adding a sharp SST front over a coastal band strip leads to weaker surface wind associated with more stable and shallow marine boundary layer. This response of wind may be due to so-called "downward mixing" mechanism (Wallace et al., 1989; Hayes et al., 1989), which was used by many authors to explain the observed tendency of surface winds to decelerate over colder flank of the SST front and accelerate over warmer flank of the SST front (cf. Small et al., 2008, and references therein): warm (cold) SST would destabilize (stabilize) the planetary boundary layer and cause enhanced (reduced) vertical turbulent mixing, increasing (decreasing) downward fluxes of horizontal momentum from the faster flow above to the slower near-surface flow. Nevertheless, a large SST anomaly (by $-3\,^{\circ}$C in the experiment of Renault et al., 2015) is needed to induce a significant weakening of wind and significant additional wind drop-off. Therefore, the SST effect can be considered as secondary compared to the orography effect over the California coast.

The combination of coastal topography and the presence of headlands, points and capes on the US west coast induces a stronger and larger wind drop-off, which in turn is associated with a positive Ekman pumping (Koračin et al., 2004; Renault et al., 2015). This characteristic differs from what is observed along central-northern Chile, where the larger drop-off (L_{d}) length, associated with a strong wind curl (Fig. 7b–c), takes place in the presence of abrupt orography and within the Coquimbo Bay system (30.25–29.25° S). There the cross-shore wind component is more intense and favors the wind curl, whereas with lower terrain and the presence of headlands the L_{d} is very small (cf. Fig. 10, Renault et al., 2015). The origin of these differences is not well known; they may be due to several factors or processes. For instance, the topographic terrain along the coast of northern Chile is much higher (for the coastal range and Andes mountains) than the terrain along the west coast of the USA. Furthermore, a feature of particular interest north of Punta Lengua de Vaca is the presence of the local atmospheric jet, which has a strong diurnal cycle and a clear seasonal variability, as a result of

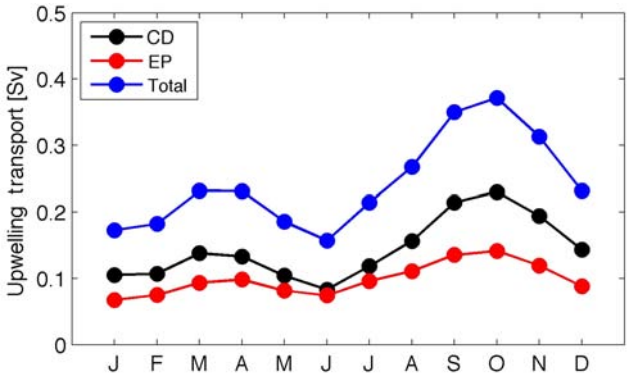

Figure 8. Contributions of coastal divergence (CD) and Ekman pumping (EP) to the vertical transport near the coast (in Sv) over the study area (27.75–32.5° S, see Fig. 7). Seasonal vertical transport associated with coastal divergence (black line), Ekman pumping (red line) and total wind induced vertical transport (blue line, sum of both vertical transports). The estimates were carried out from the WRF simulation at 4 km resolution.

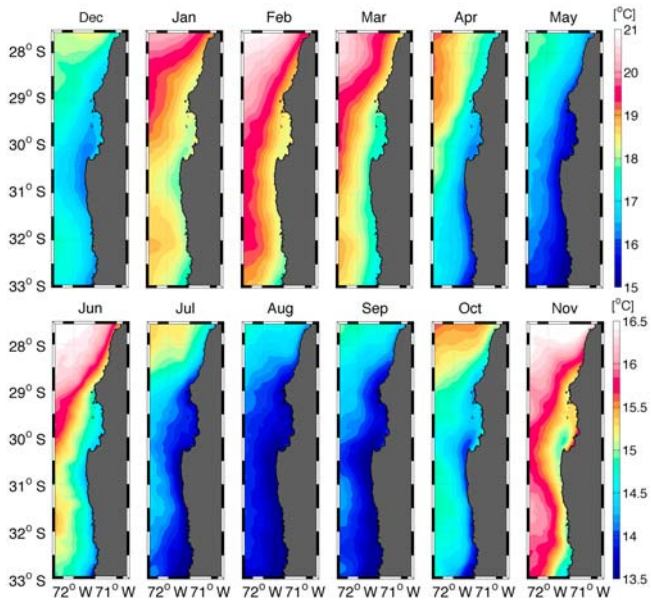

Figure 9. Annual cycle of sea surface temperature obtained using data from the Multi-scale Ultra-high Resolution (MUR). Top and bottom panels used a different color-map scale.

coastal topography that favors baroclinicity north of PLV (Garreaud et al., 2011; Rahn et al., 2011). This feature would deserve further consideration based on the experiments done with the regional atmospheric model; however, this is beyond the scope of the present study. Here the focus is on understanding the possible effect of the wind drop-off and its spatial and seasonal variability on the upwelling dynamics.

To determine the contribution of the two proposed mechanisms to the total upwelling in the region, vertical transport due to coastal divergence and Ekman pumping were meridionally integrated (from Fig. 7e and f, respectively). The contributions of both mechanisms to upwelling (Fig. 8) have a clear annual cycle with a marked semiannual component. Maximum values occur during October, with 0.23 and 0.14 Sv for coastal divergence and Ekman pumping, respectively, while the sum of both is 0.37 Sv. Coastal divergence and Ekman pumping represent 60 and 40 % of the total upwelling, respectively. This indicates that coastal divergence is the stronger upwelling mechanism. However, it should be noted that these values are the sum throughout the region, and these percentages would change if specific sectors were considered especially where Ekman pumping has a larger significance (Fig. 7).

Comparing our estimates with those obtained by Aguirre et al. (2012) from QuikSCAT wind information using a larger region (∼ 27.5–40° S), it is observed that coastal divergence from our study is lower, mainly because they estimated averages using only two values every day, which may influence the daily mean and therefore their estimates. Also their analysis did not include the wind drop-off area. The winds used in their study are stronger and so are their estimates for coastal divergence (cf. Fig. 7, Aguirre et al., 2012). However, for Ekman pumping our results are only slightly smaller than theirs. This difference is mainly due to differences in the method employed to estimate the vertical upwelling transport. In particular they use a length scale (L_d) of 150 km from the coast for their calculation, while in this study a value of 45 km was considered. However, the largest differences in the estimates of the contributions of both mechanisms to total upwelling are in the seasonal variability and the relative contribution to Ekman pumping. The seasonal variability is composed of an annual cycle with a significant semiannual component, whereas that obtained by Aguirre et al. (2012) is rather dominated by the annual cycle. This is because their estimates are based on the average over a larger region that includes the central-southern Chile region, where the wind has a significant annual variability. Moreover, the present results show a higher relative contribution of Ekman pumping to total upwelling in our region. This is partly due to a different technique for estimating this mechanism, the use of different wind products and the differences in the length of both study areas.

3.4 Annual variability of Ekman pumping and its relationship with sea surface temperature near the coast

A link between SST and wind is found throughout the world's ocean wherever there are strong SST fronts (see review by Xie, 2004; Chelton et al., 2007; Small et al., 2008). This link raises the questions of to what extent the wind drop-off could be associated with marked upwelling fronts in EBUSs. In the context of our study, it consists in evaluating the relationship between Ekman pumping and SST, considering that the difficulty to tackle this issue is related to the

fact that there is a large temporal coherence between Ekman pumping and coastal divergence, preventing a clear identification of Ekman pumping-induced SST anomalies where both processes are in phase. As an attempt to identify regions where Ekman pumping has an imprint on SST, we use the Multi-scale Ultra-high Resolution SST data set (MUR, http://mur.jpl.nasa.gov) with a spatial resolution of 1 km, which was shown to better capture SST fronts than other products off Peru (Vazquez et al., 2013). Figure 9 shows the annual cycle of the MUR SST. The satellite data were compared to in situ observations that were obtained from 13 thermistors positioned close to surface along the coastline between 28 and 32° S (these observations were obtained by Centro de Estudios Avanzados en Zonas Áridas, Coquimbo, Chile) covering the period September 2009–2012. The correlations obtained between observations and satellite data were high (0.74–0.94; most values were greater than 0.8), and the root mean square between their differences was low varying between 0.54 and 1.3 °C. This provided confidence to use MUR temperatures close to the coast in the spatio-temporal analysis done in the study region. The MUR data showed that south of 28.5° S there is a persistent surface cooling throughout the year that increases in extent (offshore) from ∼ 10 km in the northern region to ∼ 100 km in the southern region. Within this region there are prominent upwelling centers: Punta Lengua de Vaca (∼ 30.5° S), Punta Choros (∼ 29° S) and the region between 30.5 and 33° S. During most of the year a cold surface tongue extends from the south towards the great system of embayments of Coquimbo (with limits between ∼ 29.25 and 30.25° S), north of Punta Lengua de Vaca. A less intense cold surface tongue but with a similar structure is observed north of Punta Loma de Hueso (∼ 28.8° S).

An illustration of the effect of Ekman pumping on SST is presented in Fig. 10, which shows the October mean spatial distribution for wind stress, Ekman pumping, SST and SST gradient. This month was selected because the maximum values of wind stress and increased surface cooling are recorded during this period. During this month, the wind stress (Fig. 10a) was intense with maximum values of $\sim 0.15\,\mathrm{N\,m^{-2}}$, showing a clear zonal gradient (drop-off) over the entire coastal band of the study area. Note that the maximum wind stress is north of the two most prominent headlands of the region (PLV and LDH), right where the wind abruptly changes direction, creating an intense cyclonic wind curl north of both headlands. As a result of the distribution pattern of the wind stress, wind curl was negative in much of the area of interest, resulting in a positive Ekman pumping with vertical velocities of up to $4\,\mathrm{m\,d^{-1}}$ near the coast (Fig. 10b). Also, there are two areas with slightly negative pumping (light blue regions), following the pattern of the wind stress where the wind decreases away from the coast (see the wind vectors), producing a positive curl and a negative Ekman pumping. Moreover, as mentioned above (see Fig. 7), much of the southern spatial structure in Ekman pumping appears to be associated with the coastal ter-

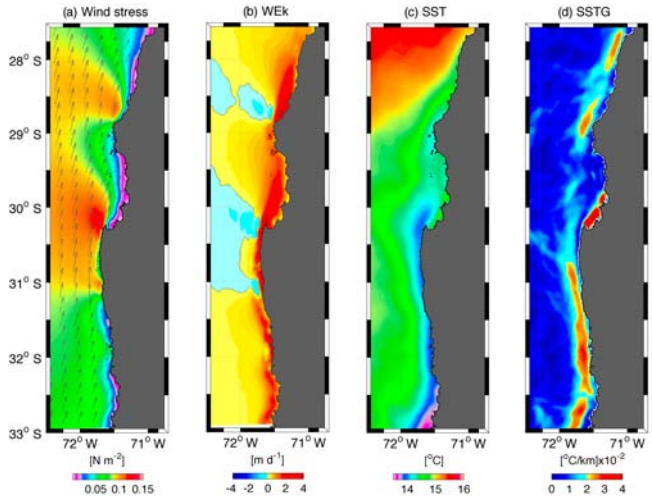

Figure 10. October mean spatial distribution for **(a)** wind stress and **(b)** Ekman pumping using the 4 km grid spacing simulation and **(c)** sea surface temperature (SST) and **(d)** SST gradient obtained from MUR observations.

rain and abrupt changes of the coastline. A good example of this is the tongue-shaped structure that extends from the upwelled waters north of Punta Lengua de Vaca entering the Coquimbo Bay system, where the upwelling induced by the Ekman transport seems unaffected (Fig. 7). As a result of a positive Ekman pumping, cold water rises to surface, causing a decrease in sea surface temperatures in a large part of the coastal region (Fig. 10c). However, this cooling is not necessarily caused by Ekman pumping throughout the region; there are other processes that would contribute to the surface cooling that will be discussed later. Despite this, the cooling inside the Coquimbo Bay system seems to be caused largely by Ekman pumping. Moreover, outside the Coquimbo Bay system high values ($> 2\,°\mathrm{C\,km^{-1}}$) of the horizontal SST gradient magnitude are distributed in a band near the coast but not attached to it (Fig. 10d) as expected for upwelling fronts. Within the Coquimbo Bay system, there is a homogeneous temperature zone, delimited by a less intense gradient in the west and a greater gradient in the smaller bays of the system, which coincides with the structure of an Ekman pumping tongue projected to the north of Punta Lengua de Vaca.

In order to further document the coupled spatio-temporal patterns of Ekman pumping and the SST field, a singular value decomposition analysis (SVD, Venegas et al., 1997) was performed. The SVD method allows the determination of statistical modes (time and space) that maximize the covariance between two data sets. Filtered time series (low-pass filter with mean half-power of 280 days) and normalized Ekman pumping and SST-MUR for the 2007–2012 period were analyzed using this method (Fig. 11). In this case the SVD analysis was successful in capturing a dominant seasonal mode. The first dominant mode accounts for 99 % of the covariance, with 43 and 87 % of the variance explained by Ek-

man pumping and SST respectively. Ekman pumping spatial pattern presents maximum values very close to the coast, primarily north of Punta Lengua de Vaca, inside the Coquimbo Bay system (29.3–30.2° S) and north of Punta Choros (28–29° S). Also, the pattern is intense near the coast between 30.2° S (south of PLV) and 32.5° S. The spatial pattern for SST presented areas with high variability associated with areas of maximum Ekman pumping, highlighting the overall variability in the bay system of Coquimbo and the area north of Loma de Hueso (∼ 28.8° S). Moreover, the correlation between the time series of expansion coefficient was −0.96 (with $R^2 = 0.92$ and significant at 95 %), indicating a strong inverse relationship, consistent with that expected for a positive pumping with upward vertical velocities that causes a surface cooling in the region. This results in a greater contribution to the north of headlands in the region (Punta Lengua de Vaca and Loma de Hueso), even within the Coquimbo Bay system, which is consistent with the results observed in Fig. 7. However, despite the high correlation obtained between both mechanisms within the seasonal scale, we cannot infer a relationship with SST only from Ekman pumping, especially where Ekman transport dominates. Also, other processes such as the direct effect of wind must play a significant role, e.g. vertical mixing (Renault et al., 2012), or processes related to mesoscale activity (filaments, meanders, eddies, etc.), which are more intense south of Punta Lengua de Vaca (Hormazabal et al., 2004), and/or in general processes related to ocean–atmosphere interaction (Chelton et al., 2007; Renault et al., 2015).

Finally, our analysis calls for more thorough study on the temperature response to wind forcing, which should involve oceanic modeling at a resolution high enough to resolve finer-scale processes. The oceanic model could be forced by the high-resolution atmospheric simulations presented in this study, improving in terms of resolution from previous modeling efforts in the region (Renault et al., 2012). The use of a high-resolution coupled ocean–atmosphere model would improve our understanding of the air–sea interactions along our study region. A plan for the development of such model is under way and will be the focus of our next study.

4 Summary

The spatial and temporal variability (annual cycle) of the coastal divergence and Ekman pumping, as well as their relative contribution to the total upwelling in the central-northern Chile was studied using winds obtained from a nested configuration of the WRF model allowing the model to reach 4 km resolution. The simulations showed a cyclonic wind curl (negative) on the coastal-band nearshore and inside the Coquimbo Bay system. This negative wind curl is mainly due to the onshore decay of the wind (wind drop-off), which presented length scales (L_d) between 8 and 45 km with a significant latitudinal variability. The wind drop-off scale is in

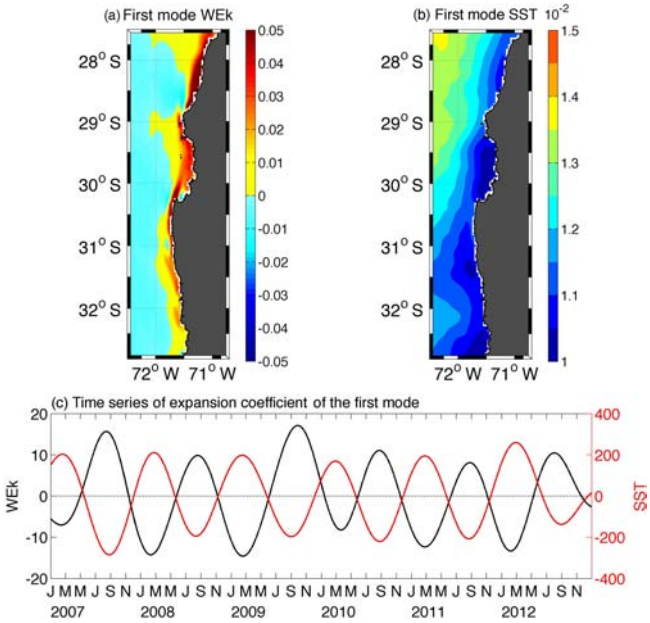

Figure 11. First SVD mode between Ekman pumping (WEk) from the WRF simulation at 4 km resolution and sea surface temperature (SST) from MUR data. **(a)** The Ekman pumping spatial component. **(b)** The SST spatial component. **(c)** The black (red) line represents the associated Ekman pumping (SST) time series. Note that the units are arbitrary.

particular larger within 29.25–30.25° S and to the north of 28.5° S. When we compared the drop-off scale with other upwelling regions, for example the coast of California (Enriquez and Friehe., 1996; Renault et al., 2015), we find that it is smaller in our study region. For instance L_d ranges from 10 and 80 km between 35 and 45° N (Renault et al., 2015). Despite such difference, the wind stress curl that resulted from this zonal wind shear generated Ekman pumping with a marked seasonality and vertical velocities at the surface that reached 4 m d^{-1}, values comparable to those observed in the California Current system.

When comparing the seasonal contribution of coastal divergence and Ekman pumping to the coastal upwelling transport in central-northern Chile, we find that there is a high seasonal coherence between the two mechanisms (> 0.8) with a maximum during spring. However, despite this high seasonal correlation there is a spatial alternation between them; that is, where one is intense the other is weak. This pattern seems to be the result of a close relationship between the topography of the coast, the shape of the coastline and the spatial scale of the wind drop-off. From this information we defined three scenarios that could explain the pattern of upwelling in the area.

Prevalence of positive Ekman pumping is associated with large L_d, observed in regions such as the Coquimbo Bay system and north of 28.5° S. The combination of high terrain and the presence of bays could explain the large L_d values.

There is a prevalence of coastal divergence with smaller values of L_d and more intense winds near the coast. This is observed in sectors characterized by a low topography and the presence of headlands as Punta Lengua de Vaca and Punta Choros.

There is a combination of both mechanisms in which neither divergence nor coastal Ekman pumping dominated over the other. This takes place to the south of 31.5° S.

The three-dimensional aspect of the coastal circulation in the region of interest (Aguirre et al., 2012) prevents a clear identification of the role of each process on SST variability, although our SVD analysis reveals areas where the similarity of the patterns of Ekman pumping and SST suggests a privileged forcing mechanism like within the Coquimbo Bay system and the area north of Loma de Hueso (∼ 28.8° S). Further studies based on the experimentation with a regional oceanic model should be carried out to better identify upwelling regimes by, for instance, using the model winds documented here at different seasons to mimic changes in the drop-off. Considering the rich marine ecosystem hosted by the region (Thiel et al., 2007) our interest is in relating aspects of the meso- to sub-mesoscale circulation (eddies and filaments) to the processes documented in this study. This is planned for future work.

Finally, the model allowed for an estimate of the nearshore (coastal fringe of ∼ 50 km) low-level circulation and evidences fine-scale structure of the wind stress curl that cannot be estimated from satellite observations. Considering the overall realism of the model simulation, our study could be used to guide field experiments and gather in situ measurements in order to gain further knowledge in the processes that constrain such features.

Acknowledgements. This work was financed by Postdoctoral FONDECYT/Chile no. 3130671 and support from Centro de Estudios Avanzados en Zonas Áridas (CEAZA), Coquimbo, Chile. Marcel Ramos, Luis Bravo and Boris Dewitte acknowledge support from FONDECYT (project 1140845) and Chilean Millennium Initiative (NC120030). Boris Dewitte and Marcel Ramos acknowledge support from FONDECYT (project 1151185). CNES (Centre National d'Etudes Spatiales, France) is thanked for financial support through the OSTST project EBUS-South. Katerina Goubanova was supported by IRD. The contribution from two reviewers and the editor is deeply appreciated; their comments and suggestions improved and enhanced this study.

Edited by: J. M. Huthnance
Reviewed by: C. Aguirre and one anonymous referee

References

Aguirre, C., Pizarro, O., Strub, P. T., Garreaud, R., and Barth, J. A.: Seasonal dynamics of the near-surface alongshore flow off central Chile, J. Geophys. Res., 117, C01006, doi:10.1029/2011JC007379, 2012.

Archer, C. L. and Jacobson, M. Z.: The Santa Cruz Eddy. Part II: Mechanisms of Formation, Mon. Weather Rev., 133, 2387–2405, 2005.

Bakun, A.: Coastal upwelling indices, west coast of North America, 1946–1971, US Dep. Commer., NOAA Tech. Rep., NMFS SSRF-671, 103 pp., 1973.

Bakun, A. and Nelson, C.: The seasonal cycle of wind stress curl in subtropical Eastern boundary current regions, J. Phys. Oceanogr., 21, 1815–1834, 1991.

Bane, J. M., Levine, M. D., Samelson, R. M., Haines, S. M., Meaux, M. F., Perlin, N., Kosro, P. M., and Boyd, T.: Atmospheric forcing of the Oregon coastal ocean during the 2001 upwelling Season, J. Geophys. Res., 110, C10S02, doi:10.1029/2004JC002653, 2005.

Beljaars, A. C. M.: The parameterization of surface fluxes in large-scale models under free convection, Q. J. Roy. Meteorol. Soc., 121, 255–270, 1994.

Bretherton, C. S. and Park, S.: A new moist turbulence parameterization in the Community Atmosphere Model, J. Climate, 22, 3422–3448, 2009.

Burk, S. D. and Thompson, W. T.: The summertime low-level jet and marine boundary layer structure along the California coast, Mon. Weather Rev., 124, 668–686, 1996.

Cambon, G., Goubanova, K., Marchesiello, P., Dewitte, B., Illig, S., and Echevin, V.: Assessing the impact of downscaled winds on a regional ocean model simulation of the Humboldt system, Ocean Model., 65, 11–24, 2013.

Capet, X. J., Marchesiello, P., and McWilliams, J. C.: Upwelling response to coastal wind profiles, Geophys. Res. Lett., 31, L13311, doi:10.1029/2004GL020123, 2004.

Chelton, D. B., Schlax, M. G., and Samelson, R. M.: Summertime coupling between sea surface temperature and wind stress in the California Current System, J. Phys. Oceanogr., 37, 495–517, 2007.

Dyer, A. J. and Hicks, B. B.: Flux–gradient relationships in the constant flux layer, Q. J. Roy. Meteorol. Soc., 96, 715–721, 1970

Edwards, K. A., Rogerson, A. M., Winant, C. D., and Rogers, D. P.: Adjustment of the marine atmospheric boundary layer to a coastal cape, J. Atmos. Sci., 58, 1511–1528, 2001.

Enriquez, A. G. and Friehe, C. A.: Effects of Wind Stress and Wind Stress Curl Variability on Coastal Upwelling, J. Phys. Oceanogr., 25, 1651–1671, 1996.

Estrade, P., Marchesiello, P., Colin de Verdiere, A., and Roy, C.: Cross-shelf structure of coastal upwelling: A two-dimensional expansion of Ekman's theory and a mechanism for inner shelf upwelling shut down, J. Mar. Res., 66, 589–616, 2008.

Garreaud, R. and Muñoz, R.: The low-level jet off the subtropical west coast of South America: Structure and variability, Mon. Weather Rev., 133, 2246–2261, 2005.

Garreaud, R., Rutllant, J., Muñoz, R., Rahn, D., Ramos, M., and Figueroa, D.: VOCALS-CUpEx: The Chilean Upwelling Experiment, Atmos. Chem. Phys., 11, 2015–2029, doi:10.5194/acp-11-2015-2011, 2011.

Gill, A. E.: Atmosphere–ocean dynamics, International Geophysics Series, 30, 403 pp., 1982.

Haack, T., Burk, S. D., Dorman, C., and Rogers, D.: Supercritical Flow Interaction within the Cape Blanco–Cape Mendocino Orographic Complex, Mon. Weather Rev., 129, 688–708, 2001.

Halpern, D.: Measurements of near-surface wind stress over an upwelling region near the Oregon coast, J. Phys. Oceanogr., 6, 108–112, 1976.

Halpern, D.: Offshore Ekman transport and Ekman pumping off Peru during the 1997–1998 El Niño, Geophys. Res. Lett., 29, 1075, doi:10.1029/2001GL014097, 2002.

Hayes, S. P., McPhaden, M. J., and Wallace, J. M.: The influence of sea surface temperature on surface wind in the eastern equatorial Pacific: weekly to monthly variability, J. Climate, 2, 1500–1506, 1989.

Hong, S. Y. and Lim, J. O.: The WRF single – moment 6 – class microphysics scheme (WSM6), J. Korean Meteor. Soc., 42, 129–151, 2006.

Hormazabal, S., Shaffer, G., and Leth, O.: Coastal transition zone off Chile, J. Geophys. Res., 109, C01021, doi:10.1029/2003JC001956, 2004.

Horvath, K., Koracin, D., Vellore, R., Jiang, J., and Belu, R.: Sub-kilometer dynamical downscaling of near-surface winds in complex terrain using WRF and MM5 mesoscale models, J. Geophys. Res., 117, D11111, doi:10.1029/2012JD017432, 2012.

Iacono, M. J., Delamere, J. S., Mlawer, E. J., Shephard, M. W., Clough, S. A., and Collins, W. D.: Radiative forcing by long–lived greenhouse gases: Calculations with the AER radiative transfer models, J. Geophys. Res., 113, D13103, doi:10.1029/2008JD009944, 2008

Jacox, M. G. and Edwards, C. A.: Upwelling source depth in the presence of nearshore wind stress curl, J. Geophys. Res., 117, C05008, doi:10.1029/2011JC007856, 2012.

Janjic, Z. I.: Comments on "Development and evaluation of a convection scheme for use in climate models", J. Atmos. Sci., 57, 3686–3686, 2000.

Jin, X., Dong, C., Kurian, J., McWilliams, J. C., Chelton, D. B., and Li, Z.: SST-Wind Interaction in Coastal Upwelling: Oceanic Simulation with Empirical Coupling, J. Phys. Oceanogr. 39, 2957–2970, 2009.

Kalnay, E., Kanamitsu, M., Kistler, R., Collins, W., Deaven, D., Gandin, L., Iredell, L., Saha, S., White, G., Woollen, J., Zhu, Y., Chelliah, D.C. M., Ebisuzaki, W., Higgins, W., Janowiak, J., Mo, K. C., Ropelewski, C., Wang, J., Leetmaa, A., Reynolds, R., Jenne, R., and Joseph, D.: The NCEP/NCAR 40-Year Re- analysis Project, B. Am. Meteor. Soc., 77, 437–471, 1996.

Koračin, D., Dorman, C. E., and Dever, E. P.: Coastal Perturbations of Marine-Layer Winds, Wind Stress, and Wind Stress Curl along California and Baja California in June 1999, J. Phys. Oceanogr., 34, 1152–1173, 2004.

Lo, J. C.-F., Yang, Z.-L., and Pielke, R. A. S.: Assessment of three dynamical climate downscaling methods using the Weather Research and Forecasting (WRF) model, J. Geophys. Res., 113, D09112, doi:10.1029/2007jd009216, 2008.

Marchesiello, P. and Estrade, P.: Upwelling limitation by geostrophic onshore flow, J. Mar. Res., 68, 37–62, 2010.

Marchesiello P., Lefevre, L., Vega, A., Couvelard, X., and Menkes, C.: Coastal upwelling, circulation and heat balance around New Caledonia's barrier reef, Mar. Poll. Bull., 61, 432–448, 2010.

Mellor, G. L.: Numerical simulation and analysis of the mean coastal circulation off California, Cont. Shelf Res., 6, 689–713, 1986.

Moraga-Opazo, J., Valle-Levinson, A., Ramos, M., and Pizarro-Koch, M.: Upwelling-Triggered near-geostrophic recirculation in an equatorward facing embayment, Cont. Shelf Res., 31, 1991–1999, 2011.

Muñoz, R. and Garreaud, R.: Dynamics of the low-level jet off the subtropical west coast of South America, Mon. Weather Rev., 133, 3661–3677, 2005.

Nelson, C. S.: Wind stress and wind-stress curl over the California Current, NOAA Tech. Rep., NMFS SSRF-714, US Dept. of Commerce, 87 pp., 1977.

Paulson, C. A.: The mathematical representation of wind speed and temperature profiles in the unstable atmospheric surface layer, J. Appl. Meteor., 9, 857–861, 1970.

Perlin, N., Skyllingstad, E., Samelson, R., and Barbour, P.: Numerical simulation of air-sea coupling during coastal upwelling, J. Phys. Oceanogr., 37, 2081–2093, 2007.

Perlin, N., Skyllingstad, E. D., and Samelson, R. M.: Coastal atmospheric circulation around an idealized cape during wind-driven upwelling studied from a coupled ocean-atmosphere model, Mon. Weather Rev., 139, 809–829, 2011.

Pickett, M. and Paduan, J. D.: Ekman transport and pumping in the California Current based on the US Navy's high-resolution atmospheric model (COAMPS), J. Geophys. Res., 108, C103327, doi:10.1029/2003JC001902, 2003.

Rahn, D. and Garreaud, R.: A synoptic climatology of the near-surface wind along the west coast of South America, Int. J. Climatol., 34, 3628–3647, doi:10.1002/joc.3724, 2013.

Rahn, D. A., Garreaud, R., and Rutllant, J.: The low-level atmospheric circulation near Tongoy Bay/point Lengua de Vaca (Chilean coast 30° S), Mon. Weather Rev., 139, 3628–3647, 2011.

Renault, L., Dewitte, B., Falvey, M., Garreaud, R., Echevin, V., and Bonjean, F.: Impact of atmospheric coastal jet off central Chile on sea surface temperature from satellite observations (2000–2007), J. Geophys. Res., 114, C08006, doi:10.1029/2008JC005083, 2009.

Renault, L., Dewitte, B., Marchesiello, P., Illig, S., Echevin, V., Cambon, G., Ramos, M., Astudillo, O., Minnis, P., and Ayers, J. K.: Upwelling response to atmospheric coastal jets off central Chile: A modeling study of the October 2000 event, J. Geophys. Res., 117, C02030, doi:10.1029/2011JC007446, 2012.

Renault, L., Hall, H., and McWilliams, J. C.: Orographic shaping of US West Coast wind profiles during the upwelling season, Clim. Dynam., 46, 273–289, doi:10.1007/s00382-015-2583-4, 2015.

Rutllant, J. and Montecino, V.: Multiscale upwelling forcing cycles and biological response off north-central Chile, Rev. Chil. Hist. Nat., 75, 217–231, 2002.

Rutllant, J. A., Muñoz, R. C., and Garreaud, R. D.: Meteorological observations on the northern Chilean coast during VOCALS-REx, Atmos. Chem. Phys., 13, 3409–3422, doi:10.5194/acp-13-3409-2013, 2013.

Shaffer, G., Hormazabal, S., Pizarro, O., Djurfeldt, L., and Salinas, S.: Seasonal and interannual variability of currents and temperature over the slope off central Chile, J. Geophys. Res., 104, 29951–29961, 1999.

Skamarock, W. C. and Klemp, J. B.: A time-split nonhydrostatic atmospheric model for weather research and forecasting applications, J. Comput. Phys., 227, 3465–3485, 2008.

Small, R. J., deSzoeke, S. P., Xie, S. P., O'Neill, L., Seo, H., Song, Q., Cornillon, P., Spall, M., and Minobe, S.: Air-sea interaction

over ocean fronts and eddies, Dynam. Atmos. Oceans, 45, 274–319, 2008.

Smith, R. L.: Upwelling, Oceanogr. Mar. Biol., 6, 11–46, 1968.

Stark, J. D., Donlon, C. J., Martin, M. J., and McCulloch, M. E.: OSTIA: An operational, high resolution, real time, global sea surface temperature analysis system, Oceans 2007 IEEE Aberdeen, conference proceedings, Marine challenges: coastline to deep sea, Aberdeen, Scotland, IEEE, 2007.

Strub, P. T., Montecino, V., Rutllant, J., and Salinas, S.: Coastal ocean circulation off western south America, in: The Sea, The Global Coastal Ocean: Regional Studies and Syntheses, edited by: Robinson, A. R. and Brink, K. H., John Wiley, New York, 11, 273–314, 1998.

Sverdrup, H. U.: Wind-driven currents in a baroclinic ocean, with application to the equatorial currents of the eastern Pacific, P. Natl. Acad. Sci. USA, 33, 318–326, 1947.

Tewari, M., Chen, F., Wang, W., Dudhia, J., LeMone, M. A., Mitchell, K., Gayno, M. Ek, G., Wegiel, J., and Cuenca, R. H.: Implementation and verification of the unified NOAH land surface model in the WRF model. 20th conference on weather analysis and forecasting/16th conference on numerical weather prediction, 11–15, 2004

Thiel, M., Macaya, E., Acuña, E., Arntz, W. E., Bastias, H., Brokordt, K., Camus, P. A., Castilla, J. C., Castro, L. R., Cortés, M., Dumont, C. P., Escribano, R., Fenández, M., Gajardo, J. A., Gaymer, C. F., Gómez, I., González, A. E., González, H., Haye, P. A., Illanes, J. C., Iriarte, J. L., Lancellotti, D. A., Luna-Jorquera, G., Luxoro, C., Manriquez, P. H., Marín, V., Muñoz, P., Navarrete, S. A., Perez, E., Poulin, E., Sellanes, J., Sepúlveda, H. H., Stotz, W., Tala, F., Thomas, A., Vargas, C. A., Vasquez, J. A., and Vega, J. M. A.: the Humboldt Current System of Northern-Central Chile Oceanographic Processes, Ecological Interactions, edited by: Gibson, R. N., Atkinson, R. J. A., and Gordon, J. D. M., Oceanogr. Mar. Biol., 45, 195–344, 2007.

Toniazzo, T., Sun, F., Mechoso, C. R., and Hall, A.: A regional modeling study of the diurnal cycle in the lower troposphere in the south-eastern tropical Pacific, Clim. Dynam., 41, 1899–1922, 2013.

Vazquez-Cuervo, J., Dewitte, B., Chin, T. M., Amstrong, E., Purca, S., and Alburqueque, E.: An analysis of SST gradient off the Peruvian coast; The impact of going to higher resolution, Remote Sens. Environ., 131, 76–84, 2013.

Venegas, S. A, Mysak, L. A., and Straub, D. N.: Atmosphere-Ocean Coupled Variability in the South Atlantic, J. Climate, 10, 2904–2920, 1997.

Wallace, J., Mitchell, T., and Deser, C.: The influence of sea-surface temperature on surface wind in the eastern equatorial Pacific: Seasonal and interannual variability, J. Climate, 2, 1492–1499, 1989.

Webb, E. K.: Profile relationships: The log-linear range, and extension to strong stability, Q. J. Roy. Meteor. Soc., 96, 67–90, 1970.

Winant, C. D., Dorman, C. E., Friehe, C. A., and Beardsley, R. C.: The marine layer off Northern California: an example of supercritical channel flow, J. Atmos. Sci., 45, 3588–3605, 1988.

Wood, R., Mechoso, C. R., Bretherton, C. S., Weller, R. A., Huebert, B., Straneo, F., Albrecht, B. A., Coe, H., Allen, G., Vaughan, G., Daum, P., Fairall, C., Chand, D., Gallardo Klenner, L., Garreaud, R., Grados, C., Covert, D. S., Bates, T. S., Krejci, R., Russell, L. M., de Szoeke, S., Brewer, A., Yuter, S. E., Springston, S. R., Chaigneau, A., Toniazzo, T., Minnis, P., Palikonda, R., Abel, S. J., Brown, W. O. J., Williams, S., Fochesatto, J., Brioude, J., and Bower, K. N.: The VAMOS Ocean-Cloud-Atmosphere-Land Study Regional Experiment (VOCALS-REx): goals, platforms, and field operations, Atmos. Chem. Phys., 11, 627–654, doi:10.5194/acp-11-627-2011, 2011.

Xie, S. P.: Satellite observations of cool ocean-atmosphere interaction, B. Am. Meteorol. Soc., 85, 195–208, 2004.

Zhang, D. L. and Anthes, R. A.: A high–resolution model of the planetary boundary layer – sensitivity tests and comparisons with SESAME – 79 data, J. Appl. Meteor., 21, 1594–1609, 1982.

Chapter 4

Response of the Central Chile Upwelling System to Coastal Wind Drop-Off

4.1 Introduction

This chapter corresponds to the content of the article "Sensitivity of the Near-Shore Oceanic Circulation Off Central Chile to Coastal Wind Profiles Characteristics" published in "Journal of Geophysical Research: Oceans" https://doi.org/10.1029/2018JC014051. In this study, we evaluated the sensitivity of upwelling dynamics to the coastal wind reduction off central Chile using a high-resolution regional oceanic model (ROMS), the experiments are forced with different wind drop-off gradients in the 50-km coastal strip. The mean characteristics of these coastal wind patterns are dynamically estimated using a regional atmospheric model (WRF), in agreement with both satellite measurements and local observations. We show that a wind drop-off in the coastal forcing induces a notorious reduction in the coastal jet intensity, a stronger poleward undercurrent and a coherent offshore Ekman current at the surface, in agreement with the available observations, and allows for reducing the cold bias along the shore. However, a wider(narrow) drop-off implies a higher(lower) reduction in both, the total upwelling mass flux and the surface cold bias. The analysis of the eddy circulation shows a substancial sensitivity in the amplitude of the mean surface EKE, a reduction of the wind stress amplitude shows a diminished mesoscale field near the coast, nevertheless, a sharp drop-off too close to the shore, would increase the mesoscale activity in the coastal transition zone. On the other hand, lateral eddy heat fluxes in the upper thermocline (above 80 m) are equally sensitive to the wind drop-off and exhibit increased coastward heat transport, that mitigates the surpluss in cooling due to horizontal Ekman advection.

JGR Oceans

RESEARCH ARTICLE
10.1029/2018JC014051

Key Points:
- The characteristics of coastal wind profiles simulated by a regional atmospheric model are sensitive to horizontal resolution
- The onshore wind reduction influences the oceanic circulation in the coastal domain and at regional scale off Central Chile
- The onshore wind reduction influences strongly the balance of processes associated to the maintenance of cool SST along the coast

Correspondence to:
O. Astudillo,
orlando.astudillo@ceaza.cl

Citation:
Astudillo, O., Dewitte, B., Mallet, M., Rutllant, J. A., Goubanova, K., Frappart, F., et al (2019). Sensitivity of the near-shore oceanic circulation off Central Chile to coastal wind profiles characteristics. *Journal of Geophysical Research: Oceans*, *124*. https://doi.org/10.1029/2018JC014051

Received 5 APR 2018
Accepted 7 JUN 2019
Accepted article online 17 JUN 2019

©2019. American Geophysical Union. All Rights Reserved.

Sensitivity of the Near-Shore Oceanic Circulation Off Central Chile to Coastal Wind Profiles Characteristics

O. Astudillo[1,2], B. Dewitte[1,2,3,4], M. Mallet[5], J. A. Rutllant[1,6], K. Goubanova[1], F. Frappart[2], M. Ramos[1,3,4,7], and L. Bravo[3,4]

[1]Centro de Estudios Avanzados en Zonas Áridas (CEAZA), La Serena, Chile, [2]Laboratoire d'Etudes en Géophysique et Océanographie Spatiales (LEGOS), Toulouse, France, [3]Departamento de Biología Marina, Facultad de Ciencias del Mar, Universidad Católica del Norte, Coquimbo, Chile, [4]Millennium Nucleus for Ecology and Sustainable Management of Oceanic Islands (ESMOI), Coquimbo, Chile, [5]CNRM UMR 3589, Météo-France/CNRS, Toulouse, France, [6]Departamento de Geofísica, Facultad de Ciencias Físicas y Matemáticas, Universidad de Chile, Santiago, Chile, [7]Centro de Innovación Acuícola Aquapacífico, Universidad Católica del Norte, Coquimbo, Chile

Abstract In Eastern Boundary Upwelling Systems (EBUS), the upwelling favorable wind speeds decrease toward the coast in the so-called wind drop-off coastal strip, which has been shown to be influential on the coastal upwelling dynamics, particularly in terms of the relative contributions of Ekman drift and Ekman suction to coastal upwelling. Currently, the wind drop-off length scale is not properly resolved by the atmospheric forcing of regional ocean models in EBUS, featuring a smoother cross-shore wind profile that results in stronger near-shore speeds that could partly explain the coastal cold bias often found in those model simulations. Here, as a case study for the upwelling system off Central Chile, the sensitivity of upwelling dynamics to the coastal wind reduction is investigated using a Regional Ocean Modeling System (ROMS). Coastal wind profiles at different resolutions are first generated using a regional atmospheric model, validated from altimeter data, and then used to correct the coarse atmospheric wind forcing used for sensitivity experiments with ROMS. It is shown that the wind drop-off correction induces a reduction in the oceanic coastal jet intensity, a stronger poleward undercurrent and a coherent offshore Ekman drift. It also yields a significant reduction of the cold bias along the coast compared to the simulation with "uncorrected" winds. Such reduction cannot be solely explained by the reduced Ekman transport only partially compensated by increase in Ekman suction. The analysis of the surface heat budget reveals in fact that an important contributor to the cooling reduction along the coast in the presence of coastal wind drop-off is the heat flux term mediated by the reduction in the mixed-layer depth. Overall, our results illustrate the nonlinear response of the upwelling dynamics to the coastal wind profiles in this region.

1. Introduction

The Humboldt Current System (hereafter HCS) along the coasts of Chile and Peru hosts one of the most productive marine ecosystems of the planet owing primarily to the persistent alongshore winds that drive coastal upwelling conditions through Ekman suction and transport. Strong nearshore equatorward winds favor Ekman divergence at the coast (Halpern, 2002; Rutllant et al., 2004), while the weakening of these alongshore winds toward the shore, known as "wind drop-off" (Capet et al., 2004; Dorman et al., 2006; Perlin et al., 2007; Renault et al., 2012), and the associated cyclonic wind stress curl, favors upward suction of colder waters. While most observational studies of Eastern Boundary Upwelling Systems (hereafter EBUS) have focused on the role of Ekman transport in many aspects of the circulation and ecosystem variability (Carr & Kearns, 2003; Chavez & Messié, 2009; Demarcq, 2009; Wang et al., 2015; among many others), the investigation of the role of Ekman suction on coastal upwelling dynamics has been somehow disregarded owing to limitations in the atmospheric data sets. Not only satellite winds cannot be observed in the coastal fringe (so-called blind zone of ~50-km width) but also atmospheric reanalyses tend to be significantly biased, which in particular consist in an overestimation of nearshore winds (e.g., Astudillo et al., 2017). It is also confusingly assumed in the literature that maximum upward velocity (upwelling) is confined to the coast in a coastal fringe of the size of the local internal Rossby radius of deformation (Croquette et al., 2007; Pickett & Paduan, 2003; Smith, 1995), whereas in fact the cross-shore width of upwelling scales with D/S, the ratio of the Ekman depth layer (D) to the bottom topographic slope (S) (Estrade et al., 2008; see also Capet et al., 2008 for sensitivity experiments to shelf resolution in a regional

model off California). Off Central Chile, characterized by a steep and narrow shelf, this scale cannot be larger than 5 km (Marchesiello & Estrade, 2010), whereas the internal Rossby radius of deformation is around 30 km (Renault et al., 2012). Therefore, mesoscale features in the nearshore winds may be more effective in driving Ekman suction than if only geostrophic adjustment of the upwelling front is assumed.

Since the pioneer modeling studies by Marchesiello et al. (2003) and Capet et al. (2004) that showed that a realistic wind drop-off is influential on the alongshore current dynamics and cross-shore eddy heat fluxes off central California, there has been more concern in the modeling community on the most appropriate wind forcing for regional EBUS modeling studies. While scatterometer winds from QuickSCAT have permitted to produce realistic seasonal oceanic simulations in most EBUS (Aguirre et al., 2012, 2014; Di Lorenzo, 2003; Penven et al., 2001; Penven et al., 2005), a surface cold bias near the coast is usually diagnosed in these simulations (Illig et al., 2014; Penven et al., 2001; Penven et al., 2005; Veitch et al., 2010; O. A. Vergara et al., 2016). As a consequence of this cold bias in regional model simulations of the southern HCS, the equatorward Chile Coastal Current (CCC) is too energetic overlapping and deepening the poleward Peru-Chile Undercurrent (PCU; Aguirre et al., 2012, 2014; Penven et al., 2005; O. Vergara et al., 2017). This results in an enhanced equatorward pressure gradient that forces a shoreward geostrophic current displacing offshore the surface Ekman current. Desbiolles et al. (2016) showed that, for the Benguela upwelling system, this cold bias is associated with an overestimated coastal wind that resulted from an earlier release of the gridded QuickSCAT winds at 0.5° resolution. An updated wind product at 0.25° resolution, using a different quality control has allowed a reduction of the blind zone off the coast to ~12.5 km (Stiles, 2014), reducing therefore the mean cold bias. While part of this bias could be also attributed to a correction of the warm bias in the satellite-based sea surface temperature (SST) data sets (Dufois et al., 2012), current wind products have in any case inherent limitations for accounting for a realistic wind drop-off (Astudillo et al., 2017), which has hampered downstreamed applications, in particular those directed toward marine resources management. This is particularly critical for the coast of Central Chile, which is embedded in an intense oxygen minimum zone that can produce coastal hypoxia depending on environmental conditions (Escribano & Schneider, 2007).

Recently, Astudillo et al. (2017) showed that the wind drop-off takes place all along the coast of the HCS, though with a significant alongshore variability. These mesoscale wind anomalies could respond to physical processes linked to coastal geometry and orography (Pickett & Paduan, 2003; Renault et al., 2015), SST-wind interactions (Boé et al., 2011; Rahn et al., 2011), and sharp changes in surface drag at the sea-land interface (Edwards et al., 2001). As yet few ocean modeling studies have been conducted for the HCS with a high enough horizontal resolution to resolve the mesoscale (i.e., $dx < 10$ km). In addition they have not used a wind forcing (except for case studies) that adequately represents the nearshore wind pattern. Therefore, there is a real need to improve our knowledge of the mesoscale characteristics of the upwelling dynamics and thermodynamics in the HCS and understand how they are linked to the cross-shore wind pattern in order to enhance the ability of regional models to reproduce realistically the observed variability near the coast and thus increase their predictive capability.

Here, we address the issue of the impact of the wind drop-off on the coastal upwelling dynamics for the Central Chile region based on the experimentation with an oceanic regional model. Our focus is on assessing the extent to which the consideration of a wind drop-off in the atmospheric forcing of the regional oceanic model can help in reducing the cold bias usually observed in simulations of the Southern Hemisphere EBUS using scatterometer winds.

The paper is organized as follows: The methodology, experiments' design, and data sets are described in section 2. In section 3, we evaluate the sensitivity of the oceanic circulation off Central Chile to the characteristics of the wind drop-off based on ROMS simulations. Concluding remarks and a discussion are presented in section 4.

2. Data, Model Configurations, and Methodology

2.1. Data

2.1.1. Gridded and Along-Track Satellite Winds

To validate atmospheric model 10-m winds over the HCS, scatterometer Sea Winds aboard the QuikSCAT satellite and the Advanced SCATterometer (ASCAT) aboard Metop-A and Metop-B satellites are used.

Table 1
Description of In Situ Data Sets for Validation

AWS/ADCP	Lat (°S)	Lon(°W)	Elevation (m a.s.l.)	Sensor height (m)	Recording interval (min)	Coast distance (km)	Operation period
Punta de Lobos (CEAZA)	28.29	71.17	22	2.5	10	0.35	2008-7-3 to 2010-2-4
Loma de hueso (CNE)	28.91	71.45	187	10	10	6.5	2006-9-28 to 2009-7-22
Lengua de Vaca (CNE)	30.24	71.62	53	10	10	0.7	2006-9-28 to 2009-7-22
Lengua de Vaca (DGF-CEAZA)	30.25	71.63	10	3.75	30	0.65	1990-3-1 to Present
COSMOS (COPAS)	30.3	71.78	−950	−10 to −110 (each 5 m)	60	13	2003-4-1 to 2006-9-30

Note. The data were provided by the following institutions: Department of Geophysics, Universidad de Chile (DGF), Centro de Estudios Avanzados en Zonas Áridas (CEAZA), National Energy Commission of the Chilean Government (CNE), and Center for Oceanographic Research in the eastern South Pacific (COPAS). Dates are formatted as year-month-day. AWS = Automatic Weather Stations; ADCP = Acoustic Doppler Current Profiler.

The data set consists in the new Level-3 gridded products, containing wind vector fields corresponding to the daily average of both Level-2 swath passes interpolated onto a regular grid of 0.25° in longitude and latitude using an objective method (Bentamy & Fillon, 2012).

However, scatterometer measurements (QuikSCAT and ASCAT) contain a 28- to 50-km-wide blind zone along the coast, limiting the description of the mesoscale atmospheric circulation within this narrow coastal fringe. To overcome this limitation, regional models need to be validated with in situ wind data or high-resolution satellite winds that could be obtained from altimetric measurements (Astudillo et al., 2017). Here we use wind speeds derived from Radar Altimeters at the Ku-band (13.575 GHz) onboard ENVISAT and Jason-1. The surface wind speeds are retrieved using the backscattering coefficient. The accuracy of scatterometer- and altimetry-derived wind products has been determined in several studies using moored buoys and intercomparison, in which the Root Mean Square (RMS) differences did not exceed 2 m/s and 20° for wind speed and direction, respectively, at global and regional scales (Astudillo et al., 2017; Bentamy et al., 2008; Bentamy & Fillon, 2012; Verhoef & Stoffelen, 2013; Vogelzang et al., 2011).

2.1.2. Satellite SST

In this study, we use two satellite-derived SST products: (1) The Operational Sea Surface Temperature and Sea Ice Analysis (OSTIA) is a 5-km gridded global SST product. Data are available from April of 2006 as daily 5-km gridded global SST. More information may be found in Donlon et al. (2012) along with a data description at: http://podaac.jpl.nasa.gov/dataset/UKMO-L4HRfnd-GLOB-OSTIA. (2) The Multi-scale Ultra-high Resolution (MUR) SST analysis is globally gridded at 1-km resolution by merging data from MODIS, AMSR-E, and AVHRR, covering 2002–present. An objective interpolation technique based on a wavelet decomposition (Chin et al., 1998) is used to process each retrieval data set with respect to its inherent resolution. More information and data description can be found at http://podaac.jpl.nasa.gov/dataset/JPL-L4UHfnd-GLOB-MUR and http://mur.jpl.nasa.gov/. The OSTIA product is used to provide the daily SST lower boundary conditions to the regional atmospheric model, whereas the MUR product is used to validate the regional oceanic model SST.

2.1.3. Geostrophic Currents

The altimeter-derived surface geostrophic currents have been used for model evaluation of the surface eddy circulation. These currents were estimated from sea level anomalies for the Globcurrent project (http://globcurrent.ifremer.fr; Rio et al., 2014) and provided by AVISO (Archiving, Validation and Interpretation of Satellite Oceanographic data) with support from the French Space Agency (Centre National d'Etudes Spatiales,). This data set contains absolute geostrophic velocities at 0.25° obtained from merged multisatellite observations (Topex/Poseidon; ERS-2; Jason-1; Envisat) over the Global Ocean.

2.1.4. In Situ Data: Meteo-Oceanographic Buoys

We have considered in situ data to validate the simulated surface winds and the vertical profile of currents near the coast. Table 1 lists the positions, start-end times, and belonging institutions of the four Automatic Weather Stations (AWS) and the mooring COSMOS instrumented with a 300-kHz Acoustic Doppler Current Profiler (ADCP).

2.2. Model Configurations and Methods

Here, we address the wind drop-off issue for the Central Chile region based on the experimentation with both an atmospheric and an oceanic regional model (see domains in Figure 1). The atmospheric model is

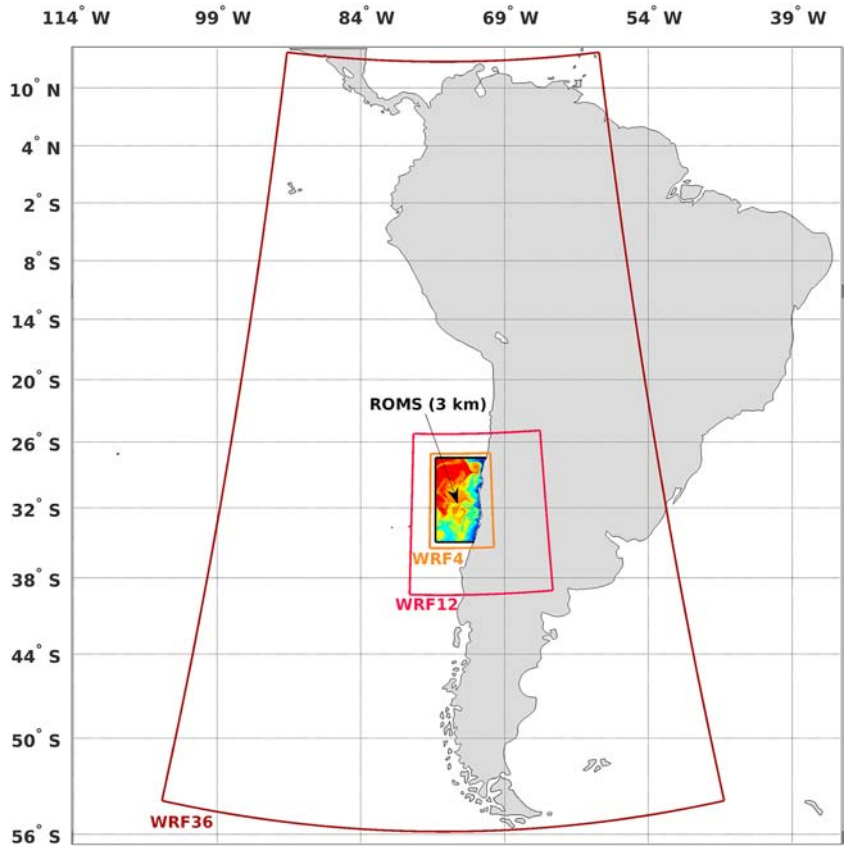

Figure 1. Models domains. The sea surface temperature field represents the Regional Ocean Modeling System (ROMS) inner domain (3 km). The maroon, red, and orange lines delimit the three Weather Research and Forecasting (WRF) domains at 36, 12, and 4 km, respectively.

used to generate atmospheric fields at different resolutions, providing, in particular, coastal wind profiles that are further used to modify the scatterometer-derived winds in the "blind zone" of the satellite. This allows conducting sensitivity experiments with the regional oceanic model in order to isolate the oceanic responses to different wind patterns in the 50-km coastal strip and diagnosing their relationship with the characteristics of the SST bias.

2.2.1. Regional Atmospheric Model Simulations

The Weather Research and Forecasting (WRF) atmospheric model using the Advanced Research WRF solver (Skamarock & Klemp, 2008) has been applied in its 3.5 version. It consists in a fully compressible non-hydrostatic dynamical core with a runtime hydrostatic option on a C-grid with terrain-following mass vertical coordinate. A full suite of parameterization and physics schemes is included in WRF, enabling its use in a broad number of applications allowing for a good resolution of the horizontal scales of the atmospheric mesoscale features involved in Ekman-driven upwelling systems (Boé et al., 2011; Bravo et al., 2016; Oerder et al., 2016; Renault et al., 2012, 2015).

The model was implemented in a multidomain configuration focused on the Central Chile coastal region (26–36°S) including three nests with increasing horizontal grid spacing over the region of interest, corresponding to resolutions of 36, 12, and 4 km, hereafter referred to as WRF36, WRF12, and WRF4, respectively (see Figure 1). The number of vertical sigma levels is 51, with a top at 50 hPa, and stretched resolution toward the surface (~30 m for the surface level). The initial and lateral boundary conditions were derived from the National Centers for Environmental Prediction (NCEP) Final Analysis Data (Kalnay et al., 1996; available online at http://dss.ucar.edu/datasets/ds083. 2/) at 1° × 1° global grid resolution every 6 hr. The SST lower boundary conditions data are based on the daily OSTIA at 0.05° × 0.05° global grid resolution (Stark et al., 2007). The model was run over the period 2007–2009. Model outputs were stored at hourly intervals for each domain resolution. The reader is referred to Bravo et al. (2016) for a detailed description of the

physics parameterizations, whose choice is based on sensitivity tests. The set of parameterizations used in the present study yields the most realistic low-level circulation in the Central Chile region.

As an additional material for assessing the realism of the simulations, we provide in Appendix A the Figures A1 and A2 and the Tables A1 and A2 that compare mean 10-m wind fields and cross-shore 10-m wind speed profiles of the model with estimates from scatterometry, altimetry (Astudillo et al., 2017), and in situ measurements, respectively.

2.2.2. Regional Oceanic Model Simulations

The oceanic simulations were performed with the Regional Ocean Modeling System (ROMS; Shchepetkin & McWilliams, 2005, 2009). ROMS solves the hydrostatic, free-surface primitive equations in 3-D curvilinear coordinates and a stretched terrain-following sigma coordinates, based on the Boussinesq approximation and hydrostatic vertical momentum balance. It has a split-explicit time stepping for the barotropic/baroclinic mode coupling, where short time steps are used to advance the surface elevation and barotropic momentum equations and where a much larger time step is used for temperature, salinity, and baroclinic momentum (Penven et al., 2005). Subgrid-scale vertical mixing is parameterized using the K-Profile Parameterization (KPP) boundary layer scheme (Large et al., 1994). It has been successfully used in previous studies of EBUS (Di Di Lorenzo, 2003; Marchesiello et al., 2003; Capet et al., 2004, 2008; Gruber et al., 2006; Mason et al., 2011; Montes et al., 2010, among many others).

In this study we have implemented a configuration with a domain covering the Central Chile coasts (27–35°S) (Figure 1) at a 3-km (1/36°) horizontal resolution. The domain is slightly smaller than the WRF innermost nest and has 37 vertical σ levels. The bottom topography is derived from the GEBCO 30 arcsec grid data set, interpolated to the model grid and smoothed as in Penven et al. (2005), in order to minimize the pressure gradient errors.

The initial and Open Boundary conditions (OBC) were obtained from a ROMS simulation, which will be referred to hereafter as R-SEP, at ~9-km (1/12°) horizontal resolution used in previous studies of the HCS (Dewitte et al., 2012; O. Vergara et al., 2017). The latter uses the Simple Ocean Data Assimilation Analysis (SODA; Carton & Giese, 2008) as OBCs, and the wind forcing was obtained from the downscaled product NCEP-DS of Goubanova et al. (2011). Atmospheric fluxes (momentum, heat, and freshwater) were derived from the bulk formulas (Fairall et al., 2003) using surface air temperature, precipitation, relative humidity as well as shortwave and longwave radiation fields from COADS 1° monthly climatology (da Silva et al., 1994). This model was run over a domain covering a significant portion of the South-East Pacific (SEP) between 12°N and 40°S so that the dynamics of the PCU is accounted for from its origin near the equator. The reader is invited to refer to Dewitte et al. (2012) and O. Vergara et al. (2017) for assessing the realism of the R-SEP simulation.

The R-SEP 3-day mean outputs are used as OBCs of the model configuration at 1/36°, so that our experimental design consists in a one-way nested domains off-line experiment that takes advantage of the "ROMS2ROMS" downscaling package described in Mason et al. (2010).

The diagnostic simulation (named hereafter CR0) was run over the child domain and uses the same atmospheric forcing as the parent domain bilinearly interpolated on the model grid where data are available (open ocean) and extrapolated in the coastal domain where data are not available. River runoffs were not incorporated for simplicity and because they are thought to have a weak influence on the processes of interest in our regional domain. The model for CR0 was run for the period 2000–2008 with a previous 2-year spin-up repeating the year 2000. CR0 is mostly used here for validation purpose and to assess the realism of the child domain configuration. The reader is invited to refer to Appendix A for assessing the realism of this model configuration.

A series of oceanic model experiments (hereafter named DO36, DO12, and DO4) is then carried out that consist in modifying the characteristics of the nearshore wind forcing (NCEP-DS) so as to mimic the 10-m wind drop-off as simulated by the WRF36, WRF12, and WRF4, respectively. The method for modifying the coastal wind profiles from the WRF outputs is detailed in Appendix B. These experiments consist in simulations over 8 years after a 2-year spin-up during which 3-day averages of the tracer equation terms, as well as model state variables were stored. The simulations consider as forcing the boundary conditions of the year 2008 that is repeated every year. This strategy is chosen so as to ease the interpretation of the results of the sensitivity experiments considering that interannual variability in the region can influence several aspects of the

Table 2
Description of Experiments With the Oceanic Regional Mesoscale Model

Name of the experiment	Period of integration	Lateral boundary conditions (OBC)	Wind forcing	Purpose
CR0	2000–2008 + 2-year spin-up, 3-day average outputs	ROMS R-SEP: 3 days and 9 km of temporal and spatial resolution, over the 2000–2008 period	NCEP-DS: daily forcing and 55 km of spatial resolution,	Validation of the high-resolution model configuration
CR	8 years + 2-year spin-up, 3-day average outputs	ROMS R-SEP: 3-day and 9 km of temporal and spatial resolution, The 2008 OBCs are repeated periodically over 8 years.	NCEP-DS: daily forcing and 55 km of spatial resolution, additionally the 2008 wind forcing is repeated periodically over the 8 years.	Control experiment for assessing the sensitivity's experiments to the cross-shore wind drop-off patterns on upwelling dynamics
DO36	Same as CR	Same as CR	Same as CR. The coastal wind amplitude is modified to mimic the wind drop-off percent as simulated by the 36-km WRF model.	Sensitivity experiment to evaluate the response of the upwelling to a "wide" coastal drop-off.
DO12	Same as CR	Same as CR	Same as CR. The coastal wind amplitude is modified to mimic the wind drop-off percent as simulated by the 12-km WRF model.	Sensitivity experiment to evaluate the response of the upwelling to a "medium" coastal drop-off.
DO4	Same as CR	Same as CR,	Same as CR. The coastal wind amplitude is modified to mimic the wind drop-off percent as simulated by the 4-km WRF model.	Sensitivity experiment to evaluate the response of the upwelling to a "sharp" coastal drop-off.

Note. ROMS = Regional Ocean Modeling System; NCEP = National Centers for Environmental Prediction.

circulation. Additionally, the year 2008 was chosen because its conditions are close to the climatological state in the region of interest (not shown).

As a benchmark for assessing the impact of a wind drop-off in the atmospheric forcing, a control run simulation CR without wind correction is conducted. CR differs from CR0 only in the fact that the year 2008 is repeated in CR while CR0 uses the boundary conditions over the period 2000–008. The different configurations of the oceanic model experiments are summarized in Table 2.

2.3. Methodology

2.3.1. Mixed-Layer Heat Budget

In order to interpret the impact of the change in wind profile on SST along the coast, we compute a mixed-layer heat budget to get insight in potentially important nonlinear processes (i.e., nonlinear advection and mixing) and their sensitivity to wind forcing. This analysis considers the rate of change of the mixed-layer temperature driven by the advection (X-ADV, Y-ADV, Z-ADV), the vertical mixing (vertical diffusion flux V-MIX), and the heat flux (FORC) terms following the equation:

$$\partial_t\langle T\rangle = \underbrace{-\left\langle u\frac{\partial T}{\partial x}\right\rangle}_{X-\mathrm{ADV}}\underbrace{-\left\langle v\frac{\partial T}{\partial y}\right\rangle}_{Y-ADV}\underbrace{-\left\langle w\frac{\partial T}{\partial z}\right\rangle}_{Z-ADV} + \underbrace{\left\langle\frac{\partial}{\partial z}\left(K_v\frac{\partial T}{\partial z}\right)\right\rangle}_{V-MIX} + \underbrace{\frac{Q^*}{\rho_w Ch} + \left\langle\frac{Q_s\frac{\partial f(z)}{\partial z}}{\rho_w C}\right\rangle}_{FORC} \tag{1}$$

where T is the model potential temperature within the mixing layer; (u,v,w) are the components of ocean currents; K_v and h are the vertical diffusion coefficient and the mixed-layer depth (MLD) estimated by ROMS KPP scheme; Q_s is the net surface solar heat flux and $f(z)$ is the fraction of the solar radiation that reaches depth z (Paulson & Simpson, 1977), Q^* contains the sum of the other surface heat flux terms, that is, long wave radiation, latent, and sensible heat fluxes. The constants ρ_w and C are the density and the specific heat capacity of seawater respectively. Brackets denote the vertical average over the mixed layer depth: $x = \frac{1}{h}\int_{-h}^{0} x\,\mathrm{d}z$. The contributions of the different terms (i.e., FORC, X-ADV, Y-ADV, Z-ADV, and V-MIX) were computed online to ensure a perfect closure of the budget. However, while the tendency terms were calculated online, the vertical averaging and the breakdown of the heat flux forcing term (FORC) were carried out off-line. Note that the temperature tendency term associated with the short wave flux is estimated

here as the difference between FORC and the contributions of the other flux terms. In this way we take into account the effect of the solar penetration within the pycnocline waters.

2.3.2. SST Changes Induced by Ekman Processes

Ekman transport (horizontal advection) and Ekman suction (vertical upward advection) are processes that tend to cool the SST near the coast, which is balanced by the surface heat flux forcing and mixing for the long-term mean and at seasonal time scales. The rate of SST change due to Ekman upwelling writes as follows (notation similar to Hong et al., 2013):

$$\left.\frac{\partial T}{\partial t}\right|_{\mathrm{upw}} = -W_e \frac{\partial T}{\partial z} \tag{2}$$

where T is the temperature, t is time, z is the vertical coordinate, and W_e is the Ekman vertical velocity (units m/s). The vertical gradient of temperature $\frac{\partial T}{\partial z}$ in equation (2) is estimated from the difference of the temperature at the surface and at the base of the mixed layer. The latter value is obtained by linear vertical interpolation to the mixed layer depth (h), estimated by the model from the planetary boundary layer KPP scheme (Large et al., 1994).

The vertical velocity, W_e, at the base of the Ekman layer is due to horizontal divergence or convergence of the Ekman transport (Smith, 1968; Bakun, 1973; Gill, 1982; Halpern, 2002):

$$W_e = \frac{\partial u_e}{\partial x} + \frac{\partial v_e}{\partial y} \tag{3}$$

where u_e and v_e are the zonal and meridional components of the Ekman volume transport (units m^3/s per meter of coast) and defined by Gill (1982) and Pickett and Paduan (2003) as

$$(u_e, v_e) = \frac{1}{\rho_w f} \boldsymbol{\tau} \times \boldsymbol{k} \tag{4}$$

where $\boldsymbol{\tau}$ is the surface wind stress vector computed using the bulk formulations (Fairall et al., 2003), fed with the daily averages of the atmospheric forcing, ρ_w is the density of seawater (assumed constant at 1,024 kg/m^3); f is the Coriolis parameter; and $\boldsymbol{k}$ is the unit vertical vector. Substituting the components of the Ekman transport (4) into equation (3) and computing the Ekman pumping/suction velocity W_e writes as follows:

$$W_e = \frac{\nabla \times \tau}{\rho_w f} + \frac{\beta \tau_x}{\rho_w f^2} \tag{5}$$

where $\nabla \times \tau$ is the wind stress curl calculated using centered derivatives, τ_x is the cross-shore wind stress component, and β is the latitudinal gradient of f along the coast off Central Chile. The second term in (5) is at least 2 orders of magnitude smaller than the first term, so it will be considered negligible.

The horizontal advective heat flux due to the Ekman transport at the surface was computed off-line as follows:

$$Q_{\mathrm{ek}} = \frac{C}{f}\left[-\tau_y \frac{\partial T}{\partial x} + \tau_x \frac{\partial T}{\partial y}\right] \tag{6}$$

where $C = 4{,}185\ \mathrm{J \cdot kg^{-1} \cdot {}^\circ C^{-1}}$ is the specific heat capacity of seawater, τ_x and τ_y are the zonal and meridional wind stress, and $\partial T/\partial x$ and $\partial T/\partial y$ are the zonal and meridional SST gradients. The Ekman horizontal velocity is the vertically averaged velocity within the Ekman layer (Yang, 2006):

$$u_{\mathrm{ek}} = \frac{u_e}{h} \tag{7a}$$

$$v_{\mathrm{ek}} = \frac{v_e}{h} \tag{7b}$$

h is the Oceanic Boundary Layer depth, or mixing layer depth, estimated by ROMS (Colas et al., 2012).

The temperature change due to the horizontal advection writes as follows:

$$\left.\frac{\partial T}{\partial t}\right|_{\mathrm{adv}} = -u_{\mathrm{ek}}\frac{\partial T}{\partial x} - v_{\mathrm{ek}}\frac{\partial T}{\partial y} \tag{8}$$

2.3.3. Eddy Kinetic Energy and Eddy Heat flux

In order to assess the effect of the representation of the wind drop-off on some aspects of the eddy field, we first estimate the mean surface Eddy Kinetic Energy (EKE) as

$$EKE = \frac{1}{2}\left(u'^2 + v'^2\right) \tag{9}$$

where u' and v' are the zonal and meridional geostrophic current anomalies, calculated here as the departure from the seasonal mean (i.e., interannual anomalies).

Changes in mean circulation along the coast associated with the wind drop-off have also the potential to change the offshore transport of water mass properties, in particular, its heat content. We will therefore estimate the mean eddy heat flux in the various oceanic simulations, which consists in calculating the covariance between the anomalies in the velocity field and temperature anomalies (Send, 1989). The eddy heat flux vector EH', is defined as

$$EH' = \left(\langle u'.T'\rangle, \langle v'.T'\rangle, \langle w'.T'\rangle\right) \tag{10}$$

where u',v',w', and T' are the zonal, meridional and vertical velocities and temperature anomalies, respectively.

3. Oceanic Model Response

3.1. Impact of the Wind Forcing on Ekman Transport and Ekman Suction

Here, we analyze the linear oceanic response to the various wind profiles. The mean wind stress of the different oceanic simulations is shown in Figure 2. Wind stress is calculated using the COARE algorithm (Fairall et al., 2003). Remember that over the offshore region the wind used to calculate the wind stress is the same in all experiments, whereas within the drop-off length scale the correction described in Appendix B is brought to the NCEP-DS winds to obtain the wind forcing for the drop-off sensitivity experiments. The differences in wind stress along the coast are notorious between experiments ranging from a uniform, wide, medium, and sharp cross-shore wind stress gradient in CR, DO36, DO12, and DO4, respectively (Figures 2a–2d). On average along the coast at the grid point nearest to the coast, the wind stress and wind stress curl (within the 50-km coastal band) reaches 0.0559, 0.0177, 0.0179, and 0.0151 (N/m^2) and -1.4, −6.21, −8.7, and −14.39 (10^{-7} N/m^3) for CR, DO36, DO12, and DO4, respectively. Note that the imposed drop-off does not change the wind stress direction.

From just the wind stress, we can infer the impact on the coastal upwelling dynamics (in the linear sense) through the estimate of Ekman transport and suction. In order to compare both upwelling processes, we had to convert Ekman suction into vertical transport by integrating the vertical velocities (equation (5)) over some offshore distance from the coast, which here corresponds to the maximum value of L_d (50 km) computed along the coast (see Appendix B). In the case of Ekman transport (equation (4)), τ is the wind stress vector at the grid point nearest to the coast. The resulting upwelling estimates, for the different wind drop-off shapes, are displayed in Figures 2e–2g. As expected all the drop-off experiments lead to a reduced (increased) upwelling by Ekman transport (Ekman suction) in relation to the control simulation (see Figures 2e and 2f). However, the increase in upwelling due to Ekman suction does not compensate for the reduction of upwelling due to Ekman transport. Interestingly all the sensitivity experiments exhibits the same upwelling deficit of ~27% as evidenced by Figure 2g that shows the total upwelling by adding the upwelling contribution of Ekman transport and suction for all the experiments.

3.2. SST

While the above analysis indicates substantial impact of the characteristics of the wind drop-off onto the linear Ekman dynamics, we also expect a sensitivity of the mixer-layer thermodynamics (i.e., SST). In this

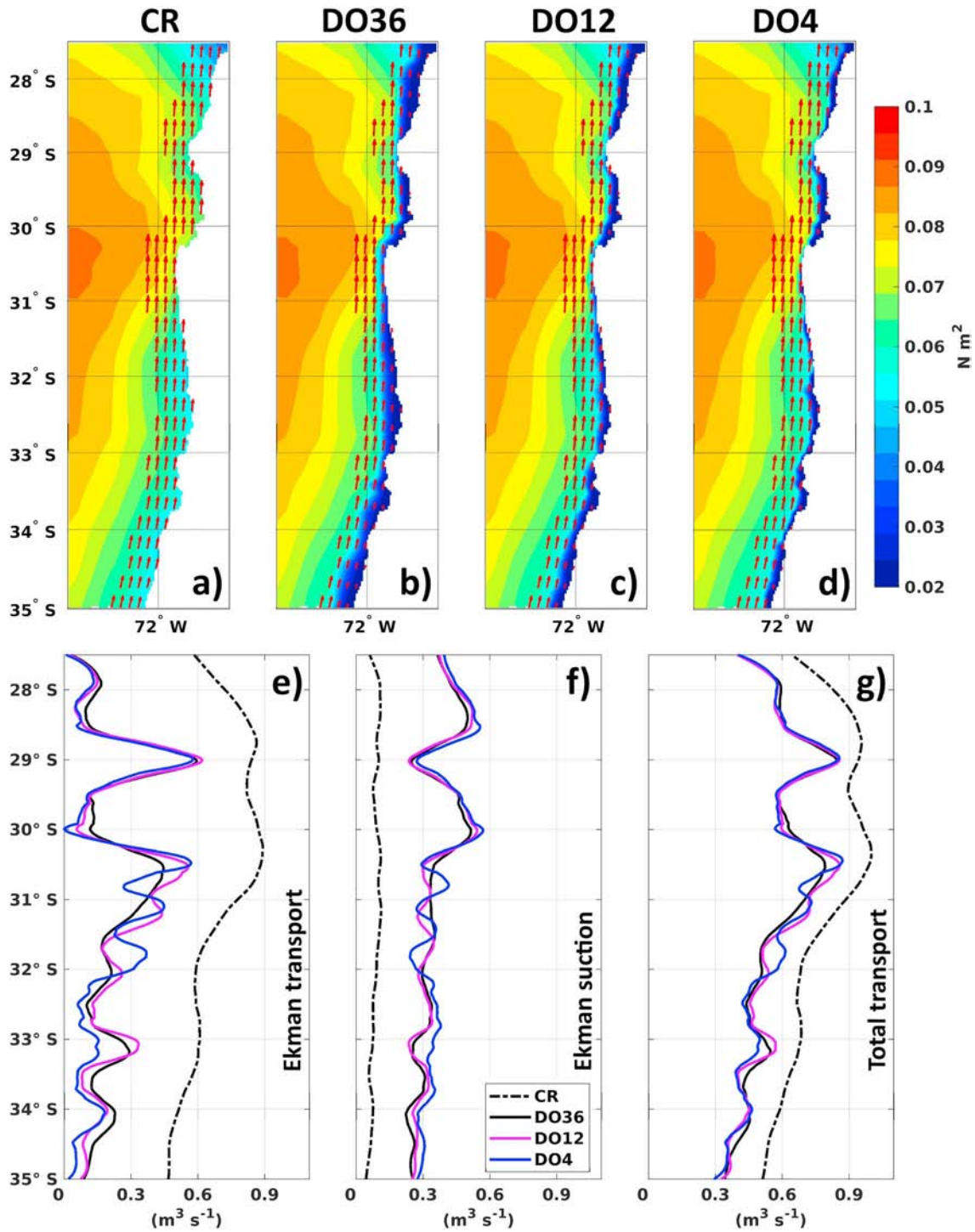

Figure 2. Mean wind stress (N/m^2) field for the various ROMS simulations: (a) CR, (b) DO36, (c) DO12, and (d) DO4. Mean wind stress vectors are displayed for the 50-km coastal band. Note the differences between simulations for the cross-shore wind vectors. Mean upwelling estimates over the simulated period (in m^3/s) as function of latitude for the various ROMS simulations. (e) Horizontal Ekman transport estimated using the wind stress at the grid cell nearest to the coast, (f) vertical transport estimated integrating Ekman suction due to wind stress curl within the 50-km coastal strip, and (g) total upwelling (Ekman transport + Ekman suction). ROMS = Regional Ocean Modeling System.

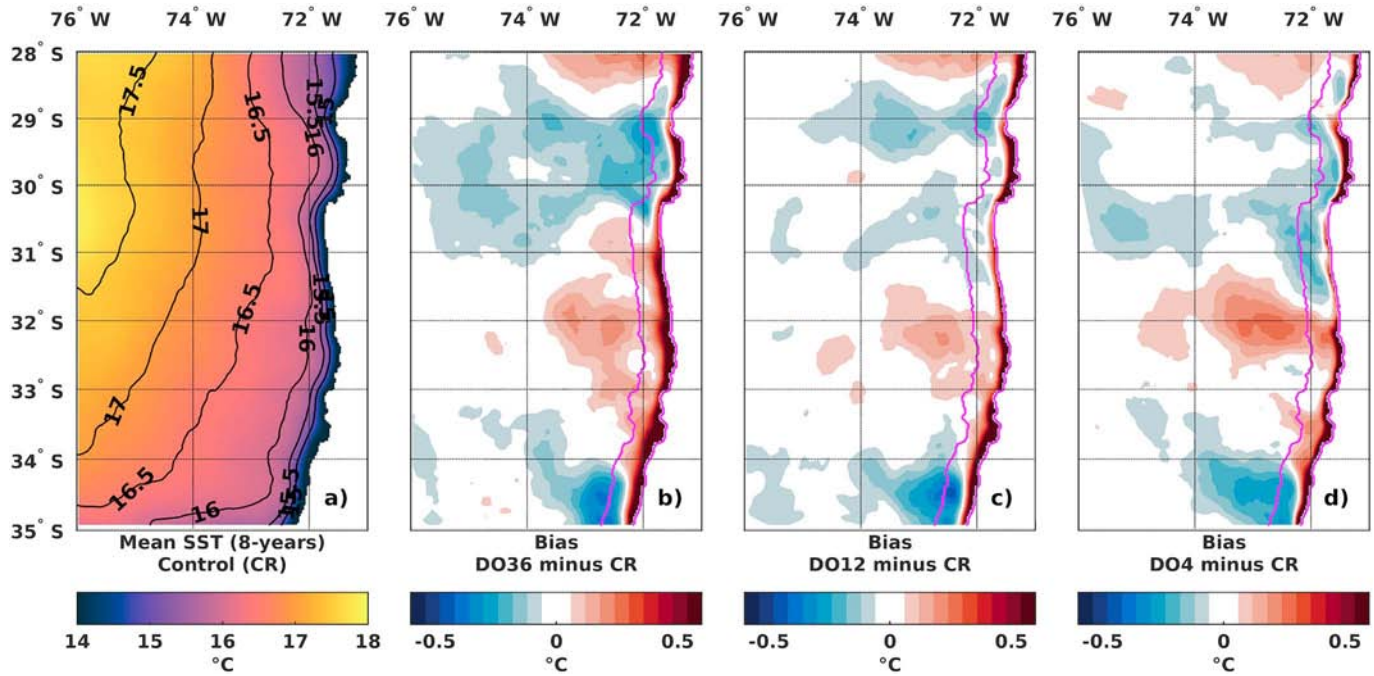

Figure 3. Spatial maps of the (a) Mean SST (°C) simulated by CR. Mean SST bias (°C) for the monthly seasonal differences between (b) DO36, (c) DO12, and (d) DO4 against the reference simulation CR. The lines in magenta indicate the limit of the 50-km coastal band and the shoreline. SST = Sea Surface Temperature.

section we diagnose such impact focusing primarily on how the consideration of a realistic wind drop-off allows reducing the cool mean SST biases along the coast found in our simulation (see section A2.1).

The mean SST in CR (Figure 3a) is shown as a benchmark and exhibits the same biased pattern than in CR0 (see Figure A3), that is, the SST onshore (offshore) is too cold (warm) and the upwelling appears too continuous in the nearshore strip. With regard to the bias reduction, the maps in Figures 3b–3d show the difference between the mean SST of the sensitivity experiments and CR so that the larger the amplitude, the larger the reduction in the cold bias. As we can see, the simulations conducted with corrected wind drop-off lead to a warmer SST along the coast, significantly participating in reducing the cool bias observed in CR. Overall, the comparison between the sensitivity's experiments and the control run, in the 50-km coastal band, indicates an improvement in the realism of the simulation as a function of the resolution: The mean (bias, RMSE) reach (0.23, 0.49), (0.16, 0.41), and (0.13, 0.42) °C for DO36, DO12, and DO4, respectively. Noteworthy, in the simulation DO4, the difference with CR is the lowest closer to the coast than in the other experiments in some regions (e.g., between 31.2°S and 32°S), which indicates that, there, the closer to the coast the wind drop-off starts, the lesser the reduction in the cold bias within the 50-km coastal fringe where most of the cold bias is observed (see Figures 3 and A3). This suggests that in these regions, the DO36 is the most skillful in reducing the cold bias and that the atmospheric simulations at 12 and 4 km tend to yield a wind drop-off too confined to the coast.

Interestingly, besides the coastal zone, the wind drop-off sensitivity differences are also observed in the so-called coastal transition zone, about 100–200 km offshore off Central Chile (e.g., along ~32°S where the wind drop off tends to yield a warm bias). Whether or not this could be associated with differences in eddy activity between CR and the DO experiments will be investigated in section 3.5.

3.3. Alongshore Currents

In order to evaluate the 3-D mean alongshore currents and their dependence on cross-shore winds, we compare the alongshore currents of the sensitivity experiments along four 100-km-long transects across the Central Chile upwelling system. The vertical sections were chosen at latitudes that present a differentiated drop-off scale by experiment (see Figure B2d), while being located near to the main upwelling centers. Figure 4 presents the meridional v component of currents (approximately alongshore) by selected zonal transects for all the experiments. Although the control simulation (CR) shares all the features that appear

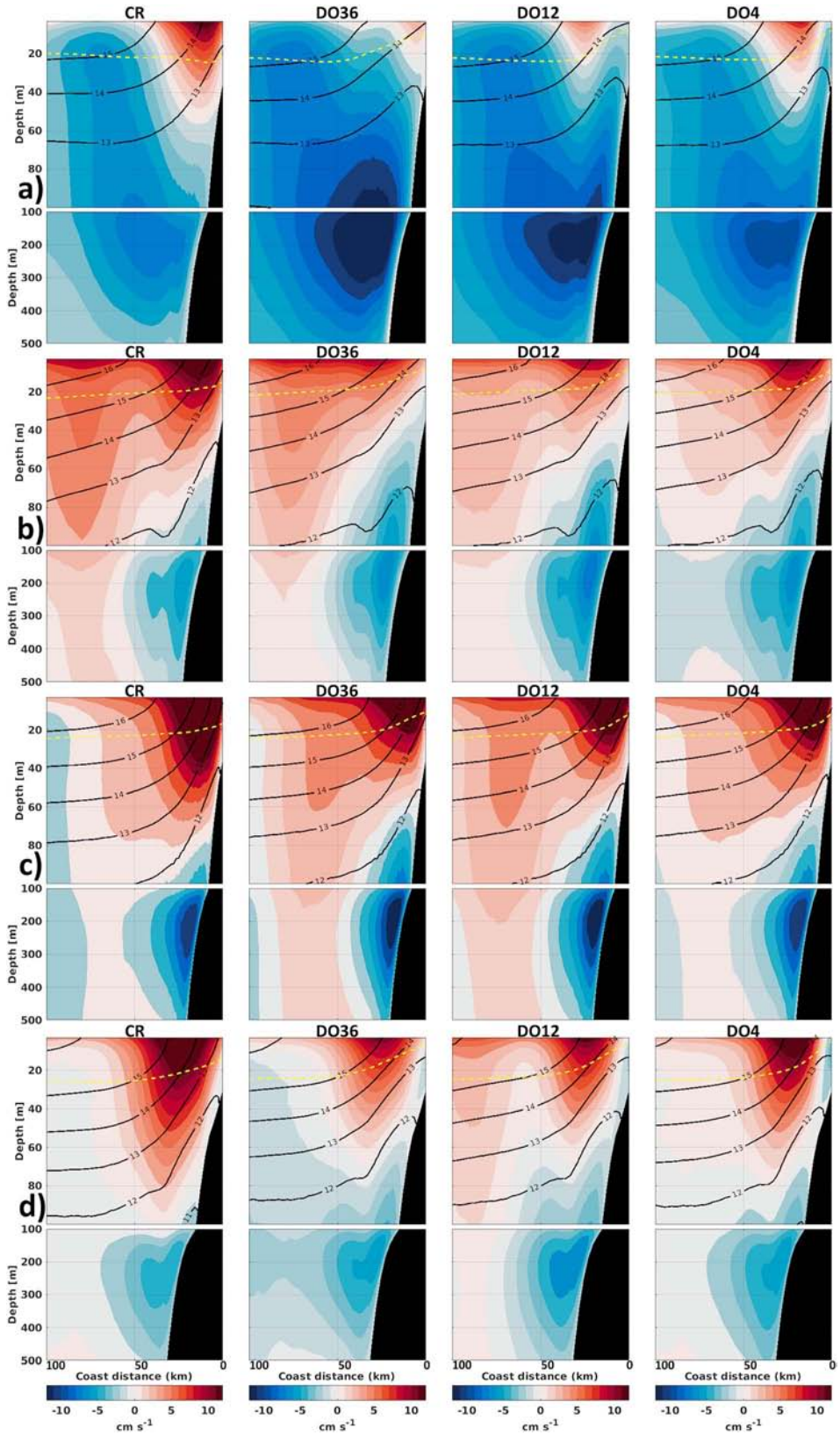

Figure 4. Mean vertical sections of meridional currents for the four experiments at (a) 28.25°S, (b) 30.3°S, (c) 31.1°S, and (d) 33.8°S. Black contours represent the mean temperature, and yellow dashed line is the mean mixed-layer depth diagnosed by K-Profile Parameterization.

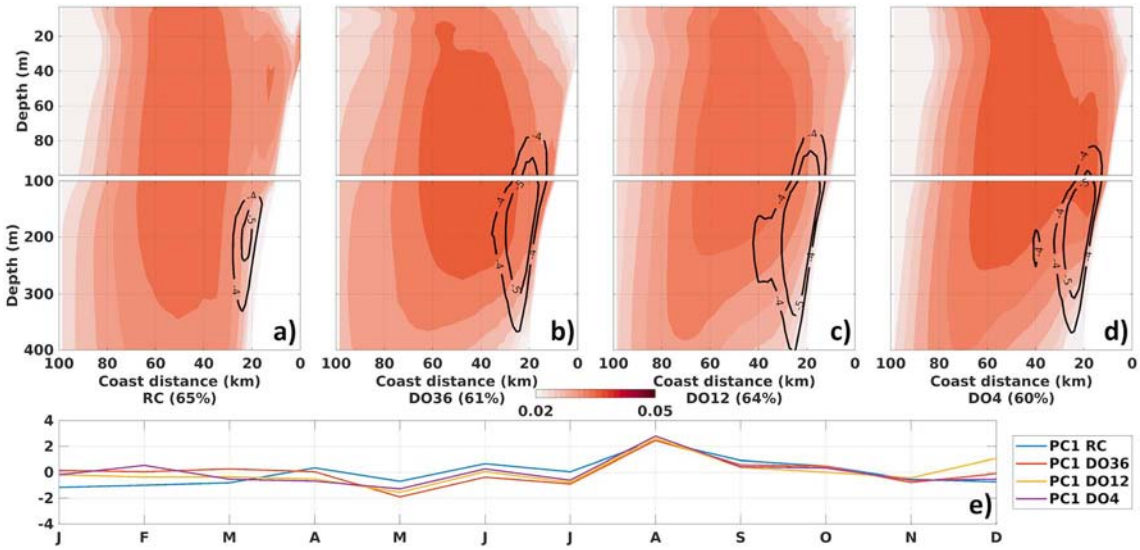

Figure 5. First Empirical Orthogonal Function mode of the meridional current seasonal anomalies (departure from long-term mean) for the vertical sections at 30.3°S for (a) CR, (b) DO36, (c) DO12, and (d) DO4, respectively. The percentage of explained variance is indicated in each panel. The thick black lines superimposed on the contour plot are the −3- and −5-cm/s isolines of the mean meridional current, which indicate the core of the mean Peru-Chile Undercurrent. (e) Corresponding time series (PCs).

in the diagnostic run (see Figure A6b), the sensitivity experiments exhibit naturally a notorious reduction in the CCC (above 60 m) and a stronger alongshore PCU (with the core at approximately 200 m.). As a result, the vertical shear of the alongshore current weakens, the isotherms tilt flattens, and the mixed layer shallows (see yellow dashed lines in Figure 4). Note that the magnitude of these responses is proportional to the resolution of the applied wind drop-off. To assess the realism of the meridional and zonal current structures, we compared them to the ADCP at 30.3°S (see Figure A7 and Table A4). The current profiles are in agreement with previous studies (see Figures 6, 3, and A4 from Aguirre et al., 2012, 2014; O. Vergara et al., 2017). However, the differences between the drop-off experiments and the current observations are reduced by almost 40 % and the correlation levels are increased with respect to the control simulation.

In order to investigate the drop-off impact on the seasonal variability, we use the standard empirical orthogonal function analysis (vonStorch & Zwiers, 1999) to obtain the statistically dominant mode of seasonal variability of the coastal circulation. Figure 5 displays the first mode pattern and its associated temporal expansion (PC1) at 30.3°S. The seasonal cycle (PC1) of the first empirical orthogonal function mode is dominated by an annual cycle component, with a peak centered in August (Figure 5e) and the largest variability at 50 km from the coast. This spatial pattern explains ~60% of the seasonal variance and represents the quasi-barotropic surface equatorward flow linked to the CCC, in connection with the low dynamic heights along the coast resulting from the equatorward winds and offshore Ekman transport (Blanco et al., 2001; O. A. Vergara et al., 2016). The PC1s of the drop-off experiments exhibit increasing correlation against the control solution (CR) depending on drop-off width (0.66, 0.67, and 0.75 for DO36, DO12, and DO4, respectively). The most remarkable drop-off impact in the peak variability pattern is its displacement toward the core of the mean PCU (contours in black lines) that suggests a modulation of the poleward undercurrent absent in CR.

3.4. Mixed-Layer Heat Budget

The contributions of the different processes to the rate of change of the mixed-layer temperature are shown in Figure 6 by spatial maps of the tendency terms along with the mixed-layer depth averaged over 8 years for the simulations CR (top row, Figures 6a–6f) and DO36 (bottom row, Figures 6g–6l). The most striking difference between the two simulations relates to the patterns of the heat-flux forcing term (FORC), which has a much larger amplitude (warming tendency) in the coastal area in DO36 than in CR. This difference can be interpreted as follows: the onshore wide wind drop-off of the DO36 experiment tends to shallow the mixed layer (see Figures 6f and 6l) through the reduction in vertical mixing (i.e., stronger cooling tendency in DO36 associated to the sharper vertical temperature gradient), which overall amplifies the warming tendency due

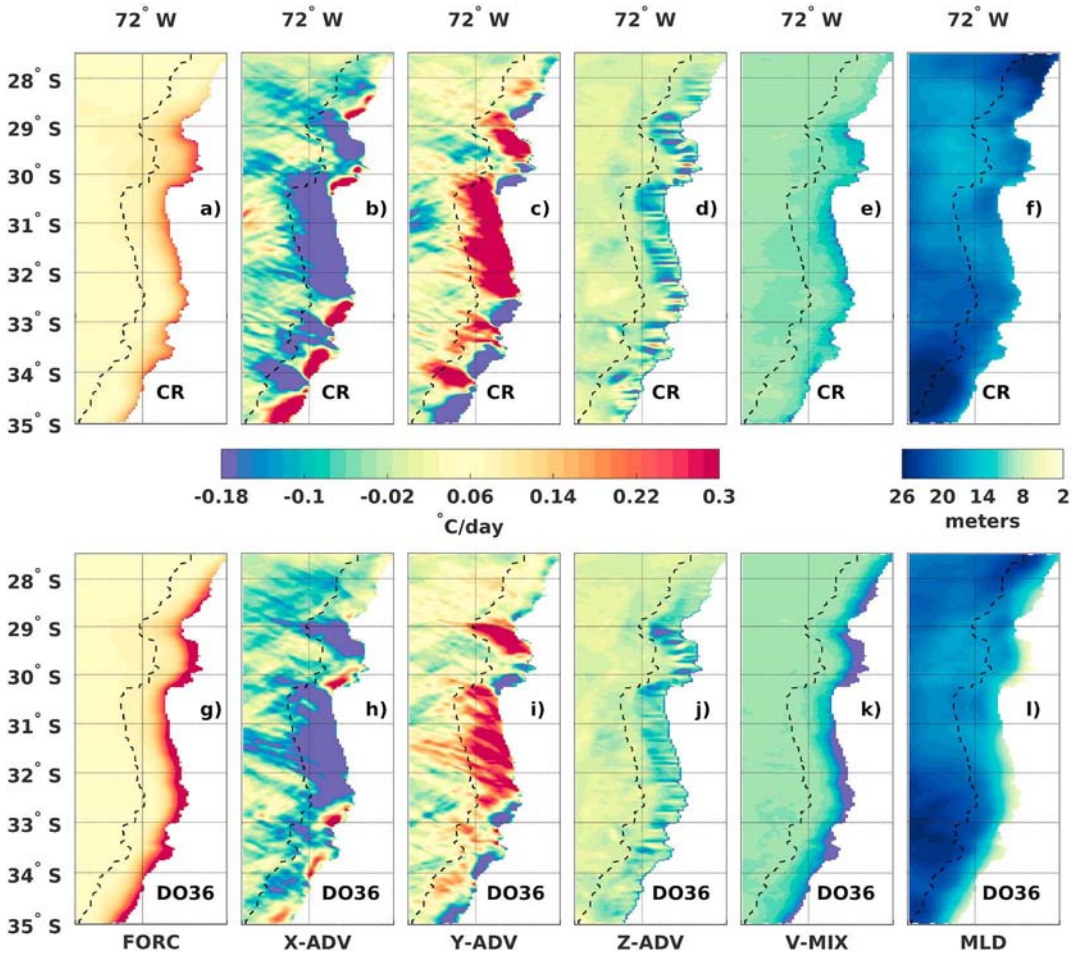

Figure 6. Mixed-layer heat budget analysis: Spatial distribution of the mean tendency terms (°C/day) and the mean mixed-layer depth (m) for the control (CR, top row) and wide drop-off (DO36, bottom row) experiments. (a and g) Heat flux forcing, (b and h) zonal advection, (c and i) meridional advection, (d and j) vertical advection, and (e and k) vertical mixing contributions along the (f and l) mixed-layer depth. The black-segmented line denotes the limit of the 50-km coastal band.

to net heat flux. Most of this increase in warming tendency is associated to change in the solar radiation term, and not to a reduction in the cooling tendency of latent heat flux owing to the reduced coastal winds in DO36. In fact, the weaker onshore winds in DO36 do not lead to a heat gain through reduction of latent heat fluxes, but instead yields a stronger cooling tendency through evaporation and long wave radiation compared to CR because of the warmer mean SST (see Figure 7). Note that such a stronger sensitivity of latent heat to SST than to surface winds was also observed in the modeling study of the Illig et al. (2014) focused on the Peru coastal upwelling. Regarding advection, the differences between CR and D036 are subtler. For vertical advection, in D036, the effect of the shallower mixed layer on the vertical temperature gradient (i.e., increase) compensates for the overall reduction in upwelling rate associated to the reduction in coastal winds compared to CR (see Figure 7). As a result, vertical advection is hardly changed between CR and D036. The patterns of the advection terms are weakly impacted by the changes in the coastal winds (spatial correlation between DO36 and CR reaches at least 0.99 for all the advection terms) and only the amplitude exhibits a notable change, larger in CR than in D036. Vertical and divergent (convergent) zonal advections (Z-ADV and X-ADV in Figures 6d, 6j and 6b, 6h) are contributors to the cooling (warming) tendency in the nearshore zone; on the other hand, meridional advection (Y-ADV in Figures 6c and 6i) is a restoring term and opposes zonal advection.

As a synthetic view of the heat budget in the different simulations, Figure 7 presents the spatial averages (°C/day) within the 50-km coastal strip of the various tendency terms for the control and sensitivity experiments. Focusing first on the cooling terms, Figure 7 indicates that zonal advection is the main contributor to the

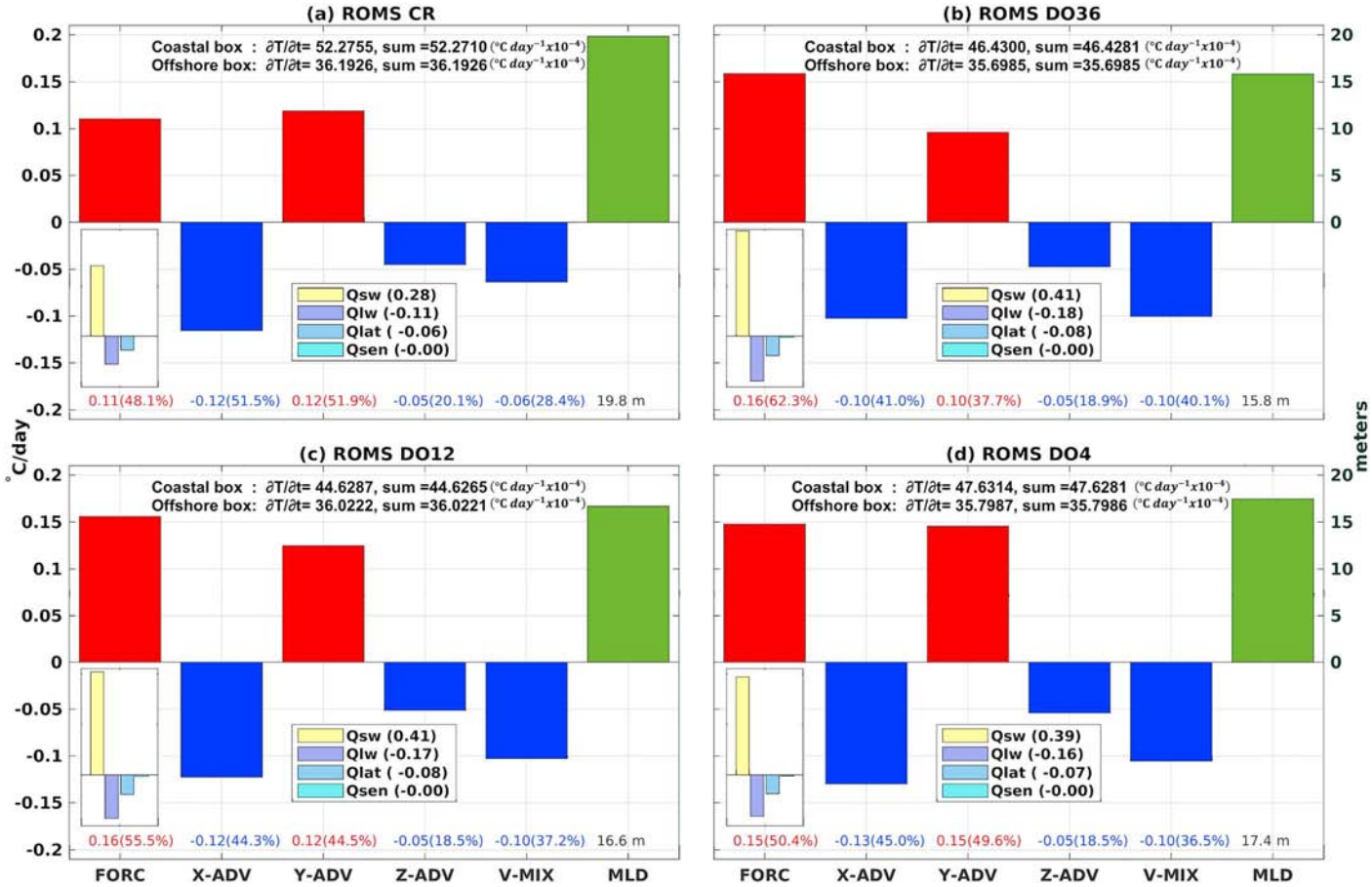

Figure 7. Mixed-layer heat budget analysis in the different simulations: tendency terms averaged over 8 years in the coastal band (50-km wide): (a) CR, (b) DO36, (c) DO12, and (d) DO4. Each bar represents the amplitude of the terms in °C/day (blue (red) for cooling (warming) tendency) and the mixed-layer depth (m). From left to right, heat flux forcing (FORC), zonal advection (X-ADV), meridional advection (Y-ADV), vertical advection (Z-ADV), vertical mixing (V-MIX) and Mixed-Layer Depth (MLD). The percentages of the contribution of the tendency terms to total cooling/warming tendency (in parentheses) are shown at the bottom of each bar. The four components of the net heat flux term are also shown in the rectangle below the FORC bar, with the mean values (in °C/days) indicated in the legend box (yellow = short wave radiation, purple = long wave radiation, blue = latent heat, and light blue = sensible heat). The mean temperature rate and summed-up contributions of the balance are shown for the coastal and offshore box in the upper part of each panel.

coastal cooling in the control simulation, whereas in the sensitivity experiments, both zonal advection and vertical mixing have a comparable contribution (see percentages of the contribution of the tendency term to total tendency at the bottom of each bars in Figure 7), consistent with the coastal wind reduction and the shallower MLD as explained above. The cooling tendency by vertical advection is hardly impacted because of the compensating effect between the reduction in zonal advection and the increase in vertical stratification in the sensitivity experiments. Note the nonlinear response of vertical advection to the changes in the drop-off shape since the vertical advection terms hardly change among the sensitivity experiments despite the notable changes in the coastal wind profiles.

Focusing now on the positive tendency terms (warming tendency), the most notorious impact of the coastal wind reduction is the increase in the contribution of heat flux forcing, which is attributed to the shallower mixed layer in the sensitivity experiment. In particular, the spatially averaged MLD in the 50-km coastal band is on average among the sensitivity experiments shallower by 3.2 m compared to CR (see green bars in Figure 7). The net heat flux term also exhibits structural changes as revealed by the changing relative contribution of solar radiation, long wave flux, sensible heat, and latent heat (see colored thinner bars in the insets of Figure 7). The solar radiation contribution is in particular increased by an average ~45% in all the sensitivity experiments compared to CR as expected by the reduction in the mixed-layer depth. Noteworthy, the cooling tendency associated to latent heat flux is increased in the sensitivity experiments

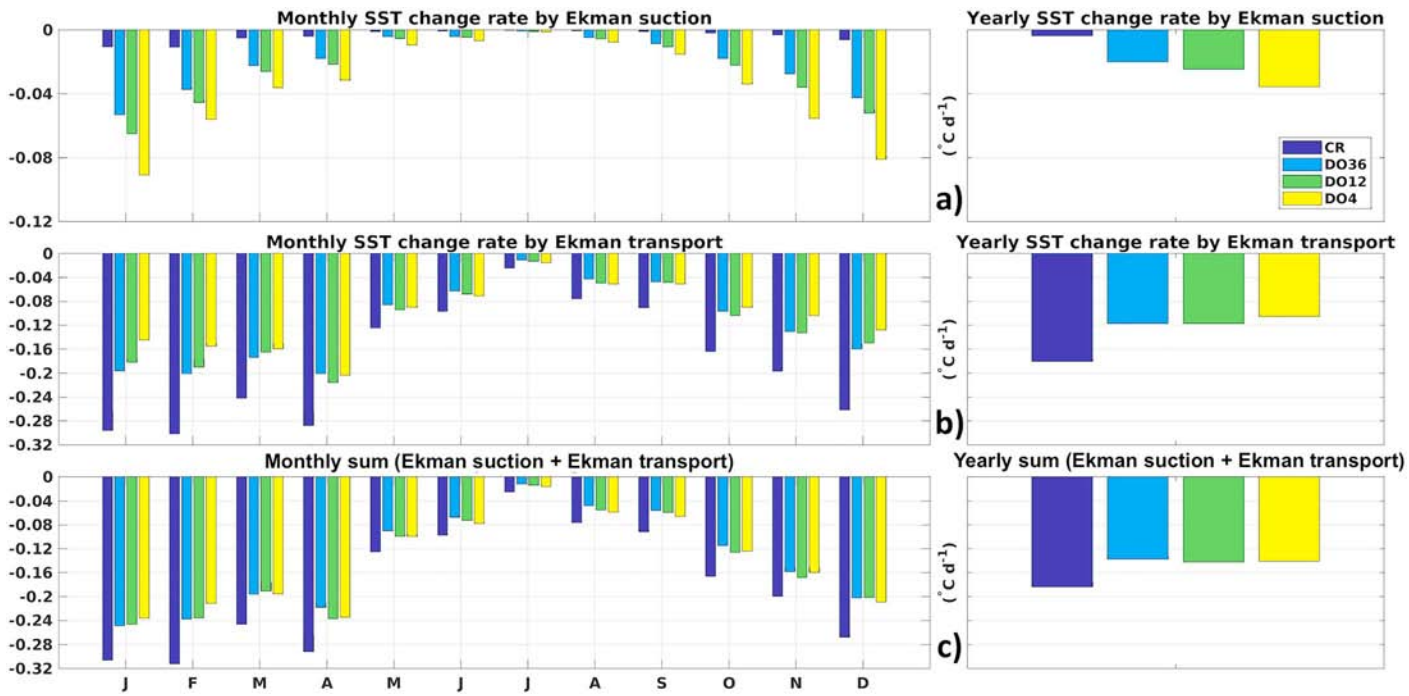

Figure 8. Seasonal variability (left column) and annual mean (right column) of the rate of Sea Surface Temperature (SST) change associated with (a) Ekman suction, (b) Ekman transport, and (c) monthly and yearly sum of Ekman suction and Ekman transport for the various regional oceanic model simulations. Results were spatially averaged over a coastal strip of 50 km and between 27.5 and 35°S (see section 2.3.2 for details of the calculation).

despite the reduction in coastal winds that would tend to reduce cooling through evaporation. However, since the mean SST is warmer in the sensitivity experiments, evaporation and long wave radiation increase, which, added to the effect of the shallower mixed-layer depth, results in an average ~50% increase among the sensitivity experiments of the cooling tendency due to those terms. Meridional advection experiences variations that mirror the ones of zonal advection. Note that although meridional advection decreases in D036 compared to CR, it becomes larger than in CR in D04 despite the presence of a drop-off. Also note that the residual of the heat budget (i.e., difference between the rate of change of the mixed-layer temperature and the sum of all the terms contributing to this tendency) was close to zero (onshore/offshore box (44.69/0.67), (18.94/0.71), (21.61/0.70), (32.17/0.66) (°C/day $\times 10^{-8}$) for CR, DO36, DO12, and DO4, respectively. The analysis thus reveals the nonlinear impact of the drop-off shape on the heat balance and indicates different "regimes" of the maintenance mechanisms of coastal SST depending of the characteristics of the coastal wind profiles. As the most obvious manifestation of such a nonlinear behavior, the FORC term is almost unchanged between the sensitivity experiments while the vertical mixing (and mixed-layer depth) increases strongly from DO36 to DO4. It also indicates that the main impact of the drop-off shape on the thermodynamics in the coastal domain is not through changes in Ekman processes-induced advection but through vertical mixing and heat fluxes, although the reduction in Ekman processes-induced advection is a primarily cause of the warmer SST.

In order to assess the effect of the changes in Ekman processes associated to the different wind profiles on SST along the coast, we follow the approach of Hong et al. (2013) to provide off-line estimates (see section 2.3.2 for details of the calculation) of their relative contributions. The seasonal cycle is considered in the analysis owing to the marked seasonality of the atmospheric circulation off Central Chile, in particular associated to the meridional migration of the low-level jet (Garreaud & Muñoz, 2005; Rahn & Garreaud, 2013; Renault et al., 2012). Figure 8 displays the rate of SST changes (mean and seasonal cycle) associated with advection processes related either to Ekman suction (vertical upward advection) or Ekman transport (horizontal advection). Results were spatially averaged over a coastal strip of 50 km. The mean and seasonal cycle of the SST change rate due to Ekman suction (Figure 8a) exhibit naturally higher amplitude in the drop-off experiments than in CR (mean change rate: −0.0038, −0.0201, −0.0246, and −0.0354

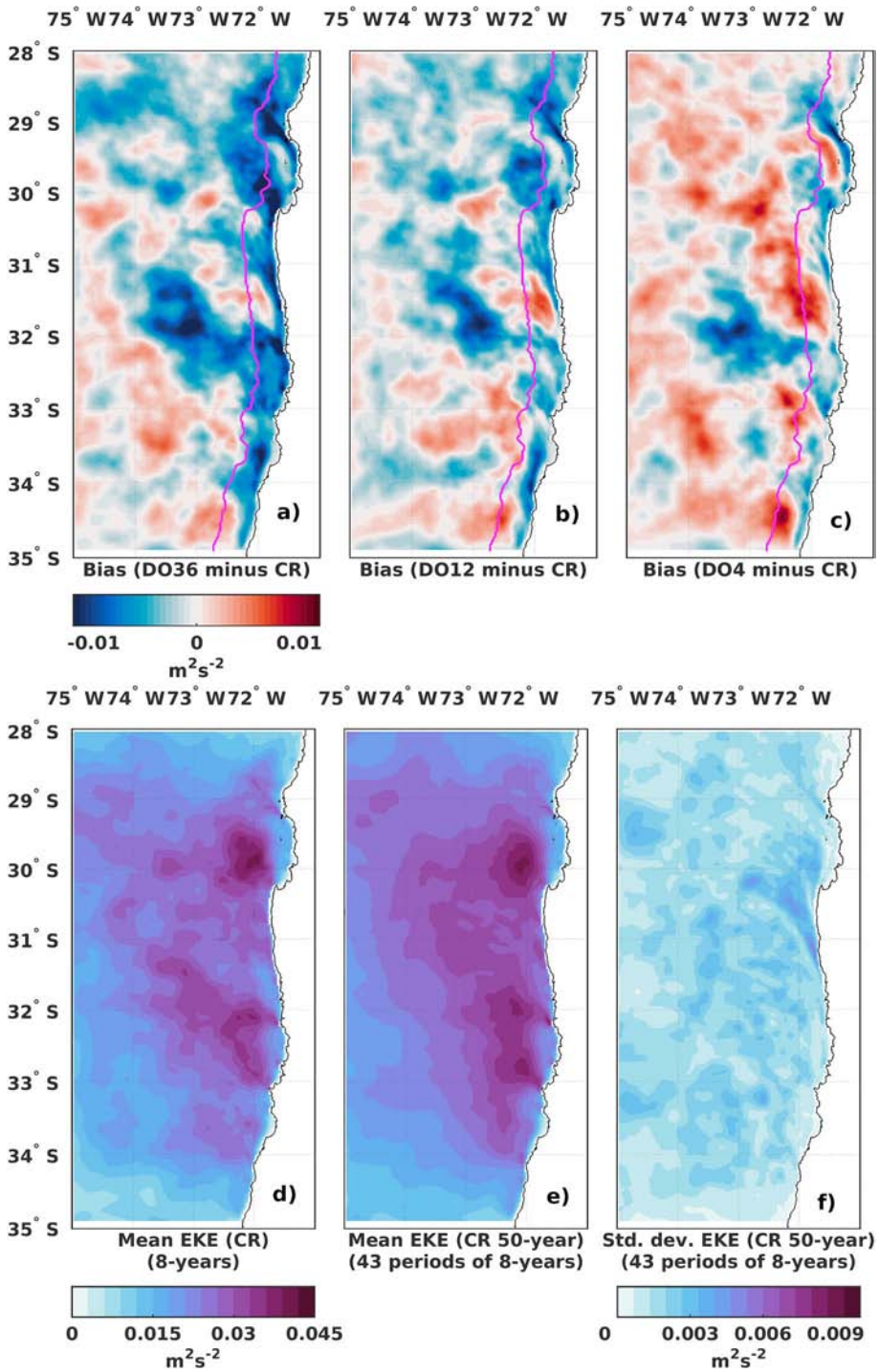

Figure 9. Spatial maps of the temporal mean EKE difference between the control and the drop-off experiments: (a) CR minus DO36, (b) CR minus DO12, and (c) CR minus DO4. (d) Mean geostrophic surface intraseasonal EKE (8 years) simulated by ROMS CR and (e) averaged from 43 chunks of 8 years sampled among a 50-year long simulation with the same characteristics than ROMS CR. (f) Dispersion amongst 43 estimates of mean EKE based on 8-year long chunks selected in the 50-year long simulation. The lines in magenta indicate the limit of the 50-km coastal band. EKE = Eddy Kinetic Energy; ROMS = Regional Ocean Modeling System.

Table 3
Statistics (Mean and Total) of 8-Year Mean Geostrophic Surface Intraseasonal EKE Between Model Solutions

Simulation name	Onshore EKE (50 km) Mean (m^2/s^2)	Onshore EKE (50 km) Total (m^2/s^2)	Offshore EKE Mean (m^2/s^2)	Offshore EKE Total (m^2/s^2)
CR	0.0206	124.1942	0.0190	957.9542
DO36	0.0152	91.7016	0.0172	868.2673
DO12	0.0177	106.8140	0.0176	889.6080
DO4	0.0200	120.4919	0.0195	981.3780

Note. Mean Eddy Kinetic Energy (EKE) values were spatially averaged and integrated in a 50-km coastal band and in the offshore region (i.e., excluding the 50-km coastal strip).

(°C/day) for CR, DO36, DO12, and DO4, respectively). Its magnitude is in phase with the seasonal warming during spring and summer, which increases the vertical gradient of temperature, providing the positive precondition for the surface cooling (Hong et al., 2013). On the other hand, the rate of SST change due to horizontal advection of temperature (Figure 8b) is weaker in the drop-off experiments compared to CR (mean change rate: −0.18, −0.1173, −0.1175, and −0.1053 (°C/day) for CR, DO36, DO12, and DO4, respectively) owing to the reduced coastal divergence in the sensitivity experiments compared to CR. In terms of total temperature change associated with Ekman processes, the main contributor to the cooling is the horizontal advection (Ekman transport) in all simulations, with mean contributions accounting for 98, 85, 83, and 75 (%) of the total contribution by Ekman dynamics for CR, DO36, DO12, and DO4, respectively (see Figure 8). However, all the sensitivity experiments yield a similar reduction (~24%) for the combined contribution of Ekman transport and suction compared to CR, suggesting a compensation between the horizontal and the vertical Ekman advection processes (see Figure 8c).

3.5. Impact on the Turbulent Flow

Since the characteristics of the wind drop-off are influential on the mean circulation along the coast, it is likely to impact the eddy field through changing the stability of the coastal currents. As a first step, we diagnose the impact on EKE. Figure 9 shows the mean EKE for CR (Figure 9d) and its difference with the mean EKE of the three sensitivity experiments (Figures 9a–9c). In the control simulation (CR), the mean EKE amplitude within the 50-km coastal strip (see Table 3) is larger than in all the sensitivity experiments (mean/total EKE 0.0206/124.1942 m^2/s^2), which is not realistic (see Figure A8). The reduction in mean EKE along the coast in the sensitivity experiments can be interpreted as resulting from the reduction of the lateral buoyancy gradient (associated with the reduced cool SST bias), which decreases the available potential energy used by baroclinic instability to produce mesoscale activity along the coast. So near the coast, the impact of the wind drop-off on Ekman dynamics associated to the geostrophic adjustment to the SST front modulating the CCC yields a direct impact on mean EKE. In fact the D036 experiment exhibits the larger reduction in EKE, which means that a wider drop-off implies a lower EKE in the coastal region. Furthermore, the sharper wind drop-off in the D04 simulation compensates the imbalance between the two Ekman processes, and its higher wind stress curl and associated Ekman suction yields the highest EKE amplitude offshore (mean/total EKE 0.0195/981.3780 m^2/s^2). Additionally, we note two regions (around 30°S and 32°) where mean EKE tends to decrease in the presence of a wind drop-off, which corresponds to the regions of largest mean EKE in the control CR simulation.

In order to establish if such changes are significant, we estimate the dispersion in mean EKE expected from random occurrence of eddies. It is estimated based on 43 chunks of 8 years from a 50-year-long simulation corresponding to forcing conditions of CR. The standard deviation among this 43 "virtual" simulations is estimated (Figure 9f) and compared to the change in mean EKE associated with the different sensitivity experiments. It indicates that changes in mean EKE due to changes in the wind profiles near the coasts are much larger than variations in mean EKE associated with different subsampling of the long-term control run experiments. This, in turn, indicates that differences between CR and the sensitivity experiments (Figures 9a–9c) are statistically significant.

To further interpret the impact of the wind drop-off on the eddy field, we estimate the mean zonal and vertical eddy heat flux (see Figure 10) along the same five transects of Figure 4. Generally, eddy advection is contained in the upper pycnocline owing to the small amplitudes of the zonal flow and temperature below ~100 m. The cross-shore lateral flux is essentially shoreward and acts to flatten the upwelling-tilted mean isothermal surfaces (Colas et al., 2012; Gruber et al., 2011; Renault, Deutsch, et al., 2016). The vertical flux is upward and its vertical divergence contributes to the restratification process yielding to the pycnocline in opposition to vertical mixing by boundary layer turbulence. The sensitivity experiments exhibit significant differences in the magnitude and location of the peak value of the mean eddy heat flux, although this is latitudinally dependent. The mean eddy flux of the control experiment (CR) exhibits a lower amplitude than the

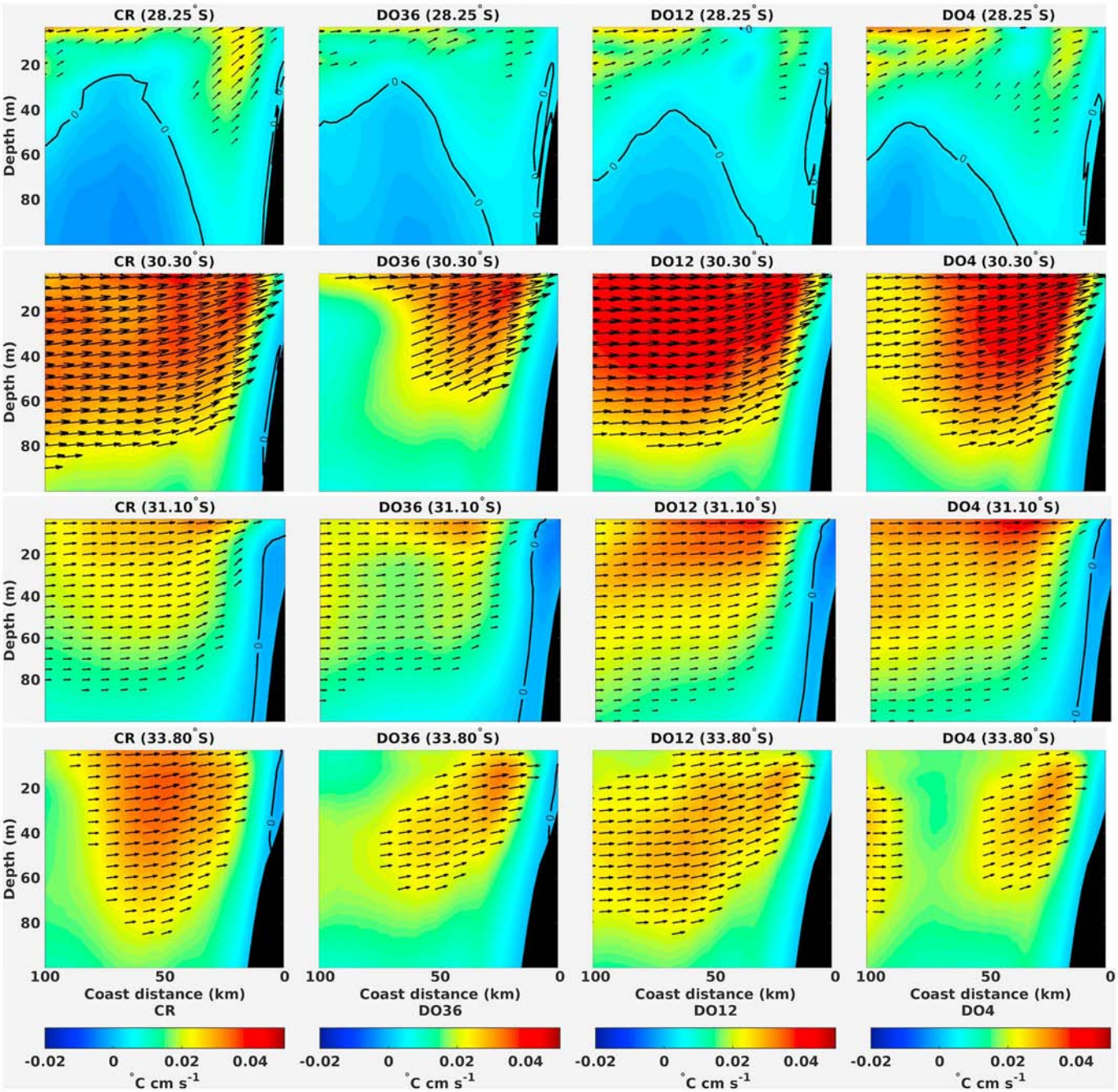

Figure 10. Mean vertical sections of the mean zonal eddy heat flux for the four experiments at (first row) 28.25°S, (second row) 30.3°S, (third row) 31.1°S, and (fourth row) 33.8°S. Black contours represent the 0 flux contour.

experiments forced with a sharp wind reduction (i.e., DO12 and DO4) for all the transects located in the regions where a cool bias was diagnosed near the coast, a sharper drop-off scale leading to a stronger eddy flux. However, the solution DO36 using a wider cross-shore gradient shows lower amplitude than the control experiment revealing the eddy heat flux sensitivity to the drop-off scale. Interestingly, the eddy heat fluxes are lower than in the control solution in all the experiments at the southern transect (33.8°S) where a warm bias was diagnosed in the coastal transition zone for the diagnostic (CR0) and control (CR) experiments.

4. Discussions and Conclusions

Our study was motivated by the need to interpret the coastal cool bias found in most regional model simulations of upwelling system using scatterometer winds that do not represent well the on-shore decrease of the winds in the coastal fringe (the so-called wind drop-off; Astudillo et al., 2017). In this case study focused on the Central Chile region, sensitivity numerical experiments with a regional ocean model to different configurations of the wind forcing were carried out in order to document the influence of mesoscale features in the alongshore winds on the upwelling dynamics. The sensitivity experiments use wind products as simulated by a regional atmospheric model (WRF) at different horizontal resolutions (36, 12, and 4 km) in a nested configuration, which provides a more objective "downscaling" of the wind drop-off pattern on the ocean model grid compared with using the "low" resolution winds (NCEP-DS) as boundary conditions in regional oceanic models.

As a preliminary step we first showed that the regional atmospheric model simulates realistic wind profiles near the coast and that the representation of the wind drop-off is sensitive to the horizontal resolution. In particular the higher the resolution, the closer to the coast the wind drop-off, consistent with previous modeling studies (Capet et al., 2004; Renault et al., 2012). We then performed four cyclic 8-year-long simulations that differ only by the cross-shore profile of the alongshore wind, ranging from a uniform cross-shore gradient to a wide, medium, and sharp drop-off shape.

The experiments reveal a large sensitivity of the thermodynamical processes to the wind drop-off; in particular, there is a notable improvement in the simulated mean SST along the coast. However, a complex balance between various processes governs the reduction of the coastal cold bias. The analysis of a mixed-layer heat budget reveals that vertical mixing is considerably reduced (i.e., its cooling tendency is larger) compared to the case of no wind drop-off. By consequence, the mixed-layer depth shoals, which impacts the amount of heat that is distributed within the mixed layer through surface heat fluxes. In fact, the net heat flux warming tendency is increased by ~45% in all the sensitivity experiments compared to the control run, while there is a weak sensitivity of the change to the resolution of the wind drop-off. Most of this increase in warming tendency is associated to the increase in the solar radiation term. On the other hand, since the mean SST is warmer in the drop-off experiments, cooling by evaporation and long wave radiation increases in ~50% among the sensitivity experiments. What sets these different nonlinear "regimes" of SST maintenance (i.e., with and without drop-off) has its primarily cause in the Ekman processes-induced changes. Indeed, the analysis of the relative contribution of Ekman suction and transport to the rate of SST change for the sensitivity experiments show that the consideration of a drop-off reduces (increases) significantly the cooling by Ekman transport (suction) over the 50-km coastal band. However, the increase in Ekman suction does not compensate for the decrease in Ekman transport, and the resulting cooling rate (i.e., associated to the total upwelling) appears relatively insensitive to the "shape" of the coastal wind profiles. However, the location where the bias reduction takes place varies among the sensitivity experiments. The sharper the drop-off the more confined to the coast the reduction of the cool bias.

In terms of the impact on the upwelling dynamics and associated circulation, the drop-off in the sensitivity experiment has first a profound dynamical impact by reducing the CCC intensity, increasing the alongshore PCU and reducing the offshore Ekman current at the surface with respect to the control run, which yields to a more realistic vertical variability of the coastal currents. Because the eddy field in this region is constrained to a large extent by the baroclinic instability of the coastal current system, the wind drop-off is also influential on the eddy activity. In fact, the sensitivity experiments exhibit significant differences in the magnitude and location of the peak value of the mean eddy heat flux, although this is latitudinally dependent. We also find that the drop-off characteristics influences significantly the EKE field over the whole model domain. In particular, the mean coastal EKE amplitude in the control simulation is larger than in all the sensitivity experiments, and the wide drop-off experiment exhibits the larger reduction in EKE. On the other hand, off shore, EKE tends to decrease in the presence of a wind drop-off. Through the eddy-induced heat transport, such a sensitivity in EKE to the wind drop-off translate into a differentiated flattening of the upwelling-tilted isotherms, which has the potential to feedback on the upwelling dynamics (Gruber et al., 2011).

To conclude, these results illustrate the strong coupling between the wind drop-off and the nonlinear ocean dynamics since the wind drop-off acts not only on all terms of the mixed-layer heat balance but also on the energy source of mesoscale activity through its influence on the vertical structure of the coastal currents.

We will now briefly review limitations of our study. First, the parameterization of the drop-off scale (see Appendix B) proposed here remains mostly empirical, which has inherent limitations. In particular, while we constrain the percentage of decay of the wind amplitude from a certain distance from the coast, there is no constraint imposed on the wind speed at the coast so that, if there is a bias in the offshore wind speed, the parameterization "propagates" it to the coast. Considering the paucity in coastal meteorological stations in this region that would otherwise allow for a better observational constraint, these results can be however considered acceptable. While altimetric data can provide a complementary useful data set to validate the method in the near-coastal region (see Appendix A and Astudillo et al., 2017), they have so far a low latitudinal resolution, which prevents a systematic validation considering that the atmospheric model simulations indicate a large latitudinal variability in the wind drop-off length and the higher-resolution wind forcing does not systematically yield the more realistic reduction of the cool bias evidenced in the control run experiment. This means that other important processes that are not realistically accounted for in our model setup may be at work locally for explaining the discrepancies between model and observations (i.e., cool biases).

One important process is related to atmospheric heat flux forcing. As evidenced by our heat budget analysis, due to the shallow mixed-layer depth near the coast, the annual mean of the rate of temperature change off Central Chile could be strongly influenced by the representation of atmospheric heat fluxes. The oceanic region off Central Chile is, in particular, characterized by the largest stratocumulus cloud deck in the world that exhibits a strong variability from diurnal to interannual scales. Near the coast the variability of low clouds is particularly high and is associated with so-called coastal clearing episodes that accompanied LLCJ and during which incoming solar radiation at sea surface can increase up to 40 W/m^2 (Garreaud & Rutllant, 2003). In our experimental setup that uses the COADS climatological radiative flux forcing (as well as surface air temperature and relative humidity used to calculate turbulent fluxes), these processes may not be properly accounted for, which may partly explain why the sharper drop off (D04) does not yield the largest reduction in the SST cold bias in some regions. Another potentially important process is oceanic mixing (vertical and horizontal diffusivity), which is highly parameterized in the model and thus dependent on model resolution. In particular, the position of the upwelling front is sensitive to where the surface and bottom boundary layers coalesce (Estrade et al., 2008). The reduced winds associated to the drop-off will tend to reduce the thickness of the boundary layer, which will displace the upwelling front further onshoreward, which may explain why in some regions the reduction of the upwelling is insensitive to the resolution of the drop-off. On the other hand, external forcing (internal tides dissipation, inertia-gravity wave, and bores) that will contribute to mixing will have an opposite effect, in particular, in shallow shelf. While the shelf off Central Chile is rather narrow compared to other upwelling systems (i.e., deep shelf), there is thus the possibility of compensating effect between Ekman dynamics and boundary layer dynamics in the positioning of the upwelling front: The sharper the drop-off the more confined the increased upwelling suction but also the thicker the bottom and surface boundary layers through increase in the PCU and surface oceanic jet. Other important processes that may explain the sensitivity of the effect of the drop-off on the reduction cold bias as a function of latitude include the presences of meridional recirculation within the upwelling zone associated to mesoscale dynamics (cf. Capet et al., 2017, for the Southern Senegal upwelling system), the interaction with details in the topography not well accounted for in our configuration, and air-sea coupling at mesoscale (cf. Renault, Molemaker, et al., 2016).

Despite the limitations mentioned above, our results offer a perspective for improving the realism of regional oceanic forced simulations of EBUS in a cost effective way by correcting relatively low resolution wind products, in particular those derived from scatterometers (e.g., QuikSCAT and ASCAT), which are the most used for regional modeling in EBUS. Simply put, we propose here a "cheap" method for correcting satellite winds (or Reanalysis products) to avoid running a fully coupled regional model although the application of this method for other EBUS would require a sensitivity analysis like the one presented here to determine the optimal resolution of the atmospheric model. Here it appears that the DO36 simulation provides the best skill in reducing the average cool bias over the study region.

Future directions of research also include the investigation of the atmospheric processes associated to the wind drop-off so as to better understand the large meridional variability in the sensitivity to the resolution of the model (i.e., the fact that the wind drop-off appears insensitive to resolution in some regions and not in others). While one could follow a similar approach than in Renault et al. (2015) (i.e., vorticity budget and sensitivity experiments to orography), this issue may also require refining topographic features in the

atmospheric model along with resolution, as well as an explicit consideration of air-sea-land coupling (i.e., using a fully coupled ocean-atmospheric regional model), accounting for the potentially important influence of SST on the Marine Boundary Layer at seasonal time scales (Bravo et al., 2016) and at higher frequencies (Garreaud et al., 2011). Local atmospheric processes, as the breeze regime tight to orographic features in the Elqui valley (Scaff et al., 2017) should also be considered.

This study is viewed as a preliminary step for addressing finer-scale variability in the oceanic circulation (i.e., bay's circulation) through downscaling experiments and to guide in the implementation of a regional observing system. In particular, CEAZA is maintaining a dense network of meteorological stations in the Coquimbo region (http://www.ceazamet.cl) and our results could provide guidance for optimizing the network. We are also aiming at carrying specific field campaigns to measure the wind drop-off in some specific regions where the model indicates a weak improvement in the mean coastal SST in order to verify the atmospheric model solution and investigate local effects (e.g., orographic effect, SST coupling). There is also a societal demand for improving the predictive capability of the marine resources and risks/hazards, and we are aiming to build upon this work to investigate some aspects of the biogeochemical response associated to changes in the characteristics of the mesoscale low-level circulation in this region, considering that this region is embedded in one of the largest OMZ of the world and hosts important fisheries. This can be handled with our modeling setup coupling with a biogeochemical model that has been used for the Peru-Chile region to simulate the OMZ seasonal variability (O. Vergara et al., 2016).

Appendix A: Models' Validation

This appendix provides material for the evaluation of the realism of the regional atmospheric and oceanographic model in terms of the mean circulation, seasonal cycle, and mesoscale dynamics. The validation is based on data from satellite, meteorological coastal stations, and a mooring.

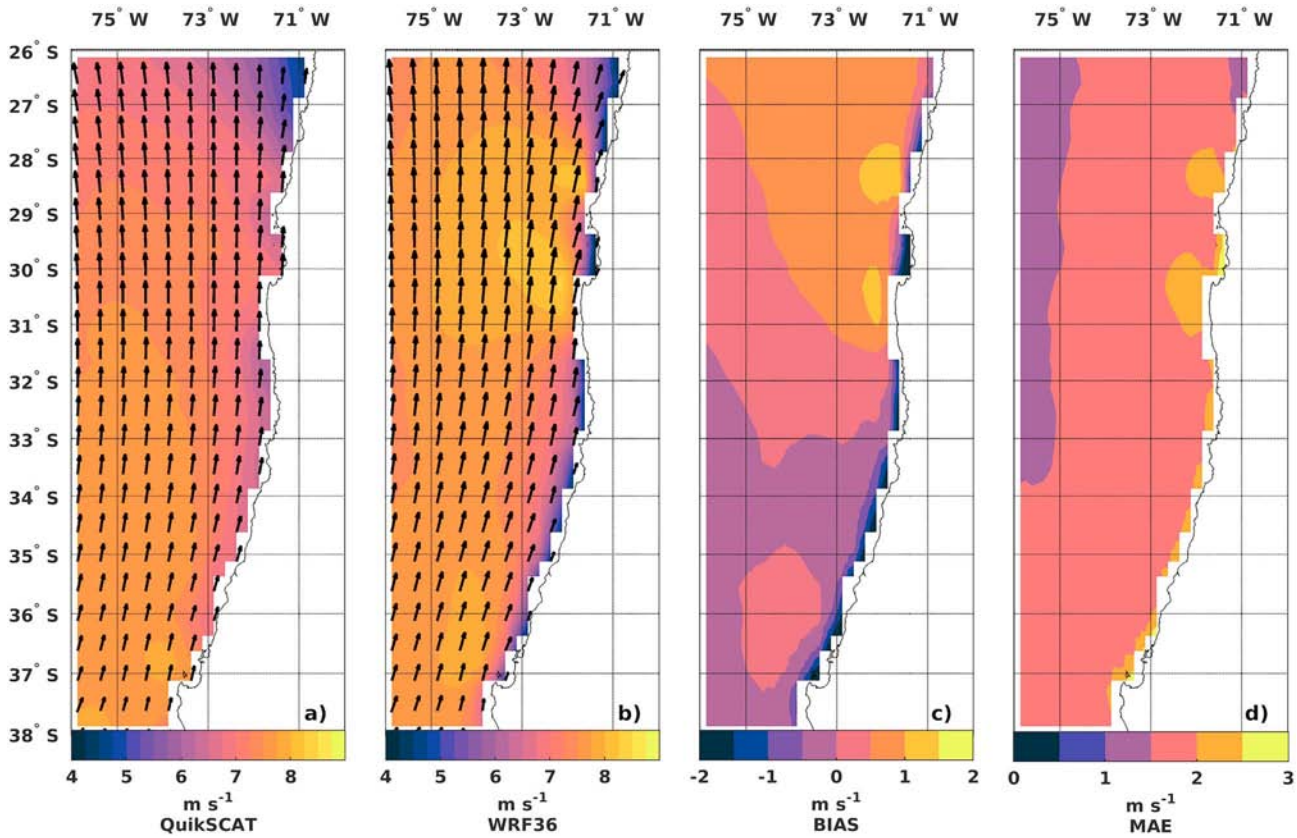

Figure A1. Spatial maps of the temporal mean of the 10-m wind magnitude (m/s) measured by (a) QuikSCAT and simulated by (b) Weather Research and Forecasting (WRF) at coarse resolution 36 km. (c) Bias (m/s) and (d) mean absolute error (MAE, m/s) for the daily differences of the 10-m wind magnitude between WRF and QuikSCAT.

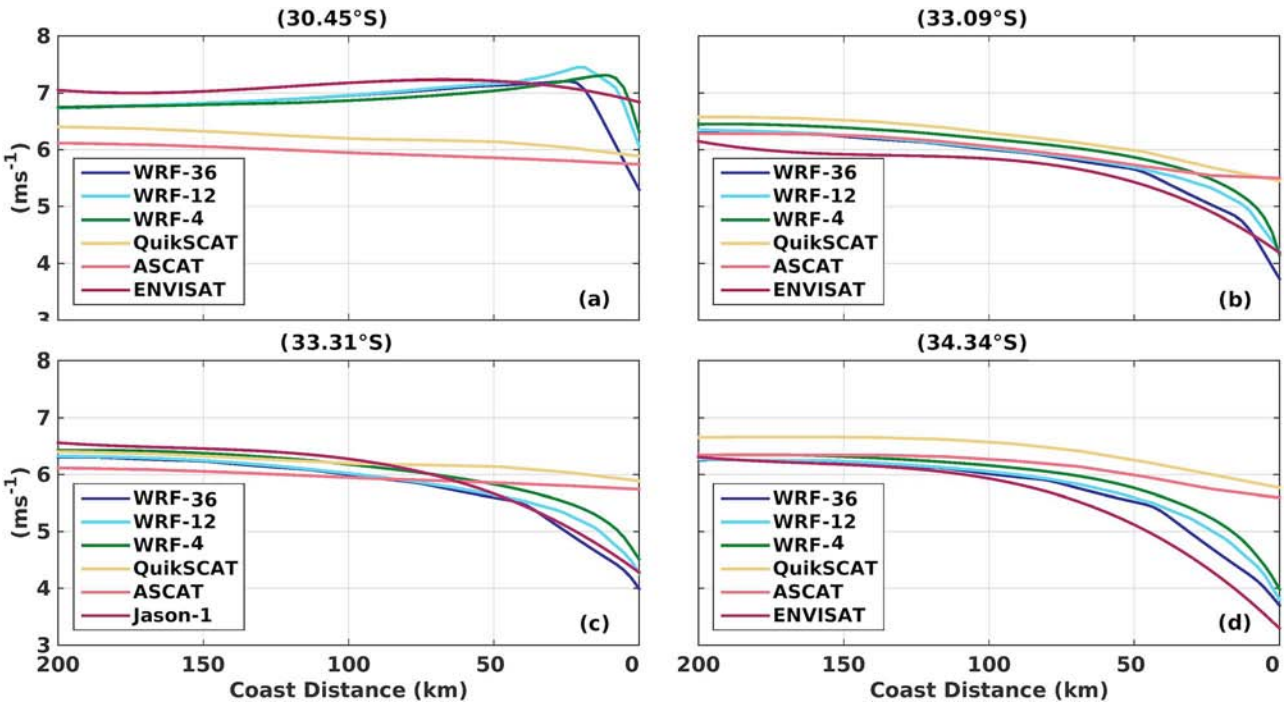

Figure A2. Mean cross-shore 10-m wind speed profiles at different latitudes: (a) 30.45°S, (b) 33.09°S, (c) 33.31°S, and (d) 34.34°S, estimated from WRF36, WRF12, WRF4, QuikSCAT, ASCAT, ENVISAT, and Jason-1 over the period 2007–2009.

Table A1
Summary of the Validation of the WRF Cross-Shore Profiles Using Scatterometers and Altimeters as Ground-Truth Reference (See Figure A2)

		Offshore (80–200 km)				Coast (0–80 km)			
Stat	Resolution	QuikSCAT	ASCAT	Envisat	Jason-1	QuikSCAT	ASCAT	Envisat	Jason-1
ρ	WRF-36	−0.32	−0.34	0.97	0.98	0.64	0.58	0.95	0.99
	WRF-12	−0.31	−0.34	0.97	0.98	0.56	0.51	0.97	0.97
	WRF-4	−0.33	−0.36	0.95	0.98	0.61	0.56	0.97	0.97
RMSE	WRF-36	0.40	0.42	0.20	0.24	1.09	1.04	0.38	0.14
	WRF-12	0.39	0.42	0.21	0.22	0.96	0.93	0.39	0.15
	WRF-4	0.32	0.42	0.30	0.09	0.84	0.84	0.51	0.29
Bias	WRF-36	0.16	0.18	0.04	0.06	1.20	1.09	0.14	0.02
	WRF-12	0.15	0.18	0.04	0.05	0.93	0.87	0.15	0.02
	WRF-4	0.10	0.17	0.09	0.00	0.71	0.70	0.26	0.08

Note. Mean Pearson's correlation coefficient (ρ), Root Mean Square Error (RMSE), and bias are provided. Statistics are obtained at the offshore (80–200 km) and coastal area (0–80 km).

Table A2
Validation Results for WRF (4 km) 10-m Wind Magnitude

Automatic Weather Station (AWS)	Observations (days)	RMSE (m/s)	MAE (m/s)	Bias (m/s)	Pearson's correlation
Punta de Lobos	283	0.5	0.4	0.2	0.8
Loma de hueso	811	1.6	1.3	1	0.8
Lengua de Vaca (CNE)	879	1.6	1.3	0.5	0.7
Lengua de Vaca (DGF)	754	1.9	1.7	1.5	0.8

Note. The analysis uses all available model/AWS daily collocations. Number of daily mean samples, RMSE, MAE, bias and correlation coefficients are shown. WRF = Weather Research and Forecasting; RMSE = Root Mean Square Error error; MAE = Mean Absolute Error; CNE = National Energy Commission of the Chilean Government; DGF = Department of Geophysics, Universidad de Chile.

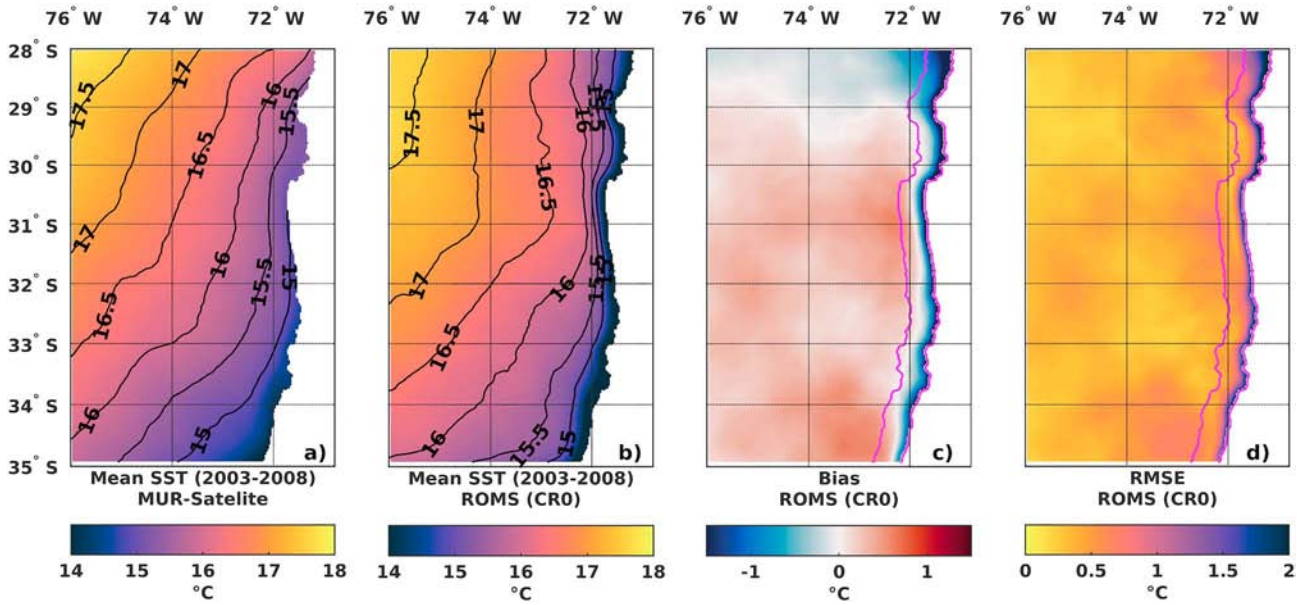

Figure A3. Spatial maps of the temporal mean of the SST (°C) over the period 2003–2008 from (a) MUR data and simulated by (b) ROMS CR0. (c) mean bias (°C), and (d) RMSE (°C) for the monthly seasonal differences between CR and MUR data. The lines in magenta indicate the limit of the 50-km coastal band and the shoreline. SST = Sea Surface Temperature; MUR = Multi-scale Ultra-high Resolution; ROMS = Regional Ocean Modeling System; RMSE = Root Mean Square Error.

A1. Atmospheric Model Evaluation

Figure A1 compares the mean near-surface WRF winds (36-km resolution) with QuikSCAT data over the simulated period (2007–2009) off Central Chile (26–36°S). Observed winds are equatorward and alongshore, with maximum wind magnitude between 30°S and 28°S. In general there is a good agreement between model and observations, both in wind strength and spatial regional patterns. Indeed, the two areas of localized wind speed maxima, the so-called coastal jets (Rahn & Garreaud, 2013), are present in both fields around major capes at Punta Lengua de Vaca (~30°S) and Punta Choros (29°S). However, the wind magnitude appears to be slightly overestimated (~8%) by the model (Figure A1b) in the coastal jet region (Garreaud & Muñoz, 2005). Note that in the nearshore band the model wind strength smoothly decreases shoreward. This wind drop-off is much less pronounced in the scatterometer winds (Figure A1a) as well as in the downscaled wind products used to force CR and CR0 oceanic simulation (not shown). The Figures A1c and A1d display the mean bias and the mean absolute error (MAE) for the daily differences between the model and the QuikSCAT data. Similar results are obtained when comparing WRF and ASCAT winds (not shown), though the agreement between WRF and ASCAT decreases unsurprisingly given that ASCAT has a systematic underestimation of the wind speed that increases with higher wind conditions (Bentamy et al., 2008; Bentamy & Fillon, 2012).

Figure A2 shows the cross-shore profile of the alongshore winds at different latitudes for the three WRF model resolutions and for satellite observations (QuikSCAT, ASCAT, ENVISAT, and Jason-1). First, the simulated WRF winds are comparable with both the scatterometry- and altimetry-derived observations in the offshore region (i.e., excluding the 80-km-width coastal band), with low bias and RMSE differences. Second, in the nearshore region (80 km) the ocean surface winds from WRF agree very well with the altimeter-derived observations and exhibit higher scores with respect to QuikSCAT and ASCAT. This is due to the scatterometer blind zone near the coast, which limit the observation of the wind drop-off profile within this coastal band. On the other hand, the small altimeter footprint and its higher resolution allow resolving the 50-km fringe along the coast. Table A1 provides the validation results for three WRF resolutions.

Finally, the statistics of the mean daily 10-m winds from the WRF innermost solution (4-km resolution) compared to the available coastal surface stations are given in Table A2. The nearshore variability simulated by WRF is in fair agreement with the observations (on average for the four stations, Pearson's correlation is

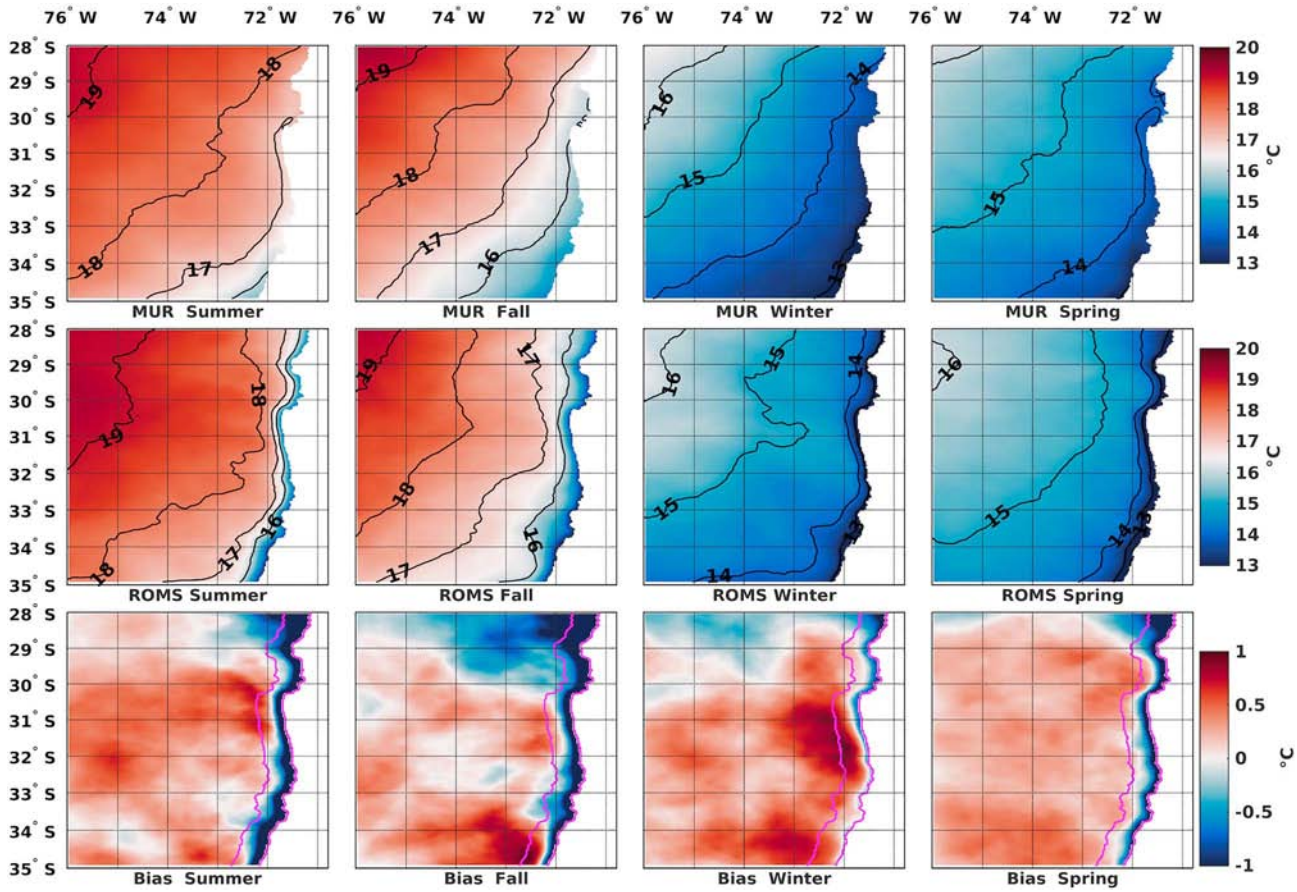

Figure A4. Spatial maps of the temporal mean seasonal of the SST (°C) over the period 2003–2008 from (top row) MUR data and simulated by (middle row) ROMS CR0. (bottom row) Seasonal SST difference between ROMS CR0 and MUR (°C). Summer, fall, winter, and spring are defined as December–February, March–May, June–August, and September–November, respectively. The lines in magenta indicate the limit of the 50-km coastal band and the shoreline. SST = Sea Surface Temperature; MUR = Multi-scale Ultra-high Resolution; ROMS = Regional Ocean Modeling System.

~0.8, bias is ~0.8 m/s, and RMSE is ~1.4 m/s). Note that the anemometer height correction has not been applied on the meteorological records.

Table A3
Validation of the ROMS SST From the CR0 Simulation Against the Satellite Product (MUR)

Season	Bias (°C) offshore	Bias (°C) coast	RMSE (°C) offshore	RMSE (°C) coast
Summer	0.22	−0.89	0.37	1.07
Fall	0.04	−0.85	0.36	1.09
Winter	0.21	0.06	0.37	0.54
Spring	0.21	−0.47	0.32	0.68
Yearly	0.17	−0.54	0.38	0.92

Note. Mean bias and RMSE are averaged over a 50-km coastal band and in the offshore region (i.e., excluding the 50-km coastal strip) and shown for seasonal and annual means. The months for calculating the seasonal means are defined as in Figure A4. ROMS = Regional Ocean Modeling System; SST = Sea Surface Temperature; MUR = Multi-Scale Ultra-High Resolution; RMSE = Root Mean Square Error.

A2. Oceanic Model Evaluation

A2.1. SST

In this section, the diagnostic ROMS solution (CR0) is evaluated. The mean state (2003–2008) of observed (MUR) and simulated SST is presented in Figures A3a and A3b. The model mean regional pattern is in good agreement with observations in the offshore region (i.e., excluding the 50-km-width coastal band) and presents a weak positive mean bias and RMSE (0.17 °C and 0.38 °C, respectively). Although both fields exhibit a cold tongue along the coast, clear signature of the wind-driven coastal upwelling, the SST differences (Figures A3c and A3d) for the monthly seasonal cycle indicate that the simulation yields excessive cooling (bias −0.54 °C, RMSE 0.92 °C) in the nearshore strip (50 km). This cold bias extends everywhere along the coast, spreading offshore northwestward off 30°S and upstream from the region of the coastal wind jets shown in Figures A1a and A1b.

In order to analyze in detail this cold bias we describe the seasonal variations of SST for MUR and ROMS CR0 in Figure A4 and Table A3. A pronounced SST seasonal cycle in the upwelling region off Central Chile is

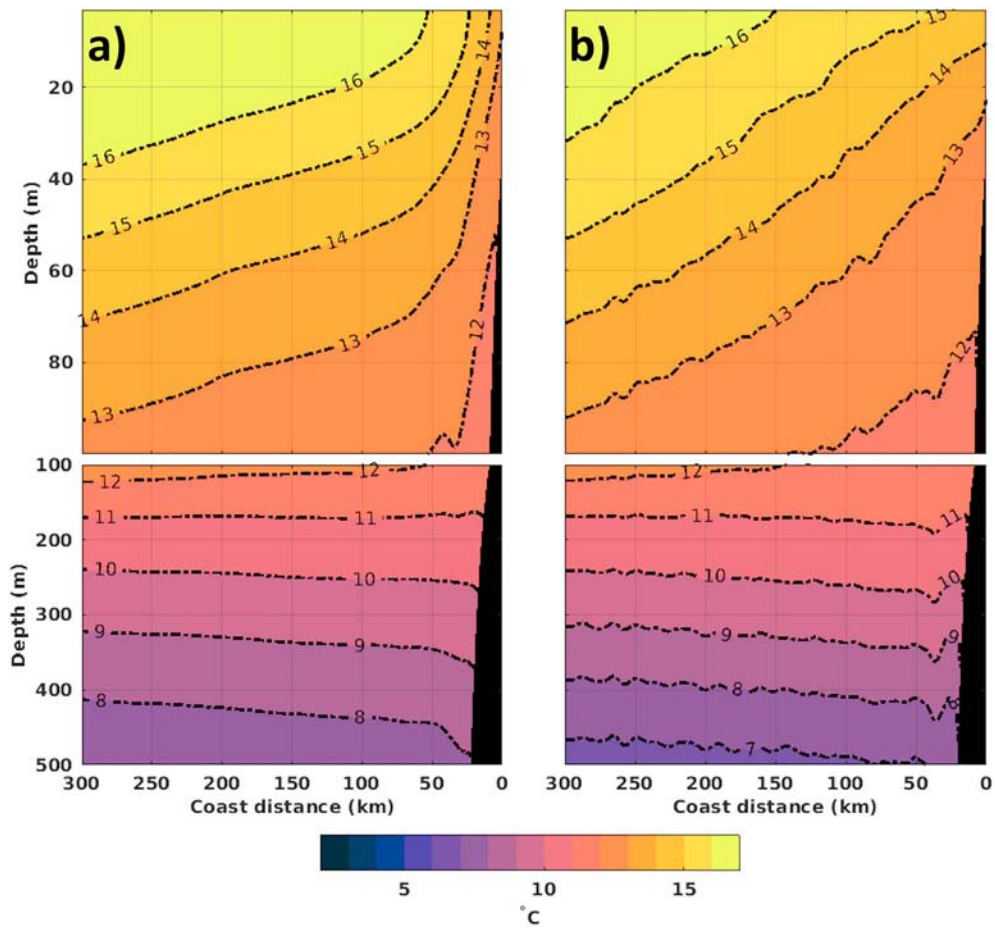

Figure A5. Mean cross-shore vertical sections of temperature at 30.3°S, for the (a) ROMS CR0 simulation and (b) CARS climatology. ROMS = Regional Ocean Modeling System; CARS = CSIRO Atlas of Regional Seas; CSIRO = Commonwealth Scientific and Industrial Research Organisation.

characterized by a westward shift of the 16 °C isotherm from the coast in summer-fall to the offshore region in winter-spring, in both MUR and ROMS (Figure A4, top and middle rows, respectively). The ROMS temperature is slightly warmer offshore (maximum bias 0.22 °C, RMSE 0.37 °C) along the year. On the other hand, the cool bias for the coastal strip evolves in evident relation with seasonal changes in alongshore winds and associated coastal upwelling response; the bias/RMSE in the 50-km coastal band ranges from 0.06/0.54 °C in winter to −0.89/1.07 °C in summer.

The near-coastal cold bias has been present in various regional model simulations of the EBUS (Penven 2001; Penven 2005; Veitch et al., 2010; Colas et al., 2012). In these studies the authors related the cold bias to the wind being too strong at the shore, which results in an imbalance between Ekman transport and Ekman suction (Capet et al., 2004; Desbiolles et al., 2016). However, such a bias could be also attributed to a warm bias in the satellite-based SST data sets. In fact, Dufois et al. (2012) suggest that any high-resolution satellite-derived data set based on a smooth SST product (e.g., MSG/SEVIRI or MODIS L3, or by using optimal interpolation), as MUR analysis, should be used with extreme care in the nearshore regions of the EBUS.

The mean temperature structure is assessed against the CARS climatology (Ridgway et al., 2002). Figure A5 displays a mean zonal section of temperature at 30.3°S for both the CARS climatology and the ROMS CR0. Both sections are in good agreement in the offshore region and in lower layers; however, the surface near-shore cold bias is evident in the sharp isotherm tilt of the model temperature (see Figure A5a).

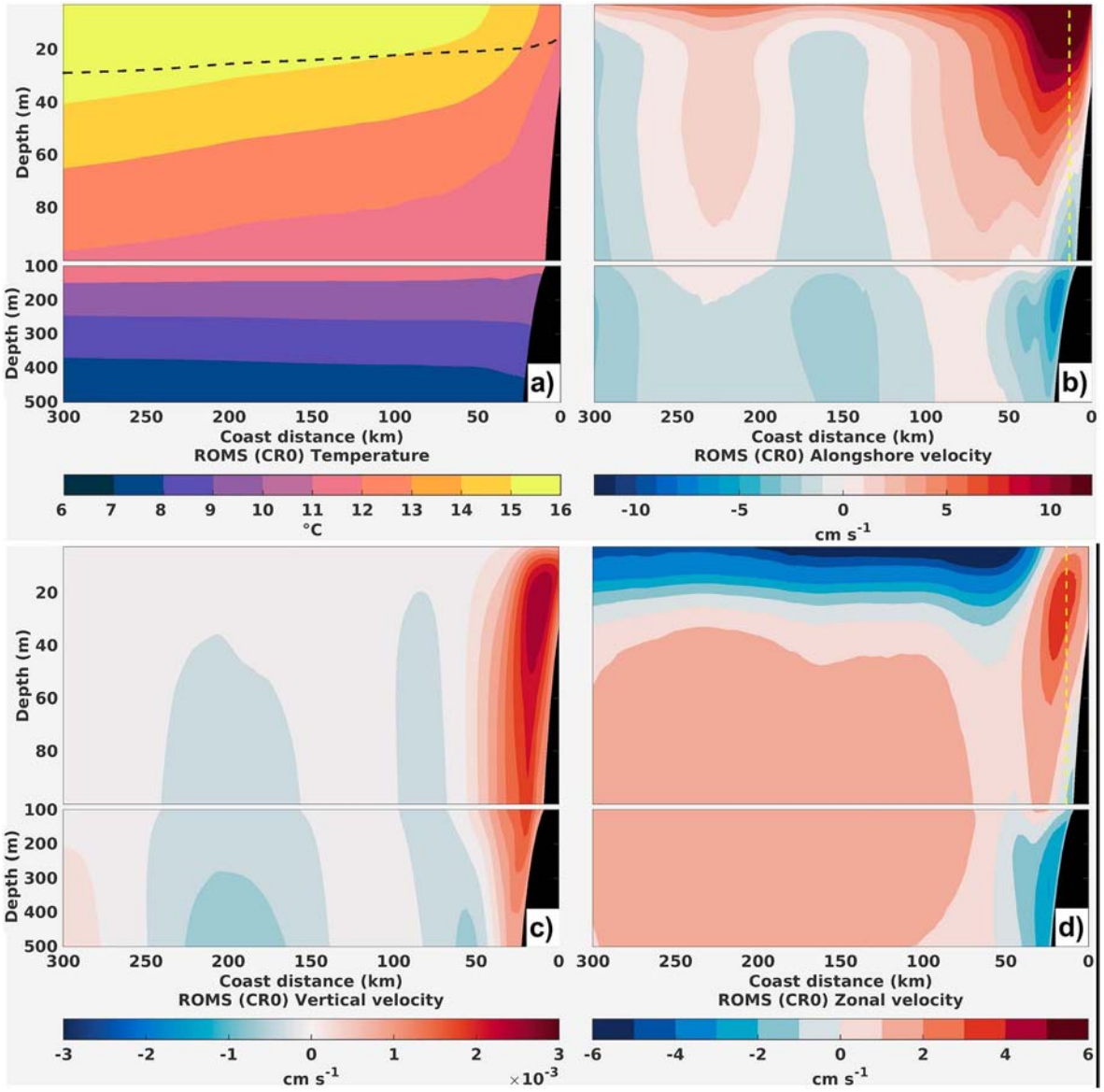

Figure A6. Cross-shore vertical sections at 30.3°S of (a) mean temperature (°C), (b) mean alongshore velocity v (m/s), (c) mean vertical velocity $\overline{w}$ (m/s), and (d) mean zonal velocity $\overline{u}$ (m/s) for the ROMS CR0 model. Dashed lines in black and yellow colors correspond to the mixed-layer depth diagnosed by KPP and to the COSMOS mooring position, respectively. ROMS = Regional Ocean Modeling System; KPP = K-Profile Parameterization.

A2.2. Mean-Seasonal Circulation

The model vertical structure of temperature and currents along a 300-km-long transect at 30°S are presented in Figure A6. Mean alongshore (meridional), cross-shore (zonal), and vertical velocities (Figures A6b–A6d) have the typical structure of a subtropical EBUS and can be compared to previous modeling studies in HCS (Aguirre et al., 2012, 2014; Cambon et al., 2013; O. A. Vergara et al., 2016; O. Vergara et al., 2017). Near the coast the prevalent upwelling conditions associated with the intense and uniform alongshore wind stress cause a surface (above a depth of 50 m) coastal jet, called CCC (mean speed of 20 cm/s) flowing toward the equator, above a subsurface poleward flow (PCU) trapped to the continental slope. This undercurrent exhibits a maximum speed core at about 150- to 300-m depth and originates from the Equatorial Undercurrent, which splits at the Galapagos Islands. One branch continues as undercurrent and turns south to form this subsurface flow. While the other southern branch, the Peru-Chile Countercurrent, at about 150 km from the coast, generates a second southward surface flow (Penven et al., 2005). Finally, farther offshore the eastern branch of the subtropical South Pacific gyre gives raise to another wind-driven equatorward

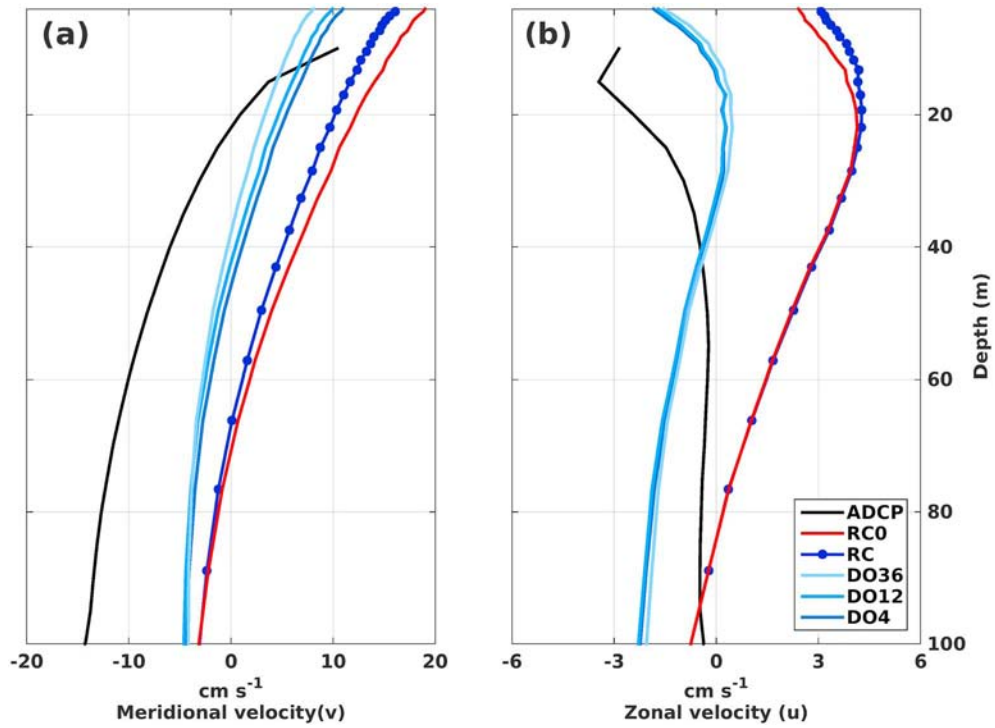

Figure A7. (a) Mean meridional and (b) zonal current profiles at 30.3°S from the COSMOS Acoustic Doppler Current Profiler (13km from the coast) and the various ROMS simulations at the mooring site. ROMS = Regional Ocean Modeling System.

surface flow. The cross-shore circulation (see Figure A6d) consists of an offshore flow within the surface Ekman layer ($u < 0$) and a weaker shoreward return flow ($u > 0$) in the subsurface thermocline supported by the equatorward alongshore pressure gradient. This geostrophic current feeds the coastal upwelling (see $w > 0$ in Figure A6c), the CCC, and the PCU. As customary in coastal upwelling systems, an isotherm tilt toward the coast is observed above 100-m depth (see Figure A6a).

Figure A7 and Table A4 display the validation of the mean velocity vertical profile against in situ currents at 30.3°S and 13 km from the coast. The mean model CCC/PCU (Figures A7a and A7b) are comparable with observations in range and structure, although the simulation overestimates/underestimates them because of strong coastal wind forcing. As a typical result in regional oceanic models of the southern HCS (Aguirre et al., 2012, 2014; O. Vergara et al., 2017), the CCC is too energetic overlapping and deepening the PCU (see Figure A6b). As a consequence, the enhanced equatorward pressure gradient forces a shoreward geostrophic current in displacing offshore the surface Ekman current at the coast (see Figure A6d). Indeed Desbiolles et al. (2016) showed that an overestimated coastal wind would impact negatively the structure of the meridional and zonal surface currents and the upwelling dynamics in the EBUS of the Benguela region. They showed that the cross-shore structure of the alongshore winds impact both the offshore and northward surface flows increasing the Ekman transport and the geostrophic adjustment and reducing the intensity and shallowness of the poleward undercurrent.

Table A4
Validation of the Mean Meridional and Zonal Current in the ROMS Experiments Against the Current Meter COSMOS Located at 30.3°S and ~13 km From the Coast

	Meridional current		Zonal current	
ROMS simulation	RMSE (cm s^{-1})	Pearson's correlation	RMSE (cm/s)	Pearson's correlation
CR0	11.5	0.97	3.5	0.61
CR	10.5	0.97	3.6	0.65
DO36	7	0.98	1.6	0.65
DO12	7	0.98	1.6	0.65
DO4	7	0.98	1.6	0.61

Note. RMSE and correlation coefficient are shown. The data were averaged for the available depths between the surface and 100 m. ROMS = Regional Ocean Modeling System; RMSE = Root Mean Square Error.

A2.3. EKE

Nearshore wind-driven currents present strong horizontal and vertical shears. Associated instabilities are the main contributors to the development of mesoscale activity off Central Chile through baroclinic and barotropic energy conversion. Cyclonic eddies populate primarily the CCC, while anticyclonic ones moderately dominate the PCU. This eddy contribution plays an important role in the mean lateral circulation by cross-shore heat flux and depletion of available mean potential energy

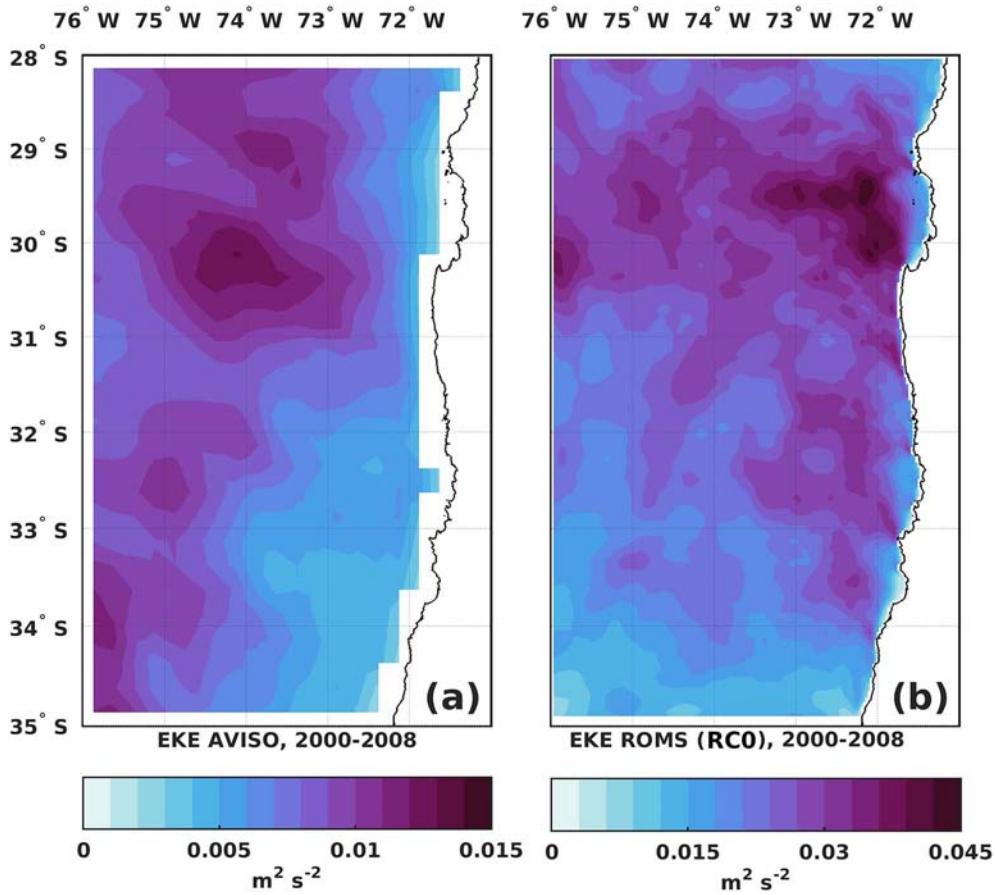

Figure A8. Spatial maps of the temporal mean of the geostrophic surface intraseasonal EKE computed from sea level pressure gradients and derived from (a) AVISO data and from (b) ROMS CR0 over the period (2000–2008). EKE = Eddy Kinetic Energy; Aviso = Archiving, Validation and Interpretation of Satellite Oceanographic; ROMS = Regional Ocean Modeling System.

(Aguirre et al., 2014; Capet et al., 2008; Colas et al., 2012; Hormazabal et al., 2004; Leth & Middleton, 2004; Marchesiello et al., 2003). The mean geostrophic surface intraseasonal EKE, a direct measure of the number and intensity of mesoscale eddy phenomena, was calculated as described in section 2.3.3 for the diagnostic ROMS model (CR0) and compared to satellite estimations (Figure A8). The model spatial pattern of EKE is similar to the one obtained by Aguirre et al. (2014) and in agreement with satellite data. Both observed and simulated fields, Figures A8a and A8b, respectively, present the highest levels of energy (>0.015 m^2/s^2 for AVISO) between 31°S and 28.5°S. However, the simulated EKE range [0–0.045 $m2/s^2$] is broader than the corresponding observed range [0–0.015 $m2/s^2$]. This overestimation was already highlighted in previous studies (Aguirre et al., 2014; Colas et al., 2012; Cambon et al., 2013; O. A. Vergara et al., 2016; O. Vergara et al., 2017) and could be attributed, in part, to a smoothing of the gridded AVISO data. Indeed, we have evidenced a higher agreement in the amplitude range of EKE (not shown) when we use low-pass-filtered (6-day averaging and Gaussian spatial filter with 30-km half-width) ROMS geostrophic velocities, as described in Capet et al. (2008).

Another common feature of the observed and modeled mesoscale activity is a nearshore EKE minimum, in concordance with the idea that EKE originates from instabilities in the nearshore region that amplify while moving offshore (Marchesiello et al., 2003). This assumption is supported in the ROMS solution that evidences a coastal sourcing of EKE around major upwelling regions near Punta Choros (~29°S), Punta Lengua de Vaca (~30°S), and Punta Curaumilla (~33°S), three regions in which atmospheric coastal jets are recurrent. This suggests that mesoscale processes are tied to the coastal topography and local wind forcing. Unfortunately, the AVISO data are not yet reliable in the coastal band to confirm this hypothesis.

Appendix B: Wind Drop-Off Characteristics and Coastal Correction

This appendix provides the details of the method to derive the drop-off length scale and to modify the coastal wind profiles from the WRF model outputs and generate the atmospheric forcing for the sensitivity experiments with ROMS (see Table 2).

B1. Estimate of Wind Drop-Off Characteristics

We follow previous studies that provide estimates of the wind drop-off based either on satellite data (Astudillo et al., 2017) or atmospheric model outputs (Bravo et al., 2016; Renault et al., 2015). The method consists in estimating the distance from the coast, that is, the wind drop-off length (L_d), from which the cross-shore profiles of the magnitude of the wind curl reaches a certain threshold. Here, when applying this wind curl threshold-based methodology, the resulting L_d values were very noisy, exhibiting a large sensitivity to the resolution of the simulated wind that is difficult to interpret all the more so as L_d exhibit already a strong meridional variability (Astudillo et al., 2017). This sensitivity results from the strong aliasing imposed by the bilinear interpolation associated with the upsampling of the WRF wind fields on the high-resolution ROMS grid. Thus, we propose here an alternative approach that provides well-correlated L_d values between the different WRF grid resolutions. First, we estimate within an offshore distance of 150 km the percentage of wind speed reduction (W_r) along the cross-shore profile with respect to its value at the coast as follows:

$$W_r(x,\mathrm{lat}) = \frac{V(x,\mathrm{lat}) - V(0,\mathrm{lat})}{V(x,\mathrm{lat})} \times 100 \tag{B1}$$

where $V(x,\mathrm{lat})$ and $V(0,\mathrm{lat})$ are the model mean wind speed at a given distance x (in meters) from the coast and at the grid point nearest to the coast, respectively (see Figures B1a and B1b). Second, the rate of wind

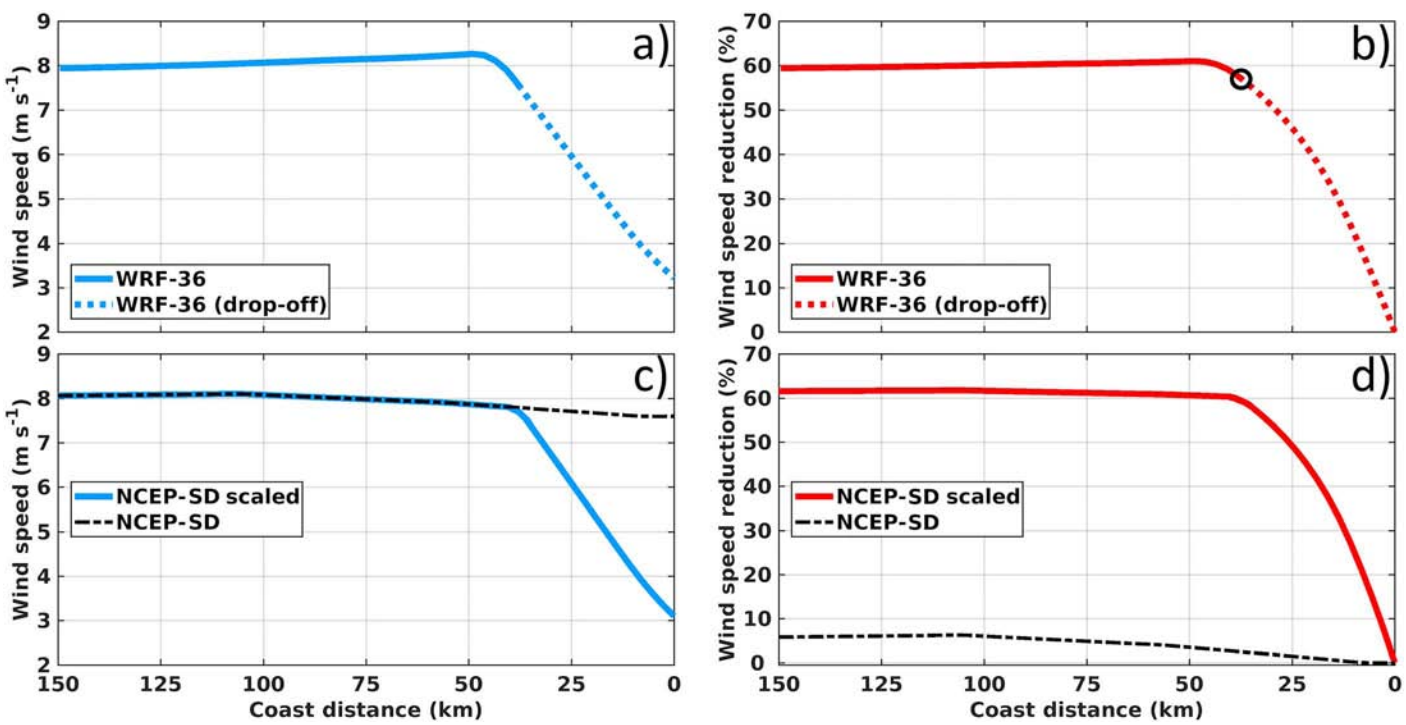

Figure B1. Cross-shore sections of mean alongshore (a) wind speed and (b) percent of wind speed reduction (W_r) at 28.24°S from WRF36 over the period 2007–2008. The black circle and the dotted segments highlight the detected drop-off length (L_d) and the drop-off zone, respectively. (c) Cross-shore section of daily mean (11 October 2008) alongshore wind speed and (d) percent of reduction (W_r) at 28.24°S from NCEP-DS before (black-dashed lines) and after (blue and red lines) the coastal correction. Note how the scaled NCEP-DS wind speed profile starts to mimic the wind drop-off as simulated by the WRF36 domain at a 37.5-km offshore distance from the coast corresponding to the WRF36 wind drop-off length (L_d). WRF = Weather Research and Forecasting; NCEP = National Centers for Environmental Prediction.

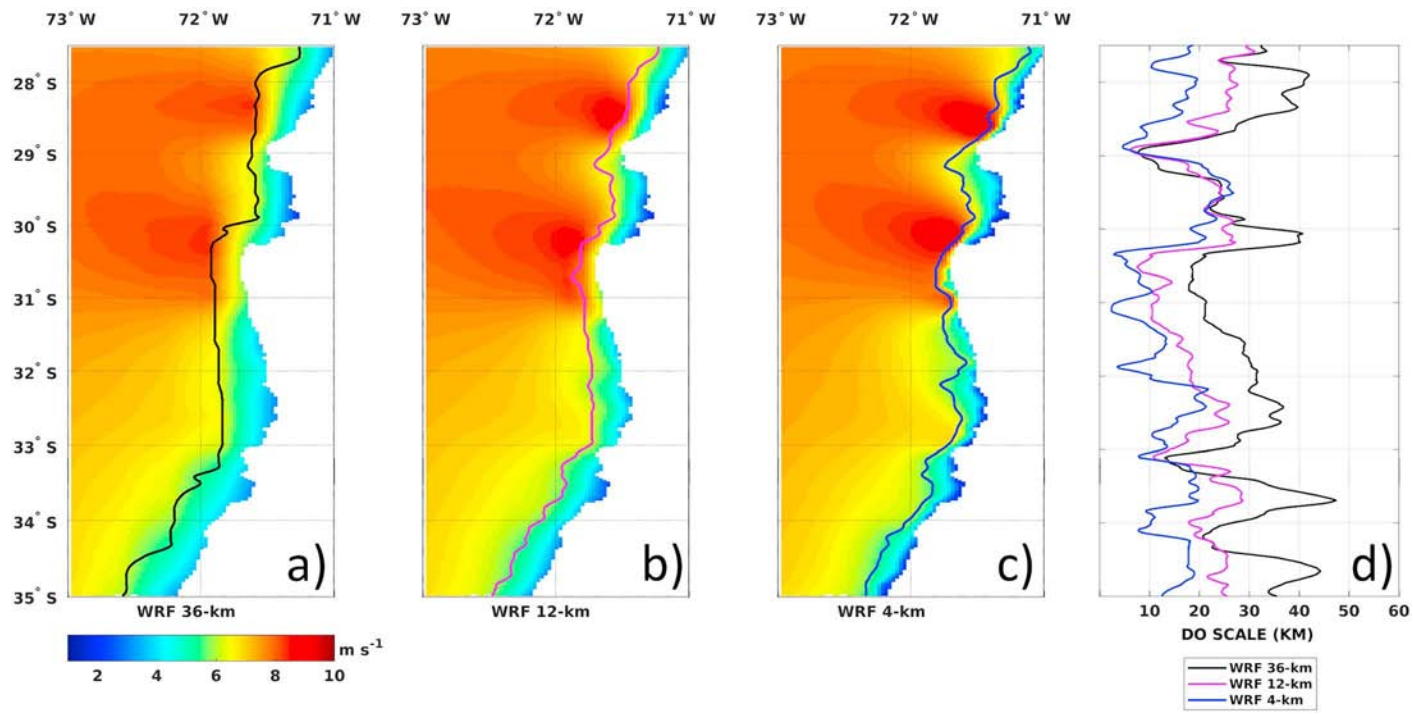

Figure B2. Spatial maps of the temporal mean of the 10-m wind magnitude (m/s) from the triple nest WRF simulation at (a) 36 km, (b) 12 km, and (c) 4 km of spatial resolution over the period 2007–2009. (d) Alongshore wind drop-off length (L_d in km) for the different model resolutions. L_d is estimated by detecting where the cross-shore wind decay rate is >0.5% per kilometer. The black, magenta, and blue lines represent the L_d length for the WRF36, WRF12, and WRF4, respectively. WRF = Weather Research and Forecasting.

decay onshore (growth offshore), corresponding to the slope of W_r at any point x, is approximated using backward differences as

$$\text{wind decay rate} = \frac{\Delta \mathrm{W}_r}{\Delta \mathrm{x}} \tag{B2}$$

Then, L_d is estimated as the offshore distance where the wind decay rate is greatest than 0.5% per kilometer. This threshold results in a better approximation to the apex of the zonal decay profile W_r that features an exponential shape near the coast. Note that equation (B1) assumes that the zonal profile is an acceptable approximation to the cross-shore one. This is based on the values of the coastline angle for the latitudinal extent (27–35°S) of the oceanic model domain that remains close to 90° (i.e., north-south coastline orientation; see green line in Figure 4 from Dewitte et al., 2008).

B2. Wind Drop-Off Characteristics and Sensitivity to Resolution

Before presenting the method to correct coastal wind profiles in the oceanic model atmospheric forcing, we first document here the latitudinal variability of the wind drop-off in the various atmospheric simulations. Figures B2a–B2c show the mean wind magnitude for each WRF domain; highlighting (color lines) the corresponding wind drop-off scales (Figure B2d). The wind drop-off is present all along the coast with L_d varying from 2 to 50 km depending on the latitude/domain. Furthermore, meridional changes in L_d are associated with orography and coastline geometry. For example, south of the main capes and northwest facing embayments and close to the main upwelling centers (e.g., Punta Choros, ~29°S; Punta Lengua de Vaca, ~30°S; and Punta Curaumilla, ~33°S) small values of L_d are recurrent. In most regions, sensitivity to the spatial resolution is observed: the higher the resolution the smaller the wind drop-off length. Only in some latitudes ranges (e.g., between 29°S and 30°S) the wind drop-off length appears relatively insensitive to the resolution of the model, which could be due to the details in the shape of the coastline and/or orography, as the alternation of promontories and bays (Astudillo et al., 2017; Renault et al., 2015).

B3. Coastal Correction of the Wind Forcing

Our oceanic model experiments are forced using a daily wind data set derived from the statistical downscaling of NCEP1 reanalysis (Kalnay et al., 1996) following the method of Goubanova et al. (2011). This product, hereinafter referred to as NCEP-DS, is based on a multiple linear regression between local/regional variables (predictand) and large-scale climate characteristics (predictors). The predictand is the near-surface wind measured by QuikSCAT scatterometer. The large-scale predictors, covering the QuikSCAT period, are the near-surface wind fields from NCEP1 reanalysis data. The statistical model is applied on wind anomalies relative to a reference mean seasonal cycle that is taken from QuikSCAT data. The statistical relationship between predictand and predictors is then used to downscale NCEP1 winds and provide valuable surface forcing for long-term oceanic regional simulations. Although this technique allows an important correction of the surface wind jet patterns off Central Peru and Central Chile (Goubanova et al., 2011), it cannot overcome the limitations of the QuikSCAT data (i.e., the blind zone). We thus complete the coastal gap in NCEP-DS with the information provided by the WRF simulations at different spatial resolution, to produce atmospheric forcing for the regional oceanic model. Specifically, we apply the wind decay percentages of the mean cross-shore WRF profiles following equation (B1) to the daily NCEP-DS winds along the coast. The NCEP-DS wind magnitude at a distance from the coast equal to the WRF wind drop-off length L_d thus starts to decrease shoreward at a rate similar to the WRF simulation until reaching a low value of wind speed at the closest grid point to the coast. As an illustration, the Figures B1c and B1d present the cross-shore wind profile at 28.24°S for the "raw" NCEP-DS wind and for the "corrected" wind based on the WRF36 simulation.

Acknowledgments
O. Astudillo, B. Dewitte, M. Ramos, F. Frappart, and K. Goubanova acknowledge supports from FONDECYT (projects 1171861 and 1151185) and from (Centre National d'Etudes Spatiales, France) through the OSTST SWANS project. O. Astudillo and J. Rutllant thank the Center for Advanced Studies in Arid Zones (CEAZA), La Serena, Chile for financial support. L. Bravo acknowledge support from CONICYT ("Concurso Nacional Inserción en la Academia, Convocatoria 2016, Folio PAI 79160044"). We thank Abderrahim Bentamy (IFREMER) for valuable discussions. We also would like to thank Catalina Aguirre and an anonymous reviewer for their constructive comments that helped to improve substantially the original manuscript. QSCAT/ASCAT gridded wind data were provided by the CERSAT and are available online at ftp://ftp.ifremer.fr/ifremer/cersat/products/gridded/. Altimetry surface wind intensity was derived from the along-track GDR data provided by the Centre de Topographie des Océans et de l'Hydrosphère (CTOH, Toulouse, France) available at http://ctoh.legos.obs-mip.fr. The MUR/OSTIA SST data are available online at http://podaac.jpl.nasa.gov/dataset/MUR-JPL-L4-GLOB-v4.1 and https://podaac.jpl.nasa.gov/dataset/UKMO-L4HRfnd-GLOB-OSTIA, from the National Aeronautics and Space Administration (NASA) at the Jet Propulsion Laboratory (JPL), California Institute of Technology. The altimeter-derived surface geostrophic currents were obtained at the Globcurrent project (http://globcurrent.ifremer.fr) and provided by AVISO (Archiving, Validation and Interpretation of Satellite Oceanographic data) with support from the French Space Agency (Centre National d'Etudes Spatiales,). In situ Meteo-Oceanographic data are distributed by the monitorig network of the Center for Advanced Studies in Arid Zones (CEAZA) at http://www.ceaza-met.cl. Model outputs analyzed in this article are available upon request to the corresponding author. This work was granted access to the HPC resources of CALMIP supercomputing center under the allocations 2017-1044 and 2018-1044.

References

Aguirre, C., Garreaud, R. D., & Rutllant, J. A. (2014). Surface ocean response to synoptic-scale variability in wind stress and heat fluxes off south-central Chile. *Dynamics of Atmospheres and Oceans*, *65*, 64–85. https://doi.org/10.1016/j.dynatmoce.2013.11.001

Aguirre, C., Pizarro, Ó., Strub, P. T., Garreaud, R., & Barth, J. A. (2012). Seasonal dynamics of the near-surface alongshore flow off central Chile. *Journal of Geophysical Research*, *117*, C01006. https://doi.org/10.1029/2011JC007379

Astudillo, O., Dewitte, B., Mallet, M., Frappart, F., Rutllant, J. A., Ramos, M., et al. (2017). Surface winds off Peru-Chile: Observing closer to the coast from radar altimetry. *Remote Sensing of Environment*, *191*, 179–196. https://doi.org/10.1016/j.rse.2017.01.010

Bakun, A. (1973). Coastal upwelling indices, west coast of North America, 1946-71. U.S. Dept. of Commerce, NOAA Tech. Rep., NMFS SSRF-671 (103p).

Bentamy, A., Croize-Fillon, D., & Perigaud, C. (2008). Characterization of ASCAT measurements based on buoy and QuikSCAT wind vector observations. *Ocean Science*, *4*(4), 265–274. https://doi.org/10.5194/os-4-265-2008

Bentamy, A., & Fillon, D. C. (2012). Gridded surface wind fields from Metop/ASCAT measurements. *International Journal of Remote Sensing*, *33*(6), 1729–1754. https://doi.org/10.1080/01431161.2011.600348

Blanco, J. L., Thomas, A. C., Carr, M.-E., & Strub, P. T. (2001). Seasonal climatology of hydrographic conditions in the upwelling region off northern Chile. *Journal of Geophysical Research*, *106*(C6), 11451–11467. https://doi.org/10.1029/2000JC000540

Boé, J., Hall, A., Colas, F., McWilliams, J. C., Qu, X., Kurian, J., & Kapnick, S. B. (2011). What shapes mesoscale wind anomalies in coastal upwelling zones? *Climate Dynamics*, *36*(11–12), 2037–2049. https://doi.org/10.1007/s00382-011-1058-5

Bravo, L., Ramos, M., Astudillo, O., Dewitte, B., & Goubanova, K. (2016). Seasonal variability of the Ekman transport and pumping in the upwelling system off central-northern Chile (30°S) based on a high-resolution atmospheric regional model (WRF). *Ocean Science*, *12*(5), 1049–1065. https://doi.org/10.5194/os-12-1049-2016

Cambon, G., Goubanova, K., Marchesiello, P., Dewitte, B., Illig, S., & Echevin, V. (2013). Assessing the impact of downscaled winds on a regional ocean model simulation of the Humboldt system. *Ocean Modelling*, *65*, 11–24. https://doi.org/10.1016/j.ocemod.2013.01.007

Capet, X., Colas, F., McWilliams, J. C., Penven, P., & Marchesiello, P. (2008). Eddies in eastern boundary subtropical upwelling systems. In *Ocean modeling in an eddying regime*. [On-line, (pp. 131–147). Washington, D. C: American Geophysical Union. https://doi.org/10.1029/177gm10

Capet, X., Estrade, P., Machu, E., Ndoye, S., Grelet, J., Lazar, A., et al. (2017). On the dynamics of the Southern Senegal upwelling center: Observed variability from synoptic to superinertial scales. *Journal of Physical Oceanography*, *47*(1), 155–180. https://doi.org/10.1175/JPO-D-15-0247.1

Capet, X. J., Marchesiello, P., & McWilliams, J. C. (2004). Upwelling response to coastal wind profiles. *Geophysical Research Letters*, *31*, L13311. https://doi.org/10.1029/2004GL020123

Carr, M.-E., & Kearns, E. J. (2003). Production regimes in four Eastern boundary current systems. *Deep Sea Research Part II: Topical Studies in Oceanography*, *50*(22–26), 3199–3221. https://doi.org/10.1016/j.dsr2.2003.07.015

Carton, J. A., & Giese, B. S. (2008). A reanalysis of ocean climate using simple ocean data assimilation (SODA). *Monthly Weather Review*, *136*(8), 2999–3017. https://doi.org/10.1175/2007MWR1978.1

Chavez, F. P., & Messié, M. (2009). A comparison of Eastern boundary upwelling ecosystems. *Progress in Oceanography*, *83*(1–4), 80–96. https://doi.org/10.1016/j.pocean.2009.07.032

Chin, T. M., Milliff, R. F., & Large, W. G. (1998). Basin-scale, high-wavenumber sea surface wind fields from a multiresolution analysis of scatterometer data. *Journal of Atmospheric and Oceanic Technology*, *15*(3), 741–763. https://doi.org/10.1175/1520-0426(1998)015<0741:BSHWSS>2.0.CO;2

Colas, F., McWilliams, J. C., Capet, X., & Kurian, J. (2012). Heat balance and eddies in the Peru-Chile current system. *Climate Dynamics*, *39*(1–2), 509–529. https://doi.org/10.1007/s00382-011-1170-6

Croquette, M., Eldin, G., Grados, C., & Tamayo, M. (2007). On differences in satellite wind products and their effects in estimating coastal upwelling processes in the South-East Pacific. *Geophysical Research Letters*, *34*, L22301. https://doi.org/10.1029/2006GL027538

da Silva, A. M., Young-Molling, C. C., & Levitus, S. (Eds) (1994). Atlas of surface marine data 1994, Volume 1. In *Algorithms and Procedures*, *NOAA Atlas NESDIS*, (Vol. 6, p. 83). Silver Spring, Md: NOAA.

Demarcq, H. (2009). Trends in primary production, sea surface temperature and wind in upwelling systems (1998–2007). *Progress in Oceanography*, *83*(1–4), 376–385. https://doi.org/10.1016/j.pocean.2009.07.022

Desbiolles, F., Blanke, B., Bentamy, A., & Roy, C. (2016). Response of the Southern Benguela upwelling system to fine-scale modifications of the coastal wind. *Journal of Marine Systems*, *156*, 46–55. https://doi.org/10.1016/j.jmarsys.2015.12.002

Dewitte, B., Ramos, M., Echevin, V., Pizarro, O., & duPenhoat, Y. (2008). Vertical structure variability in a seasonal simulation of a medium-resolution regional model of the Eastern South Pacific. *Progress in Oceanography*, *79*(2–4), 120–137. https://doi.org/10.1016/j.pocean.2008.10.014

Dewitte, B., Vazquez-Cuervo, J., Goubanova, K., Illig, S., Takahashi, K., Cambon, G., et al. (2012). Change in El Niño flavours over 1958–2008: Implications for the long-term trend of the upwelling off Peru. *Deep Sea Research Part II: Topical Studies in Oceanography*, *77-80*, 143–156. https://doi.org/10.1016/j.dsr2.2012.04.011

Di Lorenzo, E. (2003). Seasonal dynamics of the surface circulation in the Southern California current system. *Deep Sea Research Part II: Topical Studies in Oceanography*, *50*(14–16), 2371–2388. https://doi.org/10.1016/S0967-0645(03)00125-5

Donlon, C. J., Martin, M., Stark, J., Roberts-Jones, J., Fiedler, E., & Wimmer, W. (2012). The operational sea surface temperature and sea ice analysis (OSTIA) system. *Remote Sensing of Environment*, *116*, 140–158. https://doi.org/10.1016/j.rse.2010.10.017

Dorman, C. E., Dever, E. P., Largier, J., & Koračin, D. (2006). Buoy measured wind, wind stress and wind stress curl over the shelf off Bodega Bay, California. *Deep Sea Research Part II: Topical Studies in Oceanography*, *53*(25–26), 2850–2864. https://doi.org/10.1016/j.dsr2.2006.07.006

Dufois, F., Penven, P., Peter Whittle, C., & Veitch, J. (2012). On the warm nearshore bias in Pathfinder monthly SST products over Eastern boundary upwelling systems. *Ocean Modelling*, *47*, 113–118. https://doi.org/10.1016/j.ocemod.2012.01.007

Edwards, K. A., Rogerson, A. M., Winant, C. D., & Rogers, D. P. (2001). Adjustment of the marine atmospheric boundary layer to a coastal cape. *Journal of the Atmospheric Sciences*, *58*(12), 1511–1528. https://doi.org/10.1175/1520-0469(2001)058<1511:AOTMAB>2.0.CO;2

Escribano, R., & Schneider, W. (2007). The structure and functioning of the coastal upwelling system off central/southern Chile. *Progress in Oceanography*, *75*(3), 343–347. https://doi.org/10.1016/j.pocean.2007.08.020

Estrade, P., Marchesiello, P., De Verdière, A. C., & Roy, C. (2008). Cross-shelf structure of coastal upwelling: A two-dimensional extension of Ekman's theory and a mechanism for inner shelf upwelling shut down. *Journal of Marine Research. Journal of Marine Research/Yale*, *66*(5), 589–616. https://doi.org/10.1357/002224008787536790

Fairall, C. W., Bradley, E. F., Hare, J. E., Grachev, A. A., & Edson, J. B. (2003). Bulk parametrization of air–sea fluxes: Updates and verification for the COARE algorithm. *Journal of Climate*, *16*(4), 571–591. https://doi.org/10.1175/1520-0442(2003)016<0571:BPOASF>2.0.CO;2

Garreaud, R., & Muñoz, R. C. (2005). The low-level jet off the West Coast of subtropical South America: Structure and variability. *Monthly Weather Review*, *133*(8), 2246–2261. https://doi.org/10.1175/mwr2972.1

Garreaud, R., & Rutllant, J. (2003). Coastal lows along the subtropical West Coast of South America: Numerical simulation of a typical case. *Monthly Weather Review*, *131*(5), 891–908. https://doi.org/10.1175/1520-0493(2003)131<0891:CLATSW>2.0.CO;2

Garreaud, R. D., Rutllant, J. A., Muñoz, R. C., Rahn, D. A., Ramos, M., & Figueroa, D. (2011). VOCALS-: the Chilean upwelling experiment. *Atmospheric Chemistry and Physics*, *11*(5), 2015–2029. https://doi.org/10.5194/acp-11-2015-2011

Gill, A. (1982). *Atmosphere-ocean dynamics*. New York: Academic Press.

Goubanova, K., Echevin, V., Dewitte, B., Codron, F., Takahashi, K., Terray, P., & Vrac, M. (2011). Statistical downscaling of sea-surface wind over the Peru–Chile upwelling region: Diagnosing the impact of climate change from the IPSL-CM4 model. *Climate Dynamics*, *36*(7–8), 1365–1378. https://doi.org/10.1007/s00382-010-0824-0

Gruber, N., Frenzel, H., Doney, S. C., Marchesiello, P., McWilliams, J. C., Moisan, J. R., et al. (2006). Eddy-resolving simulation of plankton ecosystem dynamics in the California Current System. *Deep Sea Research Part I: Oceanographic Research Papers*, *53*(9), 1483–1516. https://doi.org/10.1016/j.dsr.2006.06.005

Gruber, N., Lachkar, Z., Frenzel, H., Marchesiello, P., Münnich, M., McWilliams, J. C., et al. (2011). Eddy-induced reduction of biological production in eastern boundary upwelling systems. *Nature Geoscience*, *4*(11), 787–792. https://doi.org/10.1038/NGEO1273

Halpern, D. (2002). Offshore Ekman transport and Ekman pumping off Peru during the 1997–1998 El Niño. *Geophysical Research Letters*, *29*(5), 1075. https://doi.org/10.1029/2001GL014097

Hong, X., Wang, S., Holt, T. R., Martin, P. J., & O'Neill, L. (2013). Modulation of the sea-surface temperature in the Southeast Pacific by the atmospheric low-level coastal jet. *Journal of Geophysical Research: Oceans*, *118*, 3979–3998. https://doi.org/10.1002/jgrc.20289

Hormazabal, S., Shaffer, G., & Leth, O. (2004). Coastal transition zone off Chile. *Journal of Geophysical Research*, *109*, C01021. https://doi.org/10.1029/2003JC001956

Illig, S., Dewitte, B., Goubanova, K., Cambon, G., Boucharel, J., Monetti, F., et al. (2014). Forcing mechanisms of intraseasonal SST variability off central Peru in 2000–2008. *Journal of Geophysical Research: Oceans*, *119*, 3548–3573. https://doi.org/10.1002/2013JC009779

Kalnay, E., Kanamitsu, M., Kistler, R., Collins, W., Deaven, D., Gandin, L., et al. (1996). The NCEP/NCAR 40-year reanalysis project. *Bulletin of the American Meteorological Society*, *77*(3), 437–471. https://doi.org/10.1175/15200477(1996)077<0437:TNYRP>2.0.CO;2

Large, W. G., McWilliams, J. C., & Doney, S. C. (1994). Oceanic vertical mixing: A review and a model with a nonlocal boundary layer parametrization. *Reviews of Geophysics*, *32*(4), 363. https://doi.org/10.1029/94RG01872

Leth, O., & Middleton, J. F. (2004). A mechanism for enhanced upwelling off central Chile: Eddy advection. *Journal of Geophysical Research*, *109*, C12020. https://doi.org/10.1029/2003JC002129

Marchesiello, P., & Estrade, P. (2010). Upwelling limitation by onshore geostrophic flow. *Journal of Marine Research. Journal of Marine Research/Yale*, *68*(1), 37–62. https://doi.org/10.1357/002224010793079004

Marchesiello, P., McWilliams, J. C., & Shchepetkin, A. (2003). Equilibrium structure and dynamics of the California Current System. *Journal of Physical Oceanography*, *33*(4), 753–783. https://doi.org/10.1175/1520-0485(2003)33<753:esadot>2.0.co;2

Mason, E., Colas, F., Molemaker, J., Shchepetkin, A. F., Troupin, C., McWilliams, J. C., & Sangrà, P. (2011). Seasonal variability of the Canary Current: A numerical study. *Journal of Geophysical Research*, *116*, C06001. https://doi.org/10.1029/2010JC006665

Mason, E., Molemaker, J., Shchepetkin, A. F., Colas, F., McWilliams, J. C., & Sangrà, P. (2010). Procedures for off-line grid nesting in regional ocean models. *Ocean Modelling*, *35*(1–2), 1–15. https://doi.org/10.1016/j.ocemod.2010.05.007

Montes, I., Colas, F., Capet, X., & Schneider, W. (2010). On the pathways of the equatorial subsurface currents in the eastern equatorial Pacific and their contributions to the Peru-Chile undercurrent. *Journal of Geophysical Research*, *115*, C09003. https://doi.org/10.1029/2009JC005710

Oerder, V., Colas, F., Echevin, V., Masson, S., Hourdin, C., Jullien, S., et al. (2016). Mesoscale SST–wind stress coupling in the Peru–Chile current system: Which mechanisms drive its seasonal variability? *Climate Dynamics*, *47*(7–8), 2309–2330. https://doi.org/10.1007/s00382-015-2965-7

Paulson, C. A., & Simpson, J. J. (1977). Irradiance measurements in the upper ocean. *Journal of Physical Oceanography*, *7*(6), 952–956. https://doi.org/10.1175/1520-0485(1977)007<0952:IMITUO>2.0.CO;2

Penven, P., Echevin, V., Pasapera, J., Colas, F., & Tam, J. (2005). Average circulation, seasonal cycle, and mesoscale dynamics of the Peru Current System: A modeling approach. *Journal of Geophysical Research*, *110*, C10021. https://doi.org/10.1029/2005JC002945

Penven, P., Roy, C., Lutjeharms, J. R. E., Colin de Verdière, A., Johnson, A., Shillington, F., et al. (2001). A regional hydrodynamic model of the Southern Benguela. *South African Journal of Science*, *97*, 472–476.

Perlin, N., Skyllingstad, E. D., Samelson, R. M., & Barbour, P. L. (2007). Numerical simulation of air–sea coupling during coastal upwelling. *Journal of Physical Oceanography*, *37*(8), 2081–2093. https://doi.org/10.1175/JPO3104.1

Pickett, M. H., & Paduan, J. D. (2003). Ekman transport and pumping in the California Current based on the U.S. Navy's high-resolution atmospheric model (COAMPS). *Journal of Geophysical Research*, *108*(C10), 3327. https://doi.org/10.1029/2003JC001902

Rahn, D. A., & Garreaud, R. D. (2013). A synoptic climatology of the near-surface wind along the west coast of South America. *International Journal of Climatology*, *34*(3), 780–792. https://doi.org/10.1002/joc.3724

Rahn, D. A., Garreaud, R. D., & Rutllant, J. A. (2011). The low-level atmospheric circulation near Tongoy Bay–Point Lengua de Vaca (Chilean Coast, 30°S). *Monthly Weather Review*, *139*(11), 3628–3647. https://doi.org/10.1175/MWR-D-11-00059.1

Renault, L., Deutsch, C., McWilliams, J. C., Frenzel, H., Liang, J.-H., & Colas, F. (2016). Partial decoupling of primary productivity from upwelling in the California Current system. *Nature Geoscience*, *9*(7), 505–508. https://doi.org/10.1038/ngeo2722

Renault, L., Dewitte, B., Marchesiello, P., Illig, S., Echevin, V., Cambon, G., et al. (2012). Upwelling response to atmospheric coastal jets off central Chile: A modeling study of the October 2000 event. *Journal of Geophysical Research*, *117*, C02030. https://doi.org/10.1029/2011JC007446

Renault, L., Hall, A., & McWilliams, J. C. (2015). Orographic shaping of US West Coast wind profiles during the upwelling season. *Climate Dynamics*, *46*(1–2), 273–289. https://doi.org/10.1007/s00382-015-2583-4

Renault, L., Molemaker, M. J., McWilliams, J. C., Shchepetkin, A. F., Lemarié, F., Chelton, D., et al. (2016). Modulation of wind work by oceanic current interaction with the atmosphere. *Journal of Physical Oceanography*, *46*(6), 1685–1704. https://doi.org/10.1175/JPO-D-15-0232.1

Ridgway, K. R., Dunn, J. R., & Wilkin, J. L. (2002). Ocean interpolation by four-dimensional weighted least squares—Application to the waters around Australasia. *Journal of Atmospheric and Oceanic Technology*, *19*(9), 1357–1375. https://doi.org/10.1175/1520-0426(2002)019<1357:OIBFDW>2.0.CO;2

Rio, M.-H., Mulet, S., & Picot, N. (2014). Beyond GOCE for the ocean circulation estimate: Synergetic use of altimetry, gravimetry, and in situ data provides new insight into geostrophic and Ekman currents. *Geophysical Research Letters*, *41*, 8918–8925. https://doi.org/10.1002/2014gl061773

Rutllant, J. A., Masotti, I., Calderón, J., & Vega, S. A. (2004). A comparison of spring coastal upwelling off central Chile at the extremes of the 1996–1997 ENSO cycle. *Continental Shelf Research*, *24*(7–8), 773–787. https://doi.org/10.1016/j.csr.2004.02.005

Scaff, L., Rutllant, J. A., Rahn, D., Gascoin, S., & Rondanelli, R. (2017). Meteorological interpretation of orographic precipitation gradients along an Andes West Slope Basin at 30°S (Elqui Valley, Chile). *Journal of Hydrometeorology*, *18*(3), 713–727. https://doi.org/10.1175/JHM-D-16-0073.1

Send, U. (1989). The origin of eddy heat fluxes in the northern California upwelling regime. *Journal of Geophysical Research*, *94*(C1), 871. https://doi.org/10.1029/JC094iC01p00871

Shchepetkin, A. F., & McWilliams, J. C. (2005). The regional oceanic modeling system (ROMS): A split-explicit, free-surface, topography-following-coordinate oceanic model. *Ocean Modelling*, *9*(4), 347–404. https://doi.org/10.1016/j.ocemod.2004.08.002

Shchepetkin, A. F., & McWilliams, J. C. (2009). Correction and commentary for "Ocean forecasting in terrain-following coordinates: Formulation and skill assessment of the regional ocean modeling system" by Haidvogel et al., J. Comp. Phys. 227, pp. 3595–3624. *Journal of Computational Physics*, *228*(24), 8985–9000. https://doi.org/10.1016/j.jcp.2009.09.002

Skamarock, W. C., & Klemp, J. B. (2008). A time-split nonhydrostatic atmospheric model for weather research and forecasting applications. *Journal of Computational Physics*, *227*(7), 3465–3485. https://doi.org/10.1016/j.jcp.2007.01.037

Smith, R. L. (1968). Upwelling. *Oceanography and Marine Biology: An Annual Review*, *6*, 11–46.

Smith, R. L. (1995). The physical processes of coastal ocean upwelling systems. In C. P. Summerhayes, et al. (Eds.), *Upwelling in the ocean: Modern processes and ancient records*, (pp. 39–64). Hoboken, N. J: John Wiley.

Stark JD, Donlon CJ, Martin MJ and McCulloch ME (2007). OSTIA: An operational, high resolution, real time, global sea surface temperature analysis system. OCEANS 2007 - Europe. paper presented at the OCEANS 2007 - Europe. IEEE. https://doi.org/10.1109/OCEANSE.2007.4302251

Stiles, B. (2014). Discovering a decade of coastal winds from scatterometers, IOVWST (International Ocean Vector Winds Science Team) meeting sponsored by NASA, FSU, COAP, EUMETSAT, , ESA and Ifremer, Brest, France, 2–4 June.

Veitch, J., Penven, P., & Shillington, F. (2010). Modeling equilibrium dynamics of the Benguela Current System. *Journal of Physical Oceanography*, *40*(9), 1942–1964. https://doi.org/10.1175/2010JPO4382.1

Vergara, O., Dewitte, B., Ramos, M., & Pizarro, O. (2017). Vertical energy flux at ENSO time scales in the subthermocline of the Southeastern Pacific. *Journal of Geophysical Research: Oceans*, *122*, 6011–6038. Http://dx.doi.org/10.1002/2016JC012614

Vergara, O., Dewitte, B., Montes, I., Garçon, V., Ramos, M., Paulmier, A., & Pizarro, O. (2016). Seasonal variability of the oxygen minimum zone off Peru in a high-resolution regional coupled model. *Biogeosciences*, *13*(15), 4389–4410. https://doi.org/10.5194/bg-13-4389-2016

Vergara, O. A., Echevín, V., Sepúlveda, H. H., Colas, F., & Quiñones, R. A. (2016). Modelling the seasonal dynamics of the Peru-Chile undercurrent off Central Chile (30–40°S). *Continental Shelf Research*, *123*, 61–79. https://doi.org/10.1016/j.csr.2016.04.001

Verhoef, A., Stoffelen, A., (2013). Validation of ASCAT coastal winds, Version 1.5 Document External Project: 2013, SAF/OSI/CDOP/KNMI/TEC/RP/176, EUMETSAT.

Vogelzang, J., Stoffelen, A., Verhoef, A., & Figa-Saldaña, J. (2011). On the quality of high-resolution scatterometer winds. *Journal of Geophysical Research*, *116*, C10033. https://doi.org/10.1029/2010JC006640

vonStorch, H., & Zwiers, F. W. (1999). *Statistical analysis in climate research*, (p. 494). Cambrigde, UK: Cambridge Univ. Press.

Wang, D., Gouhier, T. C., Menge, B. A., & Ganguly, A. R. (2015). Intensification and spatial homogenization of coastal upwelling under climate change. *Nature*, *518*(7539), 390–394. https://doi.org/10.1038/nature14235

Yang, J. (2006). The seasonal variability of the Arctic Ocean Ekman transport and its role in the mixed layer heat and salt fluxes. *Journal of Climate*, *19*(20), 5366–5387. https://doi.org/10.1175/JCLI3892.1

Chapter 5

General Conclusions and Future Work

In this thesis we have investigated the air-sea-land interactions in the Peru-Chile Upwelling System (PCUS), a major Eastern Boundary Upwelling System (EBUS) that accounts for 16 – 20% (12 million tonnes) of the global fish catch. The PCUS is driven by persistent southerly alongshore wind along the eastern side of the South East Pacific (SEP) anticyclone. This subtropical EBUS presents a marked wind-forced variability at seasonal and intraseasonal time scales associated with the meridional displacement of the surface anticyclone and zonal eastward propagation of mid-latitude frontal systems, respectively. The peak upwelling season occurs in winter off central Peru and in summer off central Chile, in the regions of occurrence of atmospheric Low-Level Jets (LLJ), which is a recurrent mesoscale feature, characterized by episodes of maximum wind speed forced by an interaction between synoptic conditions and coastal topography.

More specifically, we have studied the sensitivity of the dynamical and thermodynamical processes to the cross-shore variability of the winds near the coast in the PCUS. Our main focus was on the shoreward decrease of the surface wind speed, so-called wind drop-off, which modulates Ekman velocities, and thus, the spatial and temporal structure of the upwelling. The study of fine spatial and temporal scales associated with wind drop-off requires the compilation of wind observations and use of numerical models. We used both approaches to assess the various mechanisms occurring at these scales.

In the first part of this work, we have analyzed the data gathered by four altimeter missions (i.e. ENVISAT, Jason-1, Jason-2 and SARAL) spanning more than 10 years of satellite observations. In this analysis we benefited from the potential of radar altimeter systems to measure the surface wind speed near the coast. Indeed, the scarcity of in in-situ observations and limitations of scatterometer retrievals within a 28 to 50-km wide blind zone along the

coastal boundary impede the right description of the mesoscale atmospheric circulation within this narrow coastal fringe where the wind drop-off occurs.

The first outcome of this study is the development of a sound methodology to validate and calibrate the altimeter records against scatterometer observations. The calibration coefficients were inferred from the slope and offset of the regression between both altimeter and scatterometer instantaneous data in the offshore region (i.e. excluding the 50-km width coastal band) with values consistent with previous studies (i.e. slopes near 1.00 and small offsets). The validation of the altimetric winds with respect to scatterometer data indicates an accuracy comparable to the scatterometer measurement. In general, Jason-1 and Jason-2 exhibit higher scores than the ENVISAT and SARAL missions.

The calibrated and gridded alongtrack measurements were then used to characterize the mean state of the dominant alongshore flow, assess the along-track wind drop-off and its influence on coastal upwelling through Ekman pumping/transport. The most striking feature revealed by this analysis is the marked shoreward reduction in wind speed, or drop-off, all along the coast, independently of the offshore wind speed, although the reduction rate varies as a function of latitude. The meridional variability in the magnitude and cross-shore scale of the wind drop-off is shown to be influenced by the orography and the peculiarities of the coastline shape (i.e. bays or promontories). The upwelling estimates are in line with this meridional contrast. However in terms of overall contributions, the results suggests that on average Ekman pumping tends to dominate with respect to Ekman transport over the Peruvian coast, whereas over the central Chilean coast, the Ekman transport is the dominant process. The analysis also suggests that the altimeter data near the coast are suitable to document the seasonal cycle of the wind speed, with Jason-1/Jason-2 achieving the highest skill than ENVISAT/SARAL due wing to their shorter repeat cycle.

Our results demonstrate that the altimeter data are highly valuable for the regional modeling community interested in EBUS since they offer a benchmark dataset to validate regional atmospheric models in near coastal areas, in particular in terms of representation of wind drop-off and its alongshore variability. These results can also help in assessing the optimal resolution of regional atmospheric models (convergence issues) and thus open the possibility to investigate quantitatively to which extent the wind drop-off is influential on the regional oceanic circulation and biogeochemistry. Another practical application is to guide the extrapolation procedure of the scattetometer-based wind forcing for regional ocean modeling in EBUS, in order to adequately represent the nearshore wind structure. Unfortunately, it seems

difficult to go further and propose to “blend” altimeter and scatterometer data in order to include a near-shore drop-off in the scatterometer products, due to the relatively large gaps between altimeter tracks in the meridional direction.

In the second part, we developed a nested grid configuration of the regional atmospheric model (WRF) at three different horizontal resolutions (36km, 12km and 4km) zoomed on the central Chile region. The model was used to document the spatial and seasonal variability of the wind drop-off and its impact on the upwelling dynamics (in the linear sense) through the estimate of Ekman pumping and transport along the coast. As a first step, the simulation was validated based on satellite observations and in-situ automatic weather stations, indicating a realistic representation of the spatial and temporal variability of the wind along the coast by the model.

The simulation exhibits a cyclonic (negative in the Southern hemisphere) wind curl on a coastal-band all along the coast. This negative wind curl is mainly due to the onshore decay of the wind (wind drop-off), which presented length scales (L_d) between 8 and 45 km with a significant latitudinal variability, in agreement with the altimetry-derived wind speed data. When the resolution of the model is increased, the wind drop-off takes place closer to the coast and exhibits a larger meridional variability, consistently with previous studies. Both, wind stress and wind curl have a clear seasonal variability with annual and semiannual components. Alongshore wind stress maxima occurre in spring and fall whereas the minimum is observed in winter.

The relative contribution of the coastal divergence and Ekman pumping to the vertical transport along the coast was then evaluated taking into account the estimated wind drop-off length., The results show a meridional alternation between both mechanisms, modulated by orography and the intricate coastline. Prevalence of positive Ekman pumping is associated with large L_d values, observed in regions with high orography and the presence of embayments along the coast (ie.g. the Coquimbo bay). On the other hand, there is a prevalence of coastal divergence with smaller values of L_d and more intense winds near the coast in sectors characterized by a low topography and the presence of headlands (e.g. Punta Lengua de Vaca and Punta Choros). There is also a combination of both mechanisms in which neither divergence nor coastal Ekman pumping dominated over the other. In terms of total upwelling rates, the vertical transport induced by coastal divergence and Ekman pumping represented 60 and 40 % of the total upwelling transport, respectively.

The regional model allowed for an estimate of the nearshore (coastal fringe of ∼50km) low-level circulation evidencing fine-scale structures of the wind stress curl that cannot be estimated from satellite observations. Considering the overall realism of the model simulation, our study could be used to guide field experiments and gather in situ measurements in order to gain further knowledge in the processes that constrain such features.

The last part of this research project takes advantage of all the previous results to go further in the study of the oceanic response and the upwelling sensitivity to the coastal wind reduction off central Chile, using a validated high-resolution (2.5km) regional oceanic model (ROMS). The sensitivity experiments were forced with different wind drop-off gradients in the 50-km coastal strip. The mean characteristics of these coastal wind patterns were dynamically estimated using the above-mentioned nested configuration of the WRF model (WRF) at horizontal resolutions 36km, 12km and 4km.

The results showed that the different drop-off scales and gradients have the potential to reduce/increase notoriously the Ekman transport/pumping over the 50-km coastal band. However the increase in Ekman pumping associated with the wind drop-off does not always compensate for the decrease in Ekman transport. Overall the compensation between two processes is sensitive to the drop-off scale, i.e. a wider drop-off leads to a higher reduction in the total upwelling mass flux. The reduction in the upwelling transport implies a reduction in the coastal cool bias, reported by previous regional modeling studies in EBUS. We showed that this reduction is proportional to the regionally dependent drop-off scale: the sharper the drop-off the more confined to the coast is the reduction of the cool bias.

The SST differences between various sensitivity experiments are mainly produced by the drop-off impact on the horizontal currents. Indeed, the sensitivity experiments exhibit a notorious reduction in the Chile Coastal Current (CCC) intensity (above 60 m), a stronger alongshore Peru-Chile Undercurrent (PCUC) (with the core at approximately 200m) and a coherent offshore Ekman current at the surface, in agreement with available observations. Furthermore, these SST differences reach the Coastal Transition Zone (CTZ) in association with changes in eddy activity. In fact, in the sharp drop-off experiment the Ekman pumping contribution to the SST cooling does compensates for differences in coastal upwelling. Hence, the reduction in the mean cool bias must rely on mesoscale eddy transport, that laterally redistributes the upwelled cold water from the upper ocean, as shown in the zonal and vertical heat fluxes analysis.

In fact, the cross-shore lateral eddy heat flux is essentially shoreward and acts to flatten the upwelling-tilted mean isothermal surfaces. The vertical flux is upward and its vertical divergence contributes to the restratification process yielding to the pycnocline in opposition to vertical mixing by boundary-layer turbulence. Moreover, the sensitivity experiments exhibit significant differences in the magnitude and location of the peak value of the mean eddy heat flux, although this is latitudinally dependent. The mean eddy flux of the control experiment exhibits a lower amplitude than the experiments forced with a sharp or mean wind reduction for all the transects located in the regions where a cool bias was diagnosed near the coast. However the simulation using a wider wind cross-shore gradient shows lower amplitude than the control experiment revealing the eddy heat flux sensitivity to the drop-off scale.

Additionally, we also found that the drop-off characteristics influenced significantly the EKE field over the whole model domain. On the one hand, the mean onshore EKE amplitude in the control simulation is larger than in all the sensitivity experiments, and the wide drop-off experiment exhibits the larger reduction in EKE, which means that a wider drop-off implies a lower EKE in the coastal region. On the other hand, off shore, in the regions of largest mean EKE in the control simulation, EKE tends to decrease in the presence of a wind drop-off.

Now, we briefly review the main limitations of our study:
While altimetric data can provide a complementary useful data set to validate the coastal correction in the surface forcing of the ocean model, they have so far a low latitudinal resolution. This prevents a systematic validation considering that the atmospheric model simulations indicate a large latitudinal variability in the wind drop-off length and that the higher-resolution wind forcing does not systematically yield the more realistic reduction of the cool bias evidenced in the control run experiment. This means that other important processes that are not realistically accounted for in our model set up may be at work locally for explaining the discrepancies between model and observations (i.e. the cool bias). One potentially important process is mixing (vertical and horizontal diffusivity) that is highly parametrized in the model and dependent on model resolution. A comprehensive heat budget of the mixed layer would allow identifying the sources of the “remaining” SST bias in the sensitivity experiments, which is beyond the scope of the present study, considering the requirement to address this issue in a fully coupled framework in order to discriminate error sources among other potentially important processes (e.g. air-sea-land coupling).

As a matter of fact, regarding our modeling set up, there are several limitations that would be worth addressing in order to improve the realism of our simulations. Recent studies

indicate that the characteristics (mainly amplitude) of the turbulent flow (i.e. mean EKE) are significantly dependent on mesoscale air-sea interactions (Renault et al., 2016a,b). In particular the current feedback (i.e. the consideration of the relative wind in the wind stress formulation) has an "eddy-killing" effect reducing mean EKE, while the thermal coupling (i.e. the marine boundary layer response to underlying SST) tends to enhance mean EKE. The combined effect of these two processes has been shown to yield more realistic level of mean EKE in regional model simulations of the California upwelling system (Renault et al., 2016a). While this air-sea coupling at mesoscale is apparently mostly influential in the off-shore region where eddies emerge at the surface, it would be useful to document its effect in our modeling system using the proposed ad-hoc parameterization for taking into account for the effect of thermal coupling (Renault et al., 2016b), which is computationally cost effective compared to running a fully coupled regional model. This is planned for future work. Despite the limitation mentioned above, our results offer a perspective for improving the realism of regional oceanic forced simulations of EBUS in a cost effective way by correcting relatively low-resolution wind products, in particular those derived from scatterometers (i.e. QuickSCAT/ASCAT) which are the most used for regional modeling in EBUS.

Future directions of research also include the investigation of the atmospheric processes associated with the wind drop-off so as to better understand the large meridional variability in the sensitivity to the resolution of the model (i.e. the fact that the wind drop-off appears insensitive to resolution in some regions and not in others). While one could follow a similar approach as in Renault et al. (2015) (i.e. vorticity budget and sensitivity experiments to orography), this issue may also require refining topographic features in the atmospheric model along with resolution, as well as an explicit consideration of air-sea-land coupling (i.e. using a fully coupled ocean-atmospheric regional model) accounting for the potentially important influence of SST on the marine boundary atmospheric layer at seasonal timescales (Bravo et al., 2016) and at higher frequencies (Garreaud et al., 2011). Local atmospheric processes, as the breeze regime tight to orographic features in the Elqui valley in Coquimbo region (Scaff et al., 2017) should also be considered.

This study is also viewed as a preliminary step for addressing finer scale variability in the oceanic circulation (i.e. bay's circulation) through downscaling experiments and to guide in the implementation of a regional observing system. In particular CEAZA is maintaining a dense network of meteorological stations in the Coquimbo region (http://www.ceazamet.cl) and our results could provide guidance for optimizing this network. We are also aiming at carrying specific field campaigns to measure the wind drop-off in some key regions where

the model indicates a weak improvement in the mean coastal SST in order to verify the atmospheric model solution and investigate local effects (e.g. orographic effect, SST coupling). There is also a societal demand for improving the predictive capability of the marine resources and risks/hazards. We are aiming to build upon this work to investigate some aspects of the biogeochemical response associated with changes in the characteristics of the mesoscale low-level circulation in this regions, considering that this region is embedded in one of the largest Oxigen Minimum Zone (OMZ) of the world and hosts important fisheries. This can be handled with our modeling set up coupling with a biogeochemical model that has been used for the Peru-Chile region to simulate the OMZ seasonal variability (Vergara et al., 2016).

5.1 Conclusions et Perspectives (Français)

Dans cette thèse, nous avons étudié les interactions océan-atmosphère-continent sur le système d'upwelling du Pérou et du Chili (PCUS). Le PCUS est contraint par des vents persistants du sud le long du côté est de l'anticyclone du Pacifique Sud-Est (SEP), lesquels présente une variabilité saisonnière et intrasaisonnière associée au déplacement méridien de l'anticyclone de surface et à la propagation zonale vers l'est des systémes frontaux des latitudes moyennes (i.e. storm track), respectivement. Prés de la côte, dans une frange de quelques dizaines de kilomètre, ces vents subissent une réduction drastique, appelé drop-off qui se couple fortement à la dynamique océanique.

Pour la premier fois, nous documentons ce phénomene de drop-off a partir de données satellites, les instruments conventionnels (diffusiometres) ne fournissant pas d'information dans une zone aveugle (blind zone) côtière de l'ordre de 30 km. Nous avons analysé les données recueillies de quatre missions altimétriques (ENVISAT, Jason-1, Jason-2 et SARAL) couvrant plus de 10 ans d'observations par satellite. Dans cette analyse, nous avons profite du potentiel des systèmes altimétriques pour mesurer la vitesse du vent de surface près de la côte. Nous élaborons en particulier une méthodologie pour valider et calibrer les données altimétriques. La validation des vents altimétriques par rapport aux données du diffusiomètre indique une précision comparable à la mesure du diffusiomètre. En général, Jason-1 et Jason-2 fournissent des données de meilleure qualité que celles de ENVISAT et SARAL. L'analyse des données indique que le drop-off est un phénomène permanent le long de la cote du Pérou et du Chili mais que son intensité (ou taux de réduction) varie en fonction de la latitude. Ces variations sont reliées à l'orographie et les particularités de la ligne de côte. Les estimations de l'upwelling sont conformes à ce contraste méridional. Cependant, en termes

de contributions globales, les résultats suggèrent qu'en moyenne, le pompage d'Ekman tend à dominer le transport d'Ekman sur la côte péruvienne, alors que sur la côte centrale chilienne, le transport d'Ekman est le processus dominant. L'analyse suggère également que les données altimétriques près de la côte permettent de documenter le cycle saisonnier de la vitesse du vent, avec Jason-1/Jason-2 conduisant à de meilleures résultats en raison de leur cycle de répétition plus court.

Nos résultats montrent ainsi que les données altimétriques sont très utiles à la communauté de modélisation régionale intéressée par l'EBUS puisqu'elles offrent un ensemble de données de référence pour valider les modèles atmosphériques régionaux dans les zones côtières, en particulier en termes de représentation du drop-off et de sa variabilité le long de la côte. Ces résultats peuvent également aider à évaluer la résolution optimale des modèles atmosphériques régionaux (questions de convergence) et ouvre ainsi la possibilité d'étudier quantitativement dans quelle mesure la diminution du vent a une influence sur la circulation océanique régionale et la biogéochimie. Une autre application pratique consiste à guider la procédure d'extrapolation des produits de Reanalyses atmosphériques ou des diffusiométres pour la modélisation régionale de l'océan cótier, afin de représenter de manière réaliste la structure des vents le long de la côte. Malheureusement, il semble difficile d'aller plus loin et de proposer un "blending" des données altimètriques et diffusiomètrique prés de la côte, en raison des écarts relativement importants entre les traces altimétriques dans la direction méridionale.

Dans une seconde phase de l'étude, nous avons développé une configuration du modèle atmosphérique régional (WRF) avec des domaines emboîtés à trois résolutions horizontales différentes (36km, 12km et 4km), zoomé sur la région de Chile Central. Le modèle a été utilisé pour documenter la variabilité spatiale et saisonnière de la décroissance du vent et son impact sur la dynamique de l'upwelling (au sens linéaire) par l'estimation du pompage et du transport d'Ekman le long de la côte. Dans un premier temps, la simulation a été validée à partir d'observations satellitaires et de stations météorologiques automatiques in situ, indiquant une représentation réaliste de la variabilité spatiale et temporelle du vent côtier.

La simulation montre un rotationnel de vent cyclonique (négative dans l'hémisphère sud) sur une bande côtière tout le long de la côte. Ce dernier est explique par la décroissance du vent vers la côte, qui présentait des échelles de longueur (L_d) entre 8 et 45 km avec une variabilité latitudinale significative, en accord avec les données dérivées de l'altimétrie. Lorsque la résolution du modèle est augmentée, la drop-off se produit plus près de la côte et présente

une plus grande variabilité méridionale, conformément aux études antérieures. La tension et rotationnel de vent ont une variabilité saisonnière claire avec des composantes annuelles et semestrielles bien marquées. Le maximum de tension du vent le long de la côte se produit au printemps et à l'automne, alors que le minimum est observé en hiver.

Le modèle régional a permis d'estimer la circulation de la frange côtier (50km), ce qui met en évidence des structures à fine échelle du rotationnel de vent qui ne peuvent être estimées à partir d'observations satellitaires. En considérant le réalisme général de la simulation, notre étude pourrait être utilisée pour guider les campagnes d'échantillonnage in situ afin d'acquérir de nouvelles connaissances sur les processus qui déterminent ces caractéristiques.

La dernière partie de la thèse s'appuie sur tous les résultats précédents pour aller plus loin dans l'étude de la réponse océanique et de la sensibilité de l'upwelling à la diminution des vents côtiers au Chili central. Ce volet de l'étude est basé sur l'utilisation d'un modèle océanique régional (ROMS) à haute résolution (2.5 km). Des expériences de sensibilité ont été menées avec différents forąges atmosphériques rendant compte du drop-off du vent dans la bande côtiére de 50 km avec différentes caractéristiques. Ces forçages sont issus de la configuration emboîtés du modèle WRF (résolutions de 36 km, 12 km et 4 km).

Les résultats indiquent tout d'abord que la considération d'un drop-off réaliste dans le forçage du model océanique peut modifier de manière significative la contribution relative des processus de transport et pompage d'Ekman sur la bande côtière de 50 km. Cependant, l'augmentation du pompage d'Ekman associée à la décroissance du vent ne compense pas toujours la diminution du transport d'Ekman. Dans l'ensemble, la compensation entre deux processus est sensible à l'échelle de diminution du vent, c'est-à-dire qu'un déclin plus large entraîne une réduction plus importante du flux de masse total d'eau associé à l'upwelling. La réduction de l'upwelling implique une réduction du biais froid côtier, signalé par des études de modélisation régionale précédentes dans l'EBUS. Nous avons montré que cette réduction est proportionnelle à l'échelle de diminution du vent dépendant de la région : un drop-off plus proche à la côte génère une réduction moindre du biais froid.

Les différences en température de surface de la mer (TSM) entre les différentes expériences numériques de sensibilité sont principalement associées à l'impact de la décroissance du vent sur les courants horizontaux. En effet, les expériences de sensibilité montrent une réduction notoire de l'intensité du courant côtier chilien (au-dessus de 60 m), un courant sous-marin Pérou-Chili (PCUC) plus fort le long de la côte (avec le noyau à environ 200 m)

et un courant d'Ekman vers le large cohérent à la surface, en accord avec les observations disponibles. De plus, ces différences de TSM atteignent la zone de transition côtière (CTZ) en association avec des changements dans l'activité tourbillonnaire. En fait, dans l'expérience avec un drop-off intense et proche de la côte, la contribution du pompage d'Ekman au refroidissement de la TSM ne compense pas les différences dans l'upwelling. Par conséquent, la réduction du biais froid doit reposer sur le transport des tourbillons à méso-échelle, qui redistribue latéralement l'eau froide, comme le montre l'analyse des flux de chaleur tourbillonnaire zonaux. En outre, nous constatons également que les caractéristiques de déclin ont influencé de manière significative le champ d'énergie cinétique turbulente (de l'anglais Eddy Kinetic Energy) de surface sur l'ensemble du domaine du modèle.

Nos résultats dans leur ensemble soulèvent plusieurs questions qui mériteraient d'être abordées comme perspective de travail futur afin d'am'eliorer le réalisme des simulations et prendre en compte d'autres éléments de la complexité du système. Par example, un bilan de chaleur de la couche de mélange explicite permettrait d'identifier les sources du biais "manquants" dans les expériences de sensibilité. Cela pourrait être réalisé à partir d'une plateforme de modélisation Océan/Atmosphère entièrement couplée afin de distinguer les sources d'erreur parmi d'autres processus potentiellement importants par exemple, les interactions océan-atmosphére à fines échelles, et s'assurer que le bilan soit fermée par conservation des flux à l'interface air-mer.

Les orientations futures de la recherche comprennent également l'étude des processus atmosphériques associés à la décroissance du vent afin de mieux comprendre leur grande variabilité méridionale et sensibilité à la résolution du modèle.

Cette étude est également considérée comme une étape préliminaire pour aborder la variabilité à plus petite échelle de la circulation océanique par des expériences de réduction d'échelle et pour guider la mise en œuvre d'un système d'observation régional.

Nous visons également à mener des campagnes de terrain spécifiques pour mesurer la diminution du vent dans certaines régions clés où le modèle indique une faible amélioration de la TSM côtière moyenne afin de vérifier la solution du modèle atmosphérique et d'étudier les effets locaux (p. ex. effet orographique, couplage TSM).

Il existe également une demande sociétale pour l'amélioration de la capacité de prévision des ressources marines et des risques. Nous nous appuyons sur ces travaux pour étudier certains

aspects de la réponse biogéochimique associée aux changements dans les caractéristiques de la circulation mésoéchelle à basse altitude dans cette région, étant donné que cette région fait partie de l'une des plus grandes zones minimales d'Oxigène (OMZ) du monde et qu'elle abrite d'importantes pêcheries. Ceci peut être géré avec notre système de couplage avec un modèle biogéochimique qui a été utilisé pour la région Pérou-Chili pour simuler la variabilité saisonnière de l'OMZ.

List of Abbreviations

μM Micromole

ABL Atmospheric Boundary Layer

AltiKa Ka-band Altimeter

AMOC Atlantic Meridional Overturning Circulation

ARGOS Airborne Remote Geographic/Oceanographic System

ASCAT Advanced SCATterometer

CalCS California Current System

CFSR Climate Forecast System Reanalysis

CGCM Coupled General Circulation Model

CJ Coastal Jet

CLIVAR Climate Variability and Predictability

CMIP Coupled Model Intercomparison Project

CO_2 Carbon dioxide

COAMPS Coupled Ocean/Atmosphere Mesoscale Prediction System

CUpEx Chilean Upwelling Experiment

D_E Ekman depth

DO Dissolved Oxygen

EBC Eastern Boundary Current

EBUS Eastern Boundary Upwelling Systems

ECMWF European Centre for Medium-Range Weather Forecasts

ECUI Ekman Coastal Upwelling Index

EKE Eddy Kinetic Energy

ENVISAT ENVironment SATellite

ERS European Remote Sensing Satellite

GOES Geostationary Operational Environmental Satellite

GPP Gross Primary Productivity

HCS Humboldt Current System

IMBeR Integrated Marine Biogeochemistry and Ecosystem Research

IOC-UNESCO Intergovernmental Oceanographic Commission of UNESCO

IPCC International Climate Change Plan

JASON Joint Altimetry Satellite Oceanography Network

LLJ Low-Level Jet

LME Large Marine Ecosystem

MBL Marine Boundary Layer

ml L^{-1} Milliliter per Liter

MODIS Moderate Resolution Imaging Spectroradiometer

N_2O Nitrous oxide

NASA National Aeronautics and Space Administration

NCAR National Center for Atmospheric Research

NCEP National Centers for Environmental Prediction

NPP Net Primary Productivity

OISST Optimum Interpolation Sea Surface Temperature

OM Organic matter

OMZ Oxygen Minimum Zones

PCUS Peru-Chile Upwelling System

pH Scale of acidity

ppm Parts per million

PreVOCA Preliminary VOCALS Model Assessment

PUC Poleward UnderCurrent

QuikSCAT Quick SCATterometer

ROMS Regional Ocean Modeling System

SARAL Satellite with ARgos and ALtiKa

SCD Stratocumulus Cloud Deck

SOLAS Surface Ocean - Lower Atmosphere Study

SST Sea Surface Temperature

SVD Singular Value Decomposition

UNEP United Nations Environment Programme

UNESCO United Nations Educational, Scientific and Cultural Organization

VAMOS Variability of the American Monsoon Systems

VOCALS VAMOS Ocean-Cloud-Atmosphere-Land Study

WASWind Wave and Anemometer-based Sea-surface Wind

WRF Weather Research and Forecasting model

Bibliography

Catalina Aguirre, Óscar Pizarro, Paul T. Strub, René Garreaud, and John A. Barth. Seasonal dynamics of the near-surface alongshore flow off central chile. *Journal of Geophysical Research: Oceans*, 117(C1):n/a–n/a, Jan 2012. doi: 10.1029/2011jc007379. URL http://dx.doi.org/10.1029/2011JC007379.

Catalina Aguirre, René D. Garreaud, and José A. Rutllant. Surface ocean response to synoptic-scale variability in wind stress and heat fluxes off south-central chile. *Dynamics of Atmospheres and Oceans*, 65:64–85, Mar 2014. doi: 10.1016/j.dynatmoce.2013.11.001. URL http://dx.doi.org/10.1016/j.dynatmoce.2013.11.001.

A. Albert, V. Echevin, M. Lévy, and O. Aumont. Impact of nearshore wind stress curl on coastal circulation and primary productivity in the peru upwelling system. *Journal of Geophysical Research*, 115(C12), Dec 2010. doi: 10.1029/2010jc006569. URL http://dx.doi.org/10.1029/2010jc006569.

J. Arístegui, P. Tett, A. Hernández-Guerra, G. Basterretxea, M.F. Montero, K. Wild, P. Sangrá, S. Hernández-Leon, M. Canton, J.A. García-Braun, and et al. The influence of island-generated eddies on chlorophyll distribution: a study of mesoscale variation around gran canaria. *Deep Sea Research Part I: Oceanographic Research Papers*, 44(1):71–96, Jan 1997. doi: 10.1016/s0967-0637(96)00093-3. URL http://dx.doi.org/10.1016/S0967-0637(96)00093-3.

O. Astudillo, B. Dewitte, M. Mallet, F. Frappart, J.A. Rutllant, M. Ramos, L. Bravo, K. Goubanova, and S. Illig. Surface winds off peru-chile: Observing closer to the coast from radar altimetry. *Remote Sensing of Environment*, 191:179–196, Mar 2017. doi: 10.1016/j.rse.2017.01.010. URL http://dx.doi.org/10.1016/j.rse.2017.01.010.

A Bakun. Coastal upwelling indices, west coast of north america. us department of commerce. *NOAA Technical Report, NMFS SSRF-671*, 1973.

A. Bakun. Coastal ocean upwelling. *Science*, 247(4939):198–201, Jan 1990. doi: 10.1126/science.247.4939.198. URL http://dx.doi.org/10.1126/science.247.4939.198.

A. Bakun, B. A. Black, S. J. Bograd, M. García-Reyes, A. J. Miller, R. R. Rykaczewski, and W. J. Sydeman. Anticipated effects of climate change on coastal upwelling ecosystems. *Current Climate Change Reports*, 1(2):85–93, Mar 2015. doi: 10.1007/s40641-015-0008-4. URL http://dx.doi.org/10.1007/s40641-015-0008-4.

J. M. Bane. Atmospheric forcing of the oregon coastal ocean during the 2001 upwelling season. *Journal of Geophysical Research*, 110(C10), 2005. doi: 10.1029/2004jc002653. URL http://dx.doi.org/10.1029/2004JC002653.

E.D. Barton and J. Arístegui. The canary islands coastal transition zone – upwelling, eddies and filaments. *Progress in Oceanography*, 62(2–4):67–69, Aug 2004. doi: 10.1016/j.pocean.2004.08.003. URL http://dx.doi.org/10.1016/j.pocean.2004.08.003.

Ali Belmadani, Vincent Echevin, Francis Codron, Ken Takahashi, and Clémentine Junquas. What dynamics drive future wind scenarios for coastal upwelling off peru and chile? *Climate Dynamics*, 43(7–8):1893–1914, Dec 2013. doi: 10.1007/s00382-013-2015-2. URL http://dx.doi.org/10.1007/s00382-013-2015-2.

Sandrine Bony and Jean-Louis Dufresne. Marine boundary layer clouds at the heart of tropical cloud feedback uncertainties in climate models. *Geophysical Research Letters*, 32 (20), 2005. doi: 10.1029/2005gl023851. URL http://dx.doi.org/10.1029/2005GL023851.

Luis Bravo, Marcel Ramos, Orlando Astudillo, Boris Dewitte, and Katerina Goubanova. Seasonal variability of the ekman transport and pumping in the upwelling system off central-northern chile based on a high-resolution atmospheric regional model (wrf). *Ocean Science*, 12(5):1049–1065, Sep 2016. doi: 10.5194/os-12-1049-2016. URL http://dx.doi.org/10.5194/os-12-1049-2016.

X. Capet, E. J. Campos, and A. M. Paiva. Submesoscale activity over the argentinian shelf. *Geophysical Research Letters*, 35(15), Aug 2008. doi: 10.1029/2008gl034736. URL http://dx.doi.org/10.1029/2008GL034736.

X. J. Capet, P. Marchesiello, and J. C. McWilliams. Upwelling response to coastal wind profiles. *Geophysical Research Letters*, 31(13):n/a–n/a, Jul 2004. doi: 10.1029/2004gl020123. URL http://dx.doi.org/10.1029/2004GL020123.

Douglas G. Capone and David A. Hutchins. Microbial biogeochemistry of coastal upwelling regimes in a changing ocean. *Nature Geoscience*, 6(9):711–717, Sep 2013. doi: 10.1038/ngeo1916. URL http://dx.doi.org/10.1038/ngeo1916.

Mary-Elena Carr. Estimation of potential productivity in eastern boundary currents using remote sensing. *Deep Sea Research Part II: Topical Studies in Oceanography*, 49(1?3): 59?80, Jan 2001. doi: 10.1016/s0967-0645(01)00094-7. URL http://dx.doi.org/10.1016/S0967-0645(01)00094-7.

Alexis Chaigneau, Gérard Eldin, and Boris Dewitte. Eddy activity in the four major upwelling systems from satellite altimetry (1992–2007). *Progress in Oceanography*, 83(1–4):117–123, Dec 2009. doi: 10.1016/j.pocean.2009.07.012. URL http://dx.doi.org/10.1016/j.pocean.2009.07.012.

Zanna Chase, Peter G. Strutton, and Burke Hales. Iron links river runoff and shelf width to phytoplankton biomass along the u.s. west coast. *Geophysical Research Letters*, 34(4), Feb 2007. doi: 10.1029/2006gl028069. URL http://dx.doi.org/10.1029/2006GL028069.

Jr. Checkley, David M. and John A. Barth. Patterns and processes in the california current system. *Progress in Oceanography*, 83(1–4):49–64, Dec 2009. doi: 10.1016/j.pocean.2009.07.028. URL http://dx.doi.org/10.1016/j.pocean.2009.07.028.

Dudley Chelton and Shang-Ping Xie. Coupled ocean-atmosphere interaction at oceanic mesoscales. *Oceanography*, 23(4):52–69, Dec 2010. doi: 10.5670/oceanog.2010.05. URL http://dx.doi.org/10.5670/oceanog.2010.05.

Dudley B. Chelton, Michael G. Schlax, and Roger M. Samelson. Summertime coupling between sea surface temperature and wind stress in the california current system. *Journal of Physical Oceanography*, 37(3):495–517, Mar 2007. doi: 10.1175/jpo3025.1. URL http://dx.doi.org/10.1175/JPO3025.1.

Dudley B. Chelton, Michael G. Schlax, and Roger M. Samelson. Global observations of nonlinear mesoscale eddies. *Progress in Oceanography*, 91(2):167–216, Oct 2011. doi: 10.1016/j.pocean.2011.01.002. URL http://dx.doi.org/10.1016/j.pocean.2011.01.002.

Sallie W. Chisholm. Stirring times in the southern ocean. *Nature*, 407(6805):685–686, Oct 2000. doi: 10.1038/35037696. URL http://dx.doi.org/10.1038/35037696.

Guillem Chust, J. Icarus Allen, Laurent Bopp, Corinna Schrum, Jason Holt, Kostas Tsiaras, Marco Zavatarelli, Marina Chifflet, Heather Cannaby, Isabelle Dadou, and et al. Biomass changes and trophic amplification of plankton in a warmer ocean. *Global Change Biology*, 20(7):2124–2139, May 2014. doi: 10.1111/gcb.12562. URL http://dx.doi.org/10.1111/gcb.12562.

I.M. Cohen, P.K. Kundu, and H. Hu. *Fluid Mechanics*. Elsevier Science, 2004. ISBN 9780080470238. URL https://books.google.cl/books?id=jm1lS6EcILUC.

Marco A. Correa-Ramirez, Samuel Hormazábal, and Gabriel Yuras. Mesoscale eddies and high chlorophyll concentrations off central chile (29°–39°s). *Geophysical Research Letters*, 34(12), Jun 2007. doi: 10.1029/2007gl029541. URL http://dx.doi.org/10.1029/2007GL029541.

Marie Croquette, Gérard Eldin, Carmen Grados, and Myrian Tamayo. On differences in satellite wind products and their effects in estimating coastal upwelling processes in the south-east pacific. *Geophysical Research Letters*, 34(11), Jun 2007. doi: 10.1029/2006gl027538. URL http://dx.doi.org/10.1029/2006gl027538.

Philippe Cury and Claude Roy. Optimal environmental window and pelagic fish recruitment success in upwelling areas. *Canadian Journal of Fisheries and Aquatic Sciences*, 46(4): 670–680, Apr 1989. doi: 10.1139/f89-086. URL http://dx.doi.org/10.1139/f89-086.

B. Cushman-Roisin. *Introduction to Geophysical Fluid Dynamics*. Prentice Hall, 1994. ISBN 9780133533019. URL https://books.google.cl/books?id=nL8RAQAAIAAJ.

Simon P. de Szoeke, Christopher W. Fairall, Daniel E. Wolfe, Ludovic Bariteau, and Paquita Zuidema. Surface flux observations on the southeastern tropical pacific ocean and attribution of sst errors in coupled ocean–atmosphere models. *Journal of Climate*, 23(15): 4152–4174, Aug 2010. doi: 10.1175/2010jcli3411.1. URL http://dx.doi.org/10.1175/2010jcli3411.1.

D. P. Dee, S. M. Uppala, A. J. Simmons, P. Berrisford, P. Poli, S. Kobayashi, U. Andrae, M. A. Balmaseda, G. Balsamo, P. Bauer, and et al. The era-interim reanalysis: configuration and performance of the data assimilation system. *Quarterly Journal of the Royal Meteorological Society*, 137(656):553–597, Apr 2011. doi: 10.1002/qj.828. URL http://dx.doi.org/10.1002/qj.828.

F. Desbiolles, B. Blanke, and A. Bentamy. Short-term upwelling events at the western african coast related to synoptic atmospheric structures as derived from satellite observations. *Journal of Geophysical Research: Oceans*, 119(1):461–483, Jan 2014. doi: 10.1002/2013jc009278. URL http://dx.doi.org/10.1002/2013JC009278.

F. Desbiolles, B. Blanke, A. Bentamy, and C. Roy. Response of the southern benguela upwelling system to fine-scale modifications of the coastal wind. *Journal of Marine Systems*, 156:46–55, Apr 2016. doi: 10.1016/j.jmarsys.2015.12.002. URL http://dx.doi.org/10.1016/j.jmarsys.2015.12.002.

Emanuele Di Lorenzo. Seasonal dynamics of the surface circulation in the southern california current system. *Deep Sea Research Part II: Topical Studies in Oceanography*, 50(14–16):2371–2388, Aug 2003. doi: 10.1016/s0967-0645(03)00125-5. URL http://dx.doi.org/10.1016/S0967-0645(03)00125-5.

Changming Dong, James C. McWilliams, Yu Liu, and Dake Chen. Global heat and salt transports by eddy movement. *Nature Communications*, 5, Feb 2014. doi: 10.1038/ncomms4294. URL http://dx.doi.org/10.1038/ncomms4294.

Clive E. Dorman, Edward P. Dever, John Largier, and Darko Koračin. Buoy measured wind, wind stress and wind stress curl over the shelf off bodega bay, california. *Deep Sea Research Part II: Topical Studies in Oceanography*, 53(25–26):2850–2864, Dec 2006. doi: 10.1016/j.dsr2.2006.07.006. URL http://dx.doi.org/10.1016/j.dsr2.2006.07.006.

François Dufois, Pierrick Penven, Christo Peter Whittle, and Jennifer Veitch. On the warm nearshore bias in pathfinder monthly sst products over eastern boundary upwelling systems. *Ocean Modelling*, 47:113–118, Jan 2012. doi: 10.1016/j.ocemod.2012.01.007. URL http://dx.doi.org/10.1016/j.ocemod.2012.01.007.

Vincent Echevin, Katerina Goubanova, Ali Belmadani, and Boris Dewitte. Sensitivity of the humboldt current system to global warming: a downscaling experiment of the ipsl-cm4 model. *Climate Dynamics*, 38(3–4):761–774, May 2011. doi: 10.1007/s00382-011-1085-2. URL http://dx.doi.org/10.1007/S00382-011-1085-2.

V Walfrid Ekman. Die zusammendrueckbarkeit des meer wassers nebst einigen werten fuer wasser und quecksilber. *Publications de Circonstance*, 1(43):1–47, 1908.

Philippe Estrade, Patrick Marchesiello, Alain Colin De Verdière, and Claude Roy. Cross-shelf structure of coastal upwelling: A two — dimensional extension of ekman's theory and a mechanism for inner shelf upwelling shut down. *Journal of Marine Research*, 66(5):589–616, Sep 2008. doi: 10.1357/002224008787536790. URL http://dx.doi.org/10.1357/002224008787536790.

Mark Falvey and René D. Garreaud. Regional cooling in a warming world: Recent temperature trends in the southeast pacific and along the west coast of subtropical south america (1979–2006). *Journal of Geophysical Research*, 114(D4), Feb 2009. doi: 10.1029/2008jd010519. URL http://dx.doi.org/10.1029/2008JD010519.

Dante Figueroa and Carlos Moffat. On the influence of topography in the induction of coastal upwelling along the chilean coast. *Geophysical Research Letters*, 27(23):3905–3908, Dec 2000. doi: 10.1029/1999gl011302. URL http://dx.doi.org/10.1029/1999GL011302.

Tomas R. Fonseca. *An overview of the poleward undercurrent and upwelling along the Chilean coast*, page 203–228. American Geophysical Union, 1989. doi: 10.1029/ce034p0203. URL http://dx.doi.org/10.1029/CE034p0203.

Daniel J. Franklin, Alex J. Poulton, Michael Steinke, Jeremy Young, Ilka Peeken, and Gill Malin. Dimethylsulphide, dmsp-lyase activity and microplankton community structure inside and outside of the mauritanian upwelling. *Progress in Oceanography*, 83(1–4): 134–142, Dec 2009. doi: 10.1016/j.pocean.2009.07.011. URL http://dx.doi.org/10.1016/j.pocean.2009.07.011.

I. Frenger, N. Gruber, R. Knutti, and M. Münnich. Imprint of southern ocean eddies on winds, clouds and rainfall. *Nature Geoscience*, 6(8):608–612, Jul 2013. doi: 10.1038/ngeo1863. URL http://dx.doi.org/10.1038/ngeo1863.

Pierre Fréon, Manuel Barange, and Javier Arístegui. Eastern boundary upwelling ecosystems: Integrative and comparative approaches. *Progress in Oceanography*, 83(1–4):1–14, Dec 2009. doi: 10.1016/j.pocean.2009.08.001. URL http://dx.doi.org/10.1016/j.pocean.2009.08.001.

R. D. Garreaud, J. A. Rutllant, R. C. Muñoz, D. A. Rahn, M. Ramos, and D. Figueroa. Vocals-cupex: the chilean upwelling experiment. *Atmospheric Chemistry and Physics*, 11 (5):2015–2029, Mar 2011. doi: 10.5194/acp-11-2015-2011. URL http://dx.doi.org/10.5194/acp-11-2015-2011.

René D. Garreaud and Mark Falvey. The coastal winds off western subtropical south america in future climate scenarios. *International Journal of Climatology*, 29(4):543–554, Mar 2009. doi: 10.1002/joc.1716. URL http://dx.doi.org/10.1002/joc.1716.

RenéD. Garreaud and Ricardo C. Muñoz. The low-level jet off the west coast of subtropical south america: Structure and variability. *Monthly Weather Review*, 133(8):2246–2261, Aug 2005. doi: 10.1175/mwr2972.1. URL http://dx.doi.org/10.1175/MWR2972.1.

K. Goubanova, V. Echevin, B. Dewitte, F. Codron, K. Takahashi, P. Terray, and M. Vrac. Statistical downscaling of sea-surface wind over the peru–chile upwelling region: diagnosing the impact of climate change from the ipsl-cm4 model. *Climate Dynamics*, 36(7–8):1365–1378, May 2010. doi: 10.1007/s00382-010-0824-0. URL http://dx.doi.org/10.1007/s00382-010-0824-0.

Nicolas Gruber, Manuel Gloor, Sara E. Mikaloff Fletcher, Scott C. Doney, Stephanie Dutkiewicz, Michael J. Follows, Markus Gerber, Andrew R. Jacobson, Fortunat Joos, Keith Lindsay, and et al. Oceanic sources, sinks, and transport of atmospheric co2. *Global Biogeochemical Cycles*, 23(1):n/a–n/a, Feb 2009. doi: 10.1029/2008gb003349. URL http://dx.doi.org/10.1029/2008GB003349.

Nicolas Gruber, Zouhair Lachkar, Hartmut Frenzel, Patrick Marchesiello, Matthias Münnich, James C. McWilliams, Takeyoshi Nagai, and Gian-Kasper Plattner. Eddy-induced reduction of biological production in eastern boundary upwelling systems. *Nature Geoscience*, 4(11):787–792, Oct 2011. doi: 10.1038/ngeo1273. URL http://dx.doi.org/10.1038/NGEO1273.

Dimitri Gutiérrez, Ioanna Bouloubassi, Abdelfettah Sifeddine, Sara Purca, Katerina Goubanova, Michelle Graco, David Field, Laurence Méjanelle, Federico Velazco, Anne Lorre, and et al. Coastal cooling and increased productivity in the main upwelling zone off peru since the mid-twentieth century. *Geophysical Research Letters*, 38(7):n/a–n/a, Apr 2011. doi: 10.1029/2010gl046324. URL http://dx.doi.org/10.1029/2010GL046324.

A. E. Hill, B. Hickey, F. Shillington, P. T. Strub, K. H. Brink, E. Barton, and A. Thomas. Eastern boundary currents: a pan-regional review. In Brink and A. R., editor, *Robinson*, pages 29–68. Regional Studies and Syntheses vol. 11. John Wiley, Hoboken, N. J, The SeaThe Global Coastal Ocean, 1998.

Samuel Hormazabal. Coastal transition zone off chile. *Journal of Geophysical Research*, 109 (C1), 2004. doi: 10.1029/2003jc001956. URL http://dx.doi.org/10.1029/2003JC001956.

D. A. Hutchins, G. R. DiTullio, Y. Zhang, and K. W. Bruland. An iron limitation mosaic in the california upwelling regime. *Limnology and Oceanography*, 43(6):1037–1054, Sep 1998. doi: 10.4319/lo.1998.43.6.1037. URL http://dx.doi.org/10.4319/lo.1998.43.6.1037.

D. A. Hutchins, C. E. Hare, R. S. Weaver, Y. Zhang, G. F. Firme, G. R. DiTullio, M. B. Alm, S. F. Riseman, J. M. Maucher, M. E. Geesey, and et al. Phytoplankton iron limitation in the humboldt current and peru upwelling. *Limnology and Oceanography*, 47(4):997–1011, Jul 2002. doi: 10.4319/lo.2002.47.4.0997. URL http://dx.doi.org/10.4319/lo.2002.47.4.0997.

Serena Illig, Boris Dewitte, Katerina Goubanova, Gildas Cambon, Julien Boucharel, Florian Monetti, Carlos Romero, Sara Purca, and Roberto Flores. Forcing mechanisms of intraseasonal sst variability off central peru in 2000-2008. *Journal of Geophysical Research: Oceans*, 119(6):3548–3573, Jun 2014. doi: 10.1002/2013jc009779. URL http://dx.doi.org/10.1002/2013JC009779.

M. G. Jacox and C. A. Edwards. Upwelling source depth in the presence of nearshore wind stress curl. *Journal of Geophysical Research: Oceans*, 117(C5):n/a–n/a, May 2012. doi: 10.1029/2011jc007856. URL http://dx.doi.org/10.1029/2011JC007856.

Xin Jin, Changming Dong, Jaison Kurian, James C. McWilliams, Dudley B. Chelton, and Zhijin Li. Sst–wind interaction in coastal upwelling: Oceanic simulation with empirical coupling. *Journal of Physical Oceanography*, 39(11):2957–2970, Nov 2009. doi: 10.1175/2009jpo4205.1. URL http://dx.doi.org/10.1175/2009JPO4205.1.

A. Kock, D. L. Arévalo-Martínez, C. R. Löscher, and H. W. Bange. Extreme n2o accumulation in the coastal oxygen minimum zone off peru. *Biogeosciences*, 13(3):827–840, Feb 2016. doi: 10.5194/bg-13-827-2016. URL http://dx.doi.org/10.5194/bg-13-827-2016.

E.B. Kraus and J.A. Businger. *Atmosphere-Ocean Interaction*. Oxford Monographs on Geology and Geophysics. Oxford University Press, 1994. ISBN 9780195362084. URL https://books.google.cl/books?id=oWyM5w2np2QC.

Jochen Kämpf and Piers Chapman. *Upwelling Systems of the World*. Springer International Publishing, 2016. doi: 10.1007/978-3-319-42524-5. URL http://dx.doi.org/10.1007/978-3-319-42524-5.

Lisa A. Levin, Cynthia L. Huggett, and Karen F. Wishner. Control of deep-sea benthic community structure by oxygen and organic-matter gradients in the eastern pacific ocean. *Journal of Marine Research*, 49(4):763–800, Nov 1991. doi: 10.1357/002224091784995756. URL http://dx.doi.org/10.1357/002224091784995756.

Elizabeth A. Logerwell and Paul E. Smith. Mesoscale eddies and survival of late stage pacific sardine (sardinops sagax) larvae. *Fisheries Oceanography*, 10(1):13–25, Mar 2001. doi: 10.1046/j.1365-2419.2001.00152.x. URL http://dx.doi.org/10.1046/j.1365-2419.2001.00152.x.

Amala Mahadevan. Eddy effects on biogeochemistry. *Nature*, 506(7487):168–169, Jan 2014. doi: 10.1038/nature13048. URL http://dx.doi.org/10.1038/nature13048.

Julia V. Manganello and Bohua Huang. The influence of systematic errors in the southeast pacific on enso variability and prediction in a coupled gcm. *Climate Dynamics*, 32(7–8): 1015–1034, Apr 2008. doi: 10.1007/s00382-008-0407-5. URL http://dx.doi.org/10.1007/s00382-008-0407-5.

P. Marchesiello and P. Estrade. Eddy activity and mixing in upwelling systems: a comparative study of northwest africa and california regions. *International Journal of Earth Sciences*, 98(2):299–308, Aug 2007. doi: 10.1007/s00531-007-0235-6. URL http://dx.doi.org/10.1007/s00531-007-0235-6.

P. Marchesiello and P. Estrade. Upwelling limitation by onshore geostrophic flow. *Journal of Marine Research*, 68(1):37–62, Jan 2010. doi: 10.1357/002224010793079004. URL http://dx.doi.org/10.1357/002224010793079004.

Patrick Marchesiello, James C. McWilliams, and Alexander Shchepetkin. Equilibrium structure and dynamics of the california current system. *Journal of Physical Oceanography*, 33(4):753–783, Apr 2003. doi: 10.1175/1520-0485(2003)33<753:esadot>2.0.co;2. URL http://dx.doi.org/10.1175/1520-0485(2003)33<753:esadot>2.0.co;2.

C. R. Mechoso, R. Wood, R. Weller, C. S. Bretherton, A. D. Clarke, H. Coe, C. Fairall, J. T. Farrar, G. Feingold, R. Garreaud, and et al. Ocean–cloud–atmosphere–land interactions in the southeastern pacific: The vocals program. *Bulletin of the American Meteorological Society*, 95(3):357–375, Mar 2014. doi: 10.1175/bams-d-11-00246.1. URL http://dx.doi.org/10.1175/BAMS-D-11-00246.1.

Monique Messié, Jesus Ledesma, Dorota D. Kolber, Reiko P. Michisaki, David G. Foley, and Francisco P. Chavez. Potential new production estimates in four eastern boundary upwelling ecosystems. *Progress in Oceanography*, 83(1–4):151–158, Dec 2009. doi: 10.1016/j.pocean.2009.07.018. URL http://dx.doi.org/10.1016/j.pocean.2009.07.018.

Sarah E. Moffitt, Russell A. Moffitt, Wilson Sauthoff, Catherine V. Davis, Kathryn Hewett, and Tessa M. Hill. Paleoceanographic insights on recent oxygen minimum zone expansion: Lessons for modern oceanography. *PLOS ONE*, 10(1):e0115246, Jan 2015. doi: 10.1371/journal.pone.0115246. URL http://dx.doi.org/10.1371/journal.pone.0115246.

Volker Mohrholz, Anja Eggert, Tim Junker, Günther Nausch, Thomas Ohde, and Martin Schmidt. Cross shelf hydrographic and hydrochemical conditions and their short term variability at the northern benguela during a normal upwelling season. *Journal of Marine*

Systems, 140:92–110, Nov 2014. doi: 10.1016/j.jmarsys.2014.04.019. URL http://dx.doi.org/10.1016/j.jmarsys.2014.04.019.

Carmen E. Morales, Samuel Hormazabal, Marco Correa-Ramirez, Oscar Pizarro, Nelson Silva, Camila Fernandez, Valeria Anabalón, and M. Loreto Torreblanca. Mesoscale variability and nutrient–phytoplankton distributions off central-southern chile during the upwelling season: The influence of mesoscale eddies. *Progress in Oceanography*, 104: 17–29, Oct 2012. doi: 10.1016/j.pocean.2012.04.015. URL http://dx.doi.org/10.1016/j.pocean.2012.04.015.

Rosemary Morrow and Pierre-Yves Le Traon. Recent advances in observing mesoscale ocean dynamics with satellite altimetry. *Advances in Space Research*, 50(8):1062–1076, Oct 2012. doi: 10.1016/j.asr.2011.09.033. URL http://dx.doi.org/10.1016/j.asr.2011.09.033.

Ricardo C. Muñoz and RenéD. Garreaud. Dynamics of the low-level jet off the west coast of subtropical south america. *Monthly Weather Review*, 133(12):3661–3677, Dec 2005. doi: 10.1175/mwr3074.1. URL http://dx.doi.org/10.1175/MWR3074.1.

S. W. A. Naqvi, H. W. Bange, L. Farías, P. M. S. Monteiro, M. I. Scranton, and J. Zhang. Marine hypoxia/anoxia as a source of ch4 and n2o. *Biogeosciences*, 7(7):2159–2190, Jul 2010. doi: 10.5194/bg-7-2159-2010. URL http://dx.doi.org/10.5194/bg-7-2159-2010.

N. Narayan, A. Paul, S. Mulitza, and M. Schulz. Trends in coastal upwelling intensity during the late 20th century. *Ocean Science*, 6(3):815–823, Sep 2010. doi: 10.5194/os-6-815-2010. URL http://dx.doi.org/10.5194/os-6-815-2010.

Steven J Neshyba, Christopher NK Mooers, Robert L Smith, and Richard T Barber. *Poleward flows along eastern ocean boundaries*, volume 34. Springer Science & Business Media, 2013.

A. Paulmier and D. Ruiz-Pino. Oxygen minimum zones (omzs) in the modern ocean. *Progress in Oceanography*, 80(3–4):113–128, Mar 2009. doi: 10.1016/j.pocean.2008.08.001. URL http://dx.doi.org/10.1016/j.pocean.2008.08.001.

A. Paulmier, D. Ruiz-Pino, V. Garçon, and L. Farías. Maintaining of the eastern south pacific oxygen minimum zone (omz) off chile. *Geophysical Research Letters*, 33(20), Oct 2006. doi: 10.1029/2006gl026801. URL http://dx.doi.org/10.1029/2006GL026801.

Cori Pegliasco, Alexis Chaigneau, and Rosemary Morrow. Main eddy vertical structures observed in the four major eastern boundary upwelling systems. *Journal of Geophysical Research: Oceans*, 120(9):6008–6033, Sep 2015. doi: 10.1002/2015jc010950. URL http://dx.doi.org/10.1002/2015JC010950.

P. Penven. Average circulation, seasonal cycle, and mesoscale dynamics of the peru current system: A modeling approach. *Journal of Geophysical Research*, 110(C10), 2005. doi: 10.1029/2005jc002945. URL http://dx.doi.org/10.1029/2005JC002945.

P. Penven, C. Roy, G.B. Brundrit, Alain Colin De Verdiere, P. Fréon, A.S. Johnson, J.R.E. Lutjeharms, and F.A. Shillington. A regional hydrodynamic model of upwelling in the Southern Benguela. *South African Journal of Science*, 97:472–476, 2001. URL https://hal.archives-ouvertes.fr/hal-00310384.

Natalie Perlin, Eric D. Skyllingstad, Roger M. Samelson, and Philip L. Barbour. Numerical simulation of air–sea coupling during coastal upwelling. *Journal of Physical Oceanography*, 37(8):2081–2093, Aug 2007. doi: 10.1175/jpo3104.1. URL http://dx.doi.org/10.1175/JPO3104.1.

M. A. Peña, S. Katsev, T. Oguz, and D. Gilbert. Modeling dissolved oxygen dynamics and hypoxia. *Biogeosciences*, 7(3):933–957, Mar 2010. doi: 10.5194/bg-7-933-2010. URL http://dx.doi.org/10.5194/bg-7-933-2010.

S. Pond and G.L. Pickard. *Introductory Dynamical Oceanography*. Pergamon international library of science, technology, engineering and social studies. Butterworth-Heinemann, 1983. ISBN 9780750624961. URL https://books.google.cl/books?id=5pQf8dBYxIUC.

David A. Rahn, René D. Garreaud, and José A. Rutllant. The low-level atmospheric circulation near tongoy bay–point lengua de vaca (chilean coast, 30°s). *Monthly Weather Review*, 139(11):3628–3647, Nov 2011. doi: 10.1175/mwr-d-11-00059.1. URL http://dx.doi.org/10.1175/MWR-D-11-00059.1.

Lionel Renault, Boris Dewitte, Mark Falvey, René Garreaud, Vincent Echevin, and Fabrice Bonjean. Impact of atmospheric coastal jet off central chile on sea surface temperature from satellite observations (2000–2007). *Journal of Geophysical Research*, 114(C8), Aug 2009. doi: 10.1029/2008jc005083. URL http://dx.doi.org/10.1029/2008JC005083.

Lionel Renault, Boris Dewitte, Patrick Marchesiello, Séréna Illig, Vincent Echevin, Gildas Cambon, Marcel Ramos, Orlando Astudillo, Patrick Minnis, and J. Kirk Ayers. Upwelling response to atmospheric coastal jets off central chile: A modeling study of the october 2000 event. *Journal of Geophysical Research: Oceans*, 117(C2):n/a–n/a, Feb 2012. doi: 10.1029/2011jc007446. URL http://dx.doi.org/10.1029/2011jc007446.

Lionel Renault, Alex Hall, and James C. McWilliams. Orographic shaping of us west coast wind profiles during the upwelling season. *Climate Dynamics*, 46(1–2):273–289, Apr 2015. doi: 10.1007/s00382-015-2583-4. URL http://dx.doi.org/10.1007/s00382-015-2583-4.

Lionel Renault, Curtis Deutsch, James C. McWilliams, Hartmut Frenzel, Jun-Hong Liang, and François Colas. Partial decoupling of primary productivity from upwelling in the california current system. *Nature Geoscience*, 9(7):505–508, May 2016a. doi: 10.1038/ngeo2722. URL http://dx.doi.org/10.1038/ngeo2722.

Lionel Renault, M. Jeroen Molemaker, James C. McWilliams, Alexander F. Shchepetkin, Florian Lemarié, Dudley Chelton, Serena Illig, and Alex Hall. Modulation of wind work by oceanic current interaction with the atmosphere. *Journal of Physical Oceanography*, 46(6):1685–1704, Jun 2016b. doi: 10.1175/jpo-d-15-0232.1. URL http://dx.doi.org/10.1175/JPO-D-15-0232.1.

Ingo Richter. Climate model biases in the eastern tropical oceans: causes, impacts and ways forward. *Wiley Interdisciplinary Reviews: Climate Change*, 6(3):345–358, Mar 2015. doi: 10.1002/wcc.338. URL http://dx.doi.org/10.1002/wcc.338.

Anna Rubio, Bruno Blanke, Sabrina Speich, Nicolas Grima, and Claude Roy. Mesoscale eddy activity in the southern benguela upwelling system from satellite altimetry and model data. *Progress in Oceanography*, 83(1–4):288–295, Dec 2009. doi: 10.1016/j.pocean.2009.07.029. URL http://dx.doi.org/10.1016/j.pocean.2009.07.029.

JOSÉ Rutllant and VIVIAN Montecino. Multiscale upwelling forcing cycles and biological response off north-central chile. *Revista Chilena de Historia Natural*, 75(217):e231, 2002.

Ryan R. Rykaczewski, John P. Dunne, William J. Sydeman, Marisol García-Reyes, Bryan A. Black, and Steven J. Bograd. Poleward displacement of coastal upwelling-favorable winds in the ocean's eastern boundary currents through the 21st century. *Geophysical Research Letters*, 42(15):6424–6431, Aug 2015. doi: 10.1002/2015gl064694. URL http://dx.doi.org/10.1002/2015GL064694.

J. L. Sarmiento, R. Murnane, C. L. Quere, R. Keeling, and R. G. Williams. Air-sea co2 transfer and the carbon budget of the north atlantic [and discussion]. *Philosophical Transactions of the Royal Society B: Biological Sciences*, 348(1324):211–219, May 1995. doi: 10.1098/rstb.1995.0063. URL http://dx.doi.org/10.1098/rstb.1995.0063.

Lucia Scaff, Jose A. Rutllant, David Rahn, Simon Gascoin, and Roberto Rondanelli. Meteorological interpretation of orographic precipitation gradients along an andes west slope basin at 30°s (elqui valley, chile). *Journal of Hydrometeorology*, 18(3):713–727, Mar 2017. doi: 10.1175/jhm-d-16-0073.1. URL http://dx.doi.org/10.1175/JHM-D-16-0073.1.

Harald Schunck, Gaute Lavik, Dhwani K. Desai, Tobias Großkopf, Tim Kalvelage, Carolin R. Löscher, Aurélien Paulmier, Sergio Contreras, Herbert Siegel, Moritz Holtappels, and et al. Giant hydrogen sulfide plume in the oxygen minimum zone off peru supports chemolithoautotrophy. *PLoS ONE*, 8(8):e68661, Aug 2013. doi: 10.1371/journal.pone.0068661. URL http://dx.doi.org/10.1371/journal.pone.0068661.

Gary Shaffer, Samuel Hormazabal, Oscar Pizarro, and Sergio Salinas. Seasonal and interannual variability of currents and temperature off central chile. *Journal of Geophysical Research: Oceans*, 104(C12):29951–29961, Dec 1999. doi: 10.1029/1999jc900253. URL http://dx.doi.org/10.1029/1999JC900253.

Kenneth Sherman and Gotthilf Hempel. The unep large marine ecosystem report: A perspective on changing conditions in lmes of the world's regional seas. 2008.

L. Stramma, H. W. Bange, R. Czeschel, A. Lorenzo, and M. Frank. On the role of mesoscale eddies for the biological productivity and biogeochemistry in the eastern tropical pacific ocean off peru. *Biogeosciences*, 10(11):7293–7306, Nov 2013. doi: 10.5194/bg-10-7293-2013. URL http://dx.doi.org/10.5194/bg-10-7293-2013.

P. Ted Strub, Vincent Combes, Frank A. Shillington, and Oscar Pizarro. *Currents and Processes along the Eastern Boundaries*, page 339–384. Elsevier, 2013. doi: 10.1016/b978-0-12-391851-2.00014-3. URL http://dx.doi.org/10.1016/B978-0-12-391851-2.00014-3.

Harald Ulrich Sverdrup. Wind-driven currents in a baroclinic ocean; with application to the equatorial currents of the eastern pacific. *Proceedings of the National Academy of Sciences*, 33(11):318–326, 1947.

Lynne D Talley. *Descriptive physical oceanography: an introduction*. Academic press, 2011.

Hiroki Tokinaga and Shang-Ping Xie. Wave- and anemometer-based sea surface wind (waswind) for climate change analysis*. *Journal of Climate*, 24(1):267–285, Jan 2011. doi: 10.1175/2010jcli3789.1. URL http://dx.doi.org/10.1175/2010JCLI3789.1.

O. Ulloa, D. E. Canfield, E. F. DeLong, R. M. Letelier, and F. J. Stewart. Microbial oceanography of anoxic oxygen minimum zones. *Proceedings of the National Academy of Sciences*, 109(40):15996–16003, Sep 2012. doi: 10.1073/pnas.1205009109. URL http://dx.doi.org/10.1073/pnas.1205009109.

Gabriel Vargas, Silvio Pantoja, José A. Rutllant, Carina B. Lange, and Luc Ortlieb. Enhancement of coastal upwelling and interdecadal enso-like variability in the peru-chile current since late 19th century. *Geophysical Research Letters*, 34(13):n/a–n/a, Jul 2007. doi: 10.1029/2006gl028812. URL http://dx.doi.org/10.1029/2006GL028812.

Jennifer Veitch, Pierrick Penven, and Frank Shillington. Modeling equilibrium dynamics of the benguela current system. *Journal of Physical Oceanography*, 40(9):1942–1964, Sep 2010. doi: 10.1175/2010jpo4382.1. URL http://dx.doi.org/10.1175/2010JPO4382.1.

Odette A. Vergara, Vincent Echevín, Héctor H. Sepúlveda, Francois Colas, and Renato A. Quiñones. Modelling the seasonal dynamics of the peru-chile undercurrent off central chile (30–40°s). *Continental Shelf Research*, 123:61–79, Jul 2016. doi: 10.1016/j.csr.2016.04.001. URL http://dx.doi.org/10.1016/j.csr.2016.04.001.

A. B. Villas Bôas, O. T. Sato, A. Chaigneau, and G. P. Castelão. The signature of mesoscale eddies on the air-sea turbulent heat fluxes in the south atlantic ocean. *Geophysical Research Letters*, 42(6):1856–1862, Mar 2015. doi: 10.1002/2015gl063105. URL http://dx.doi.org/10.1002/2015GL063105.

Chunzai Wang, Liping Zhang, Sang-Ki Lee, Lixin Wu, and Carlos R. Mechoso. A global perspective on cmip5 climate model biases. *Nature Climate Change*, 4(3):201–205, Feb 2014. doi: 10.1038/nclimate2118. URL http://dx.doi.org/10.1038/NCLIMATE2118.

Daiwei Wang, Tarik C. Gouhier, Bruce A. Menge, and Auroop R. Ganguly. Intensification and spatial homogenization of coastal upwelling under climate change. *Nature*, 518 (7539):390–394, Feb 2015. doi: 10.1038/nature14235. URL http://dx.doi.org/10.1038/nature14235.

R. Wood, C. R. Mechoso, C. S. Bretherton, R. A. Weller, B. Huebert, F. Straneo, B. A. Albrecht, H. Coe, G. Allen, G. Vaughan, and et al. The vamos ocean-cloud-atmosphere-land study regional experiment (vocals-rex): goals, platforms, and field operations. *Atmospheric Chemistry and Physics*, 11(2):627–654, Jan 2011. doi: 10.5194/acp-11-627-2011. URL http://dx.doi.org/10.5194/acp-11-627-2011.

M. C. Wyant, R. Wood, C. S. Bretherton, C. R. Mechoso, J. Bacmeister, M. A. Balmaseda, B. Barrett, F. Codron, P. Earnshaw, J. Fast, and et al. The prevoca experiment: modeling the lower troposphere in the southeast pacific. *Atmospheric Chemistry and Physics*, 10 (10):4757–4774, May 2010. doi: 10.5194/acp-10-4757-2010. URL http://dx.doi.org/10.5194/acp-10-4757-2010.

Jin-Yi Yu and Carlos R. Mechoso. Links between annual variations of peruvian stratocumulus clouds and of sst in the eastern equatorial pacific. *Journal of Climate*, 12(11):3305–3318, Nov 1999. doi: 10.1175/1520-0442(1999)012<3305:lbavop>2.0.co;2. URL http://dx.doi.org/10.1175/1520-0442(1999)012<3305:LBAVOP>2.0.CO;2.